

MICROSTRUCTURAL PREDICTION IN METAL CUTTING AND IMPROVEMENT OF
MACHINABILITY AND SURFACE INTEGRITY VIA LASER-ASSISTED MACHINING

A Dissertation

Submitted to the Faculty

of

Purdue University

by

Hongtao Ding

In Partial Fulfillment of the

Requirements for the Degree

of

Doctor of Philosophy

May 2012

Purdue University

West Lafayette, Indiana

To my wife, Ting Lu.

ACKNOWLEDGEMENTS

First and foremost, I must thank Dr. Yung C. Shin, who guided me through my PhD research and introduced me to the exciting fields of laser-assisted machining and material process modeling. His invaluable advices have directed my research work and inspired me to find the solutions to the difficult problems I encountered. I would also like to thank Dr. Klod Kokini, Dr. Ganesh Subbarayan, Dr. Gary Cheng and Dr. Keith Bowman for serving on my examination and advisory committee and for providing me with ample guidance.

I have been very fortunate to work with Ninggang Shen, Yinggang Tian, Gary Hedberg, Tyler Davis, Benxin Wu, Wenda Tan, Yunfeng Cao, Shaoyi Wen and Neil Bailey, who as fellow graduate students helped me immensely for my research. I would like to thank them for making my PhD at Purdue an enjoyable experience.

I would like to thank Mike Sherwood and John Wheeler for their help on machining experiments. I would also like to thank Dave Roberts, Diana Akers and all other staffs in the ME department for their help.

I am grateful for having the best family and I thank my wife, Ting, for her sacrifice and her love throughout my PhD. I want to thank my parents and sister for their unwavering support.

TABLE OF CONTENTS

	Page
LIST OF TABLES.....	viii
LIST OF FIGURES.....	x
ABSTRACT	xiv
CHAPTER 1. INTRODUCTION.....	1
1.1. Rationale.....	1
1.2. Laser-Assisted Machining	4
1.2.1. Laser-Assisted Machining of Difficult-to-Machine Metal Alloys.....	4
1.2.2. Laser-Assisted Micromachining of Difficult-to-Machine Metal Alloys	6
1.3. Thermal and Mechanical Modeling of Laser-Assisted Machining	9
1.3.1. Thermal Modeling of Laser-Assisted Machining.....	9
1.3.2. Mechanical Modeling of Machining	10
1.4. Microstructure Alteration in Metal Cutting.....	13
1.4.1. Grain Refinement in Cutting	13
1.4.2. Phase Change in Steel Cutting	19
1.4.3. White Layer Formation Mechanisms.....	22
1.5. Research Objectives.....	25
1.6. Dissertation Outline.....	26
CHAPTER 2. THERMAL AND MECHANICAL MODELING OF MACHINING PROCESSES.....	28
2.1. Coupled Eulerian-Lagrangian Modeling of Orthogonal Cutting	28
2.1.1. CEL Modeling	28
2.1.2. Model Validation.....	29
2.2. Finite Element Modeling of Laser-Assisted Micro-Milling.....	31
2.2.1. LAMM Experimental Work	31
2.2.2. Strain Gradient Constitutive Model.....	35

	Page
2.2.3. FE Models of Chip Formation Analysis.....	37
2.2.4. Validation of Cutting Force	38
2.3. Thermal and Mechanical Modeling Analysis of Laser-Assisted Micro-Milling	40
2.3.1. Workpiece Temperature Increase due to Laser Heating.....	40
2.3.2. Workpiece Temperature after Multi LAMM Cycles.....	44
2.3.3. Tool Temperature after Multi LAMM Cycles	47
2.3.4. Chip Formation and Temperature Effect on Workpiece Flow Stress	49
2.3.5. Tool Wear Analysis in Laser-Assisted Side Cutting	51
2.3.6. Surface Integrity Analysis.....	54
2.4. Summary.....	56
CHAPTER 3. GRAIN REFINEMENT MODELING IN MACHINING	58
3.1. Dislocation Density-Based Material Model	58
3.2. Determination of Material Model Parameters.....	62
3.3. Simulations of Grain Refinement by Machining	66
3.3.1. Chip Formation and Deformation Field	67
3.3.2. Grain Refinement.....	69
3.3.3. Discussions	77
3.4. Summary.....	78
CHAPTER 4. PHASE CHANGE MODELING IN MACHINING.....	80
4.1. Phase Transformation Kinetics	80
4.2. Constituent Phase Properties of AISI 1045 Steel.....	82
4.3. Metallo-thermo-mechanical Coupling.....	86
4.4. Simulations	88
4.4.1. Implementation of the Material Models	88
4.4.2. Orthogonal Cutting Experiments of 1045 Steel.....	89
4.5. Simulation Results	92
4.6. Discussions.....	99
4.7. Summary.....	101
CHAPTER 5. MULTI-PHYSICS MODELING OF MICROSTRUCTURE ALTERATION IN HARD TURNING.....	102
5.1. Hard Turning Experiments.....	102

	Page
5.2. Models	103
5.2.1. Material Properties and Constitutive Models of AISI 52100 Steel	103
5.2.2. Phase Transformation Kinetics and Metallo-thermo-mechanical Coupling	104
5.2.3. Grain Refinement and Dislocation Density Evolution.....	106
5.2.4. Numerical Solution	107
5.3. Results and Discussions	109
5.4. Summary.....	117
CHAPTER 6. SURFACE INTEGRITY ANALYSIS OF LASER-ASSISTED MACHINING OF HARDENED	
STEEL PARTS	118
6.1. Problem Statement.....	118
6.2. Improvement of LAM Thermal Model.....	119
6.2.1. Thermal Modeling of Laser-Assisted Face Turning.....	119
6.2.2. Thermal Modeling of Laser-Assisted Profile Turning.....	126
6.3. LAM Process and Modeling	130
6.3.1. Experimental Setup.....	130
6.3.2. Temperature Prediction and Measurement.....	133
6.3.3. Microstructural Prediction of the LAM Process.....	138
6.4. Surface Integrity Analysis.....	141
6.4.1. LAM Experiments.....	141
6.4.2. Surface Finish.....	142
6.4.3. Precise Size Control.....	143
6.4.4. Microstructures	144
6.4.5. Hardness	145
6.4.6. Residual Stress	146
6.4.7. Discussions.....	149
6.5. Summary.....	150
CHAPTER 7. CONCLUSIONS AND FUTURE WORK	
7.1. Summary.....	151
7.2. Conclusions	155
7.3. Future Work.....	155

	Page
LIST OF REFERENCES	158
VITA.....	177

LIST OF TABLES

Table	Page
Table 2.1. CEL model validation test conditions	30
Table 2.2. Johnson-Cook type constitutive model parameters for AISI 316L.....	30
Table 2.3. LAMM side cutting tests of bulk workpiece configuration	34
Table 2.4. LAMM side cutting tests of fin workpiece configuration.....	34
Table 2.5. Johnson-Cook constitutive model parameters of the workpiece materials.....	36
Table 2.6. Strain gradient parameters of the workpiece materials.....	36
Table 2.7. Thermal properties of the workpiece materials	41
Table 2.8. Absorptivity of the workpiece materials at CO ₂ laser wavelength of 10.6 μm	41
Table 3.1. Orthogonal cutting tests simulated for Al 6061 T6 and OFHC Cu.....	63
Table 3.2. Material thermo-mechanical properties.....	65
Table 3.3. Material constitutive model parameters	65
Table 3.4. Dislocation density-based model parameters	65
Table 3.5. Simulation results for orthogonal cutting of Al 6061 T6 and OFHC Cu.....	75
Table 4.1. Microstructural properties for AISI 1045 steel	82
Table 4.2. Physical properties of constituent phases for AISI 1045 steel	84
Table 4.3. The constitutive model parameters of constituent phases for AISI 1045 steel.....	86
Table 4.4. Orthogonal cutting conditions for AISI 1045 steel.....	90
Table 4.5. Comparison of model predictions with experimental data from	95
Table 5.1. Hard turning conditions	103
Table 5.2. Physical properties of constituent phases for AISI 52100 steel.....	104
Table 5.3. Constitutive model parameters of phases for AISI 52100 steel.....	104
Table 5.4. Dislocation density-model constants.....	107
Table 6.1. Dislocation density-model constants of 4130 steel.....	139
Table 6.2. LAM experimental conditions	141

Table.....	Page
Table 6.3. X-ray parameters for 4340 steel	147

LIST OF FIGURES

Figure	Page
Figure 1.1. Chip formation relative to chip load and cutting edge radius	7
Figure 1.2. TEM images of grain refinement of CP Ti.	18
Figure 1.3. Metallo-thermo-mechanical coupling in cutting of steels.....	20
Figure 1.4. Phase changes in hypo-eutectoid steel during heating.....	21
Figure 1.5. Processing map of the white layers formed during machining of AISI 52100 steel. ...	24
Figure 2.1. CEL model setup schematic	29
Figure 2.2. Comparison of predicted cutting force with experiments.....	30
Figure 2.3. Comparison of predicted temperature distributions for Test 2	31
Figure 2.4. LAMM test configurations	32
Figure 2.5. Johnson-Cook and strain gradient constitutive behaviors of the workpiece materials.	36
Figure 2.6. FE models of chip formation	37
Figure 2.7. Measured and predicted cutting forces in micromachining of hardened H13 steels .	40
Figure 2.8. Temperature fields of Ti6Al4V undergoing LAMM side cutting	42
Figure 2.9. Temperature predictions by the prismatic thermal model	43
Figure 2.10. Thermal analyses in fin workpiece side cutting of 422SS	44
Figure 2.11. Workpiece nodal temperature histories in conventional micro-milling and LAMM of 422SS	46
Figure 2.12. Heat transfer analysis of the tool	48
Figure 2.13. Tool cutting edge temperatures in LAMM of 422SS under the condition of 422fin-2.	49
Figure 2.14. Chip formation and cutting temperatures of LAMM bulk side cutting of 422SS at 60 μ s cutting time under the condition of 422bulk-3 ($V=18.85\text{m/min}$).....	50
Figure 2.15. Temperatures and flow stresses in LAMM side cutting of 422SS.....	51

Figure	Page
Figure 2.16. Tool geometry and tool wear mode after 33 minutes LAMM fin side cutting 422fin-2	52
Figure 2.17. Tool wear for fin side cutting of 422SS and IN-718 under the conditions of 422fin-1, 2 and 718fin-1, 3	52
Figure 2.18. Tool wear predictions for fin side cutting of 422SS	54
Figure 2.19. Workpiece velocity fields of Inconel 718 undergoing fin side cutting tests 718 fin 1 and 3	55
Figure 2.20. Machined side surface finish by fin side cutting of Inconel 718 and 422SS	56
Figure 3.1. Flow chart for CEL modeling using the dislocation density-based material model.....	62
Figure 3.2. Dislocation density-based plasticity model predictions	66
Figure 3.3. Shear strain rate for cutting of OFHC copper under condition: $V=0.01$ m/s, $\alpha=10^\circ$ and $doc=0.1$ mm.....	67
Figure 3.4. Cumulative shear strain along path-1 for cutting of OFHC copper under condition: $V=0.01$ m/s, $\alpha=10^\circ$ and $doc=0.1$ mm.....	68
Figure 3.5. Average shear strain and chip thickness for cutting of Al 6061 T6 under conditions Al1-3	69
Figure 3.6. Predicted microstructural evolution for cutting of OFHC Cu under conditions Cu3 ..	70
Figure 3.7. Predicted grain size distribution in the chips for Al 6061 T6.	72
Figure 3.8. Grain size in the chips for Al 6061 T6 under conditions Al1-3 with varying tool rake angles	73
Figure 3.9. Grain size in the chips for OFHC Cu under conditions Cu1-4 with varying cutting speeds.....	75
Figure 3.10. Grain misorientation angle distribution for cutting test Cu4 at a cutting speed of 1.25 m/s.....	76
Figure 4.1. Temperature-dependent physical properties of phases for AISI 1045 steel	85
Figure 4.2. Constitutive model predictions vs. SHPB test results	86
Figure 4.3. Flowchart for implementation of the material model.....	89
Figure 4.4. Predictions of temperature, Mises stress and phase field for tests A7 and A8.....	94
Figure 4.5. Comparison of the deformed chip thickness predicted with the experimental data ..	96

Figure	Page
Figure 4.6. Prediction of volume fraction of austenite in the chip and comparison of the predicted T_{int} with experimental data	98
Figure 4.7. Comparison of the predicted cutting force with experimental data	99
Figure 4.8. Comparison of the predicted temperature and cutting force with the predicted values using an extended Oxley's predictive machining theory	101
Figure 5.1. Time-Temperature-Transformation cooling diagram for AISI 52100 steel	106
Figure 5.2. Hard turning simulation via AdvantEdge FEM	108
Figure 5.3. Simulation results of cutting force for Tests B1-B3	110
Figure 5.4. Simulation results of surface microstructure for tests A1 and A2	112
Figure 5.5. Refined surface microstructures	113
Figure 5.6. Simulation results of surface microhardness for tests A1 and A2	114
Figure 5.7. Simulation results of subsurface residual stress profile for tests A1 and A2	115
Figure 5.8. Simulation results of martensitic transformation layer thickness for tests B1-B5	116
Figure 6.1. Current and proposed methods for machining a transmission shaft	119
Figure 6.2. Sketch of the laser-assisted facing of a cylindrical workpiece with one laser	120
Figure 6.3. Sketch of the laser spot and machine chamfer in laser-assisted face turning	124
Figure 6.4. Sketch of partial deactivating control volumes and laser absorption at the boundary	124
Figure 6.5. Heat transfer at the boundary control volumes	124
Figure 6.6. Program flow in the LAM thermal model	126
Figure 6.7. Simulation result of laser-assisted face turning	126
Figure 6.8. A representative case study of laser-assisted profile turning	127
Figure 6.9. The machine chamfer in different stages	128
Figure 6.10. Mesh generation in laser-assisted profile turning	129
Figure 6.11. 2D temperature simulations at the tool position in laser-assisted profile turning ..	129
Figure 6.12. 3D temperature simulations in laser-assisted profile turning	130
Figure 6.13. LAM experimental setup with both the CO2 and Nd:YAG laser	131
Figure 6.14. Geometry of the hollow shaft of varying-thickness	131
Figure 6.15. Diagram of the CO2 and Nd:YAG lasers in the machined chamfer	132

Figure	Page
Figure 6.16. Thermal model predictions at absorptivity of 0.78 and thermocouple measurements during an absorptivity test for the graphite coated surface to the Nd:YAG laser ...	134
Figure 6.17. 2D temperature distributions in a hollow shaft workpiece undergoing LAM	135
Figure 6.18. 3D temperature distribution in a hollow shaft workpiece undergoing LAM.....	136
Figure 6.19. Schematic of the IR camera temperature measurement	137
Figure 6.20. Temperature measurements and thermal model predictions in a hollow shaft undergoing LAM	138
Figure 6.21. Comparison of measured and predicted flow stress at elevated temperatures of 4130 steel	139
Figure 6.22. Simulation results of workpiece microstructure	140
Figure 6.23. Temperature effect on specific cutting energy of hardened 4130 steel	142
Figure 6.24. Temperature effects on surface finish of hardened 4130 steel	143
Figure 6.25. Effect of thermal expansion on size control	144
Figure 6.26. Optical microscopy of microstructures of the subsurface after LAM at speed of 180 m/min, feed of 0.075 mm/rev and various T_{mr} , 200X.	145
Figure 6.27. Histograms of the hardness of the parts before and after LAM.....	146
Figure 6.28. Subsurface hardness after LAM at speed of 180 m/min and feed of 0.075 mm/rev	146
Figure 6.29. Surface residual stress of LAM of 4130.....	147
Figure 6.30. Subsurface residual stress of LAM of 4130.....	149

ABSTRACT

Ding, Hongtao. Ph.D., Purdue University, May 2012. Microstructural Prediction in Metal Cutting and Improvement of Machinability and Surface Integrity via Laser-Assisted Machining. Major Professor: Yung C. Shin, School of Mechanical Engineering.

This study is concerned with the predictive modeling of surface microstructure alterations in terms of grain refinement due to mechanical deformation and thermally driven phase transformation during the machining process. To model grain refinement, a dislocation density-based numerical framework is developed to simulate the chip formation, cutting temperature and grain size during orthogonal cutting of Al 6061 T6 and OFHC Cu; to model phase change, a truly coupled metallo-thermo-mechanical scheme is proposed to considerate mechanical deformation, thermal history, and phase transformation kinetics in orthogonal cutting of AISI 1045 steel under various conditions. The developed metallo-thermo-mechanical coupled analysis is then applied to the three-dimensional (3D) hard turning process for bearing steels to investigate the surface microstructure alteration, particularly the white layer formation mechanisms incorporating both the thermally driven phase transformation and mechanical grain refinement due to severe plastic deformation.

To carry on the microstructural evolution simulation and improve computational efficiency, a coupled Eulerian-Lagrangian (CEL) model is developed to simulate steady-state chip formation in two-dimensional (2D) orthogonal cutting by using the commercial software Abaqus. 3D hard turning simulations are undertaken via AdvantEdge FEM software incorporating the material user subroutine for various hard turning conditions. A novel, arbitrary-Lagrangian–Eulerian (ALE) based finite element scheme is developed in ABAQUS to simulate the micro-milling cycles, and a strain gradient constitutive material model is incorporated to model the size effect in micro-milling. Through a quantitative assessment using the experimental data, the model simulations demonstrate the essential characteristics of the deformation field and microstructural evolution mechanism during cutting.

Microstructure and surface integrity is further studied experimentally and numerically for difficult-to-machine materials during laser-assisted machining. One-step laser-assisted machining process is proposed for hardened AISI 4130 steel to replace the hard turning and grinding operations. A heat transfer model is developed to predict the temperature field inside the workpiece of complex geometry undergoing laser-assisted profile turning. Microstructure of 4130 steel workpiece is simulated using the 3D nose turning option in AdvantEdge FEM by considering both phase transformation kinetics and grain refinement. The surface integrity analysis is experimentally studied by changing heating and operating conditions, viz., average material removal temperature, cutting speed and feed.

CHAPTER 1. INTRODUCTION

1.1. Rationale

As design requirements increase in modern machines and products, material processing technologies advance at an escalating speed to create high performance materials with ever stronger strength and higher abrasive, corrosive, or heat resistance. Accordingly pertinent machining methods also have to be developed to accurately shape these new materials into products. The use of high strength metallic materials, such as hardened steels, nickel-based heat resistant superalloys and titanium alloys, is becoming increasingly common in aerospace, automotive, energy, medical, and mining applications [1-5]. These advanced materials have very favorable properties, which allow components to function under high-temperature and/or highly stressed operating environments. However, these materials are traditionally considered to be difficult-to-machine because they have a very strong tendency to strain hardening, maintain their high strength even at elevated temperatures, or even worse for the case of titanium alloys, their low thermal conductivity keeps much of the heat generated during machining very near the tool tip, causing extreme temperatures on the tool faces [6, 7]. Conventional machining processes for these materials are notoriously affected by slow machining speeds and/or frequent tool changes due to short tool lives.

The ever increasing demand for the use of these high performance alloys motivates technological developments of advanced tools, including carbides with a multi-layer of ceramic coatings, whisker-reinforced ceramics, and PCBN (poly-cubic-boron-nitride) tools, and innovations of machining processes like laser-assisted machining (LAM). Ceramics and PCBN tools have increased the rate of productivity for difficult to machine alloys, but their use is still constrained by rapid tool wear or chipping, which results in short tool lives. LAM is the process of locally preheating a workpiece with a focused laser beam ahead of the material cutting location. By lowering the material strength in the cutting area at a certain elevated temperature, LAM can achieve lower cutting force, slower tool wear progression rate, higher

material removal rate and better surface quality [5-18]. Nowadays, LAM has been widely accepted as a promising alternative machining process for difficult-to-machine materials as the developments in laser technology provide economic, high power, easily transportable lasers like fiber lasers, diode lasers and Nd:YAG lasers [1, 19]. These improvements coupled with the multi-functionality of lasers in various manufacturing processes promise large potential benefits that may be received from LAM of difficult-to-machine metal alloys.

The concept of LAM has been expanded to micro scale cutting of difficult-to-machine materials. As miniaturization of products grows in complexity and shrinks requisite feature size in many applications, the need to manufacture parts with complex features as small as a few microns to a high precision has expanded from conventional soft materials like aluminum and copper to much stronger engineering alloys. The size effect such that specific cutting energy at the micro-scale is much higher than at the macro-scale makes micromachining of difficult-to-machine materials even more difficult [20, 21]. The high specific cutting force cannot be sustained by micro-sized tools, which usually results in a catastrophic failure of the tool and a poor finished surface. Softening the workpiece material using a controlled laser beam focused ahead of the cutting position reduces cutting forces and has the potential for extending the practical application domains of the mechanical micromachining process. Sharing the similar idea to LAM, laser-assisted micromachining (LAMM), due to its great process flexibility, is a promising technology, offering the desired capability of producing complex, 3D, and high aspect ratio micro features in steels, titanium alloys, and nickel-based superalloys [22, 23].

The challenge lies in optimizing the laser-assisted micro and macro machining processes so that the temperature required for the large decrease in workpiece strength does not shorten the life of the cutting tool or adversely affect the finished surface quality and part dimensions. The LAM process must show a significant improvement in tool life, while good machined surface integrity has to be maintained to ensure the requisite functionality of the component. LAM will only become economically viable and justifiable for industrial use if it can be proved versatile in different application domains. A high material removal rate and a long tool life are the main purposes of LAM to achieve low cost roughing operations, while good machined surface integrity and tight dimensional tolerance are the major considerations in applying LAM to finishing operations. The limited adoption of LAM as the final finishing process is basically due to: (1) the lack of the appreciation of its total benefits compared with traditional finish grinding

processes, and (2) the lack of knowledge of the effect of the LAM process on the performance of the finished components. Performance of the components is dictated by the texture and integrity of the machined surface. Machined surface integrity problems, such as poor surface finish, material side flow, high tensile stress, grain enlargement, subsurface defects like microcracks, a heat affected area with phase change, a softened machined surface layer and the hardened surface white layer of extreme hardness and brittleness, are all concerns in the final or semi-final finishing processes. To determine the true feasibility of LAM it is important to investigate resultant surface roughness, surface hardness, residual stress and microstructures. Although many LAM studies have experimentally shown improved surface finish, reduced subsurface defects, a hardness profile similar to that of conventional machining and no existence of heat affected zone given a properly design of laser heating, the possible change of grain microstructure and phase composition, in particular, has not been investigated, although it is one of the main concerns industry has in applying LAM to finishing processes.

Grain sizes in the chip and on the machined surface tend to become smaller due to the severe plastic deformation (SPD) occurring in a cutting process. As a matter of fact, machining, particularly plane-strain orthogonal cutting as a means of SPD processing, has recently been exploited to refine the microstructure from tens of micrometers or greater to a few hundred nanometers. Compared to other SPD processes such as equal channel angular processing (ECAP), high pressure torsion (HPT) and cold rolling, machining only needs one pass to create large enough strain required for the creation of sub-micron grain sizes in the chip and can be performed at near-ambient temperature for high strength alloys [24]. It has been shown that machining is a flexible and controllable method for producing ultra-fine grained (UFG) microstructures for various metals and alloys, such as copper [25-27], aluminum alloys [27, 28], titanium [29, 30], nickel-based superalloys [30] and steels [27, 30]. Experimentally, many studies have shown a relationship between grain size and strain level in cutting [27-35] for a range of cutting conditions; however, there is no physics-based model, analytical or empirical, available in literature to quantitatively predict the change of grain sizes during machining to the author's best knowledge. It remains a tough technical challenge to predict the grain size change in the workpiece undergoing a high strain rate deformation with a complex temperature contour due to laser heating in a LAM process. A predictive model based on the grain refinement mechanism in machining is critically needed to better design and optimize the

process parameters, such as the cutting speed, temperature, depth of cut and tool geometry, etc., for producing the desirable microstructures by LAM. Metallurgical transformation occurs in the chip or on the workpiece machined surface due to intense, localized and rapid thermal-mechanical working during machining. This is especially evident in high-speed machining, thermally enhanced machining, grinding and hard turning with severe tool wear [36-39]. To improve the machining process and understand the resultant microstructure, it is necessary to develop a physics-based machining model to predict the microstructure alterations in terms of both phase change and grain size.

1.2. Laser-Assisted Machining

1.2.1. Laser-Assisted Machining of Difficult-to-Machine Metal Alloys

LAM implements the concepts of thermally-assisted machining using a laser as the heating source. During LAM, the workpiece material is locally heated and softened by a focused laser beam and then removed by a conventional cutting tool. Recently, LAM has been considered as an alternative process for machining of high strength materials like ceramics [9-15, 40, 41], metal matrix composites [18], high temperature alloys [6, 9], hardened steels [8, 42-45] and compacted graphite iron [5]. Extensive experimental investigations conducted so far have shown the feasibility of LAM and its advantages over conventional machining methods in terms of surface finish, tool wear, specific cutting energy, and subsurface integrity. Moreover, machining is carried out dry without needing a coolant, which reduces the cost associated with the purchase and the treatment of lubricants and makes the process more environmental friendly. LAM can also increase the number of operations possible with the same machine. For example, a laser equipped lathe is able to carry out laser deburring and thermal surface treatments.

For LAM of hardened steel, Gratiot et al. [42] characterized the laser power-cutting speed relations in machining of hardened AISI 1042 steel and found the cutting forces could be reduced by 70%. Germain et al. [43, 44] reported the surface finish and residual stress produced by LAM of hardened AISI 52100 steel, wherein the surface roughness R_a ranged from 0.6 to 0.75 μm with a small feed rate of 0.1 mm/rev, the residual stress became more tensile and the stress penetration depth became shallower when compared to conventional cutting. Dumitrescu et al.

[45] showed that LAM suppressed machining chatter and saw tooth chip formation and improved tool life by as much as 100% for AISI D2 tool steel.

Anderson et al. [6] experimentally evaluated the machinability of Inconel 718 under varying conditions by examining tool wear, cutting forces and surface finish. With the increasing material removal temperature from room temperature to around 540 °C, the benefit of LAM was demonstrated by a 25% decrease in specific cutting force, a 2–3-fold improvement in surface roughness and a 200–300% increase in ceramic tool life over conventional machining. Moreover, an economic analysis showed significant benefits of LAM of Inconel 718 over conventional machining with carbide and ceramic inserts. Attia et al. [46] conducted the high-speed (highest about 500 m/min) finish turning experiments of Inconel 718 with SiAlON ceramic. Compared to conventional machining, the surface finish and the material removal rate were improved by over 25% and 800%, respectively, due to a significant drop in the cutting forces. Surface integrity remained intact with the absence of phase change or microdefects. The chemical compositions were quite consistent before and after both conventional and LAM. However, their experiments did not maintain a constant material removal temperature in the cutting zone for varying cutting speeds.

Dandekar et al. [7] investigated the tool life during LAM of titanium alloys with various material removal temperatures. The optimum material removal temperature during LAM of Ti6Al4V alloy was found to be 250 °C at which the balance between the heat generated due to plastic deformation and the heat produced by laser energy input was achieved and the cobalt-diffusion controlled crater wear was minimized. Under this material removal temperature, tool life was improved 1.7 times by LAM for cutting speeds below 107 m/min compared with conventional machining. Yang et al. [47] developed a 3D finite element model using ANSYS to predict the heat affected zone during laser assisted machining of Ti6Al4V. A good correlation was achieved between the prediction and experimental observations of heat affected zone. However, the peak temperature in the laser spot was overestimated to be about 600°C above the melting point, which inevitably casts some doubts in their temperature predictions.

The majority of published research shown above has focused on the improvement of feasibility and machinability of difficult –to-machine materials with LAM wherein higher material removal rates and longer tool life are usually pursued in optimizing the LAM parameters. Few studies have systemically investigated the best LAM parameter combination to achieve superior

surface integrity of components. Surface integrity after a finishing process is a central attribute to the performance and behavior of various manufactured parts. In finish turning, surface quality and integrity are often of great concern because of their impact on product performance [48, 49]. LAM will only become economically viable and justifiable for industrial use if it can be proved versatile in achieving higher material removal rate, longer tool life and/or superior surface integrity in machining of different difficult-to-machine materials.

1.2.2. Laser-Assisted Micromachining of Difficult-to-Machine Metal Alloys

Micromachining, micro-milling in particular, due to its great process flexibility, is a promising technology for the manufacture of durable, high temperature and wear resistant micro-dies and micro-molds made of hardened tool steels with relative high accuracy. However, micro-milling of difficult-to-machine metal alloys still remains a great technological challenge in industry due to the unpredictable tool life of micro endmills, machined surface integrity and part dimension accuracy. The needs for micromachining have expanded from conventional soft materials like aluminum and copper to much stronger engineering materials such as high-temperature superalloys [22], hardened tool steels [20, 50, 51], stainless steels [22, 23], titanium alloys [22] and ceramics [52].

The size effect contributes to the fundamental difference in the process mechanism between micromachining and conventional macro-machining, and the analytical and numerical solutions available for macro-machining cannot be assumed to be valid for micromachining operations particularly for the small undeformed chip thickness. In micromachining, the cutting edge radius (r_e) of the micro tools is comparable to the undeformed chip thickness (h) and in some occasions less than the size of the workpiece material grain size. The substantial reduction in the ratio (λ) of undeformed chip thickness to cutting edge radius has a profound influence on the specific cutting force, chip formation and surface integrity in micromachining. Figure 1.1 illustrates the change of material removal mechanism in micromachining for a constant chip load but with varying tool cutting edge radii. Cutting is the dominant mechanism for a fresh tool with h greater than r_e , but ploughing with workpiece material elastic recovery plays a more important role as r_e increases to a size close to h . Ploughing eventually becomes dominant as r_e increases to be much greater than h and no chip forms beyond this condition. More specific cutting energy will be spent in the material plastic deformation due to ploughing

than shearing in cutting. The size effect in micromachining has been extensively studied theoretically and experimentally, but the focus has been mainly on soft materials like aluminum alloys [53], copper [54] and mild carbon steels [55]. Only a handful of studies have investigated the size effect in micromachining of difficult-to-machine materials. Aramcharoen and Mativenga [20] experimentally explored the size effect on the specific cutting force, surface finish and burr formation in micro slotting of hardened H13 tool steel with a hardness of 45 HRC using a 900 μm diameter tungsten carbide endmill. Their study has shown that the specific cutting force of hardened H13 steel increased drastically to around 100 GPa as the ratio λ decreases to 0.2. Shelton and Shin [23] conducted laser-assisted micro slotting experiments of difficult-to-machine materials such as titanium alloy Ti6Al4V, AISI 316 and 422 stainless steels with 100 μm diameter tungsten carbide endmills and numerically modeled the size effect on specific cutting force under orthogonal cutting conditions.

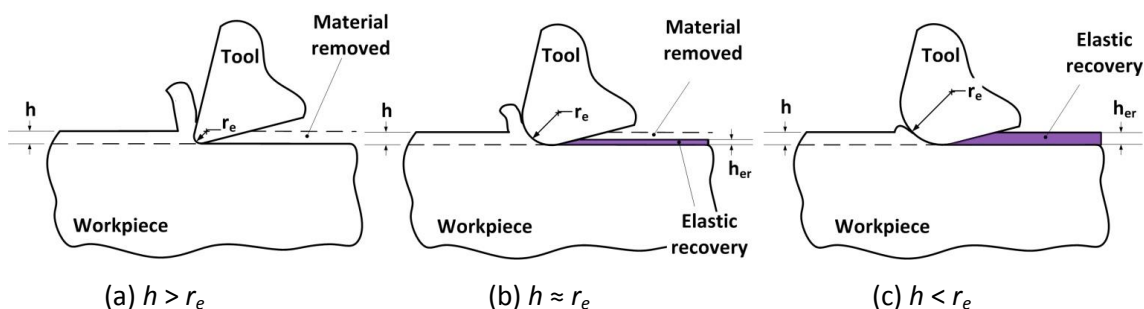


Figure 1.1. Chip formation relative to chip load and cutting edge radius.

Many theoretical and experimental attempts have been made to analyze surface integrity in micromachining. Liu et al. [55-57] studied the surface roughness achieved in micromachining of aluminum alloy 6082-T6 and carbon steel 1041 and their study showed that the resultant surface roughness was a product of the tradeoff between the effect of minimum chip thickness and the traditional effect of feed rate. For cutting ratio λ greater than 1, the surface roughness increased with increasing feed per tooth, while for cutting ratio λ less than 1, roughness increased with decreasing feed due to the material elastic recovery. A similar phenomenon was observed for micro slotting of harden H13 steel [20]. The most frequently observed surface defects on the machined surface by micromachining were dimples, prows, microvoids, and microcracks [58]. For carbon steel with a dual phase structure of pearlite and

ferrite, dimples were found on the machined surface at the pearlite-ferrite grain boundary, which indicated a great effect of the inhomogeneous microstructure on machined surface integrity undergoing severe plastic deformation. Their study showed that prows resulted from the broken-down built-up edge (BUE) from the tool tip. Prows were hardened workpiece materials that had undergone severe plastic deformation under the tool nose with a hardness value 2 to 3 times greater than that of the original workpiece [58]. Burr formation is another critical issue in micromachining processes since it affects the functionality of the microcomponent and damages the part dimension and geometric tolerance. The mechanism of burr formation in micromachining has been reported to be dominated by the interaction between cutting edge radius and feed per tooth, while cutting speed, undeformed chip thickness, tool edge radius, feed rate, and workpiece materials all contributed to burr formation in micromachining [59].

Micro-tools such as micro endmills and drills are generally made from tungsten carbide (WC) with cobalt as the binder. Progression of tool wear in micromachining is dominated by the friction between the tool and the workpiece. For a small depth of cut in micromachining, a tool with a greater edge radius with respect to undeformed chip thickness increases the tool-work friction and wears at a faster rate [21]. Filiz et al. [60] investigated the wear progression of 254 μm diameter WC endmills in cutting of copper at cutting speeds ranging from 40 to 120 m/min and feed ranging from 0.75 to 6 μm per tooth. Their study showed that WC tools wore at a 5-time faster rate when the ratio λ reduced from about 3 to 0.4 for all the cutting speeds investigated.

To improve the tool performance in micromachining of difficult-to-machine materials, recently, laser-assisted micromachining (LAMM) has been implemented on high-temperature superalloys [22, 23], hardened tool steels [61-64], stainless steels [22, 23] and titanium alloys [22, 23]. Shelton and Shin [23] conducted the laser-assisted micro slotting tests of Ti6Al4V, stainless steels AISI 422 and AISI 316 with tungsten carbide micro end mills. The improvement of surface roughness on the machined surface of AISI 422 and AISI 316 was found to be up to 37%. Their study showed that LAMM resulted in less built-up edge (BUE) than conventional micromachining and significantly reduced the edge burrs for AISI 422. Shelton and Shin [22] conducted laser-assisted micro side cutting tests of AISI 316, AISI 422, Ti6Al4V, and Inconel 718 in a fin structure with tungsten carbide tools. The fin structure was found to be more suitable

for LAMM in a side-cutting configuration than the bulk workpiece due to the ease of the laser heating arrangement and practical applicability. Their study showed that burrs of Ti6Al4V and Inconel 718 were drastically reduced with the laser-assist. The tool life for AISI 422 was increased by almost 6 folds in LAMM than that of conventional micro milling. Joen and Prefferkorn [65] conducted laser-assisted micro milling tests of aluminum 6061T6 and 1018 steel with tungsten carbide end mills. Their study showed that the laser-assist micro milling increased chip loads by about 30-45% and reduced cutting forces. However, laser preheating was found to increase burr formation. Melkote et al. [51] conducted an experimental study of the laser-assisted micro-milling process for a hardened A2 tool steel with the hardness of 62 HRC using a TiAlN-coated tungsten carbide 4-flute ball endmills. A low tool wear rate was obtained in their LAMM tests and the surface roughness was consistently lower in LAMM than conventional micro-milling. Increasing cutting speed resulted in increasing the surface roughness with laser heating while improving the groove depth accuracy. However, there was not a clear trend without the laser-assist. Singh et al. [61] modeled the size of the heat affected zone (HAZ) using a transient 3D finite element thermal model with ANSYS and their study showed that there would be no residual HAZ in the workpiece after micro cutting with the well-designed laser and cutting parameters. Singh and Melkote [64] developed an analytical model to predict cutting forces and presented the effects of depth of cut, laser power, and cutting speed.

1.3. Thermal and Mechanical Modeling of Laser-Assisted Machining

1.3.1. Thermal Modeling of Laser-Assisted Machining

Laser-assisted machining implements the concepts of thermally-assisted machining using a laser as the heating source. During LAM, the workpiece material is locally heated and softened by a focused laser beam and then removed by a conventional cutting tool. Determination of the temperature field in a workpiece undergoing LAM is critical, since the benefits of LAM can be achieved and optimized only when the workpiece is heated properly. Transient, 3D, finite volume thermal models have been developed for laser-assisted turning (longitudinal) and milling processes by the Laser-Assisted Materials Processing Lab at Purdue University [9, 12, 14]. The Graphic User Interfaces (GUI's) developed for these thermal models run as standard Windows application software. Once the parameters of operating condition,

workpiece material and boundary condition are defined, then the model simulates a 3D transient temperature field in the workpiece during LAM.

Almost all industrial products have some curved surfaces to be machined. Profile turning operations are more commonly performed on ever stronger and tougher materials to attain certain functional features like high wear and tear resistance and longer fatigue life. A finishing operation is usually the last machining step to generate the component's final surface, shape and dimensions, which are crucial to ensuring those functionalities. Traditional finishing operations are grinding processes, which usually involve a costly set up, yield low material removal rates and have a lack of a flexibility [4]. Laser-assisted profile turning provides a potential economical alternative to finish grinding processes for these difficult-to-machine components with the benefits of lower set up cost, high flexibility, higher material removal rates, and no need of the environmentally hazardous coolant.

For machining a part with more complex geometric features like profile finishing of a crank shaft, the LAM thermal model needs to be further expanded to face turning and profiling. Transient, three-dimensional cylindrical thermal models have been developed for laser-assisted face and profile turning processes. In these models, the laser heat absorption is modeled as a Lagrangian-type heat source in synchronized with the moving tool motion, the heat transfer governing equations are discretized over the rotating cylindrical workpiece domain, and workpiece material removal is modeled by partially or completely deactivating control volumes along the complex predefined tool path [14].

1.3.2. Mechanical Modeling of Machining

A tremendous amount of research has been done in modeling machining processes analytically or numerically. Compared to analytical or empirical models, the development of computers in recent years has allowed researcher to study machining processes through sophisticated numerical techniques. Among them, the finite element (FE) analysis is the most used and effective numerical method. FE analyses have been conducted in different aspects of machining processes such as predictions of cutting force, cutting temperature, chip formation, tool wear, white layer, residual stress, hardness, microstructure, etc.

Continuous or serrated chip formations of hardened steels, heat-resistant alloys and titanium alloys depend on cutting conditions and can be modeled using FE models with material

constitutive models. Miguelez et al. [66, 67] and Nasr et al. [68, 69] proposed Coupled Eulerian-Lagrangian (CEL) FE models to simulate the continuous chip formation and residual stresses of stainless steels and tool steels in steady-state cutting using commercial software ABAQUS/EXPLICIT. Umbrello and Filice [70] developed a 2D FE model for serrated chip formation in the hard turning of AISI 52100 in terms of white and dark layer formation by Deform-2D, which was validated by experimental observation. Lorentzon et al. [71] simulated the serrated chip formation of Inconel 718 with the Cockroft-Latham fracture criterion using MSC. Marc. Calamaz et al. [72] and Sima and Ozel [73] developed 2D FE models to simulate the serrated chip formation of Ti6Al4V with thermal softening material constitutive models using FE software Forge and Deform-2D, respectively. Umbrello [74] developed a 2D FE model by Deform-2D to simulate the serrated chip formation of Ti6Al4V with a thermal softening material constitutive model and the Cockroft-Latham fracture criterion.

Tool wear during cutting can be predicted with FE models. Dandekar et al. [7] and Rao et al. [75] predicted the tool wear of uncoated carbide in turning of Ti6Al4V based on Hua and Shivpuri's crater wear rate model [76] with a 3D FE model by AdvantEdge. Lorentzon and Jarvstrat [77] predicted the tool wear of cemented carbide tool in turning of Inconel 718 with a 2D FE model by Deform-2D with Usui's model [78].

Kapoor and Devor's group from the University of Illinois at Urbana-Champaign published several papers on microstructure-based modeling of micromachining of two major materials, i.e., a ductile iron [79-86] and a carbon nanotube reinforced polymeric composite material [87, 88]. The selection of the ductile iron is due to two reasons: (i) it is a soft material and has a relatively good machinability under the micromachining condition; (ii) it has significant heterogeneous microstructures with harder pearlite particles enclosed by softer ferrite matrix. They have shown that microstructure-based finite element modeling of micromachining of the ductile iron with the built-in Baumann-Chiesa-Johnson (BCJ) model was able to better predict the cutting force than the prediction based on the homogeneous material model and was also able to predict the material damage in the cutting zone. Although chip segregation was simulated by the built-in material constitutive models of constituents in their work, a very rough machined surface was simulated, which looked quite different from the actual chip morphology. Remeshing the workpiece after each step might be needed to better predict the chip segregation and smooth the machined surface profile.

A number of finite element (FE) models have been proposed to simulate the chip formation in micromachining by simplifying the 3D milling processes to 2D orthogonal cutting processes, but few of them modeled the actual chip formation with varying undeformed chip thickness in the milling cycle. Özel et al. [89] developed a 2D FE model for micro slotting of aluminum alloy 2024-T6 and AISI 4340 steel to simulate the chip formation and cutting force within a complete slot cutting cycle of one flute using commercial software DEFORM-2D. Although a complete chip formation was simulated with the DEFORM platform, the predicted cutting force was not validated with the cutting force data measured from their micro slotting tests. To model the size effect in micromachining at a micro length scale, Liu and Melkote [53, 90] and Lai et al. [54] applied material strain gradient plasticity models to simulate orthogonal cutting of aluminum alloy 5083-H116 and copper, respectively. Liu and Melkote [90] showed that the strain gradient plasticity model was able to simulate the drastic increase of specific cutting force as λ decreased from 4 to 0.6 in micromachining and their simulated specific cutting force matched well with the experimental data. With the strain gradient plasticity model developed for copper at the micro level, Lai et al. [54] predicted a great increase of specific cutting force to around 45 GPa as the ratio λ decreased to about 0.2 in micro-milling by using an analytical slip line model. As discussed above on the 2D FE modeling work, the current FE modeling techniques still have shortcomings in correctly and efficiently modeling the chip formation with varying chip thickness and the significant size effect in micro-milling processes.

In Chapter 2, thermal and mechanical modeling analyses are presented to investigate the performance of LAMM of difficult-to-machine materials in side cutting configurations of both bulk and fin workpieces. The transient, 3D finite volume prismatic thermal model developed by Tian et al. [91] is used to analyze the material temperature increase in the machined chamfer due to laser heating for the two LAMM configurations. The 2D finite element models developed by Ding et al. [92] are adapted to simulate the continuous chip formation with varying chip thickness in LAMM side cutting with the strain gradient material constitutive models. Cutting temperatures and workpiece flow stresses are characterized in the cutting zone. Steady-state tool and workpiece temperatures after multiple LAMM cycles are predicted with heat transfer models. Tool wear progression, BUE formation and surface integrity are studied with the FE models.

1.4. Microstructure Alteration in Metal Cutting

During machining processes, materials often behave in a complicated manner involving severe plastic deformation, phase change, grain size change, fracture, etc. Microstructure alterations occur in the chip or on the workpiece machined surface due to intense, localized and rapid thermal mechanical working during machining.

1.4.1. Grain Refinement in Cutting

There has been a lot of research interest in the manufacture of ultra-fine grained (UFG) metals for their enhanced strength and hardness by employing SPD processing techniques. Machining, particularly plane-strain orthogonal cutting as a means of SPD processing, has recently been exploited to refine the microstructure from tens of micrometers or greater to a few hundred nanometers. During the chip formation, the achieved large-strain deformation under plane-strain condition is to some extent similar to that in the widely applied SPD technique of equal channel angular processing (ECAP). But unlike ECAP, machining only needs a single pass to create large enough strains required for the creation of sub-micron grain sizes in the chips and can be performed at near-ambient temperature for high strength alloys. The level of plastic strain imposed during cutting can be controlled by an appropriate choice of the rake angle of the cutting tool. The material processing rate and the strain rate of the plastic deformation can also be easily controlled by regulating the cutting speed and/or depth of cut. Hence as a flexible and controllable SPD method for producing UFG microstructures, plane-strain orthogonal cutting has been experimentally studied for various polycrystalline metallic materials, such as aluminum alloys [32], copper [25, 27, 34], nickel-based superalloys [27], steels [27] and titanium [29]. In these experimental studies, the microstructural evolution, namely grain size changes, textures and misorientations in the machined chips, are usually measured by using transmission electron microscope (TEM), x-ray diffraction (XRD) or electron backscattering diffraction (EBSD) techniques. Hardness of the resultant chips is measured by micro- or nano-indentation hardness tests in comparison with that of the bulk material before cutting. High-speed images of the deformation field can be acquired by using a high speed camera system and the strain rate field and the accumulative strain can then be derived by using the particle image velocimetry (PIV) technique. The large-strain in the chip formation by machining has been generally used as a qualitative measure to the grain size change in the experimental results. For

instance, Swaminathan et al. [27] undertook orthogonal cutting experiments of oxygen-free high thermal conductivity (OFHC) copper with cutting tools of varying rake angles and showed that the grain size in the chip decreased as the shear strain increased: average grain size was above 1 μm for a shear strain of 3, about 400 nm for a shear strain of 8, and about 200 nm for a shear strain above 13. To keep the cutting temperature low and suppress grain dynamic recovery, low cutting speeds, for example, 0.01 or 0.05 m/s, were usually applied for copper and aluminum alloys in these tests. It is noted that the aforementioned experimental conclusions, or any other experimental observations of strain-grain size relationship in those resultant UFG microstructures reported in [25, 27, 29, 32, 34], cannot be simply extended to a different process condition or a different material, because each cutting condition for each material is unique and all the process parameters affect the resultant microstructures.

To effectively design the machining process parameters, such as the tool rake angle, cutting speed and temperature, for materials with varying thermo-mechanical properties and improve the quality of the resultant microstructures, it is necessary to investigate the microstructure refinement mechanism during machining and is desirable to have an analytical model for predicting the microstructural evolution in terms of both grain size and misorientation. While the aforementioned experimental work has produced a significant body of knowledge with regard to microstructure and properties of machined materials, there is no quantitative grain refinement model available in literature for plane-strain orthogonal cutting of metals to the authors' best knowledge.

Many theoretical attempts have been made to analyze grain refinement in a regular SPD process such as ECAP. Petryk et al. [93] proposed a quantitative relationship between strain hardening and equiaxed grain size and modeled the grain size change for an ECAP process and a multi-axis compression test. Beygelzimer [94] proposed kinetic equations of grain refinement and pore generation by using a self-similarity hypothesis for the grain refining mechanism, and mathematically modeled the grain refinement during a general deformation process. These aforementioned models assumed that grain size depended only on strain, not on other involved process parameters like strain rate or temperature, and hence were not suitable for modeling a complex thermo-mechanical dynamic process such as machining.

Numerous dislocation density-based approaches have been applied for constitutive modeling of metals to couple the material dynamic response with the microstructural evolution

during complex dynamic deformation processes. Arsenlis and Parks [95, 96] proposed a continuum constitutive model based on internal variables characterizing crystallographic dislocation density, which evolves based on fundamental concepts in dislocation mechanics such as the conservation of Burgers vector in multiplication and annihilation processes. Their model was implemented to investigate the tensile behavior of single crystal aluminum, which not only captured the mechanical stress-strain response well, but also showed that the development of underlying dislocation structure is responsible for the plastic behavior. Ma and Roters [97] proposed a dislocation density-based constitutive model for the face-centered cubic (FCC) crystal structure, which considers the mechanical interaction between mobile dislocations and grain boundaries. The dislocation density-based constitutive model was implemented into a crystal-plasticity finite element (FE) framework to model hot compression tests of aluminum single crystals [97]. In a follow up study, they further expanded the dislocation density-based constitutive model to the body-centered cubic (BCC) crystal structure using dislocation density variables as internal state variables and numerically simulated plane strain compression of a pure niobium bicrystal [98]. Their proposed model showed that a combination of the strain gradient and grain boundary effect was able to reproduce the experimental findings; however, so far their modeling approach has been limited to studying polycrystal micro-mechanics at small spatial scales.

Recently, several dislocation density-based material models have been proposed to model the physics of grain refinement during SPD processes involving multi-process variables. Mohamed [99] modeled the obtainable minimum grain size during a ball milling process of various metals by balancing the hardening rate arising from the dislocation generation and the recovery rate caused by dislocation annihilation. The proposed model was useful in assessing the achievable minimum grain size under different process conditions, but was not suitable for modeling the significant variance of grain sizes or microstructure textures for a monotonic deformation such as machining. Starink et al. [100] predicted grain refinement during SPD using the volume averaged number of dislocations generated and proposed a strain hardening function considering the effect of minor obstacle particles. Their proposed model dealt with grain refinement during a SPD process with a strain greater than 3, but with no strain rate dependence and a limited range of process temperature; hence, the model was not suitable for modeling grain refinement in machining with a wide range of cutting speeds and high

temperature gradients. Estrin et al. [101] and Tóth et al. [102] presented a set of differential equations to evaluate the dislocation density evolution rates and applied the dislocation density-based material plasticity model to grain refinement in the ECAP processes of various materials such as copper [103], aluminum [104] and IF (interstitial-free) steel [105, 106]. The nucleation of dislocations due to deformation, annihilation of dislocations due to dynamic recovery, and interaction of dislocations between the dislocation cell interiors and cell walls were evaluated based on the deformation process state variables. Their proposed dislocation density-based material plasticity model was compatible with the material constitutive models developed under varying conditions of strains, strain rates and temperatures and can be adapted to model other deformation processes with high strain rates or high temperature gradients such as a Taylor impact test [107] or a machining process. For example, recently their model has been adapted by Hosseini and Kazeminezhad with slight modifications on the cell size coefficient [108] and the work softening mechanism [109], and implemented in a FE model for predicting the flow stress evolution of copper undergoing SPD processes of repetitive corrugation and straightening (RCS) and constrained groove pressing (CGP). The hardness enhancement predicted by the model showed a good agreement with experimental measurements. Hence, the dislocation density-based material plasticity model presented in [101, 102] was selected for modeling grain refinement, evolution of the dislocation cell structure and chip formation of by machining.

Indeed, a dislocation cell structure with high dislocation density is commonly observed in metal workpieces treated by a variety of SPD processes. Figure 1.2 shows the transmission electron microscope (TEM) images of commercially pure titanium (CP Ti) workpieces produced by (a-b) orthogonal cutting [29], (c-d) multi-pass cold rolling [110], (e) ten-pass ECAP plus cold rolling with 77% thickness reduction [111], (f) two-pass ECAP [112], (g) multi-pass hydrostatic extrusion [113] and (h) surface mechanical attrition treatment (SMAT) processes [114]. Figure 1.2 (a) shows a TEM micrograph of a chip machined with the $+20^\circ$ rake angle tool, of which microstructure consists of sub-100 nm dislocation cells/grains interspersed with elongated, less developed subgrain structures. Figure 1.2 (b) shows a nanocrystalline microstructure resulting from deformation of CP Ti to an effective strain of 3.5 using a -20° rake angle tool. Most of the subgrain structures are well delineated in Figure 1.2 (b) corresponding to a material that has undergone considerable microstructure refinement, due to the larger values of shear strain.

TEM observations in Figure 1.2 (c) showed that cold rolling with a strain of 0.92 gave rise to a cellular microstructure with a high dislocation density but rather wide and loose cell boundaries. Cold rolling with a strain of 2.66 leads to a considerable refinement of the microstructure and simultaneously to an increase in dislocation density, as can be seen in Figure 1.2 (d). The cellular microstructure of CP Ti is refined from an inhomogeneous structure of cells/grains ranging from a hundred nanometers to a few micrometers achieved at a strain of 0.92 to an equiaxed structure of cells/grains of approximately 200 nm achieved at a strain of 2.66. The formation of a similar lamellar structure of high dislocation density and a cell/grain size of sub-200 nm is also observed in CP Ti workpieces processed at an equivalent plastic strain of over 3 by ECAP, hydrostatic extrusion and SMAT as can be seen in Figure 1.2 (e-h). The microstructural evolutions of CP Ti produced by SPD processes have all shown a similar pattern: at the early stage of deformation, a very high dislocation density is introduced, which leads to the formation of lamellar structure consisting of dislocation cells with thick cell walls and low angles of misorientation [115]. Deformation twinning plays a role for the refinement of CP Ti workpiece at the early stage deformation; however, twinning is found to saturate at an equivalent strain of about 0.1-0.2 for CP Ti [110, 112, 116]. Indeed, no twinning boundaries can be observed in the microstructures of CP Ti workpieces at a high strain produced by various SPD processes, i.e., orthogonal cutting [29], multi-pass cold rolling [110, 117], multi-pass ECAP plus cold rolling [24, 111, 118], multi-pass ECAP [111, 112], multi-pass hydrostatic extrusion [113] and SMAT [114, 116]. As the strain increases, the thickness of the cell walls decreases and the original grains break down and become subdivided into smaller sub-grains. The dislocation cell walls evolve into grain boundaries (GBs), and ultimately an array of ultrafine grains with high-angle non-equilibrium GBs are formed, as can be seen in Figure 1.2 (a-h).

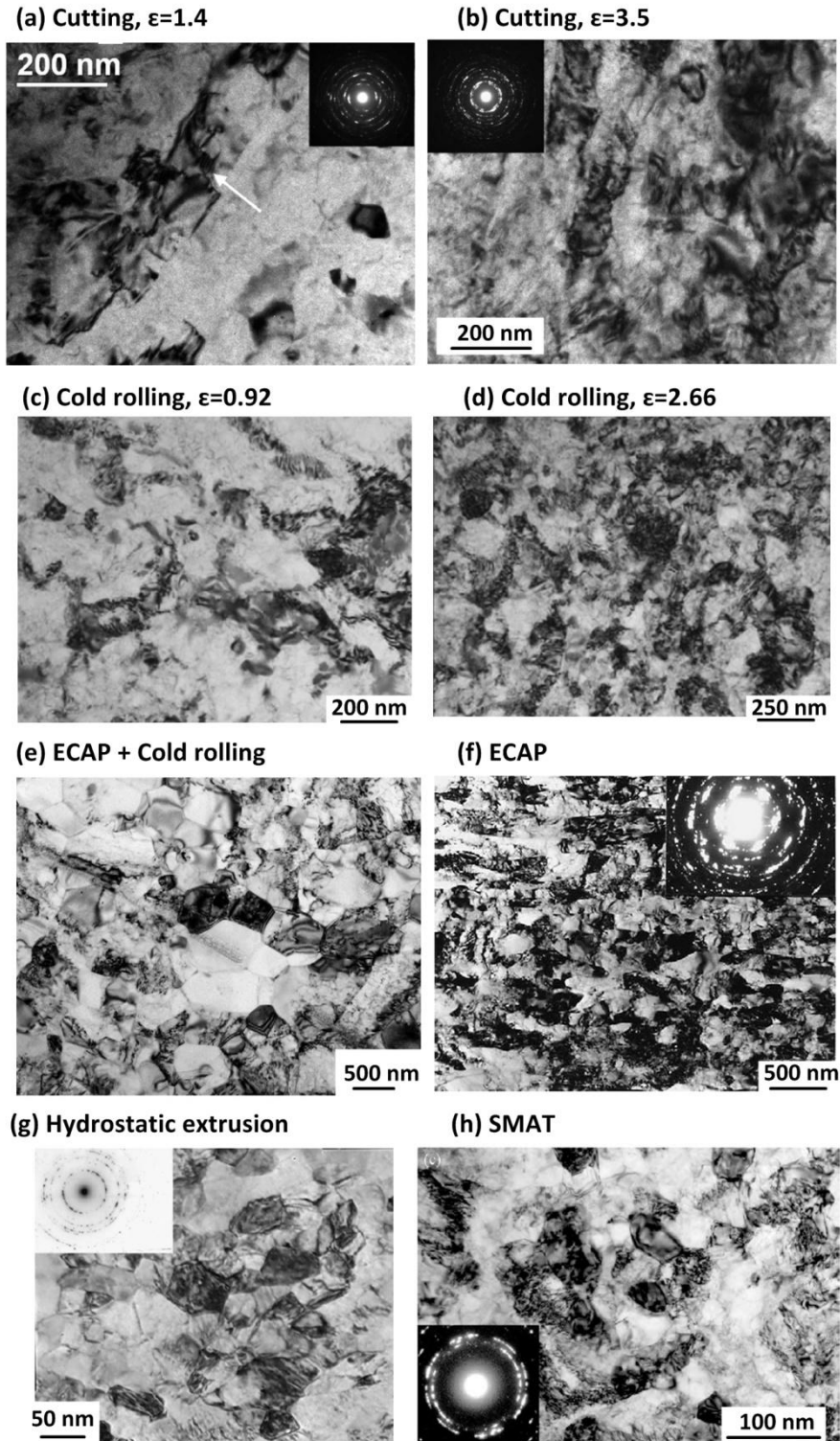


Figure 1.2. TEM images of grain refinement of CP Ti produced by (a-b) orthogonal cutting [29], (c-d) multi-pass cold rolling [110], (e) ECAP plus cold rolling [111], (f) ECAP [112], (g) hydrostatic extrusion [113] and (h) SMAT [114].

In Chapter 3, the suitability of this dislocation density-based model is investigated for predicting the microstructure evolution at large strain, high strain rate and high temperature gradients and a finite element based numerical framework is developed to model both chip formation and grain refinement in machining. A CEL finite element model embedded with the dislocation density subroutine is developed to model the severe plastic deformation and grain refinement and grain misorientation during a steady-state cutting process. Multiple orthogonal cutting tests of aluminum alloy 6061 T6 and OFHC Cu, both of which are of great technology and commerce importance, are modeled at various cutting conditions: cutting speed ranges from 0.01 to 1.25 m/s, rake angle ranges from -20° to 20° , and depth of cut ranges from 0.1 to 0.3 mm. The dislocation density-based material models, consisting of both grain size and misorientation angle, are calibrated to replicate the observed material constitutive mechanical behaviors under various strains, strain rates and temperatures in the cutting processes. The chip formation and the evolution of microstructure in terms of both grain size and grain misorientation during cutting are simulated with the CEL finite element model embedded with the dislocation density subroutines developed for both materials. Modeling results are presented in chip formation, strains, strain rates, temperatures, grain sizes and dislocation densities in comparison with the actual measurements during orthogonal cutting. The effects of important cutting process parameters like cutting speed, tool rake angle and temperature on grain refinement and misorientation angles are discussed to great details.

1.4.2. Phase Change in Steel Cutting

As the heat generated in the cutting process raises the workpiece material temperature above its critical phase transformation temperature, a metallurgical transformation will occur, and the attendant latent heat and volume change due to the transformation will affect the machining process. Mechanical deformation, heat transfer, and microstructure are all strongly coupled together, each affecting the others, and these effects has been termed metallo-thermo-mechanical coupling [119-121], which is schematically illustrated in Figure 1.3. Temperature fields affect the stress state through thermal softening and thermal strains caused by temperature gradients, which also affect microstructural changes according to phase transformation kinetics. Mechanical work caused by plastic deformation or friction generates a lot of heat and alters the temperature field. Large strains can also assist in phase

transformations, called strain-induced transformation. Phase changes, in turn, affect the stress state by causing dilatation strain. The thermo-mechanical properties of the phase constituents change radically as the transformation occurs, which will drastically change the material behavior during cutting. The latent heat from solid phase transformations can also alter the temperature field. And finally, chemical concentrations, such as carbon content in carbon steels, will have an effect on all three fields. Such extensive interaction/coupling between the plastic deformation, heat transfer, and microstructure evolution creates difficulties in numerical modeling of machining of steels and has rarely been considered. Essentially, all of these deeply coupled phenomena ought to be solved simultaneously to correctly understand the effects of phase transformation on cutting performance and surface integrity of steel parts. Hence it is critically needed to develop a predictive model based on the metallo-thermo-mechanical coupled mechanisms.

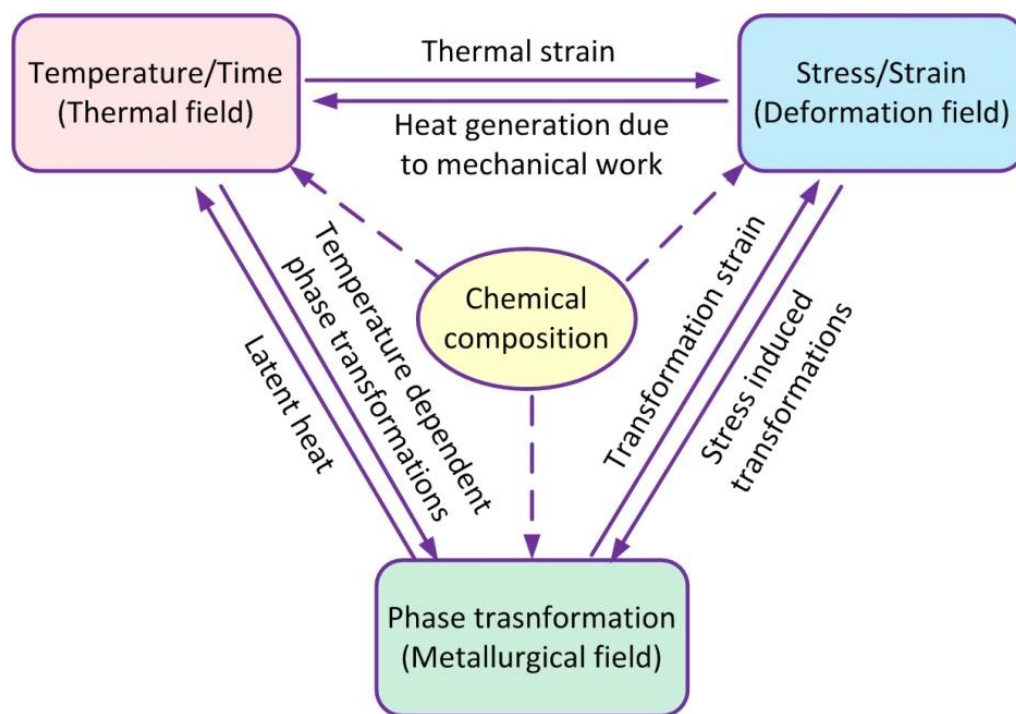


Figure 1.3. Metallo-thermo-mechanical coupling in cutting of steels (adapted from [119]).

Phase change in cutting can be explained in details by orthogonal cutting of American Iron and Steel Institute (AISI) 1045 steel. The workpiece material AISI 1045 steel has significant relevance in the automotive and heavy equipment industries, and is widely used in

manufacturing processes that involve high-speed machining operations. AISI 1045 steel is hypo-eutectoid steel consisting of pearlite (P) and proeutectoid ferrite (α). As depicted in Figure 1.4, when the material is locally heated to a temperature above the eutectic temperature, A_{c1} , the pearlite colonies begin to transform to austenite (γ), while the proeutectoid ferrite remains unaffected. However, as temperature increases further, carbon from newly formed austenite diffuses into the low carbon ferrite. If kept above A_{c1} temperature for a sufficient amount of time the carbon distribution will become homogeneous. If the austenization temperature, A_{c3} , is exceeded, then any remaining ferrite will transform to austenite. As the material cools down, austenite transforms to martensite at high cooling rates, while it will transform to both martensite and bainite at lower cooling rates [122-124]. Chou and Evans [36] estimated the surface cooling rate in hard turning of hardened steel to be on the order of 10^4 °C/s. Due to the fast cooling rate in cutting, some of the austenite has no time to transform and remains in the surface layer.

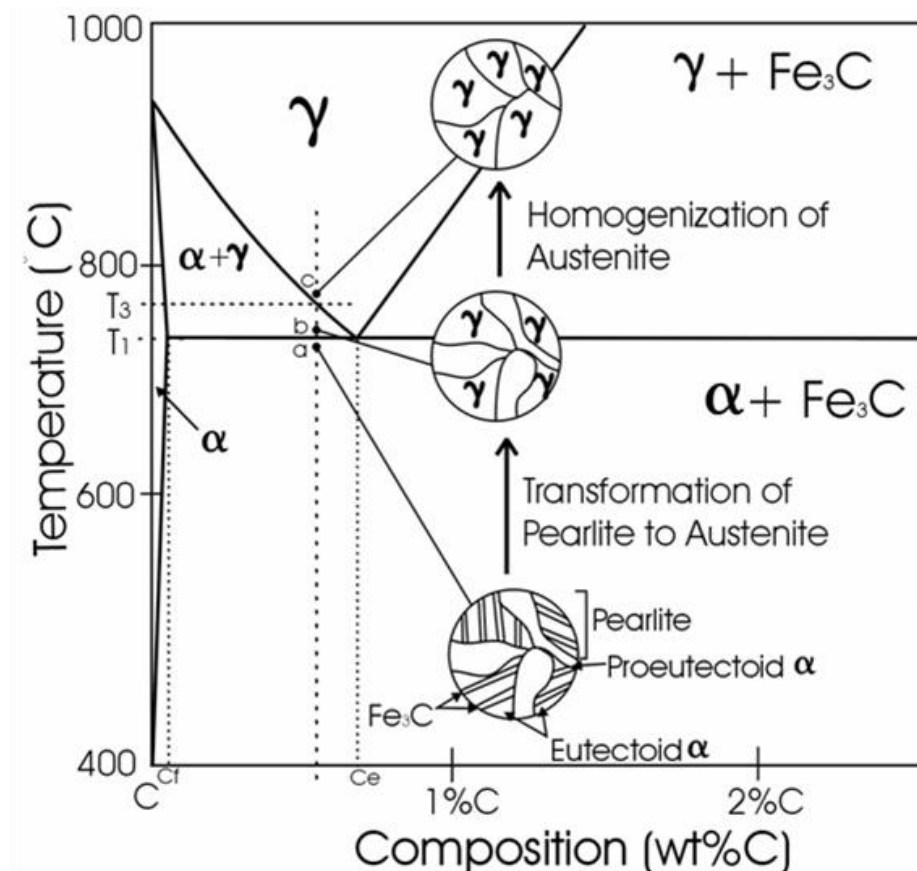


Figure 1.4. Phase changes in hypo-eutectoid steel during heating (adapted from [124]).

Although an enormous amount of work has been reported on modeling of steel cutting, only a handful of researchers have attempted to explicitly model phase formation in machining of steels. Mahdi and Zhang [125, 126] developed a finite element (FE) framework to predict phase transformations in grinding. Chou and Evans [36] used an analytical thermal modeling approach to predict white layer formation due to phase transformation in hard turning of AISI 52100 steel workpieces. Umbrello and Filice [70] developed a two-dimensional (2D) FE framework to predict white/dark layer thickness due to quenching/tempering and surface hardness in orthogonal cutting of hardened AISI 52100 steel. Ramesh and Melkote [127] applied a kinetics model of phase transformation to 2D FE simulations of orthogonal cutting of hardened AISI 52100 steel using commercial software ABAQUS. Their simulations attempted to capture the phase transformation due to thermal, stress, and strain effects in a surface layer. The white layer thickness and subsurface residual stress predicted by the model were shown to be in good agreement with the experimental data. However, these aforementioned models did not consider the feedback of phase change on the material thermal, elastic and constitutive viscoplastic behaviors in cutting. Burns et al. [128, 129] have reported that for carbon steels like AISI 1045 steel and AISI 1075 steel phase transformation drastically changed the material constitutive behaviors at high temperatures from those at lower temperatures prior to phase change, and indicated that the constitutive models developed without considering the phase change effect often are not suitable for modeling of cutting of steel at high cutting speeds.

In Chapter 4, a 2D FE framework is proposed for orthogonal cutting of AISI 1045 steel based on a metallo-thermo-mechanical coupled material model. Cutting temperature, phase composition, chip morphology, and cutting force are all solved simultaneously. Comparisons of model predictions with experimental data are presented and the results are discussed.

1.4.3. White Layer Formation Mechanisms

The so-called hard turning process involves the single point turning of hardened bearing steels as an alternative to grinding operations. During the hard turning process, steels often behave in a complicated manner involving dynamic phase transformation (DPT), fracture, severe plastic deformation (SPD), grain size change, and etc. Undesirable microstructural changes can be induced within the near-surface layers after hard turning, which is often termed as “white layer” because it appears to be featureless and white when viewed under an optical microscope.

Griffiths [130] attributes white layer formation to one or more of the following possible mechanisms: (1) rapid heating and quenching, which results in phase transformation, (2) severe plastic deformation, which produces a refined homogeneous structure, and (3) surface reaction with the environment, e.g., nitriding. It is well acknowledged that metallurgical transformation occurs in the chip or on the workpiece machined surface due to intense, localized and rapid thermo-mechanical working during hard turning [36, 37, 39]. Indeed, hard turning operations, particularly at high cutting speeds or with cutting tools severely worn, often lead to high cutting temperatures and hence white layers as a result of austenitization followed by partial transformation into martensite (the residue being retained austenite) [131]. An ultrafine grain structure has long been observed within the near-surface layers produced by hard machining. Studies of hard drilling of a commercial bearing steel (type SUJ2) in a tempered martensite structure by Li et al. [132] and Todaka et al. [133] showed that the white layers formed on the machined surfaces were composed of refined equiaxed nanocrystalline grains. They stipulated that the ultrafine structure layer on the machined surface is produced by both thermal- and deformation- driven phase transformations together with a large strain gradient and high strain rates. Ramesh et al. [134] suggested that white layers produced by hard turning of AISI 52100 steel with a hardness of 62 HRC at low-to-moderate cutting speeds are largely due to the grain refinement induced by SPD, whereas white layer formation at high cutting speeds is mainly due to thermally driven phase transformation. Umbrello et al. [135] and Li et al. [132] showed that both cutting parameters and initial workpiece hardness play vital roles in the white layer formation. Umbrello et al. [135] proposed a processing map as a function of the initial hardness of the workpiece and cutting speed as shown in Figure 1.5. It can be seen in Figure 1.5 that white layer formation in hard turning results from a combined effect of both thermally driven phase transformation and SPD. It is noted that the effect of cutting speed on white layer formation illustrated in Figure 1.5 contradicts the findings of the microstructure analysis in [134] for an AISI 52100 steel workpiece with an initial hardness of 62 HRC.

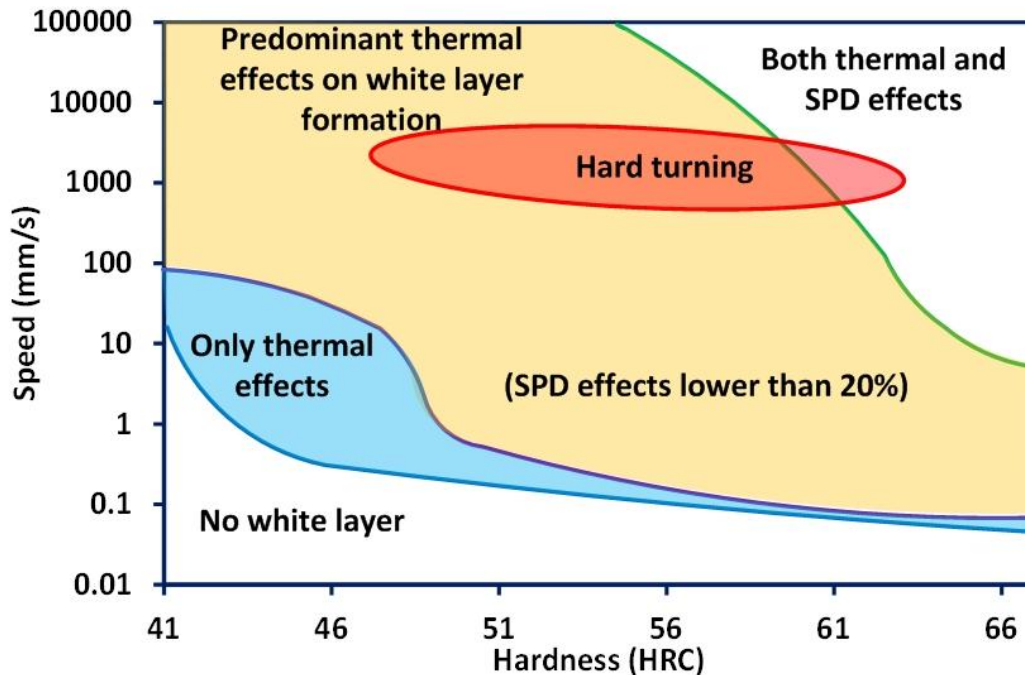


Figure 1.5. Processing map of the white layers formed during machining of AISI 52100 steel. Adapted from [135].

Thermally driven phase transformation has been exclusively modeled to investigate the formation of white layer in hard turning of bearing steels. Chou and Evans [36] used an analytical thermal modeling approach to predict white layer formation due to phase transformation in hard turning of AISI 52100 steel workpieces. Shi and Liu [136] developed a two-dimensional (2D) finite element (FE) analysis to simulate orthogonal cutting of hardened AISI 52100 steel using commercial software ABAQUS and analyzed the phase transformation on the chips from the temperature prediction. They found that high temperatures around the secondary shear zone causes fast re-austenitization and martensitic transformation, while other parts of the chips retain the original tempered martensitic structure. Ramesh and Melkote [127] modeled phase transformation kinetics in orthogonal cutting of hardened AISI 52100 steel using ABAQUS, which captured the phase transformation due to thermal, stress, and strain effects within the near-surface layers. The white layer thickness and subsurface residual stress predicted by the model were shown to be in good agreement with the experimental data. Umbrello and Jawahir [137] and Umbrello et al. [135] developed a 2D FE framework to predict white/dark layer thickness due to quenching/tempering and surface hardness in orthogonal

cutting of hardened AISI 52100 steel using commercial software DEFORM 2D. In particular, a hardness-based flow stress model was implemented in the FE code and an empirical model was developed for describing the phase transformations that create white and dark layers.

These aforementioned models did not consider the mechanism of grain refinement in the formation of white layer. Although ultrafine grain structures have been widely observed in the near-machined surface layers, very limited work has been attempted on modeling surface grain refinement due to SPD in hard turning. Only one study by Caruso et al. [138], to the author's best knowledge, attempted to model the grain size change in orthogonal cutting of hardened AISI 52100 using an empirical relationship, which was "calibrated" using the measured grain size values. To improve the process and understand the resultant microstructure after hard turning, it is necessary to investigate the microstructure refinement mechanism during the hard turning process and is desirable to have an analytical model for predicting resultant grain sizes.

In Chapter 5, a 3D FE framework is proposed for predicting the microstructure change in hard turning of AISI 52100 steel using a multi-physics model, which for the first time considers both phase transformation and grain refinement. The method proposed in this study takes a metallo-thermo-mechanical coupled frame work developed in Chapter 4 and solve for mechanical deformation, heat transfer, and microstructure simultaneously. Critical surface microstructure attributes such as grain refinement, phase change, microhardness, and residual stress are all discussed in this analysis.

1.5. Research Objectives

The objectives of this study are (i) to predict the microstructure alterations in metals and alloys subjected to cutting with a wide range of cutting conditions, and (ii) to improve the machinability and surface integrity of difficult-to-machine metal alloys via laser-assisted machining in both macro and micro scales. The specific objectives are as follows:

1. Develop new machining simulation methods
 - a) Develop a computationally efficient CEL based finite element model to simulate the steady-state orthogonal cutting process.

- b) Develop a numerical model with strain gradient plasticity to simulate the size effect in micro-milling.
2. Predictive modeling of grain refinement in metal cutting
 - a) Establish a physics-based numerical method for predicting the grain size change in metals and metal alloys undergoing SPD processes with a range of temperatures, strains and strain rates.
 - b) Apply this numerical method to different materials under different cutting conditions to predict grain size change due to SPD.
 3. Predictive modeling of phase change in steel cutting
 - a) Develop a metallo-thermo-mechanical coupled model to solve for grain size, phase composition, chip morphology, cutting temperature and cutting force simultaneously.
 - a) Apply the multi-physics model to hard turning and laser-assisted machining processes to quantitatively predict the microstructural change.
 4. Improve the machinability and surface integrity of difficult-to-machine metal alloys via laser-assisted machining in both micro and macro scales
 - a) Develop one-step LAM process for finish machining of difficult-to-machine alloys.
 - b) Study the laser-assist effect on surface quality and subsurface integrity in terms of surface finish, size control, microhardness, microstructures and residual stresses.
 - c) Develop numerical models to predict the tool performance, material machinability and surface integrity during the LAM process.

1.6. Dissertation Outline

In Chapter 2, novel numerical methods are proposed to model the chip formation during the steady-state orthogonal cutting and interrupted micro-milling processes.

In Chapter 3, a dislocation density-based material model is proposed to model grain size refinement due to severe plastic deformation in metal cutting.

In Chapter 4, a metallo-thermo-mechanical coupled model is developed to predict the phase change effect during orthogonal cutting of AISI 1045 steel.

In Chapter 5, the mechanisms of grain refinement and phase transformation are both included in modeling the surface microstructure alteration during 3D hard turning of AISI 52100 steel.

In Chapter 6, one-step LAM process is presented for finish machining of hardened steels. Surface integrity is examined experimentally and numerically with the developed models.

In Chapter 7, conclusions and recommendations for future work are given.

CHAPTER 2. THERMAL AND MECHANICAL MODELING OF MACHINING PROCESSES

In this chapter, novel Coupled Eulerian-Lagrangian and arbitrary-Lagrangian–Eulerian based finite element models are proposed to model the chip formation during a steady-state plane-strain orthogonal cutting process and a complete micro-milling cycle, respectively. The steady-state workpiece and tool cutting temperatures after multiple micro-milling cycles are analyzed with a heat transfer model based on the chip formation analysis and the prismatic thermal model predictions. The FE model results are discussed on chip formation, flow stresses, temperatures and velocity fields in great details, which relate to the surface integrity analysis and built-up edge (BUE) formation in micro-milling.

2.1. Coupled Eulerian-Lagrangian Modeling of Orthogonal Cutting

2.1.1. CEL Modeling

A coupled Eulerian-Lagrangian (CEL) model was developed to simulate steady-state chip formation and grain refinement in two-dimensional (2D) orthogonal cutting by using the commercial software Abaqus 6.10.1. Fully coupled thermo–mechanical Abaqus/Explicit analysis was carried out for orthogonal cutting. Quadrilateral, four-node, linearly interpolated elements with automatic hourglass control and reduced integration were used. Figure 2.1 shows the 2D CEL model setup with applied mechanical boundary conditions, where cutting takes place under plane strain condition. The arbitrary-Lagrangian–Eulerian (ALE) technique was used in the whole domain of workpiece, which was divided into four regions (Zone 1-4) to simulate material flow during cutting, as can be seen in Figure 2.1. During the simulation, material flows into the workpiece mesh from the left inlet surface of zone-1, passes zone-2 around the tool tip, and exits the simulation domain from the right outlet surface of zone-3 and the top surface of zone-4. Eulerian zones 1 and 2 remain mesh constrained at the left inlet and fully in space, respectively, while Lagrangian zones 3 and 4 grow in size generating the machined part and the

chip, respectively. The chip morphology continuously evolves by either inflation or deflation until reaching a steady state. No chip separation criterion was required by the CEL model. Mass scaling is often used in Abaqus/Explicit for computational efficiency in some dynamic analyses that contain very small elements [139] and a moderate mass scaling factor of 10 was used in the simulation to save the simulation time. A mesh-sensitivity analysis was conducted in several trial simulations, and the optimal mesh scheme was found to have about 5000 elements in total with the minimum element size of 5 μm in the workpiece, which considers both computational precision and time.

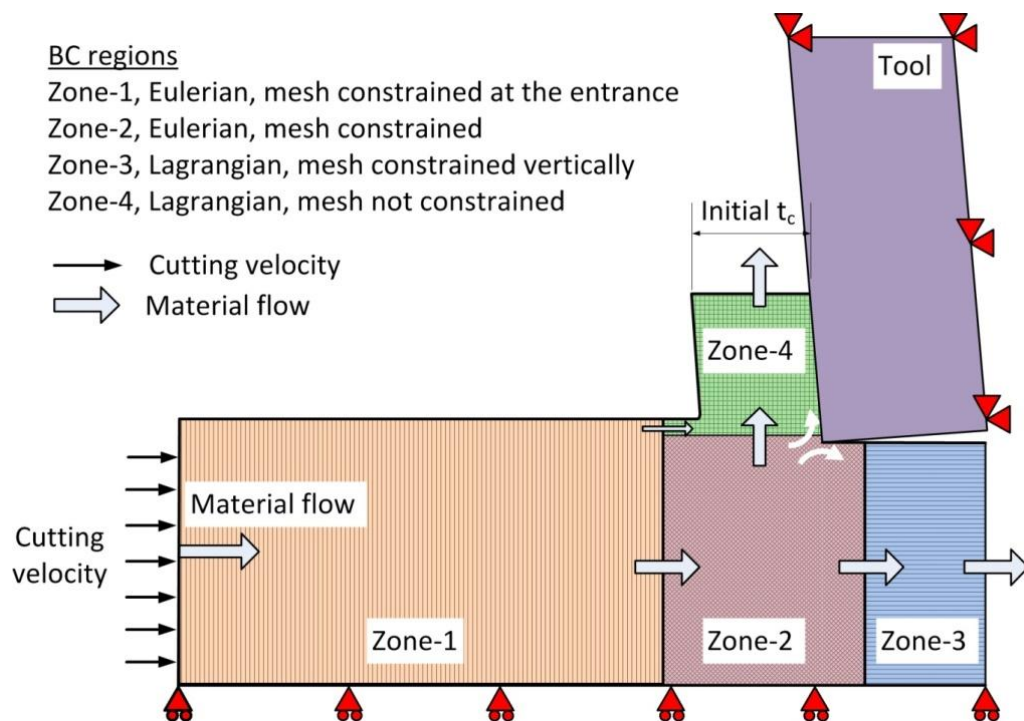


Figure 2.1. CEL model setup schematic.

2.1.2. Model Validation

To assess the validity of the CEL model, 2D orthogonal cutting conditions listed in Table 2.1 were simulated to compare the predicted cutting force with the experimental results [66, 67]. Workpiece material constitutive models used in the simulation are given in Table 2.2. A friction coefficient of 0.4 was used to define the tool-chip interaction in the simulations same as in [67]. Figure 2.2 and Figure 2.3 show the comparison of the cutting force and temperature

predictions with the experimental results, respectively. The cutting force matches well with the experimental results for all three tool rake angles. Nearly identical chip morphology and temperature profile were predicted by the CEL model in comparison with the predictions made by Miguélez et al. [66]. These results thus validate the CEL model for simulating 2D steady-state orthogonal cutting.

Table 2.1. CEL model validation test conditions [66, 67].

Test	Workpiece Material	Tool Material	Tool edge radius (μm)	Cutting speed (m/s)	Feed (mm)	Rake angle ($^\circ$)
1	AISI 316L	Kennametal	20	2	0.1	-6
2			20	2	0.1	0
3		K313	20	2	0.1	8

Table 2.2. Johnson-Cook type constitutive model parameters for AISI 316L [67].

Material	A_{JC} (MPa)	B_{JC} (MPa)	n_{JC}	C_{JC}	m_{JC}
AISI 316L	514	514	0.508	0.042	0.533

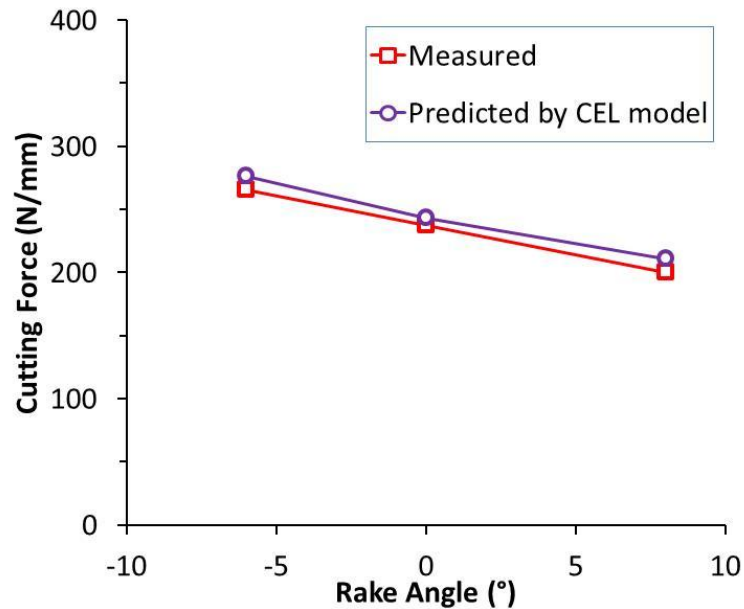


Figure 2.2. Comparison of predicted cutting force with experiments.

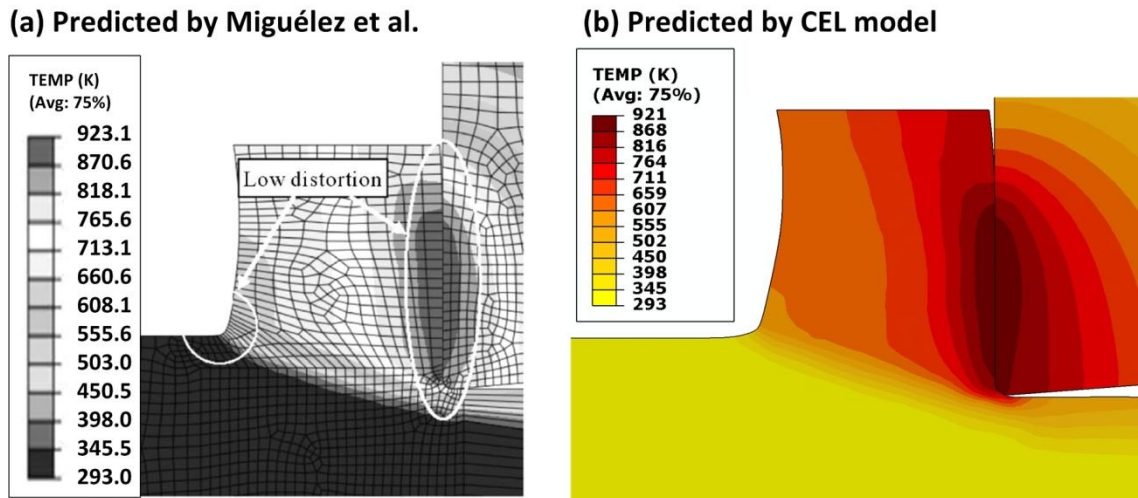


Figure 2.3. Comparison of predicted temperature distributions for Test 2.

2.2. Finite Element Modeling of Laser-Assisted Micro-Milling

Chip formation during micro-milling with varying uncut chip thickness was simulated with the strain gradient based finite element model for the two LAMM configurations. An arbitrary-Lagrangian–Eulerian (ALE) based finite element explicit scheme was developed with the commercial software ABAQUS to model the chip formation in micro-milling. The technique of remesh/solution mapping was developed to remesh the workpiece domain to enable a continuous simulation of chip formation and transfer the simulation results between ABAQUS explicit and implicit analyses.

2.2.1. LAMM Experimental Work

Laser-assisted micro-milling experiments were carried out on a three-axis CNC controlled micro-milling system that includes a Precise SC-40 spindle with a maximum rotational speed of 90k RPM and provides movement of the workpiece relative to the tool with a 1 μm resolution. A Synrad 48-2 CO₂ laser with a peak power output of 25 W and the necessary optics were mounted to the spindle fixture. A flexible nozzle was attached to the spindle mounting fixture allowing for an adjustable flow of assist gas during LAMM. Two-flute tungsten carbide endmills were used with the tool diameter ranging from 100 to 300 μm . Figure 2.4 (a) shows the LAMM optical path and (b-c) show the schematics of two LAMM configurations used in this

study. The LAMM bulk side cutting tests were performed along the top edges of bulk prismatic workpieces of about 55(L)X20(H)X20(W) mm in size, while the fin side cutting tests were performed on workpieces with fin structures of 55(L)X3(H)X(0.8-1.5)(W) mm in size. A smaller elliptical laser beam with the spot size of 150X260 μm was positioned on the workpiece side surface ahead of the tool in LAMM bulk side cutting, while a larger beam with the laser spot size of 360X510 μm was positioned on the workpiece top surface with a greater laser-tool lead distance in LAMM fin side cutting. The narrow width of the fins allowed for a more uniform temperature profile and lower peak temperatures to be achieved compared to the bulk workpiece geometry. To be consistent, the coordinate system was defined with respect to the workpiece as shown in Figure 2.4 such that feed direction is X axis and axial depth of cut direction is Z axis. The milling mode was down milling for the side cutting configurations. Note that the laser spot size (D_x , D_y and D_z), the laser-tool lead distance (L_x , L_y and L_z), the tool size (D_{tool}) and the depth of cut (Doc_y and Doc_z) were approximately scaled in Figure 2.4 to illustrate the differences in the two setups. The laser-tool lead distance in the workpiece feed direction was defined as the distance between the laser spot center and the boundary of the machined chamfer in the side cutting configurations.

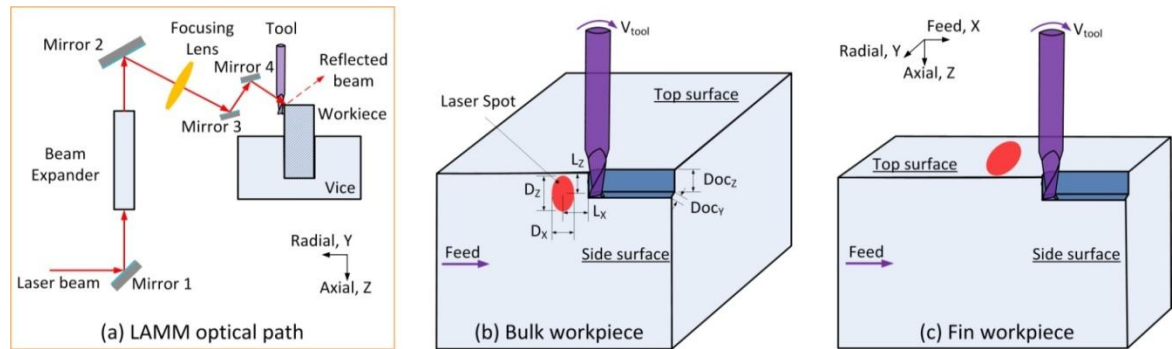


Figure 2.4. LAMM test configurations.

Table 2.3 and Table 2.4 give the test conditions for the side cutting of bulk workpiece and fin structure configurations, respectively. The average material removal temperature, T_{mr-avg} , refers to the weighted average material temperature in the machined chamfer purely due to the laser heating, and will be discussed in details in Section 2.3. Multiple laser power levels were used in the LAMM tests to study the temperature effect on the LAMM process. Tool wear was measured for both bulk and fin LAMM side cutting tests. For LAMM side cutting of the bulk

workpiece configuration, the laser scanned the unmachined surface ahead of the cutting tool, and multiple cutting tests were performed on multiple workpieces. For LAMM side cutting of the fin structure, multiple fin side cutting tests were performed along the same workpiece side with the laser scanning the top surface in multi passes. Post-inspections after micro-milling experiments were carried out to investigate the resultant surface integrity, machined part size and tool wear. A JEOL JSM-T330 scanning electron microscope (SEM) and a Zeiss optical microscope were used to examine machined workpieces and tools.

Table 2.3. LAMM side cutting tests of bulk workpiece configuration.

<i>Material</i>	<i>Test</i>	D_{tool} (μm)	r_e (μm)	V (<i>m/min</i>)	h_{max} (μm)	λ (h_{max}/r_e)	$Doc_y \times Doc_z$ (μm)	P (<i>W</i>)	$D_x \times D_z$ (μm)	$L_x \times L_z$ (μm)	T_{mr-avg} ($^{\circ}C$)
422SS	422bulk-1							-	-	-	20
	422bulk-2	100	≈ 0.5	18.85	0.83	1.67	5X150	12.5	150X260	150X150	330
	422bulk-3							15.5	150X260	150X150	400
	422bulk-4							18.75	150X260	150X150	480
Tibulk-1	-							-	-	20	
Ti64	Tibulk-2							2.7	150X260	150X150	242
	Tibulk-3	100	≈ 0.5	18.85	0.83	1.67	5X150	4	150X260	150X150	338
	Tibulk-4							5.3	150X260	150X150	435
	Tibulk-5							6.7	150X260	150X150	532

Table 2.4. LAMM side cutting tests of fin workpiece configuration.

<i>Material</i>	<i>Test</i>	D_{tool} (μm)	r_e (μm)	V (<i>m/min</i>)	h_{max} (μm)	λ (h_{max}/r_e)	$Doc_y \times Doc_z$ (μm)	P (<i>W</i>)	$D_x \times D_y$ (μm)	$L_x \times L_y$ (μm)	T_{mr-avg} ($^{\circ}C$)
422SS	422fin-1	150	≈ 0.5	28.3	0.83	1.67	5X250	-	-	-	20
	422fin-2							20.4	360X510	400X255	354
IN718	718fin-1							-	-	-	20
	718fin-2	300	≈ 0.5	58.8	0.83	1.67	10X200	17.4	360X510	400X255	396
	718fin-3							20.6	360X510	400X255	468
Tifin-1	-							-	-	20	
Ti64	Tifin-2							14.5	360X510	400X255	421

2.2.2. Strain Gradient Constitutive Model

Table 2.5 shows the Johnson-Cook type material constitutive plasticity model parameters of the workpiece materials. These constitutive models describe the material flow stress at various strains, strain rates and temperatures occurring in cutting. However, the flow stress models are independent of the length scale in the FE simulation and hence are not suitable for describing the significant size effect in micro cutting.

The strain gradient plasticity model is briefly presented in this section and more detailed descriptions can be found from the work of Liu and Melkote [53] and Lai et al. [54]. In strain gradient plasticity, a length scale is introduced through the coefficients of spatial gradients of strain components and can be used to model the size effect in micro-milling. The strain gradient constitutive model can be expressed explicitly as

$$\sigma = (A + B\varepsilon^n) \left(1 + c \log \frac{\dot{\varepsilon}}{\dot{\varepsilon}_o} \right) \left(1 - \left(\frac{T - T_{ref}}{T_m - T_{ref}} \right)^m \right) \left(1 + \frac{18a^2 b G^2}{L \left((A + B\varepsilon^n) \left(1 + c \log \frac{\dot{\varepsilon}}{\dot{\varepsilon}_o} \right) \left(1 - \left(\frac{T - T_{ref}}{T_m - T_{ref}} \right)^m \right) \right)^2} \right)^\mu \right)^{1/2} \quad (2.1)$$

where L is the length parameter. The strain gradient plasticity was programmed as a material subroutine in ABAQUS. Table 2.6 gives the model parameters of the workpiece materials used in the FE simulations. The length L used in the simulation was chosen to be the uncut chip thickness, which varied as a function of the angle of tool rotation. To properly estimate the total dislocation density in the strain gradient plasticity model, a constant μ of 0.38 was adopted for modeling the workpiece materials in micro-milling from the work of Lai et al. [54] and Joshi and Melkote [140]. Figure 2.5 compares the Johnson-Cook and strain gradient constitutive behaviors of the workpiece materials for the maximum uncut chip thickness of 0.83 μm , strain rate of 10^5 s^{-1} and temperature of 400 $^\circ\text{C}$. It can be seen that the strain gradient constitutive model predicts higher flow stresses by including the size effect. For example, the strain gradient plasticity model of Inconel 718 shows a flow stress of 2,876 MPa at an equivalent strain of 1, while the conventional Johnson-Cook model of Inconel 718 shows a flow stress of 1,845 MPa under the same condition.

Table 2.5. Johnson-Cook constitutive model parameters of the workpiece materials.

Material	A (MPa)	B (MPa)	n	C	m	$\dot{\epsilon}_0$ (s^{-1})	T_m ($^{\circ}C$)
422SS [141]	870	400	0.4	0.015	0.5	0.01	1520
IN718 [142]	980	1370	0.164	0.02	1.03	1	1300
Ti64 [74]	782.7	498.4	0.28	0.028	1	1E-5	1660

Table 2.6. Strain gradient parameters of the workpiece materials.

Material	G (GPa)	b (nm)	a	μ
422SS [143]	$-0.0439T(^{\circ}C)+85.709$	0.248	0.5	0.38
IN718 [144]	$-0.0225 T(^{\circ}C)+86.003$	0.249	0.5	0.38
Ti64 [145]	$-0.0241 T(^{\circ}C)+41.097$	0.295	0.5	0.38

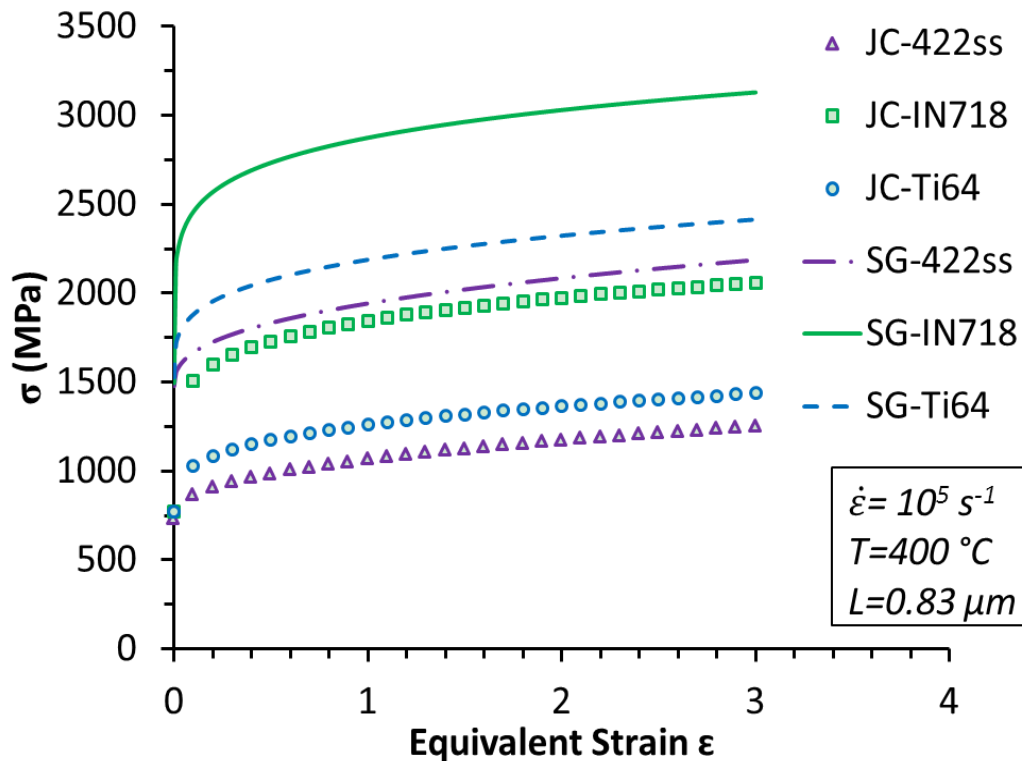


Figure 2.5. Johnson-Cook and strain gradient constitutive behaviors of the workpiece materials.

2.2.3. FE Models of Chip Formation Analysis

The 3D micro-milling process as illustrated in Figure 2.4 can be approximated as the sum of a deck of 2D deformation-process sections with finite sectional heights twisted at the helix angle of the endmill in an orderly fashion. Because the sectional height can be chosen to be very small, the tool helix angle has little effect and the section can be treated as straight one in the tool axial direction. Figure 2.6 (a) shows the 2D sectional view of LAMM side cutting. A simplified geometry of one cutting flute was modeled in the simulation, while considering the actual tool cutting edge radius, tool radial rake angle and relief angle. For LAMM side cutting of both bulk and fin configurations, the simulation started from θ_{max} , around 20° to 26° depending on the actual cutting parameters, to simulate a complete cutting cycle of one flute as can be seen in Figure 2.6 (b).

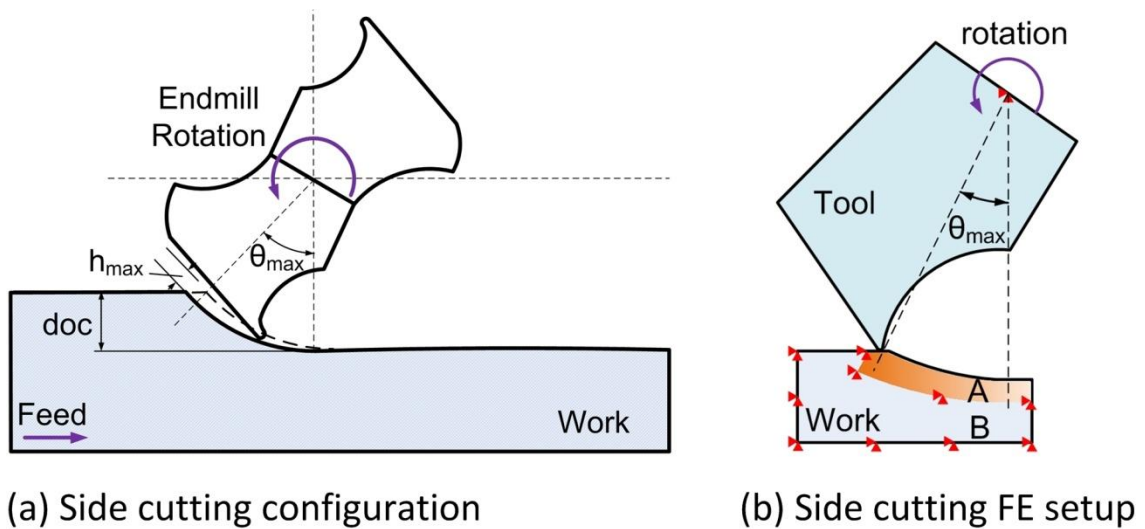


Figure 2.6. FE models of chip formation.

Fully coupled thermo–mechanical Abaqus/Explicit analysis was carried out for micro-milling simulations. Quadrilateral, four-node, bilinear displacement and temperature elements with automatic hourglass control and reduced integration were used. The workpiece temperature predicted by the thermal model was used as the initial workpiece temperature in the simulations of the first milling cycles, while the steady-state cutting temperature after many milling cycles is determined by additional heat transfer analysis as will be discussed in Section 2.3. The ALE and remeshing techniques developed by Ding et al. [92] were applied in the

Abaqus/Explicit analysis steps to simulate chip formation without using any chip separation criterion. To save the computation cost for ALE, the workpiece domain was artificially divided into two sections of *A* and *B*. ALE was applied to the top section *A* with a fine mesh, while the bottom section *B* was fixed in space with no ALE defined but to work as a heat sink. A constant thermal conductance of $10^5 \text{ W/K}\cdot\text{mm}^2$ was used to define the interface between sections *A* and *B* for the materials studied, which was deliberately set high enough to ensure the continuity of temperature across the interface between the sections. As a result, no stress was simulated in section *B*, but a continuous temperature contour was simulated by properly accounting for heat conduction.

The top section *A* has a sectional width of $6 \mu\text{m}$ for the LAMM side cutting models. A prescribed rotational speed was applied to the tool center and the workpiece elements in section *A* deformed into the chip were simulated with the smoothing techniques of ALE. A constant frictional coefficient of 0.65 was adopted for the tool-work interface [89] for all the materials investigated in this study. An ABAQUS/Explicit simulation step of $20 \mu\text{s}$ or 7° tool rotation at a cutting speed of 18.85 m/min can be completed with the ALE technique in a reasonable computation time. However, a longer step cannot be simulated due to excessive distortion of the workpiece mesh around the tool nose even with ALE. To simulate the chip formation continuously for a longer period of time, for instance, 26° tool rotation for a complete cutting cycle, remeshing the deformed workpiece is required. However the mesh-to-mesh solution mapping technique is only available in ABAQUS/Implicit. An ABAQUS/Implicit step was developed between two continuous explicit steps for remeshing the distorted workpiece mesh and mapping the simulation results from the previous explicit step to the following one. A very short period of time, say $0.001 \mu\text{s}$, was simulated for the implicit step and remesh was optimized in the deformed workpiece domain using ABAQUS/CAE.

2.2.4. Validation of Cutting Force

To determine the validity of the model, the FE model with the strain gradient plasticity has been applied to prediction of the cutting forces in micro-milling of hardened H13 steel with the hardness of 45 HRC and laser-assisted micro-grooving of hardened H13 steel with the hardness of 42 HRC conducted by Aramcharoen and Mativenga [20] and Singh and Melkote [63], respectively. The simulation results of the cutting force in micro-milling are briefly presented

here and more detailed descriptions can be found from the authors' early work [92]. Figure 2.7 (a) compares the predicted specific cutting forces with the experimental data in micro-milling tests with ratio λ varying from 0.2 to 2. It is evident that FE simulations with the strain gradient plasticity model show a significant size effect in the specific cutting force in micro-milling and match well with the experimental data for various λ ratios by Aramcharoen and Mativenga [20]. Simulations with the Johnson-Cook model predict the size effect to some extent due to the increase of tool cutting edge radius in micro slotting; however, it was not able to simulate the extreme high specific cutting force occurring in micro cutting for ratio λ less than 0.5. To further assess the validity of the numerical models and temperature effect on cutting force in LAMM, the prismatic thermal model has been applied to model the temperature rise due to laser-assist in laser-assisted micro-grooving of hardened H13 steel using a 35W solid-state ytterbium-doped fiber laser of a wavelength of 1060 nm studied by Singh et al. [61]. For laser-assisted micro-grooving using a laser beam size of 110 μm , a scanning speed of 10 mm/min and depth of cut of 25 μm , the temperature rise predicted by the prismatic thermal model matched well with the temperature measurement using the K-type thermocouples of 75 μm diameter and the prediction errors are all within 10% at thermocouples at distances ranging from 20 to 200 μm from the laser beam center for laser power ranging from 5 to 10 W. Using the simulated steady-state temperature field as the temperature condition and the strain gradient plasticity with a material length scale L of 25 μm (equivalent of the uncut chip thickness), the cutting forces in the tangential (F_c) and radial (F_r) directions were predicted using the FE model for the laser-assisted micro-grooving process. Figure 2.7 (b) shows the comparison of the predicted cutting forces with the experimental data provided by Singh and Melkote [63] and it is evident that FE simulations match very well with the experimental measurement with prediction errors well below 5%. The simulation results thus validated the efficacy of the prismatic thermal model and the FE model with the strain gradient plasticity model for simulating the LAMM process.

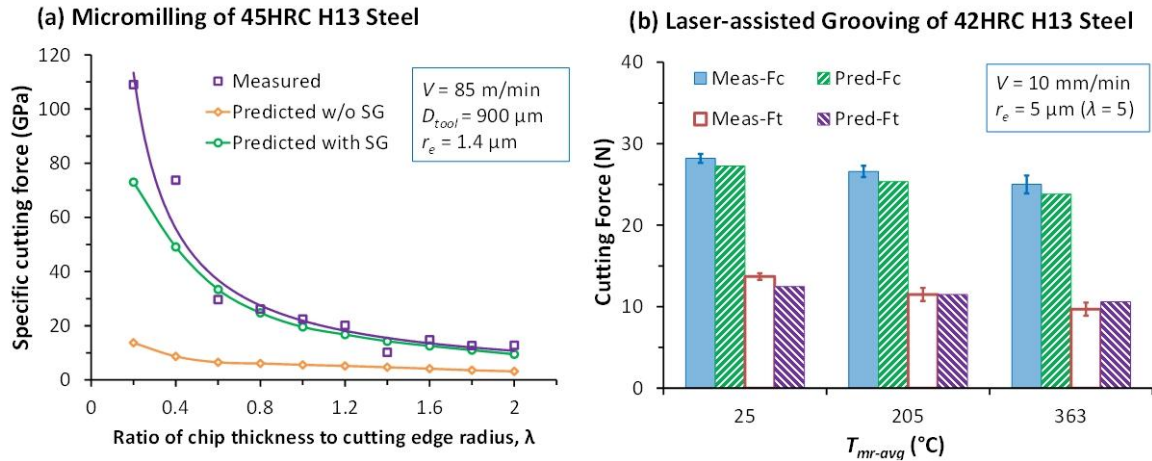


Figure 2.7. Measured and predicted cutting forces in micromachining of hardened H13 steels.

2.3. Thermal and Mechanical Modeling Analysis of Laser-Assisted Micro-Milling

In this section, the workpiece temperature predicted by the prismatic thermal model was used as the initial workpiece temperature in the simulations of first milling cycles, while the steady-state cutting temperature was investigated by a heat transfer analysis of multi micro-milling cycles.

2.3.1. Workpiece Temperature Increase due to Laser Heating

In LAMM, the temperature distribution in a workpiece is very critical for the tool performance in LAMM and surface integrity analysis such as heat affected zone. Therefore, the thermal analysis in the machined chamfer is very critical for both theoretical investigation and experiment design of different configurations. A transient, 3D finite volume prismatic thermal model has been developed by the authors' research group for laser-assisted milling studies [91]. The model calculates the temperature distribution throughout any prismatic workpiece during a transient laser heating process. The prismatic thermal model was used to accurately predict the temperature distribution due the laser heating in different LAMM configurations.

The thermo-mechanical properties of the tool material were obtained from Park [146], while the temperature-dependent thermal properties of the workpiece materials were found from the Thermophysical Properties of Matter Database [143], which are given in Table 2.7 as functions of temperature. The absorptivity of the workpiece material depends on the laser

parameters and workpiece surface condition. Table 2.8 gives the absorptivity of the workpiece materials at CO₂ laser wavelength of 10.6 μm, which was measured for both fin and bulk workpiece specimens by Shelton and Shin [22]. The workpiece surface was scanned by the CO₂ laser repeatedly in multi-pass LAMM fin side cutting, while the workpiece surface was scanned only once in LAMM bulk side cutting. The measured absorptivity was about 0.4 for the four workpiece materials with small variances. For Inconel 718, with the similar peak temperatures, T_p , the specimen surface was oxidized more in the fin absorptivity test due to multi-pass laser scans and a higher absorptivity was obtained. While for 422SS and Ti64, the peak temperatures were 332 and 170 °C lower in the fin absorptivity tests than those in the bulk absorptivity tests, respectively, and hence specimen surfaces were less oxidized for the fin specimens, which explains lower absorptivity values were measured in the fin absorptivity tests for these two materials.

Table 2.7. Thermal properties of the workpiece materials [143].

Material	Density (kg/m ³)	Thermal Conductivity (W/m-K)	Specific Heat (J/kg-K)
422SS	7780	$19.78 + 0.017T - 8.83 \times 10^{-6}T^2$ (for $T < 925K$) 28 (for $T \geq 925K$)	478 (for $T < 493K$) $1177.3 - 3.9932T + 0.0067848T^2 - 3.1466 \times 10^{-6}T^3$ (for $493K \leq T \leq 1145K$) $1112.2 - 0.4098T$ (for $1145K < T \leq 1325K$) 570 (for $T > 1325K$)
IN718	8180	$6.86 + 0.0151T$	$363.91 + 0.213T$
Ti64	4470	$6.65 - 0.0012T + 1 \times 10^{-5}T^2$ (for $T < 1250K$) 20.8 (for $T \geq 1250K$)	$415.52 + 0.2293T$ (for $T < 1473K$) 756 (for $T \geq 1473K$)

Table 2.8. Absorptivity of the workpiece materials at CO₂ laser wavelength of 10.6 μm [22].

Material	Bulk workpiece	T_p (°C)	Fin workpiece	T_p (°C)
422SS	0.40±0.03	1208	0.38±0.03	876
IN718	0.36±0.02	1117	0.46±0.05	1028
Ti64	0.45±0.04	1098	0.38±0.02	928

Figure 2.8 shows the predicted workpiece temperature fields of Ti6Al4V undergoing LAMM. The material temperature, $T_{mr}(Z,\theta)$, is defined as the workpiece temperature at the tool rotational angle of θ and cutting depth of Z in the machined chamfer due to the laser heating, while the average material temperature, T_{mr-avg} , is the weighted average workpiece temperature of the cutting chamfer using the weighting factor of undeformed chip thickness. It can be seen that some temperature variances can be observed along the cutting depth for LAMM side cutting. Figure 2.9 (a) shows the laser power effects on T_{mr-avg} and temperature variance of the machined chamfer of LAMM side cutting of various workpiece materials. T_{mr-avg} increases largely in a linear trend as the laser power increases. As workpiece materials have different thermal properties, i.e., thermal conductivity and specific heat, the workpiece temperature field varies greatly for different materials even with the same absorbed laser power and experimental condition. For example, T_{mr-avg} of Ti6Al4V is much higher than that of 422SS given the same laser power as can be seen in Figure 2.9 (a). Compared to the other materials, the low thermal conductivity of Ti6Al4V tends to produce a more notable temperature gradient in the cutting chamfer. Figure 2.9 (b) shows the temperature profiles in the machined chamfer of Ti6Al4V for different configurations. T_{mr} varies by 20°C and 30 °C within the depth of cut of 150 and 200 μm for LAMM side cutting of bulk and fin workpiece configurations, respectively.

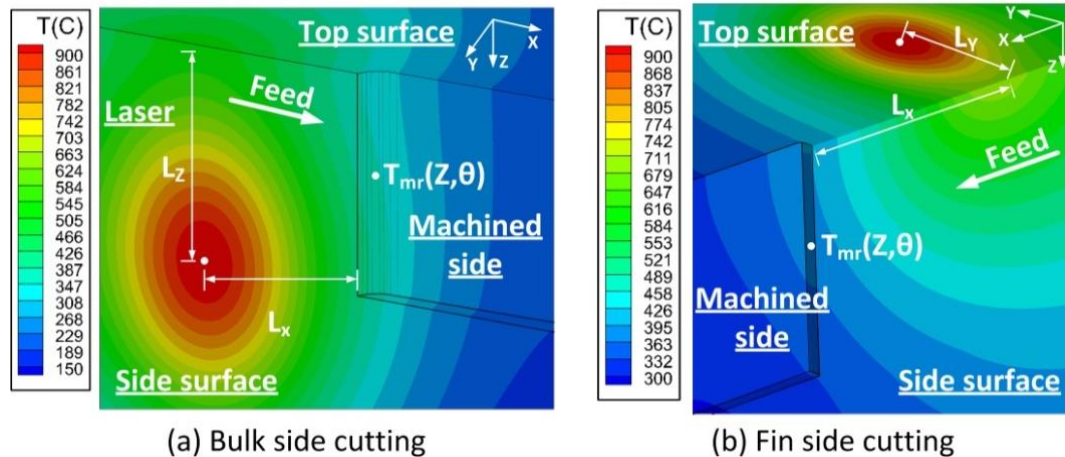


Figure 2.8. Temperature fields of Ti6Al4V undergoing LAMM side cutting.

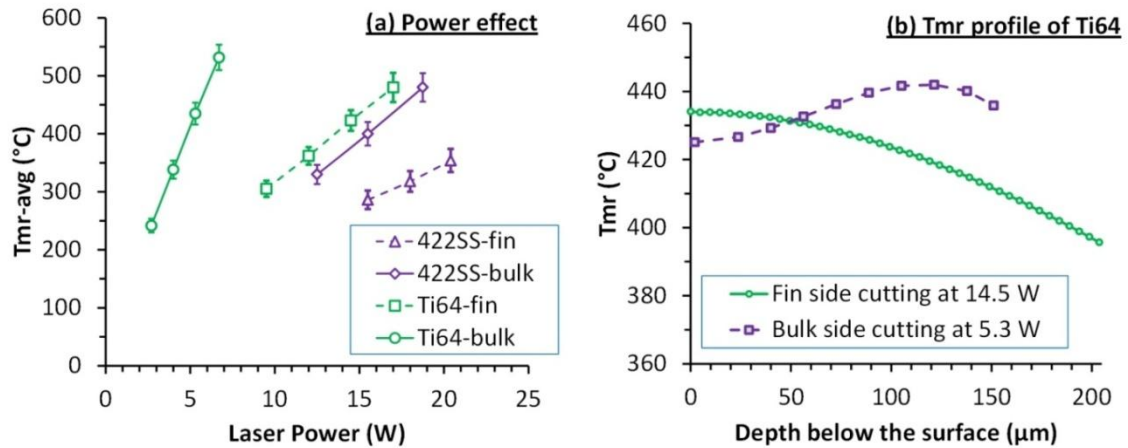


Figure 2.9. Temperature predictions by the prismatic thermal model.

Figure 2.10 shows the temperature distributions at different cutting depths for LAMM side cutting of 422SS of the fin configuration. High temperature gradients exist within a shallow depth near the laser spot center, while the temperature gradients decrease drastically as the heat dissipates as can be seen by comparing Figure 2.10 (a) to Figure 2.10 (b) and (c). T_{mr-avg} of the cutting chamfer only drops from 365 °C to 338 °C from 5 μm to 245 μm below the top surface. The boxed domain of 60X30 μm shown in Figure 2.10 is designated as the finite element cutting simulation domain, where temperature distribution predicted by the thermal model defines the initial temperature for the cutting simulation. It can be seen that the workpiece temperatures vary by less than 20 °C within the cutting simulation domains. In the following sections, unless the location is specified, the temperature profile predicted in the middle of the depths of cut was used as the initial condition for the workpiece in the FE simulations.

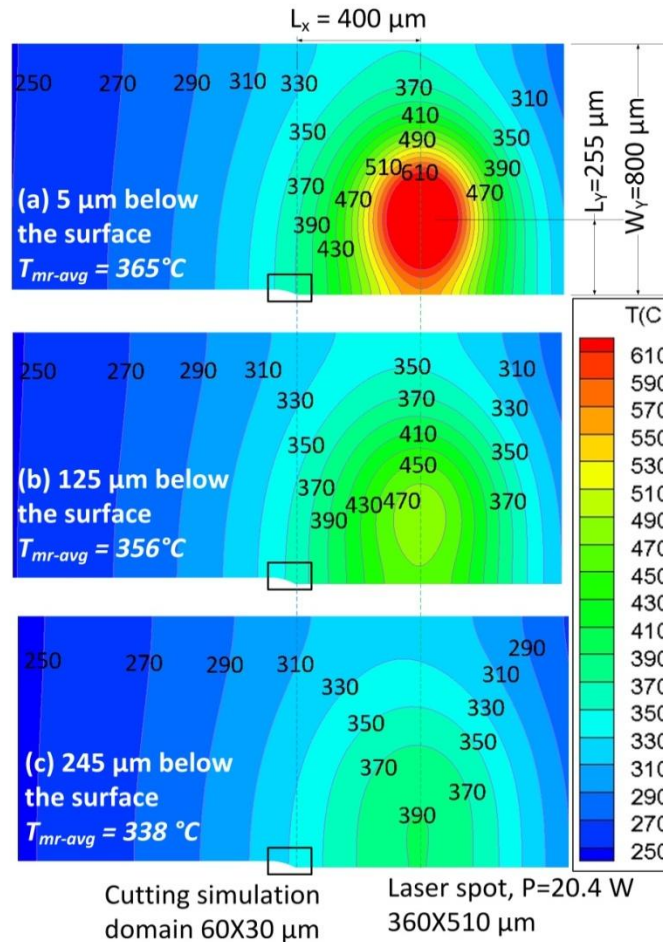


Figure 2.10. Thermal analyses in fin workpiece side cutting of 422SS.

2.3.2. Workpiece Temperature after Multi LAMM Cycles

The FE chip formation simulation was limited to one micro-milling cycle, because coupled thermo-mechanical analysis is too expensive in computation using any commercial finite element software. To correctly model the steady-state cutting temperature only achieved after many milling cycles, a heat transfer analysis was performed on the bulk and fin workpieces after the chip formation analysis for further milling cycles at a low computation cost. In the chip formation analysis, the modeled workpiece was smaller than the actual one to save the computation cost, but it was extended to close to the actual size in the heat transfer analysis for the proper thermal boundary conditions. The ABAQUS/Explicit solver was used in the heat transfer analysis of the bulk and fin workpieces for many milling cycles. In each conventional micro-milling cycle, the workpiece material is heated locally by heat generation due to plastic

deformation and friction at the tool-chip and tool-workpiece interfaces as the tool flute is engaged, while it cools down due to heat conduction to the bulk material and heat convection to air as the flute leaves. If the local heat generation is not dissipated completely to the bulk material by heat conduction and the environment by heat convection, the temperature of the workpiece will get an increment in the following milling cycle due to the remaining heat. Different than in conventional micro-milling, the workpiece material temperature, T_{mr} , is already increased to a few hundreds of degrees in Celsius higher than the tool temperature due to the laser heating in LAMM, and the material cutting temperature in the deformation zone, T_{shear} , might drop several dozens of degrees from T_{mr} due to the heat conduction to the relative cool tool.

As the cutting flute approaches, the total heat flux to the local material due to cutting is composed of heat generation term \dot{q}_{pl} converted from plastic deformation and frictional heat term \dot{q}_{fw} . Deformation heat flux is given by

$$\dot{q}_{pl} = \eta_{pl} \sigma \dot{\epsilon} \quad (2.2)$$

where η_{pl} specifies the fraction of deformation energy converted into thermal energy (0.9 was used), σ is the material flow stress, and $\dot{\epsilon}$ is the material strain rate. Frictional heat flux is created due to the sliding friction between the workpiece material and the tool face. The amount of frictional heat flux into the workpiece is given by

$$\dot{q}_{fw} = \xi \eta_f \tau_s \dot{\gamma} \quad (2.3)$$

where η_f specifies the fraction of mechanical energy converted into thermal energy (0.9 was used), τ_s is the frictional stress, $\dot{\gamma}$ is the slip rate, and ξ gives the fraction of the generated heat flowing into the workpiece (0.5 was used). The conductive heat flux, \dot{q}_c , conducted away by the tool is defined by the temperature difference of tool-chip and tool-workpiece at the interface by

$$\dot{q}_c = k_{gap} (T_{work/chip} - T_{tool}) \quad (2.4)$$

where k_{gap} is the gap conductance. The gap conductance in the heat transfer analysis was 10^4 W/K·mm² when the tool face node is in contact with the chip and the workpiece. When the tool face node had no contact with the chip and the workpiece, the gap conductance was set to zero. The contact status of the tool face node at a time point was derived from the value of normal pressure at the corresponding time point in the chip formation analysis of the first milling cycle.

All these heat flux components are varying from node to node and the nodal heat flux data were obtained from the FE chip formation analysis of one milling cycle. A time-dependent nodal heat flux subroutine was created for the heat transfer analysis of multi cycles, in which the heat flux was used as periodic heat input along the milling paths. The temperature fields predicted by the LAMM thermal model were used as the boundary conditions in the heat transfer analysis.

To determine if the workpiece temperature field reaches its quasi steady state, the temperature histories of central nodes on the machined slot were tracked for the conventional and LAMM side cutting of 422SS with the heat transfer analysis. Figure 2.11 (a) shows the nodal temperature history of two conventional fin side cutting cycles, and it can be seen that the material temperature (T_{shear}) in the cutting zone increases to about 120 °C as the flute approaches but drops to the ambient temperature (T_{ss}) as the flute leaves within the first milling cycle. Figure 2.11 (b) tracks the nodal temperature histories of two LAMM fin side cutting cycles. The material shearing temperature drops to about 342 °C as the flute approaches but reverses quickly to the initial T_{mr} of 356 °C as the flute leaves within the first milling cycle. These findings prove that the simulation of the first side cutting cycle of either LAMM or conventional configuration predicts the steady-state cutting temperature. As discussed above, the continuous laser heating input in LAMM compensates for the heat loss conducted away by the tool material and increases the material temperature back to steady-state T_{mr} prior to the following cutting cycle. The simulated steady-state temperature fields were then used for setting the temperature conditions in the chip formation analysis of LAMM side cutting.

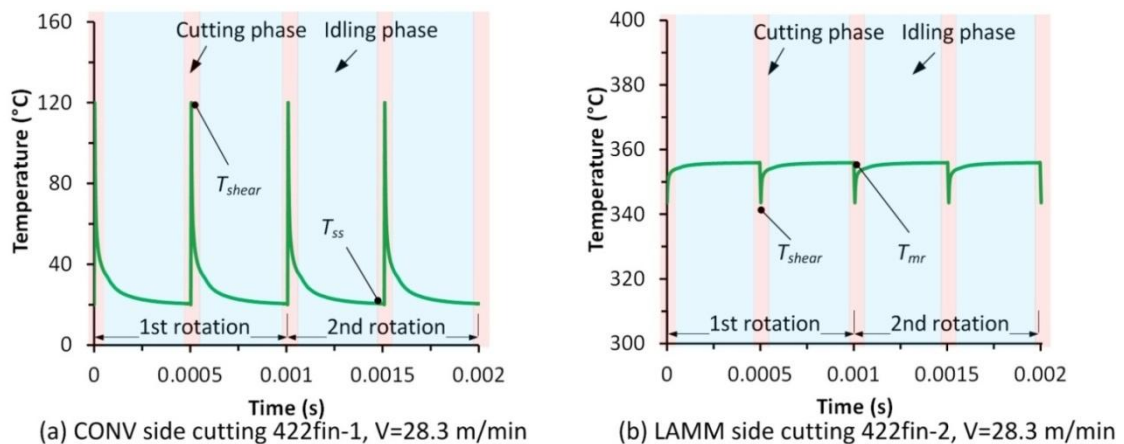


Figure 2.11. Workpiece nodal temperature histories in conventional micro-milling and LAMM of 422SS.

2.3.3. Tool Temperature after Multi LAMM Cycles

A heat transfer analysis was also carried on the cutting tool for multiple fin side cutting cycles in order to get the steady-state tool temperature for the correct calculation of tool wear. For the tool flute, each milling cycle includes a cutting and an idling phase. The tool is heated in the cutting phase by the heat flux at the tool-chip and tool-workpiece interfaces, and then the heat is dissipated to the tool bulk material by conduction and to the air by convection. An implicit heat transfer analysis with ABAQUS/Standard solver was conducted to model the tool temperature history of multiple LAMM side cutting cycles. Although in the cutting simulation the cutting tool rotates continuously, in the heat transfer analysis it is fixed spatially. The tool geometry and mesh in chip formation analysis were inherited and used in the heat transfer analysis. The 2D first-order four node diffusive element, DC2D4, was chosen to mesh the tool geometry in the heat transfer analysis.

Figure 2.12 illustrates the boundary heat flux conditions in the tool heat transfer analysis. In the cutting phase the cutting tool is heated and the total heat flux is composed of frictional heat flux \dot{q}_{ft} and conductive heat flux \dot{q}_c . The conductive heat flux caused by the temperature difference of tool-chip and tool-workpiece at the interface is calculated by Eqn. 2.4. The amount of frictional heat flux into the cutting tool is given

$$\dot{q}_{ft} = (1 - \xi) \eta_f \tau_s \dot{\gamma}. \quad (2.5)$$

Therefore, conductive heat flux was temperature dependent. Both the heat flux components were varying from node to node and the basic nodal heat flux data were obtained from the chip formation analysis. In the cooling phase of milling operation, if the heat in the tool is not emitted completely to the environment by heat convection and heat radiation, the temperature of the tool will get an increase in the following milling cycle due to the remaining heat. The convective heat transfer coefficient h from a high-speed rotating tool was obtained by using an empirical correlation of Nusselt number for a rotating cylinder [147] as

$$\overline{Nu} = 0.318 Re_r^{0.571} \quad (2.6)$$

where Re_r is the Reynolds number for the rotating tool in air. The calculated convective heat transfer coefficient h ranged from 118 to 138 W/m²K for micro endmill diameter ranging from

100 to 300 μm rotating at 60k RPM. Constant temperature was assumed at the tool core area. The time-dependent nodal heat flux subroutine was created for both the cutting and cooling phases of multi LAMM cycles.

To determine after how many milling cycles the tool temperature field reaches its quasi steady state, the tool temperature distribution simulated for multiple milling cycles was examined. It is found that the tool temperature distribution after multiple milling cycles was identical to the one after the first milling cycle. Figure 2.13 shows the tool cutting edge temperature histories of the two flutes in multiple LAMM fin side cutting cycles under the condition of 422fin-2 with a cutting speed of 28.3 m/min. It can be seen that the tool tip temperature increases to about 250 $^{\circ}\text{C}$ during cutting, but then drops quickly to the ambient temperature during the first tenth of cooling phase period.

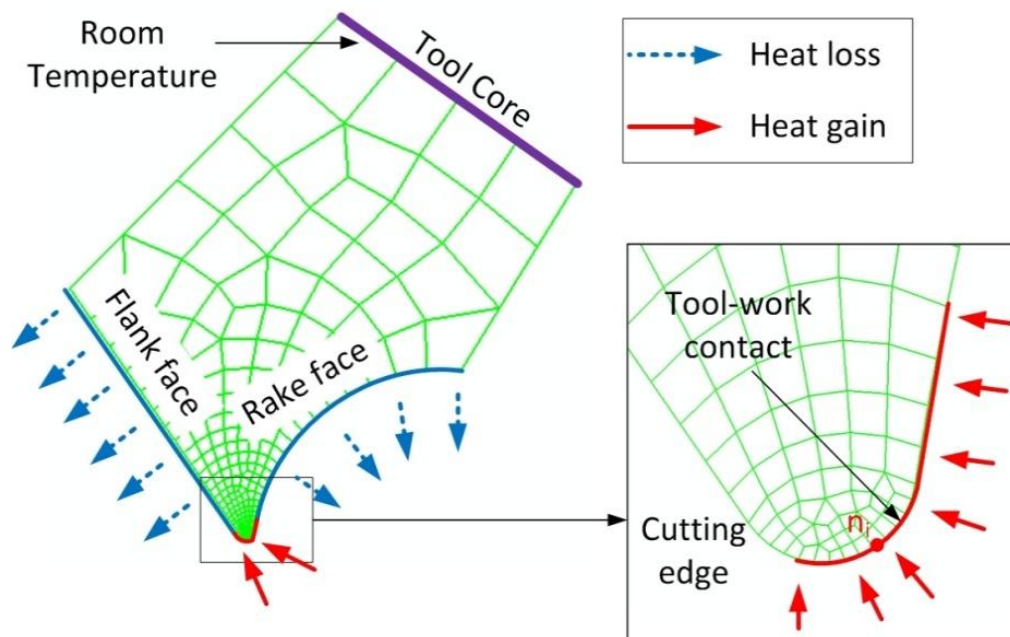


Figure 2.12. Heat transfer analysis of the tool.

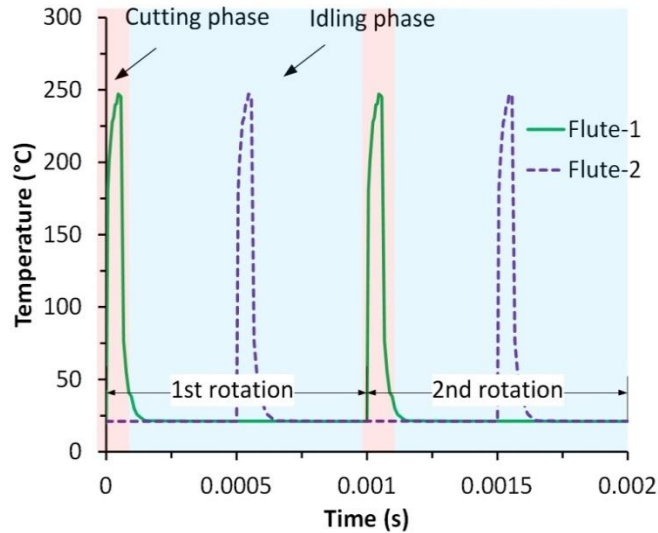


Figure 2.13. Tool cutting edge temperatures in LAMM of 422SS under the condition of 422fin-2.

2.3.4. Chip Formation and Temperature Effect on Workpiece Flow Stress

Continuous chip formation within a complete LAMM side cutting cycle with a $0.5\ \mu\text{m}$ edge radius micro tool is shown in Figure 2.14. Five ABAQUS/Explicit steps were simulated for the cutting cycle. Four ABAQUS/Implicit intermittent steps were used to remesh the distorted workpiece mesh from the previous explicit step and map the simulation results from the earlier step to the following one. Strain gradient plasticity was used in all the time steps with the average uncut chip thickness as the material length scale L , which was updated for each remeshed step to account for the varying uncut chip thickness at different tool rotation angles. Deformed chip thickness grew thicker in the beginning $30\ \mu\text{s}$ cutting time even with a decreasing uncut chip thickness. The model simulated necking of chip formation after approximately $50\ \mu\text{s}$. The simulated shear zone temperature, T_{shear} , in the primary deformation zone was about $370\ ^\circ\text{C}$, which was lower than T_{mr} of $400\ ^\circ\text{C}$ due to the heat conduction from the deformation zone to the tool material. Figure 2.14 (b) shows the predicted tool temperature distribution with a peak temperature of $216\ ^\circ\text{C}$ at $60\ \mu\text{s}$ cutting time.

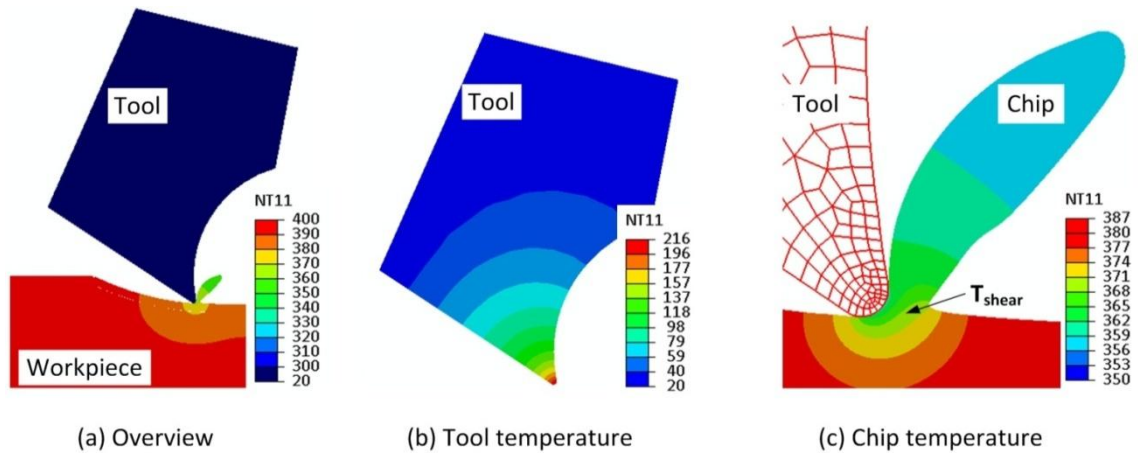


Figure 2.14. Chip formation and cutting temperatures of LAMM bulk side cutting of 422SS at 60 μ s cutting time under the condition of 422bulk-3 ($V=18.85\text{m/min}$).

Figure 2.15 (a) shows the temperatures and flow stresses in the primary deformation zone in LAMM bulk side cutting tests of 422SS. As can be seen in Figure 2.15 (a), flow stress reduced linearly from 2557 MPa under conventional bulk side cutting test condition to 1927 MPa under LAMM condition with T_{mr-avg} of 480 °C. It is interesting to note that the simulated shear zone temperature was higher than the average material temperature as the laser power drops to below 8 W, while it became lower than T_{mr-avg} at higher laser powers due to the heat conduction to the tool. Multiple simulations were also run using temperatures at different depth of cuts to investigate any temperature effect on cutting. Figure 2.15 (b) shows the effect of temperature variances in the cutting depth on the workpiece flow stresses for LAMM side cutting of 422SS of fin configuration. With a temperature variance of about 30 °C in the axial depth of cut of 250 μm , almost constant flow stress of 2082 MPa was predicted with a negligible variance of 50 MPa in the cutting depth. Uniform workpiece specific cutting energy was predicted along the cutting depth of 250 μm , which would produce uniform tool wear profile along the flute cutting edge.

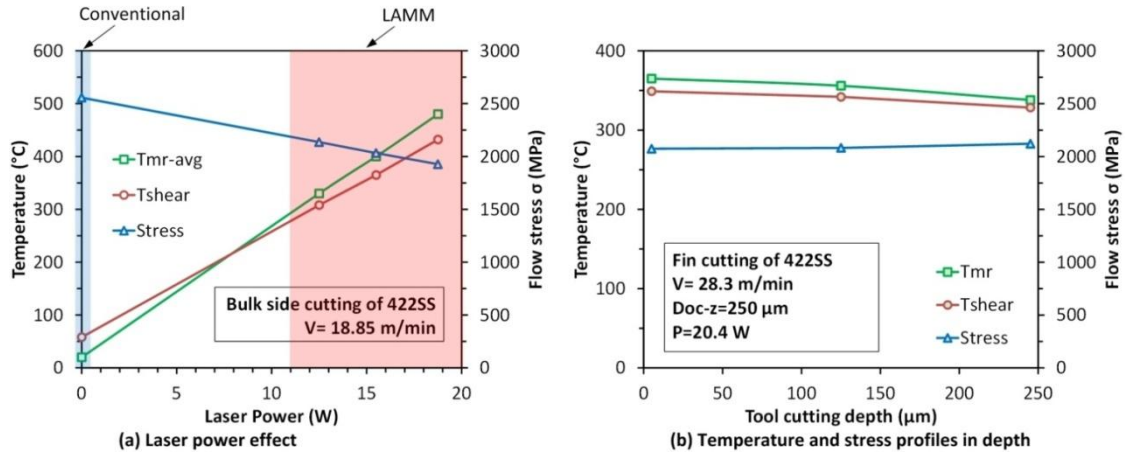


Figure 2.15. Temperatures and flow stresses in LAMM side cutting of 422SS.

2.3.5. Tool Wear Analysis in Laser-Assisted Side Cutting

Figure 2.16 shows a new tool and the tool wear mode after 33 minutes of LAMM fin side cutting of 422SS. The flank wear was measured with the microscope or SEM by calculating the decrease from the width of land of the tool flank surface after cutting. The tool cutting edge radius was measured with SEM. It can be seen in Figure 2.16 (b) that a uniform flank wear has been developed along the long helix cutting edge of the flute, which corroborates the FE prediction of uniform flow stresses and temperatures along the edge. Figure 2.17 shows the tool wear comparison of conventional and LAMM fin side cutting of 422SS and Inconel 718. The micro endmills have been continuously used in LAMM fin side cutting of 422SS for 33 minutes, compared with the 5.5 minutes of cutting time used in the conventional cutting. Increasing T_{mr-avg} to 354°C helped reduced the tool wear rate from 0.73 to 0.12 $\mu\text{m}/\text{min}$ for fin side cutting of 422SS, while increasing T_{mr-avg} to 451°C helped reduced the tool wear rate from 0.9 to 0.25 $\mu\text{m}/\text{min}$ for fin side cutting of Inconel 718.

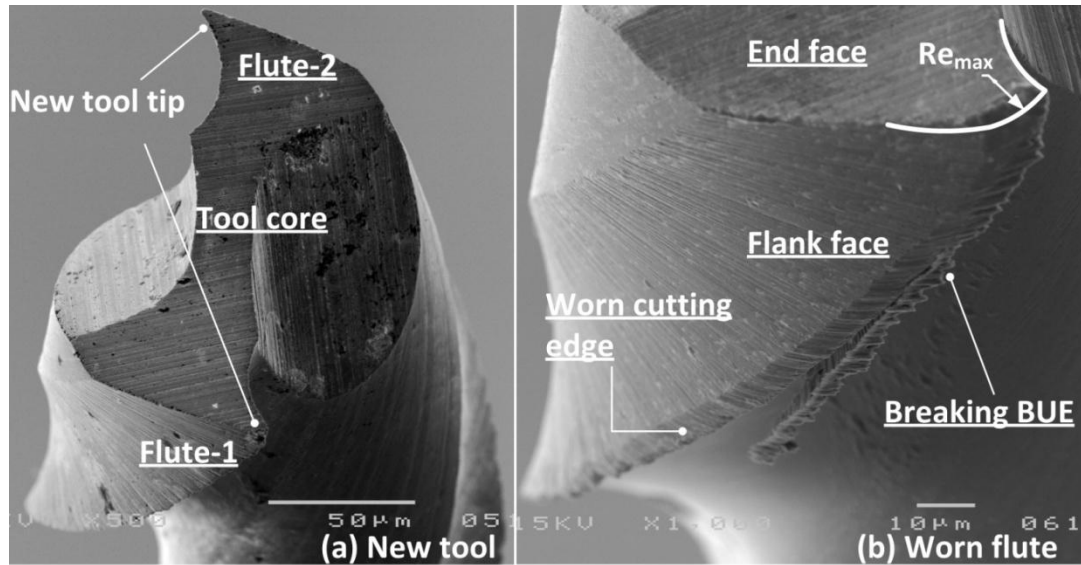


Figure 2.16. Tool geometry and tool wear mode after 33 minutes LAMM fin side cutting 422fin-2 [22].

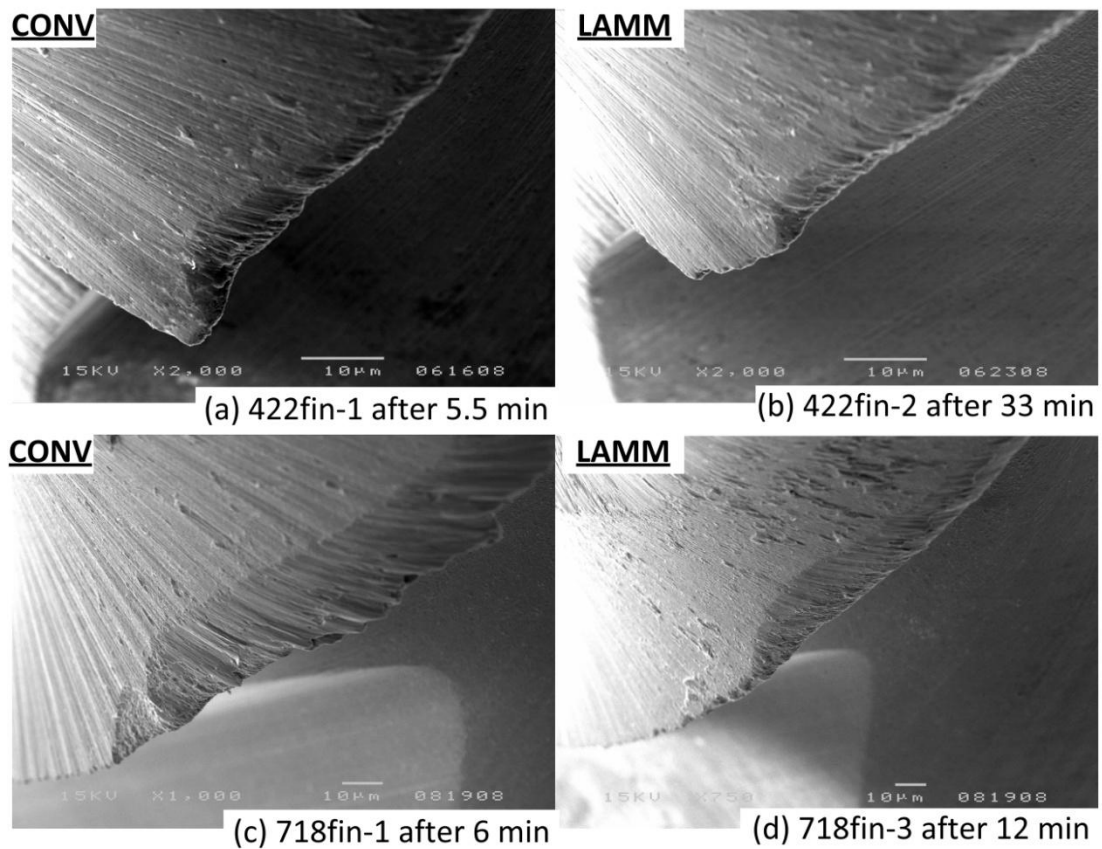


Figure 2.17. Tool wear for fin side cutting of 422SS and IN-718 under the conditions of 422fin-1, 2 and 718fin-1, 3.

Approximately, a linear tool wear progression at a steady rate was observed along the tool cutting edge radius and flank surface in micro-milling and LAMM of multiple difficult-to-machine alloys [22, 92], and hence an uniform wear rate is assumed in this tool wear study. To model the tool wear rate during micro side cutting tests, Usui's tool wear rate model [78] was modified to include the size effect in micro cutting, which is given by

$$\frac{dW}{dt} = C\sigma_t^n v_s e^{-p/T_{tool}} \quad (2.7)$$

where $\frac{dW}{dt}$ is the rate of volume loss per unit contact area per unit time ($\mu\text{m}/\text{min}$), σ_t is the normal pressure (GPa) on tool face, T_{tool} is the tool temperature in Celsius degree, v_s is the sliding velocity (m/s) between the chip and the cutting tool, and C , n and p are tool wear characteristic constants. The model includes three variables: sliding velocity between the chip and the cutting tool, tool temperature and normal pressure on the tool face, which were provided by the FE simulations of the micro side cutting process using a constant moderate tool cutting edge radius of $2 \mu\text{m}$. The constants in the tool wear rate model depend on the workpiece material, tool material and cutting parameters. The constants were derived by curve fitting the tool wear rate data measured from the bulk side cutting tests, and are given by $n=11.8$, $p=20.65$ and $C=1.0617\text{E-}7$. Figure 2.18 shows the tool wear rate model predictions of the fin side cutting tests. It can be seen that the developed tool wear rate model can correctly predict the tool wear rate in LAMM fin side cutting.

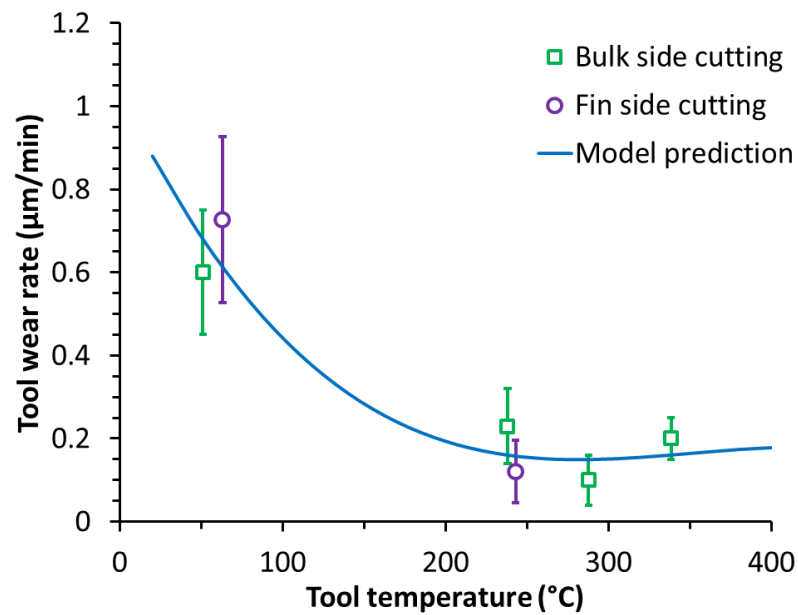


Figure 2.18. Tool wear predictions for fin side cutting of 422SS.

2.3.6. Surface Integrity Analysis

The transition of material removal mechanism from cutting to ploughing was investigated by the FE model using different tool cutting edge radii. Figure 2.19 shows the chip formation within the first 10 μs of LAMM and conventional fin side cutting with different tool edge radius of 0.5 and 4.2 μm . It can be seen that cutting is the main material removal mechanism when the ratio λ is 1.67, while ploughing plays the dominant role with no chip formed as λ decreases to 0.2. Velocity fields simulated with various cutting ratios in Figure 2.19 (c) and (d) show larger triangle zones of stagnant workpiece material during side cutting for λ of 0.2 than those for λ of 1.67, which indicates BUE would form more often as tool wears to have a large r_e . It is also readily seen that increasing T_{mr-avg} helps decrease the size of the stagnant triangle zone: the workpiece material stagnant zone is almost eliminated for λ of 1.67 undergoing LAMM compared with conventional micro-milling, while it becomes smaller and less stagnant for λ of 0.2 undergoing LAMM compared with conventional cutting.

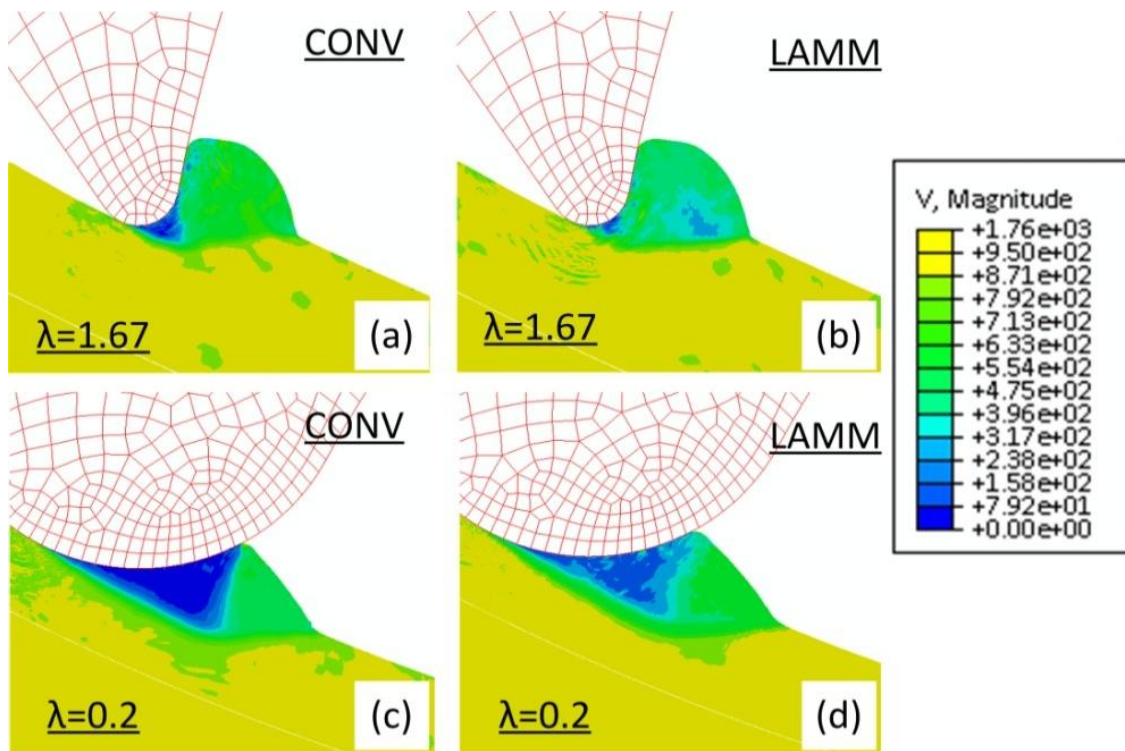


Figure 2.19. Workpiece velocity fields of Inconel 718 undergoing fin side cutting tests 718 fin 1 and 3.

Figure 2.20 shows the machined side surface finish produced by conventional and LAMM fin side cutting with tools worn to the similar extent. Comparing the Inconel 718 surface finish between Figure 2.20 (a) and (b), longer, larger edge burrs and more prows can be observed remaining on the top surface and machined side surface, respectively, produced by conventional cutting than LAMM side cutting. Similarly, more prows can be observed remaining on the machined side surface after 5.5 minutes conventional cutting of 422SS than those produced after 33 minutes of LAMM side cutting. It is interesting to note that no prows can be observed on the upper half of the machined side surface of 422SS produced by LAMM, while some prows are observed on the lower half, which might be caused by more severe tool wear there. The experimental observation of BUE breaking off the worn tool as shown in Figure 2.16 (b) confirmed the model predictions of BUE. The surface defect of prows remaining on the machined surface was the result of BUE's that have broken off from the tool nose [58]. The model predictions that LAMM would eliminate the BUE formation at a large λ of 1.67 or reduce the BUE formation at a small λ of 0.2 corroborate the experimental observation of more and larger prows remaining on the machined surface produced by conventional cutting than LAMM.

It is already known that increasing the cutting speed will reduce the formation of BUE [148]. However due to the micro size of the endmill, the maximum spindle speed of micromachining apparatus usually limits the available highest cutting speed. It is validated that LAMM can eliminate or reduce BUE in micromachining of difficult-to-machine materials even at a relatively low cutting speed with proper heating the workpiece material prior to the cutting tool. The developed FE model in this study does not require the shape of BUE to be known and thus serves as a useful tool to assess the BUE formation in micromachining under different conditions.

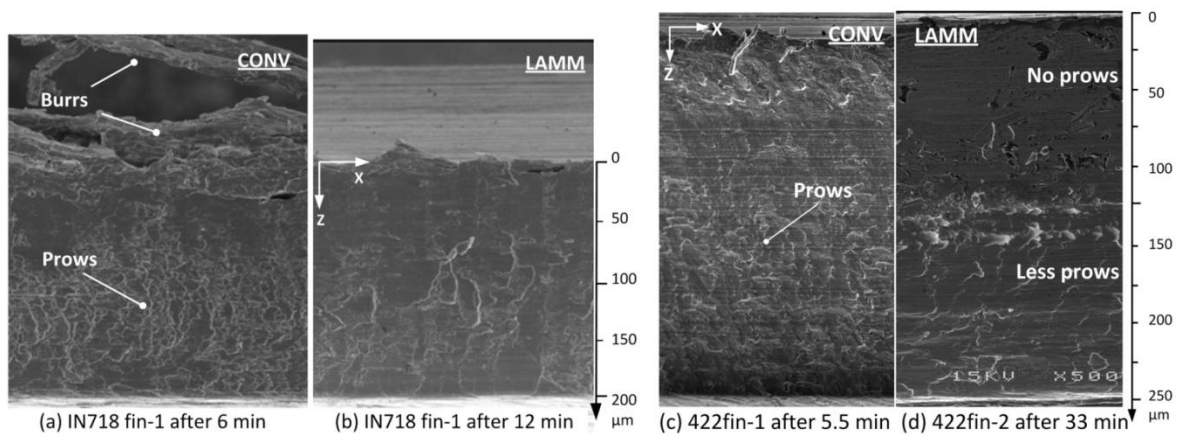


Figure 2.20. Machined side surface finish by fin side cutting of Inconel 718 and 422SS.

2.4. Summary

In this chapter, the workpiece temperature increase due to the laser heating and temperature variances in the cutting zone was examined by a transient, 3D prismatic thermal model for various LAMM test configurations. The thermal analysis proved that the fin workpiece structure was the optimal design for LAMM within the present system constraints with a temperature variance of 10 to 15 °C in the machined chamfer. The steady-state cutting temperature after many micromilling cycles was determined by the heat transfer analysis. Using the simulated steady-state temperature fields as the temperature conditions, continuous chip formation with varying undeformed chip thickness was achieved by 2D FE models embedded with the strain gradient constitutive models. It is shown that the workpiece flow stress drops by about 20-25% as the temperature is creased to 250-450 °C. A uniform workpiece specific

cutting energy was predicted along the cutting depth of 250 μm in LAMM fin side cutting. An empirical tool wear model was derived for a tungsten carbide tool in fin side cutting based on LAMM bulk side cutting simulations and experimental tool wear rate, and the steady-state tool temperature was predicted by the heat transfer analysis. The model predicted that the tool wear rate drops from 0.62 to 0.15 $\mu\text{m}/\text{min}$ as the workpiece temperature increases from the ambient temperature to about 354 $^{\circ}\text{C}$ in fin side cutting of 422SS, which was in good agreement with the tool wear measurements. The FE model simulations showed that LAMM can eliminate or reduce BUE formation in micromachining of difficult-to-machine materials with proper heating of the workpiece material prior to the mechanical cutting.

CHAPTER 3. GRAIN REFINEMENT MODELING IN MACHINING

In this chapter, dislocation density-based material models are presented to model grain size refinement and grain misorientation during severe plastic deformation processes of various materials under varying strain rates and temperatures. A coupled Eulerian-Lagrangian (CEL) finite element model embedded with the dislocation density subroutine is developed to simulate the severe plastic deformation and grain refinement during steady-state plane-strain orthogonal cutting processes. Simulation results of grain refinement and grain misorientation are discussed for Al 6061 T6 and OFHC Cu in details.

3.1. Dislocation Density-Based Material Model

Estrin and other researchers presented a set of differential equations to evaluate the dislocation density evolution rates and applied the dislocation density-based material model to grain refinement in the ECAP processes of various materials such as aluminum [104], copper [103] and IF steel [105]. Their proposed dislocation density-based material model is compatible with the material constitutive models developed under varying conditions of strains, strain rates and temperatures and has been adapted to model other deformation processes with high strain rates or high temperature gradients such as a Taylor impact test of copper [107] and a machining process of titanium [24]. Hence their dislocation density-based material model is adopted for modeling grain refinement by cutting in this study.

In the model, a dislocation cell structure is assumed to form during deformation, which consists of two parts, dislocation cell walls and cell interiors, and obeys a rule of mixtures. Different types of dislocation densities are distinguished in the model: the cell interior dislocation density (ρ_c) and the cell wall dislocation density (ρ_w), which is further divided into two distinct groups of statistical dislocation density (ρ_{ws}) and geometrically necessary

dislocation density (ρ_{wg}). The evolutions of the dislocation densities ρ_c , ρ_{ws} and ρ_{wg} follows different routes and are governed by the following equations:

$$\dot{\rho}_c = \alpha^* \frac{1}{\sqrt{3}b} \sqrt{\rho_{ws} + \rho_{wg}} \dot{\gamma}_w^r - \beta^* \frac{6}{bd(1-f)^{1/3}} \dot{\gamma}_c^r - k_o \left(\frac{\dot{\gamma}_c^r}{\dot{\gamma}_o} \right)^{-1/n} \rho_c \dot{\gamma}_c^r \quad (3.1)$$

$$\dot{\rho}_{ws} = \beta^* \frac{\sqrt{3}(1-f)}{fb} \sqrt{\rho_{ws} + \rho_{wg}} \dot{\gamma}_c^r + (1-\xi) \beta^* \frac{6(1-f)^2}{bdf} \dot{\gamma}_c^r - k_o \left(\frac{\dot{\gamma}_w^r}{\dot{\gamma}_o} \right)^{-1/n} \rho_{ws} \dot{\gamma}_w^r \quad (3.2)$$

$$\dot{\rho}_{wg} = \xi \beta^* \frac{6(1-f)^2}{bdf} \dot{\gamma}_c^r. \quad (3.3)$$

The first terms of Eqs. 3.1 and 3.2 on the right side correspond to the generation of dislocations due to the activation of Frank–Read sources; the second terms denote the transfer of cell interior dislocations to cell walls where they are woven in; the last terms represent the annihilation of dislocations leading to dynamic recovery in the course of straining. The density of geometrically necessary dislocations is assumed to arise from a fraction (ξ) of the dislocations incoming into cell walls from the cell interiors as shown in Eq. 3.3. α^* , β^* and k_o are dislocation evolution rate control parameters for the material, n is a temperature sensitivity parameter, f is the volume fraction of the dislocation cell wall, b is the magnitude of the Burgers vector of the material, d is the dislocation cell size, $\dot{\gamma}_w^r$ and $\dot{\gamma}_c^r$ are the resolved shear strain rates for the cell walls and interiors, respectively, and $\dot{\gamma}_o$ is the reference resolved shear strain rate. It is assumed that the resolved shear strain rate across the cell walls and cell interiors are equal, $\dot{\gamma}_w^r = \dot{\gamma}_c^r = \dot{\gamma}^r$, which satisfies the strain compatibility along the interface between interiors and boundaries. The resolved shear strain rate $\dot{\gamma}^r$ can be calculated by the von Mises strain rate $\dot{\epsilon}$ by using $\dot{\gamma}^r = M\dot{\epsilon}$, where M is the Taylor factor.

Volume fraction f of the dislocation cell wall, total dislocation density ρ_{tot} and grain size d are given as follows:

$$f = f_\infty + (f_o - f_\infty) e^{\left(-\frac{\dot{\gamma}^r}{\dot{\gamma}^r} \right)} \quad (3.4)$$

$$\rho_{tot} = f(\rho_{ws} + \rho_{wg}) + (1-f)\rho_c \quad (3.5)$$

$$d = \frac{K}{\sqrt{\rho_{tot}}} \quad (3.6)$$

where f_o and f_∞ are the initial and saturation volume fractions of cell walls, respectively, and the average cell size d is assumed to scale with the inverse of the square root of total dislocation density ρ_{tot} . The resolved shear strain rate $\dot{\gamma}^r$ can then be integrated with the dislocation densities to obtain the resolved shear stress τ^r as follows:

$$\tau_c^r = \alpha G b \sqrt{\rho_c} \left(\frac{\dot{\gamma}_c^r}{\dot{\gamma}_o} \right)^{1/m} \quad (3.7)$$

$$\tau_w^r = \alpha G b \sqrt{\rho_{ws} + \rho_{wg}} \left(\frac{\dot{\gamma}_w^r}{\dot{\gamma}_o} \right)^{1/m} \quad (3.8)$$

$$\tau^r = f \tau_w^r + (1-f) \tau_c^r \quad (3.9)$$

where m is the strain rate sensitivity of the material.

Geometrically necessary dislocations contribute to an imbalance in the Burgers vector in a dislocation cell wall and thus lead to misorientation buildup across the wall. The statistical dislocations do not produce misorientation across the boundary [149] and hence their effect on grain misorientation is omitted in this study. The absolute value of the misorientation angle between the neighboring cells induced by deformation (θ_{int}) is then given by:

$$\theta_{int} = \arctan(b \sqrt{\rho_{wg}}). \quad (3.10)$$

In the course of the accumulation of misorientation with straining, the efficiency of cell walls as places for storage of incoming cell interior dislocations increases. Therefore, the cell wall dislocation evolution rate parameter β^* is given as a function of the misorientation angle:

$$\beta^* = \beta_\infty + (\beta_o - \beta_\infty) e^{\left(\frac{-\theta}{\pi/12} \right)} \quad (3.11)$$

where β_o and β_∞ are the initial and saturation value of parameter β^* , respectively. The total misorientation frequency distribution ($v(\theta)$) can be split into two parts: the deformation-induced misorientation angle distribution ($v_{int}(\theta)$) as already defined above and the residual

grain boundary misorientation angle distribution ($\nu_{GB}(\theta)$) that comes from the periphery of the original large grain and its neighbors situated at the opposite side of the same initial grain boundary [149]. The rule of mixture can be used to get the total misorientation frequency distribution

$$\nu(\theta) = f\nu_{\text{int}}(\theta) + (1-f)\nu_{GB}(\theta). \quad (3.12)$$

In the simulation, a random initial texture with the Mackenzie distribution [150] is assumed for $\nu_{GB}(\theta)$, which remains little changed due to the absence of a topological connection between the large original grains.

The CEL model incorporated the dislocation density-based material model subroutines written in FORTRAN and calculated the dislocation fields in the workpiece during the cutting simulation. Figure 3.1 shows the flow chart for CEL modeling using the dislocation density-based material model.

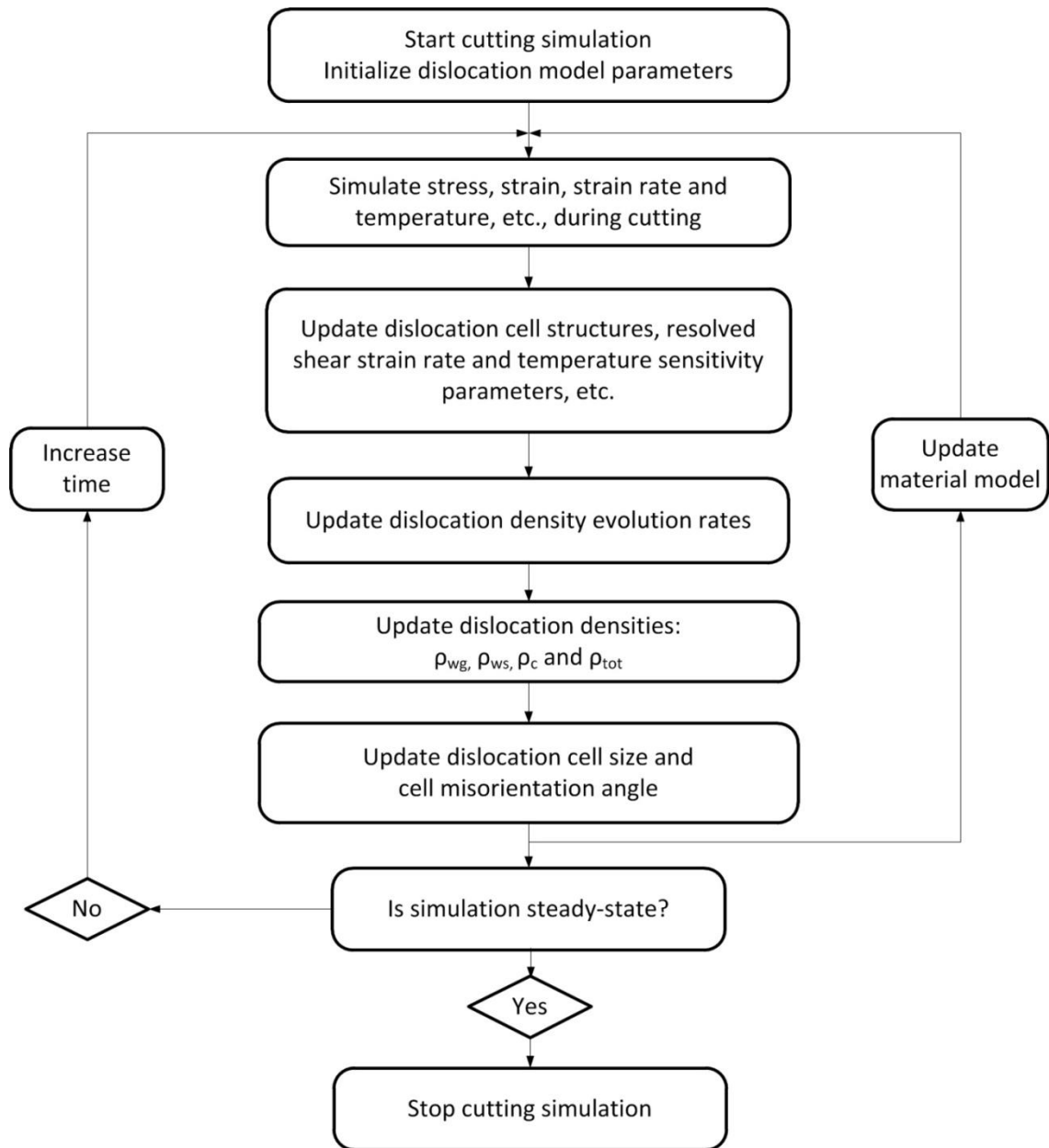


Figure 3.1. Flow chart for CEL modeling using the dislocation density-based material model.

3.2. Determination of Material Model Parameters

To study the effects of cutting processing parameters on grain refinement and misorientation, microstructural evolution was simulated for multiple plane-strain orthogonal cutting tests of Al 6061 T6 and OFHC Cu. Interest in these materials is motivated by their extensive applications in industry and their potential attractiveness of enhanced mechanical

strength with an ultra-fine grained microstructure. Dry cutting tests cited from multiple sources were carried out at room temperature under various conditions for the materials as given in Table 3.1. Test conditions Al1~Al3 were conducted for Al 6061 T6 using the same machining parameters with more negative tool rake angles from 20° to -20° , which were aimed to study the effect of increasing the applied strain on grain refinement. Different cutting speeds, ranging from 0.02 to 1.25 m/s, and tool rake angles, ranging from 20° to -20°, were used in test conditions Cu1~Cu4 for OFHC copper to study the combining effects of applied strains, strain rates, and temperatures on the microstructural evolution during cutting.

Table 3.1. Orthogonal cutting tests simulated for Al 6061 T6 and OFHC Cu.

<i>Material</i>	<i>Test</i>	<i>Initial grain size (μm)</i>	<i>V (m/s)</i>	<i>f (mm)</i>	<i>α (°)</i>	<i>Reference</i>
Al 6061 T6	Al1	~75	0.01	0.15	20	Shankar et al. [32]
	Al2	~75	0.01	0.15	-5	Shankar et al. [32]
	Al3	~75	0.01	0.15	-20	Shankar et al. [32]
OFHC Copper	Cu1	~50	0.02	0.11	-20	Swaminathan et al. [27]
	Cu2	~50	0.05	0.3	20	Shekhar et al. [34]
	Cu3	~50	0.6	0.3	-5	Ni and Alpas [25]
	Cu4	~50	1.25	0.3	20	Shekhar et al. [34]

The material thermal and mechanical properties are given in Table 3.2. The material Johnson-cook constitutive plastic model is shown as follows:

$$\sigma = \left(A_{JC} + B_{JC} \varepsilon^{n_{JC}} \right) \left(1 + C_{JC} \ln \left(\frac{\dot{\varepsilon}}{\dot{\varepsilon}_o} \right) \right) \left(1 - \left(\frac{T - T_{ref}}{T_m - T_{ref}} \right)^{m_{JC}} \right). \quad (3.13)$$

The Johnson-cook model parameters for Al 6061 T6 and OFHC Cu are given in Table 3.3. The dislocation density-based material models were developed using Matlab to replicate the observed material constitutive behaviors under various strains, strain rates and temperatures similar to those occurring in cutting or other SPD processes. The reference strain rate was set as 150 s⁻¹ for cutting of Al 6061 T6 at a cutting speed of 0.01 m/s, while the reference strain rates

were set as 200 and 4000 s⁻¹ for cutting of OFHC Cu at low (conditions Cu1 and Cu2) and high (conditions Cu3 and Cu4) cutting speeds, respectively. The dislocation density evolution rate control parameters, i.e., the dynamic coefficients of dislocation generation (α^*), interaction between the cell walls and interiors (β^*) and dislocation annihilation (k_o), were calibrated for Al 6061 T6 and OFHC Cu according to the flow stress data given by the material Johnson-cook constitutive models. Constant parameters α^* and β^* were identified as 0.06 and 0.01 for Al 6061 T6, respectively, while α^* and β^* were identified as 0.04 and 0.01 for OFHC Cu, respectively. The temperature sensitivity coefficients m and n were given as follows:

$$m = \frac{A}{T} \quad (3.15)$$

$$n = \frac{B}{T} \quad (3.16)$$

where A and B were adopted as 50,000 and 14,900 for Al 6061 T6 [151], respectively, while A and B were adopted as 30,000 and 14,900 for OFHC Cu [107], respectively. The dislocation annihilation rate parameter k_o increases as the workpiece temperature increases. A constant k_o has usually been used in ECAP models because the temperature profile is more uniform during the ECAP process than in cutting. For the temperature range from ambient to 175 °C, k_o linearly increases from 5.2 to 7.6 for Al 6061 T6. For the temperature range from ambient to 300 °C, k_o linearly increases from 9.0 to 10.2 for cutting of OFHC Cu at low cutting speeds of 0.02 and 0.05 m/s, while it linearly increases from 12.0 to 16.1 for cutting of OFHC Cu at high cutting speeds of 0.6 and 1.25 m/s,. A constant fraction (ξ) of 0.1 was used for the evolution of the geometrically necessary dislocations, which was adapted from the modeling work of copper by Toth et al. [102]. A constant β_∞ of 0.12 was used in the grain misorientation simulations of OFHC Cu, which was adapted from modeling ECAP process of copper by Estrin and Kim [149]. The other non-mentioned material constants for the two material models were generally derived from an earlier study of ECAP process of pure aluminum [104] and copper [103]. The dislocation density model parameters are given in Table 3.4.

Table 3.2. Material Thermo-mechanical Properties.

Material	E (GPa)	G (GPa)	ν	b (nm)	ρ (kg/m ³)	T_m (°C)	Thermal expansion (10 ⁻⁶ /°C)	Thermal conductivity (W/m·K)	Specific heat (J/kg·K)
Al 6061-T6	68.9	26	0.33	0.286	2700	582	23.6	167	896
OFHC Cu	~116	48	0.34	0.256	8960	1083	16.6	400	385

Table 3.3. Material Constitutive Model Parameters.

Material	A_{JC} (MPa)	B_{JC} (MPa)	n_{JC}	C_{JC}	m_{JC}	T_{ref} (°C)	T_m (°C)	$\dot{\epsilon}_o$ (1/s)
Al 6061-T6 [152]	324.0	114.0	0.42	0.002	1.34	25	582	1
Cu (OFHC) [153]	90	292	0.31	0.025	1.09	25	1083	1

Table 3.4. Dislocation Density-Based Model Parameters.

Material	α^*	β^*	k_o	A (K)	B (K)	$\dot{\gamma}_o$	f_o	f_∞	K	M	$\tilde{\gamma}^r$	ρ_{wo} (mm ⁻²)	ρ_{co} (mm ⁻²)	b (mm)	α
Al 6061 T6	0.06	0.01	5.2-7.6	50,000	14,900	150	0.25	0.06	30	3.06	3.2	1E7	1E8	2.86E-7	0.25
OFHC Cu (low speed)	0.04	0.01	9.0-10.2	30,000	14,900	200	0.25	0.077	10	3.06	3.2	1E7	1E8	2.56E-7	0.25
OFHC Cu (high speed)	0.04	0.01	12.0-16.1	30,000	14,900	4E3	0.25	0.077	10	3.06	3.2	1E7	1E8	2.56E-7	0.25

Figure 3.2 shows the comparisons of the dislocation density-based material model predictions of the stress-strain relationships with the flow stress data that are measured or predicted from a material constitutive model at different temperatures and strain rates for all four different materials. The good agreement proved that the identified model parameters are accurate enough to predict the stress-strain relationships under different temperatures and strain rates, which validates the dislocation density-based plasticity models.

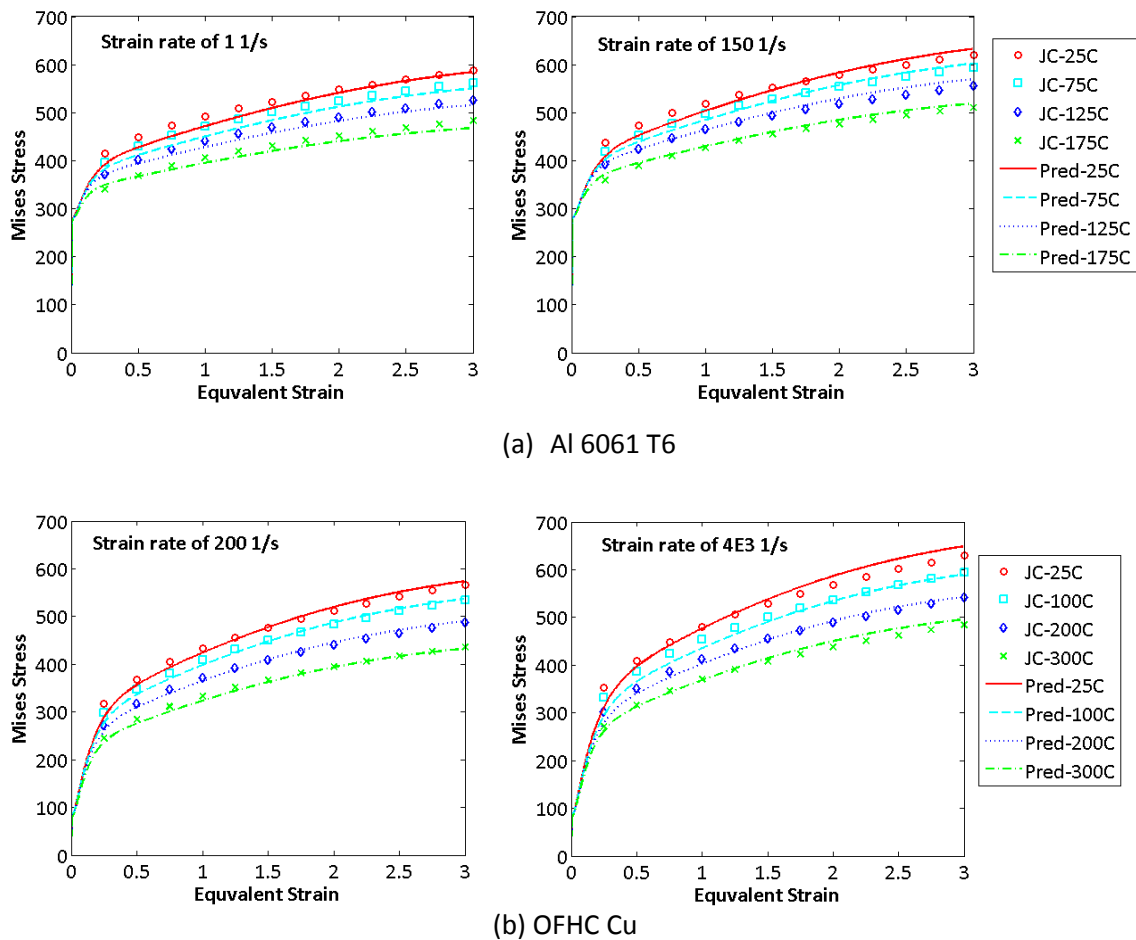


Figure 3.2. Dislocation density-based plasticity model predictions.

3.3. Simulations of Grain Refinement by Machining

The parameters of the dislocation density-based material models described above have been used to simulate the microstructural evolution during cutting of Al 6061 T6 and OFHC Cu. The simulated chip morphologies and deformation fields under various cutting conditions are

first examined in comparison with experimental results to assess the validity of the numerical solution. The predicted grain size and grain misorientation angle in the machined chips are then discussed.

3.3.1. Chip Formation and Deformation Field

Figure 3.3 shows an example of strain rate field predicted by the CEL model in comparison with the measurement conducted by using a high speed camera system [27] during orthogonal cutting of OFHC Cu at a cutting speed of 0.01 m/s with a 10° rake angle tool. It can be seen that the model prediction matched well with the measurement: a narrow, high-rate concentrated zone along the shear plane separated the machined chip from the bulk material; the model predicted shear strain rate of about 200 s^{-1} for a cutting speed of 0.01 m/s was very close to the measured rate in the primary shear zone. The predicted formation of a long continuous chip was nearly identical to the actual chip, as can be seen in Figure 3.3. The shear strain field in the chip was also examined. Figure 3.4 shows a comparison of the model prediction and the actual measurement of the cumulative shear strain along the middle line of the chip flow, which again are in a good agreement. The magnitude of the average shear strain in the chip was predicted to be about 4.5, while the measured average strain was 4.6 for the cutting test of OFHC Cu with the 10° rake angle tool.

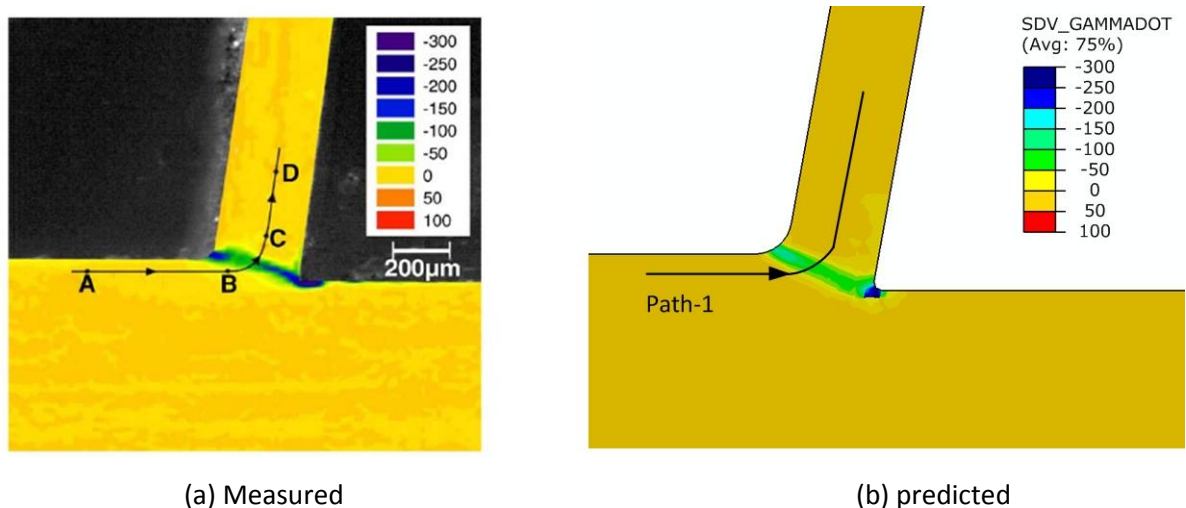


Figure 3.3. Shear strain rate for cutting of OFHC copper under condition: $V=0.01 \text{ m/s}$, $\alpha=10^\circ$ and $\text{doc}=0.1 \text{ mm}$.

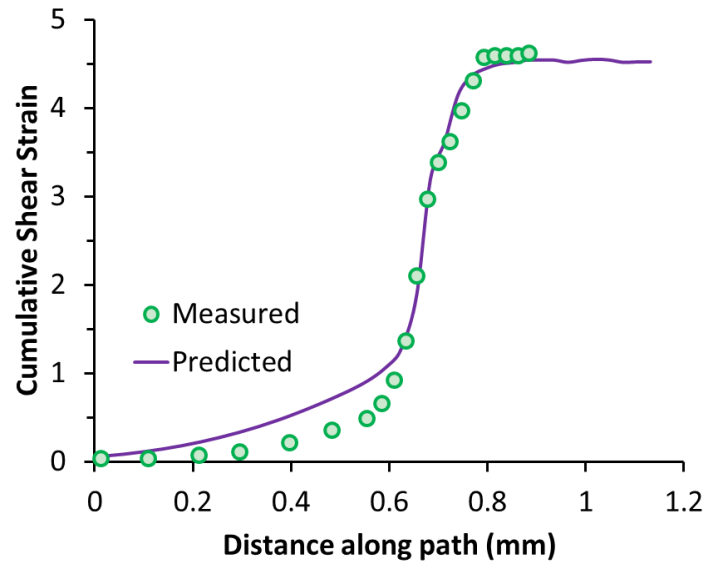
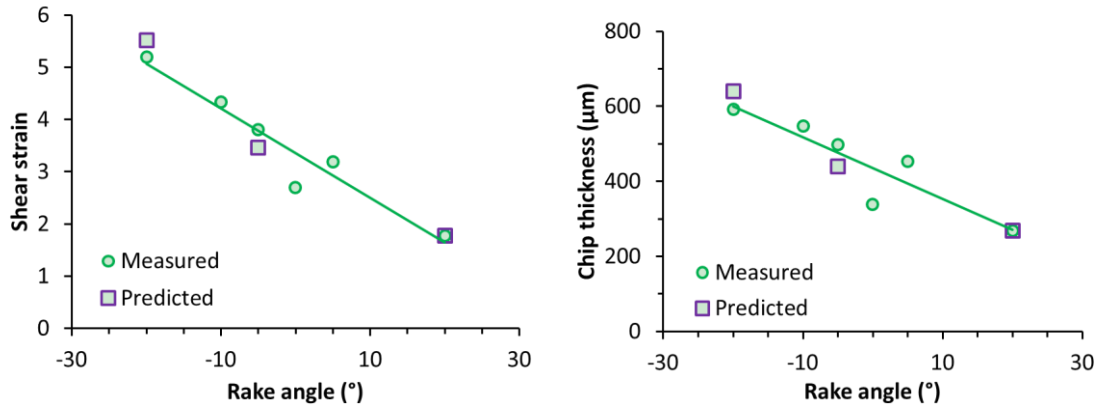


Figure 3.4. Cumulative shear strain along path-1 for cutting of OFHC copper under condition: $V=0.01$ m/s, $\alpha=10^\circ$ and $doc=0.1$ mm.

The machined chip morphology and the achieved strain in the chip vary greatly in cutting of different materials with different cutting tools. Figure 3.5 shows the predictions of average shear strains in the chips and machined chip thicknesses for cutting of Al 6061 T6 at a cutting speed of 0.01 m/s with different tool rake angles in comparison with those measured by Shankar et al. [32]. The predicted average shear strains in the chips were 1.8, 3.5, and 5.5 for the rake angle of 20° , -5° and -20° , respectively; while the measured average shear strains in the chips were 1.8, 3.8 to 5.2 for the rake angle of 20° , -5° and -20° , respectively. The predicted average machined chip thicknesses were 0.27, 0.44, and 0.64 mm for the rake angle of 20° , -5° and -20° , respectively; while the measured average machined chip thicknesses were 0.27, 0.5 and 0.6 mm for the rake angle of 20° , -5° and -20° , respectively. As can be seen in Figure 3.5, the model correctly captured the effect of tool rake angle on the deformation field. A more negative rake angle tool produces a thicker chip and imposes a larger strain on the chip.



(a) Shear strain (b) predicted machined chip thickness
 Figure 3.5. Average shear strain and chip thickness for cutting of Al 6061 T6 under conditions A1-3.

3.3.2. Grain Refinement

Figure 3.6 shows the model predicted steady-state distributions of equivalent strain, total dislocation density and grain size in the OFHC Cu workpiece under cutting condition Cu3 at a cutting speed of 0.6 m/s with a -5° rake angle tool. Generally, it is noted that the simulated dislocation field stops evolving as the chip morphology reaches a steady state during the simulation. Ni and Alpas investigated material microstructural evolution of annealed OFHC Cu under the same cutting condition [25], and their measured TEM micrographs at three different stages of chip formation, i.e., bulk material prior to cutting, primary deformation zone and chip, are also shown in Figure 3.6 along with the model predictions. As can be seen in the TEM micrograph I, prior to cutting and straining, loosely tangled dislocation structures are present in the coarsely-grained annealed bulk material. The equivalent strain drastically increases as the workpiece material passes the shear plane and enters the primary deformation zone, and the dislocation cell structures are greatly elongated due to severe straining as can be observed from the TEM micrograph II. New dislocations dramatically increase on the cell walls and some are blocked by the subgrain boundaries. As the deformation continues into the steady-state chip zone, elongated subgrains break up and are reoriented into ultrafine equiaxed grains, as can be confirmed from the TEM micrograph III. In the steady-state chip, the predicted equivalent strain is unevenly distributed, with the largest strain of about 4 predicted in the secondary shear zone along the tool-chip contact and on the machined surface. A very steep strain gradient is predicted in a shallow layer below the machined subsurface. Dislocations accumulate more as

strain increases, and hence the two shares a similar contour pattern in the chip. As can be seen in Figure 3.6, the grain size distribution largely reverses the pattern of the strain and dislocation density distribution, with finer grains of about 200 nm on the outer regions and coarser grains of about 300 nm in the center of the chip produced under condition Cu3.

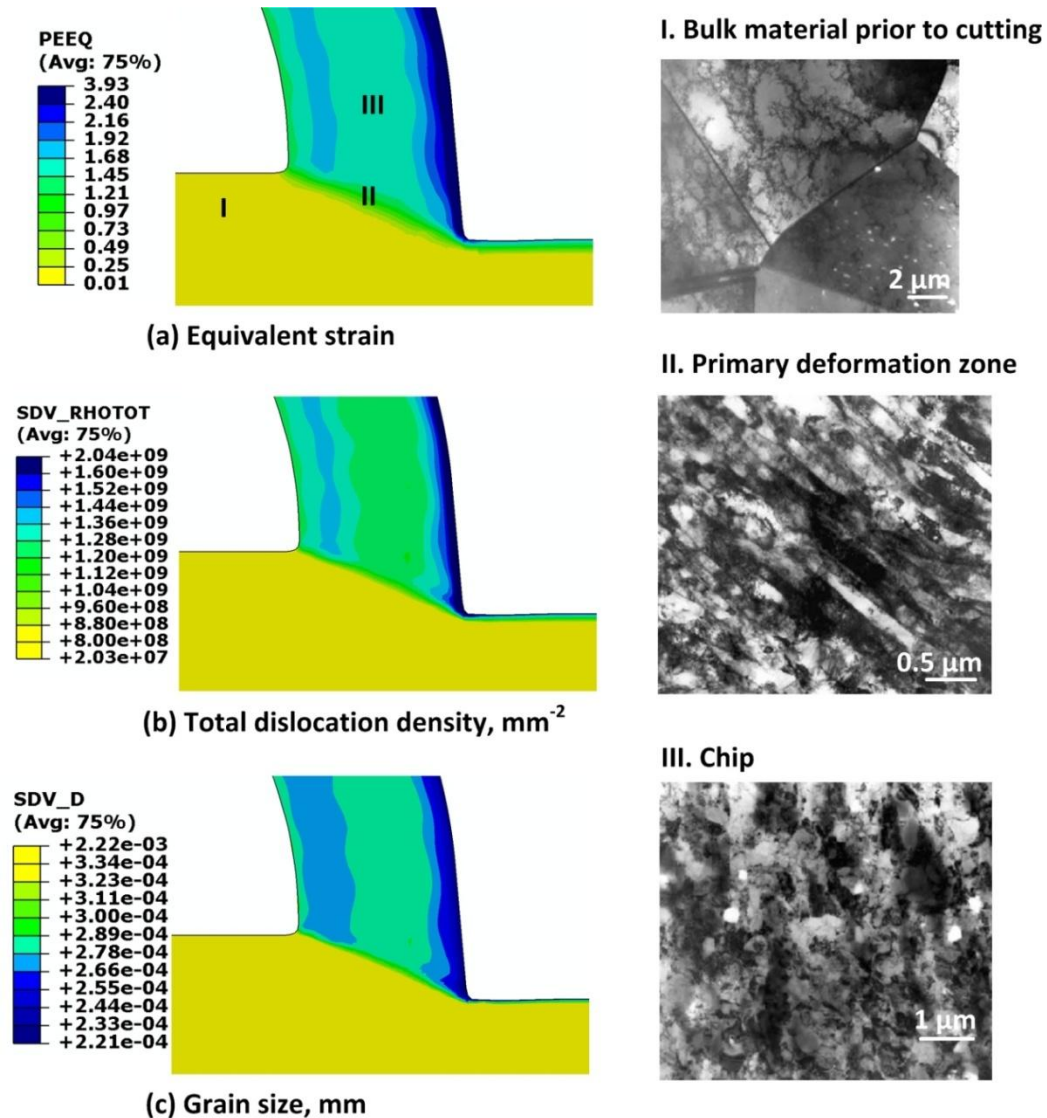
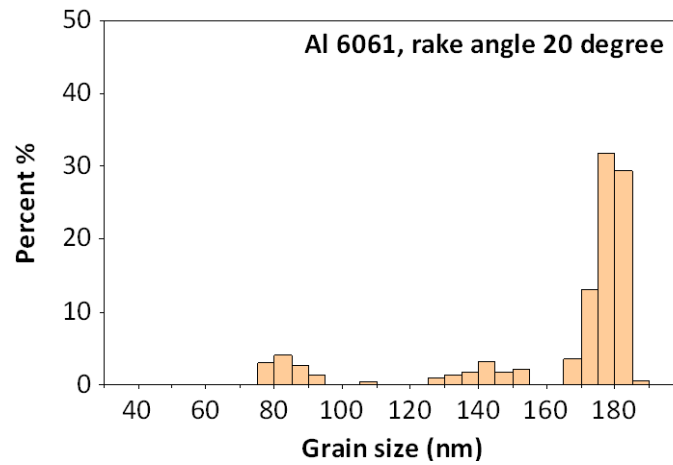


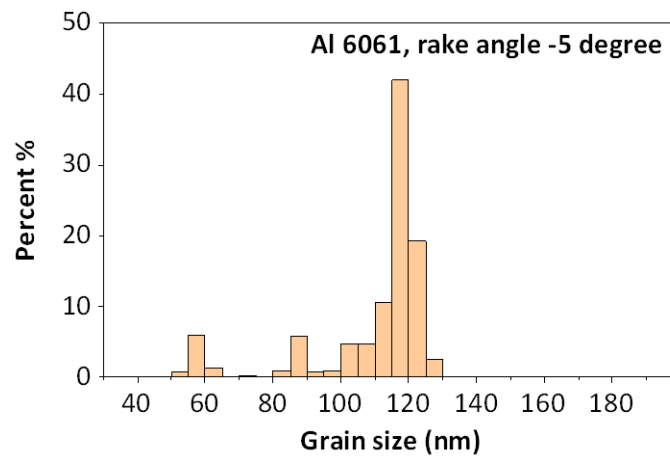
Figure 3.6. Predicted microstructural evolution for cutting of OFHC Cu under conditions Cu3 (a) Equivalent strain (b) total dislocation density, mm⁻² (c) grain size, mm.

I, loosely distribution of dislocations in the bulk material prior to cutting; II, elongated dislocation cell in the primary deformation zone; III, equiaxed sub-micron grains in the chip [25].

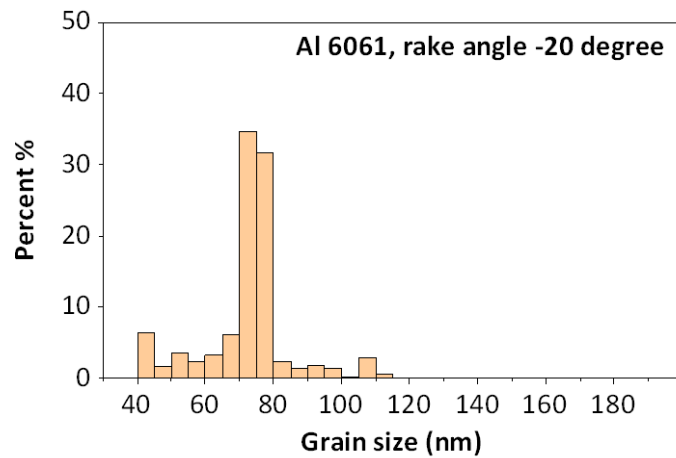
The level of strain plays the most significant role in the grain refinement process. Figure 3.7 shows the model predicted histograms of the refined grain size distributions in the machined chips of Al 6061 T6 under cutting conditions of A11-3 with the same cutting speed but using tools with varying rake angles. The predicted ranges of the grain size in the chip were from 80 to 180 nm, 60 to 130 nm and 40 to 110 nm for using 20°, -5° and -20° rake angle tools, respectively. The model predictions of the average grain size in the machined chips of Al 6061 T6 under these aforementioned conditions are compared with the measured values as can be seen in Figure 3.8. It can be seen that the predictions of the average grain size were very close to the measurements at all three levels of strains. Both the measurements and model predictions show a similar trend such that a more negative rake angle tool can help further reduce the grain size in the chip by applying a larger strain. The data of the grain size measurement variance was not available to the authors and hence is not shown in this study.



(a)



(b)



(c)

Figure 3.7. Predicted grain size distribution in the chips for Al 6061 T6. (a) Rake angle of 20° (b) rake angle of -5° (c) rake angle of -20°.

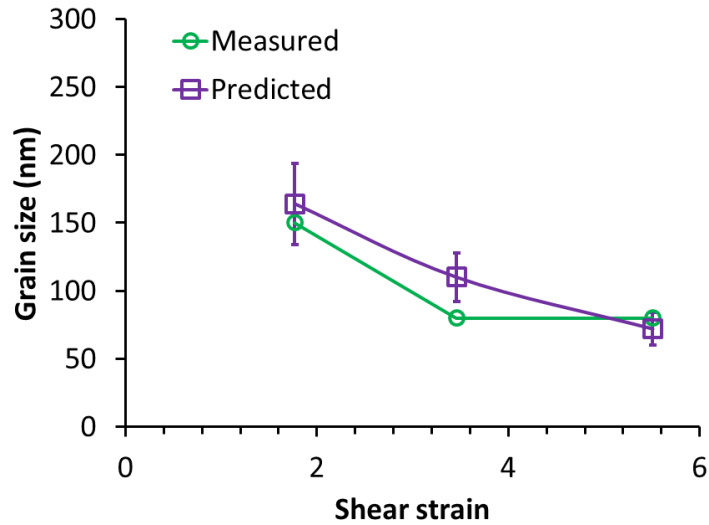


Figure 3.8. Grain size in the chips for Al 6061 T6 under conditions A1-3 with varying tool rake angles.

The effects of the other important cutting parameters such as cutting speed and cutting temperature were investigated in this study with simulations of cutting of OFHC Cu under various cutting conditions and the simulation results are given in Table 3.5. The average equivalent strain, $\bar{\epsilon}$, and the average temperature rise, $\overline{\Delta T}$, in the chip were obtained by averaging the simulated von Mises equivalent strains and temperature rises in the chip above the primary deformation zone, respectively. The model predictions of the average grain size in the chip generally matched well with the measured values for all the tests of Al 6061 T6 and OFHC Cu under varying cutting conditions except for a greater discrepancy under the cutting condition Cu4 at a high cutting speed of 1.25 m/s. The effects of the cutting speed, tool rake angle and cutting temperature on the resultant grain size in the chip are depicted in Figure 3.9. Comparing cutting tests of Cu2 and Cu4 with the same cutting tool and similar applied strains, it is readily seen that a high cutting speed of 1.25 m/s caused a 126 °C temperature rise in the chip, while a low cutting speed of 0.05 m/s induced only a 27 °C temperature rise. Strain rates of about 200 and 4,000 s^{-1} were predicted for tests Cu2 and Cu4, respectively. Both the high strain rate and high temperature in the chip of test Cu4 contributed to a coarser grain size of 1 to 2 μm than a finer grain size of about 0.4 μm of test Cu2. Comparing cutting test Cu3 to Cu4 with similar cutting temperatures, we can see that a combined effect of a larger strain of 1.56 and a lower cutting speed of 0.6 m/s contributed to a finer grain size of about 200 nm in test

Cu3. In other words, small applied strain, high cutting speed and high cutting temperature are all the factors contributing to a coarser grain structure during cutting, and vice versa. Altering the applied strain by selecting different rake angle tools might not be effective in designing grain refinement experiments if the effects of other cutting parameters are omitted. This further validates the necessity of developing such a numerical model as in this study, which captures the underlying physics during the cutting process by considering all the important process parameters.

Table 3.5. Simulation results for orthogonal cutting of Al 6061 T6 and OFHC Cu.

Material	Test	Feed (mm)	Rake angle, α (°)	Initial grain size (μm)	Cutting speed (m/s)	Average equivalent strain in chip, $\bar{\epsilon}$	Average temperature rise in chip, $\bar{\Delta T}$ (°C)	Measured grain size in chip (nm)	Predicted grain size in chip (nm)
Al 6061 T6	Al1	0.15	20	~75	0.01	~0.89	~8	~150	164±30
	Al2	0.15	-5	~75	0.01	~1.85	~12	~80	110±18
	Al3	0.15	-20	~75	0.01	~3.01	~16	~80	72±12
OFHC Cu	Cu1	0.11	-20	~50	0.02	~2.96	~12	216±104	244±20
	Cu2	0.3	20	~50	0.05	~0.86	~27	446±262	357±40
	Cu3	0.3	-5	~50	0.6	~1.56	~135	220±95	274±25
	Cu4	0.3	20	~50	1.25	~0.88	~126	1135±559	559±50

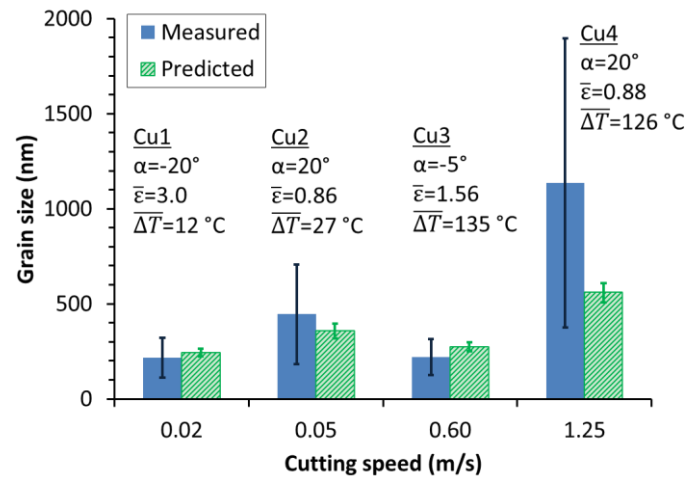


Figure 3.9. Grain size in the chips for OFHC Cu under conditions Cu1-4 with varying cutting speeds.

Geometrically necessary dislocation densities were simulated for cutting of OFHC Cu under conditions Cu2 and Cu4 with the developed numerical framework and the grain misorientation angles were predicted. Figure 3.10 shows the histograms of the misorientation angle distributions predicted by the numerical model to the measured one under cutting condition Cu4. A reasonably good agreement can be seen between the predicted and measured distributions of misorientation angle. The measurement data showed that 67% and 85% of the misorientations were below 15° and 40° for test Cu4, respectively, while the model prediction showed that 69% and 88% of the misorientations were below 15° and 40°, respectively. The measured average grain misorientation angles were 17° and 29° for cutting tests of Cu4 and Cu2, respectively, while the model predicted the average misorientation angles of 19° and 35° for cutting tests of Cu4 and Cu2, respectively. It can be seen that a low cutting speed of 0.05 m/s and a low temperature rise of 27 °C under the condition Cu2 produces a more randomly orientated microstructure than a high cutting speed of 1.25 m/s and a high temperature rise of 126 °C under the condition Cu4.

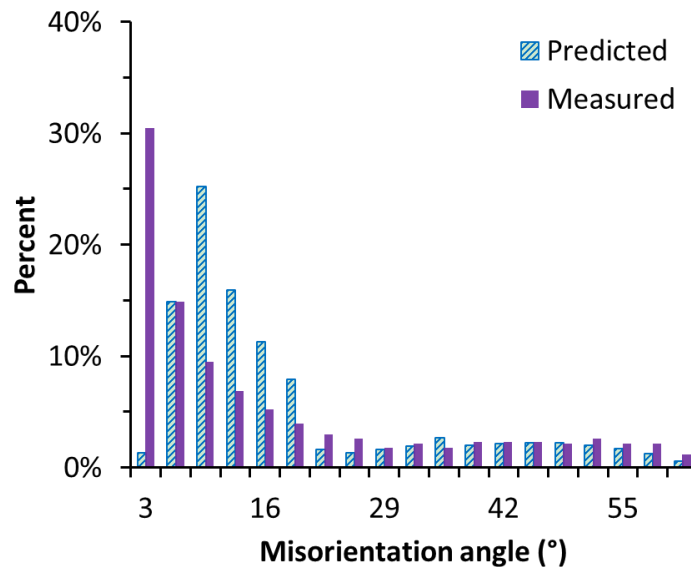


Figure 3.10. Grain misorientation angle distribution for cutting test Cu4 at a cutting speed of 1.25 m/s.

3.3.3. Discussions

Smaller variances in the grain size were simulated, compared to the measured data. The variance in the measured grain size data ranged from about 100 nm for a more uniform equiaxed grain structure to about 500 nm for a mixed grain structure with both fine and coarse grains existing. The discrepancy, particularly the one under condition Cu4 at a high cutting speed of 1.25 m/s, between the measurement and model prediction variances are possibly caused by the following reasons. First, a uniform grain size distribution was assumed as the initial condition in the simulations, which omitted the significant variance of the grain sizes usually seen in the bulk material prior to cutting. The initial inhomogeneous microstructure might play a role in the grain size variance of the resultant microstructure after the cold deformation by high-speed cutting. Second, the model output the grain size by using Eq. 3.6 and used a constant K for the calculation of grain size, which might over-simplified the grain size-dislocation density relationship. Finally, although twinning usually exists in the material before the primary deformation zone and diminishes as the material enters the chip with an increase of strain, deformation twins might be retained in the chip at a higher cutting speed [154] and affect the dislocation mobility and grain refinement to some extent. A bimodal distribution of grain size of 500 nm and 2 μm was experimentally observed in the machined chip produced at a high cutting speed of 1.25 m/s under condition Cu4 [34]. The coarser grains in this case might be a result of the grain dynamic recovery due to a high temperature (the predicted maximum temperature in the chip was about 180 °C) and the retained twins at the high cutting speed of 1.25 m/s. Nonetheless, the model predicted average grain sizes are in good agreement with the measurement for all the conditions, and the effect of the tool rake angle, cutting speed and cutting temperature are all well captured by the numerical model.

Particular forms of equations have been used to describe the shape of the misorientation angle distribution: for example, a Rayleigh distribution function was used to model the misorientation angle distribution induced by a severe deformation and a scaling analysis was conducted to determine the distributions at particular strains [155]. The numerical framework developed in this study simulates the misorientation of all dislocation cells and the misorientation angle distribution is obtained without imposing any predefined probability density functions. The misorientation angle modeled this way has been fully integrated with the

dislocation density-based material model, which can be easily adapted for different processes with different materials.

3.4. Summary

In this chapter, a dislocation density-based numerical framework was developed to simulate grain refinement in orthogonal cutting of Al 6061 T6 and OFHC Cu at strain rates as high as $4,000 \text{ s}^{-1}$. The dislocation density-based material models were calibrated to reproduce the observed material constitutive behaviors under various strains, strain rates and temperatures similar to those occurring in the cutting and cold rolling processes. Multiple orthogonal cutting tests, cutting speed ranging from 0.01 to 1.25 m/s, rake angle ranging from -20° to 20° , and depth of cut ranging from 0.1 to 0.3 mm, were simulated using the CEL finite analysis embedded with the dislocation density subroutines to investigate the effects of cutting parameters on the grain refinement mechanism during cutting.

The CEL model predictions of steady-state chip formation, strain and strain rate distributions in the chip all matched well with the actual measurements. The model predictions of the average grain size in the chip generally matched well with the measured values for all the tests of Al 6061 T6 and OFHC Cu under varying cutting conditions. Both the measurements and model predictions showed that the grain size in the machined chips of Al 6061 T6 were refined from an initial grain size of $75 \mu\text{m}$ to about 160, 100 and 80 nm under varying levels of applied shear strains ranging from 1.8 to 5.2 imposed by tool rake angles ranging from 20° to -20° . Selecting a more negative rake angle tool generally helps further reduce the grain size in the chip for applying a larger strain, but cutting speed and cutting temperature also have to be carefully designed to obtain an optimum microstructure in terms of both grain size and misorientation angle. A small applied strain, high cutting speed and high cutting temperature all contribute to a coarser elongated grain structure during cutting, while a more randomly orientated microstructure would be achieved at a low cutting speed. The simulation results demonstrated that the essential characteristics of the deformation field and grain refinement mechanism during cutting were well captured by the dislocation density-based material models. The numerical framework developed in this study has been shown to be a useful tool to predict

grain refinement and can be used to better design cutting process parameters to achieve optimum refined microstructures.

CHAPTER 4. PHASE CHANGE MODELING IN MACHINING

This chapter is concerned with prediction of the phase change effect on orthogonal cutting of AISI 1045 steel. A metallo-thermo-mechanical coupled material model is developed, and the CEL finite element model is used to solve the evolution of phase constituents, cutting temperature, chip morphology, and cutting force simultaneously using ABAQUS. The model validity is assessed using the experimental data for orthogonal cutting of AISI 1045 steel under various conditions.

4.1. Phase Transformation Kinetics

To account for the evolution of the phase composition of the workpiece material during machining, phase transformation kinetics is solved simultaneously with the energy equation at each time step. For a more detailed presentation of the kinetics model, readers are referred to the work by Skvarenina and Shin [123] and Bailey et al. [121], but a brief explanation is given below.

The workpiece material, AISI 1045 steel, had a uniform microstructure of 57% pearlite and 43% ferrite with an average grain size of 3-8 μm prior to machining [156]. The phases formed by diffusive transformation during cooling are classified as ferrite, pearlite and bainite, while martensite forms via a diffusionless transformation. During heating above the A_{C1} eutectoid temperature, pearlite and ferrite-pearlite interface transform to austenite and ferrite-austenite interface, respectively. According to Ashby and Easterling [122], the pearlite dissolution is governed by

$$L\lambda = 2Dt \tag{4.1}$$

where D is the diffusion coefficient, L is the radius of the pearlite colony, λ is the average plate spacing in the pearlite colony, and t is time. The pearlite colony radius can be approximated by

$$L \approx \frac{g}{2f_i^{1/3}} \quad (4.2)$$

where g is the average grain size and f_i is the volume fraction of pearlite within the material. Since metal cutting is non-isothermal, D is a function of temperature. The quantity Dt is given by

$$Dt = \int_{t_1}^{t_2} D_0 \exp\left(-\frac{Q}{RT(t)}\right) dt \quad (4.3)$$

where D_0 is the pre-exponential coefficient of carbon diffusion in ferrite and Q is the activation energy. This equation is integrated from the time when the temperature rises above the A_{C1} eutectoid temperature until the current time in the model. The cell transforms to either austenite or ferrite-austenite interface depending on its initial condition, once the following relationship is satisfied:

$$L\lambda \geq 2 \int_{t_1}^{t_2} D_0 \exp\left(-\frac{Q}{RT(t)}\right) dt. \quad (4.4)$$

As the workpiece begins to cool, austenite is transformed to martensite if the cooling rate is fast enough or to bainite if the cooling rate is slower. In order to determine if bainite formation will occur, the current cooling time of a material undergoing non-isothermal transformation is compared with the amount of time required to begin bainite formation in an isothermal process. Sheil's Additivity Rule discretizes the process over a number of time steps, allowing for non-isothermal calculations [121]. If the integral in Eq. 4.5 reaches a value of 1 before the temperature drops below the martensite formation temperature, bainite will begin to form [157].

$$\int_0^t \frac{dt}{t_a(T)} \geq 1. \quad (4.5)$$

Here dt is the length of a time-step, $t_a(T)$ is the incubation time required isothermally at temperature T for bainite to form, and t is the current cooling time of an austenite cell in the model. Under the parameters used in this study, bainite is not formed because the cooling rate is sufficiently fast, thereby avoiding formation of bainite. Once the temperature has dropped

below the martensite formation temperature, M_s , the following equation is used to calculate the volume fraction of martensite in the cooling process [121, 158-161].

$$f_m = f_\gamma^* \left(1 - e^{-0.011(M_s - T)}\right). \quad (4.6)$$

Here f_γ^* is the volume fraction of austenite at the time when temperature reaches M_s . If the cooling rate is sufficiently fast, i.e., no bainite is formed, all austenite that does not change into martensite will be considered retained austenite. The specific coefficients of the phase constituents and other relevant microstructural properties were determined from literature data [121, 162-164] for AISI 1045 steel, summarized in Table 4.1. The percent volume change ($\Delta V/V$) due to phase transformation from one phase to another is also given in Table 4.1.

Table 4.1. Microstructural properties for AISI 1045 steel [121, 162-164].

Property	Value	Property	Value
Pre-exponential carbon in ferrite, $D_{\alpha\alpha}$	$6 \times 10^{-5} \text{ m}^2/\text{s}$	Initial volume fraction of pearlite, f	57%
Pre-exponential carbon in austenite, $D_{\alpha\gamma}$	$1 \times 10^{-5} \text{ m}^2/\text{s}$	$\Delta V/V_{p-\gamma}$, pearlite to austenite	-0.33%
Activation energy ferrite, Q_α	80 kJ/mol	$\Delta V/V_{\alpha-\gamma}$, ferrite to austenite	-0.38%
Activation energy austenite, Q_γ	135 kJ/mol	$\Delta V/V_{\gamma-M}$, austenite to martensite	1.026%
Universal gas constant, R	8.314 J/molK	A_{C1} (°C) [163]	727
Pearlite grain spacing, λ	0.5 μm	A_{C3} (°C) [163]	800
Diameter of pearlite grain, L	5 μm	M_s (°C) [164]	324

4.2. Constituent Phase Properties of AISI 1045 Steel

The AISI 1045 steel workpiece has an initial microstructure of ferrite-pearlite prior to machining. When the material temperature is raised above its austenitic temperature, the ferrite-pearlite transforms to austenite, and then the austenite transforms to martensite as the temperature cools down quickly. Table 4.2 shows the temperature-dependent physical properties of constituent phases of ferrite-pearlite, austenite and martensite for AISI 1045 steel adopted from literature data [164-168]. Figure 4.1 plots the temperature-dependent physical properties of constituent phases for AISI 1045 steel, which clearly shows the radical difference in

thermo-mechanical properties such as density, thermal conductivity and specific heat for different constituent phases.

For AISI 1045 steel consisting of pearlite and ferrite prior to the phase change, Jaspers and Dautzenberg [169] experimentally obtained the material parameters in the Johnson-Cook (JC) constitutive plasticity model using the split-Hopkinson pressure bar (SHPB) tests at temperatures ranging from room temperature to 500 °C. However, Burns et al. [129] conducted SHPB tests of the AISI 1045 steel specimens at various temperatures from 644 °C to 942 °C, and reported that the specimens tested at temperatures higher than 800 °C showed a drastic decrease in material strength than those at temperatures from room temperature to 651 °C. Their SHPB measurements showed that the JC model only works for AISI 1045 steel at low temperatures prior to phase transformation. As the material temperature increases and phase transformation occurs, a different constitutive model is needed to correctly describe the mechanical behavior for AISI 1045 steel. The same phenomenon of drastic change in constitutive behavior was also observed for another carbon steel (AISI 1075 steel) due to transformation of pearlite to austenite at temperatures ranging from 588 °C to 875 °C [128].

Table 4.2. Physical properties of constituent phases for AISI 1045 steel.

Property	Phase	Temperature-dependent functions
Elastic modulus E (GPa)	Austenite (>1073 K) [165]	$E = 227.08 - 0.0929T$
	Ferrite-Pearlite (<873 K) [166]	$E = 250.29 - 0.1086T$
	Martensite (<873 K) [165]	$E = 214.9 - 0.0533T$
Density ρ (kg/m ³)	Austenite (>1041 K) [164]	$\rho = 8190 - 0.49T$
	Ferrite-Pearlite (<985 K) [164]	$\rho = 7919.7 - 0.2149T - 0.000102T^2$
	Martensite [167, 168]	$\rho = 7859.5 - 0.2667T$
Poisson ratio ν	Austenite (>1073 K) [165]	$\nu = 0.345$
	Ferrite-Pearlite (<873 K) [166]	$\nu = 0.30$
	Martensite (<873 K) [165]	$\nu = 0.2667 + 5 \times 10^{-5}T$
Thermal expansion α (10 ⁻⁶ K ⁻¹)	Austenite (>1073 K) [165]	$\alpha = 21$
	Ferrite-Pearlite (<973 K) [166]	$\alpha = 8.8608 + 0.0068T$
	Martensite (<873 K) [121]	$\alpha = 11$
Thermal conductivity k (W/m·K)	Austenite (>1073 K) [166]	$k = 295.36 - 0.4382T + 0.0002T^2$
	Ferrite-Pearlite (<973 K) [166]	$k = 51.638 - 0.0228T$
	Martensite (<873 K) [165]	$k = 49.052 - 0.0217T$
Specific heat C_p (J/kg·K)	Austenite (>1041 K) [164]	$C_p = 439 + 0.1142T$
	Ferrite (<873 K) [164]	$C_p = 435 + 0.102T + 0.000541T^2$
	Ferrite-Pearlite (<873 K) [164]	$C_p = 447 + 0.081T + 0.000495T^2$
	Martensite (<873 K) [165]	$C_p = 416.2 + 0.2862T$

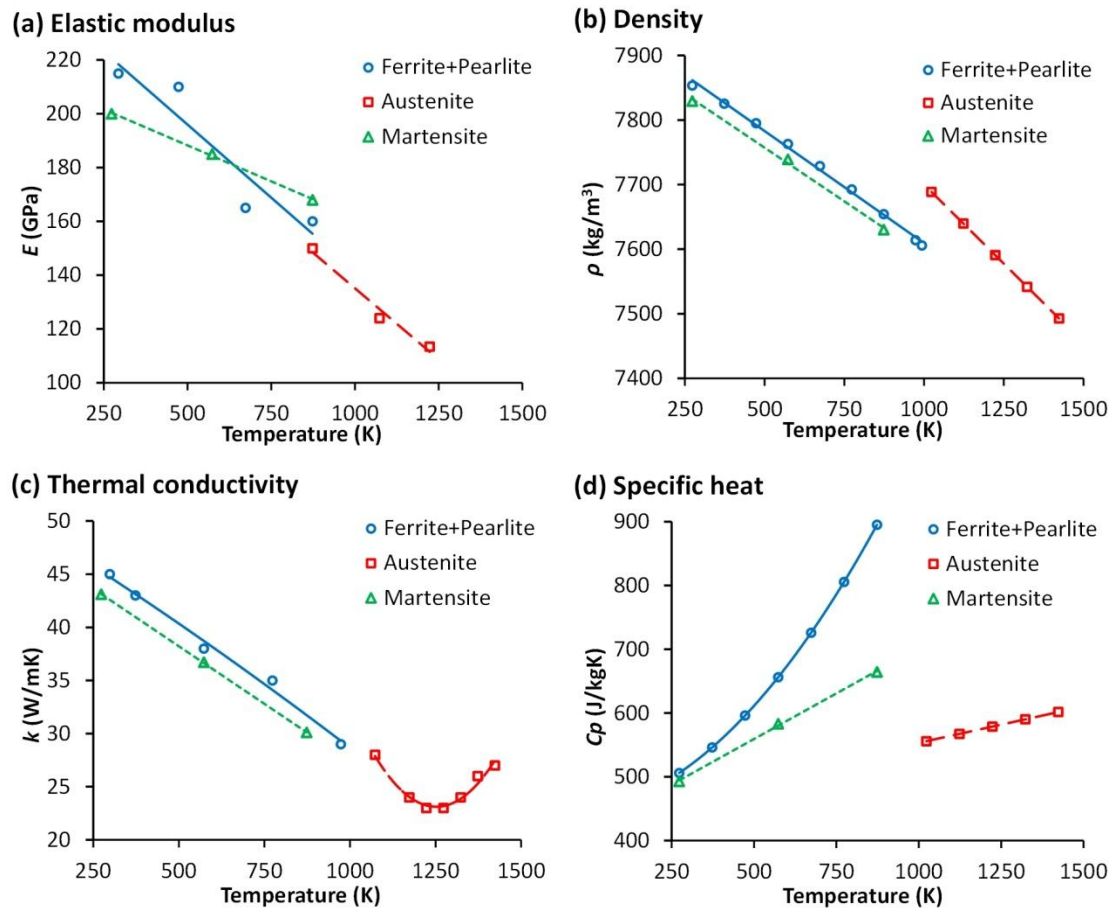


Figure 4.1. Temperature-dependent physical properties of phases for AISI 1045 steel (data from [164-168]).

The constitutive models for AISI 1045 steel of austenite and martensite were adopted from the work by Iwamoto et al. [170], who reported constitutive equations for the primary phases of martensite and austenite of the 304 austenitic stainless steels with 0.06wt% carbon. The constitutive models for austenite and martensite considering strain, strain rate and temperature are given as follows:

$$\sigma = \left(C_1 (1 - e^{-C_2 \epsilon})^{C_3} + C_4 e^{-C_5 T} \right) \left(\frac{\dot{\epsilon}}{\dot{\epsilon}_0} \right)^m \quad (4.7)$$

Table 4.3 shows the constitutive model parameters for all the constituent phases of AISI 1045 steel. Figure 4.2 shows the predicted flow stresses for AISI 1045 steel in the temperature range from the ambient to 1000 °C in comparison with the experimental data in [129]. It can be seen

that the predicted material behaviors match well with the experimental data obtained at different temperatures with different phase compositions.

Table 4.3. The constitutive model parameters of constituent phases for AISI 1045 steel.

Phase	A_{JC} (MPa)	B_{JC} (MPa)	n_{JC}	C_{JC}	m_{JC}	$\dot{\epsilon}_o$ (1/s)	T_m (K)
Ferrite-Pearlite (<773 K) [129, 169]	553.1	600.8	0.234	0.0134	2	1	1733
Phase	m	$\dot{\epsilon}_o$ (1/s)	C_1	C_2	C_3	C_4	C_5
Austenite [170, 171]	0.01	5E-4	2084.2	0.31	0.58	1023.9	0.005
Martensite [170, 171]	0.01	5E-4	1180.7	17.8	7.66	1983	0.0059

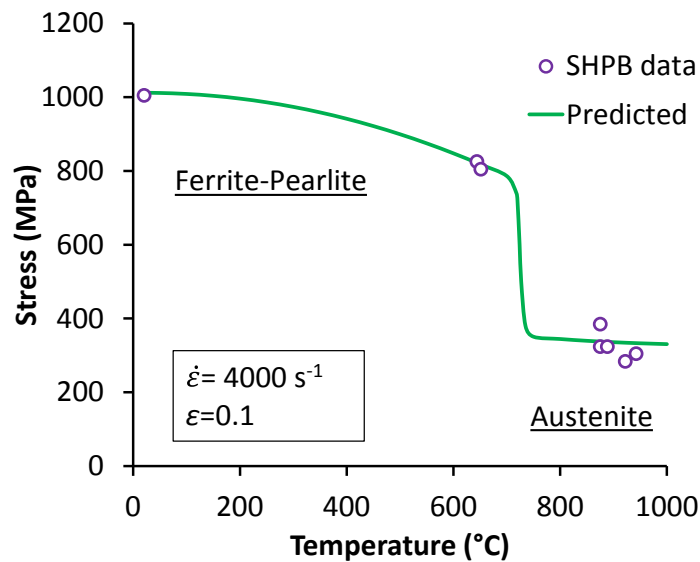


Figure 4.2. Constitutive model predictions vs. SHPB test results (SHPB data from [129]).

4.3. Metallo-thermo-mechanical Coupling

In the course of phase transformation during the cutting process, an additional strain is induced by the microstructure evolution along with the mechanical and thermal strains. The phase transformation also produces transformation-induced plasticity. This can be represented analytically by adding a separate strain component to the total strain function. Hence, the total

strain increment ($\Delta\varepsilon$) for a steel undergoing solid-state phase transformation can be written as the sum of the individual components of the strain as follows [121, 158-160, 172]

$$\Delta\varepsilon = \Delta\varepsilon^E + \Delta\varepsilon^P + \Delta\varepsilon^T + \Delta\varepsilon^{\Delta V} + \Delta\varepsilon^{TrP} \quad (4.8)$$

where $\Delta\varepsilon^E$, $\Delta\varepsilon^P$, $\Delta\varepsilon^T$, $\Delta\varepsilon^{\Delta V}$ and $\Delta\varepsilon^{TrP}$ represent the strain increments due to elastic, plastic, thermal, volumetric dilatation and transformation-induced plasticity, respectively. The elastic strain increment $\Delta\varepsilon^E$ is calculated using the isotropic Hook's law with temperature-dependent Young's modulus and Poisson's ratio for different constituent phases as given in Table 4.2. The rate-independent constitutive models were used for the plastic strain increment of $\Delta\varepsilon^P$. The thermal strain increment $\Delta\varepsilon^T$ is computed using the coefficient of thermal expansion by [121, 173]

$$\Delta\varepsilon^T = \left(\sum \alpha_i f_i \right) \Delta T \quad (4.9)$$

where f_i is the phase fraction of phase i , and α_i is the coefficient of thermal expansion for phase i , which are given in Table 4.2. When a given volume in a workpiece undergoes transformation from one phase to another, the microstructural pattern transforms. For example, austenite changing to martensite will transform from a face-centered cubic (FCC) body structure to a body-centered tetragonal (BCT) structure, thereby dilating the volume. The strain increment due to this volumetric dilatation is given by [121, 172]

$$\Delta\varepsilon^{\Delta V} = \frac{1}{3} \frac{\Delta V}{V} \Delta f \quad (4.10)$$

where the percent volume change $\Delta V/V$ due to phase transformation from one phase to another is given in Table 4.1 and Δf is the change in phase fraction during the time increment. Unlike austenitic transformation, the formation of martensite induces transformation plasticity, which is also produced when dilatational strains interact with the already-existing stress field [121, 158, 159]. It has been reported that transformation plasticity produces a mechanical effect on the stresses and strains equivalent to that induced when the yield stress of the steel is reduced by a certain extent over the phase transformation temperature range [174, 175]. Lee and Chang [158, 159] reported that a reduction of 30 MPa in the value of yield stress can

represent the mechanical effect of transformation plasticity via the formation of martensite. This simplified and approximate approach is employed in this work in order to incorporate the transformation plasticity into the FE model.

4.4. Simulations

4.4.1. Implementation of the Material Models

The metallo-thermo-mechanical coupled material model was implemented in the commercial software ABAQUS 6.11.1 Explicit using the user-defined material subroutines of VUHARD and VUSDFLD programmed in FORTRAN. A flowchart showing the various steps in the computational scheme employed in this work is given in Figure 4.3. The evolution of phase constituents of the workpiece material was modeled in the user-defined subroutine of VUSDFLD using the phase transformation kinetics model described in Section 4.1. The user defined state and field variables for the phase constituents were constantly updated from the inputs of the thermal and mechanical fields. The thermo-mechanical properties of the workpiece material were defined using metallurgical field variable-dependent data as given in Section 4.2. The constitutive plasticity models for the phase constituents were implemented in the user-defined subroutine of VUHARD, which included the material behavior dependent on metallurgical field variables and defined the derivatives of the yield stress with respect to the independent variables, such as strain, strain rate, and temperature. In VUHARD, the phase fraction of each phase is used to calculate the phase-dependent volumetric dilatation strain, and account for the effect of transformation-induced plasticity strain. NLGEOM flag was used within the ABAQUS/Explicit step to specify a large-displacement formulation and to ensure applicability to finite deformation/strain in the simulation. Abaqus/Explicit internally uses classical J2 plasticity theory to generalize the scalar model given in the VUHARD user subroutine to multiaxial stress states in the simulation [139]. During the simulation, the material subroutines were constantly called at all material points of elements to calculate the material flow stresses and the user-defined solution-dependent metallurgical field variables.

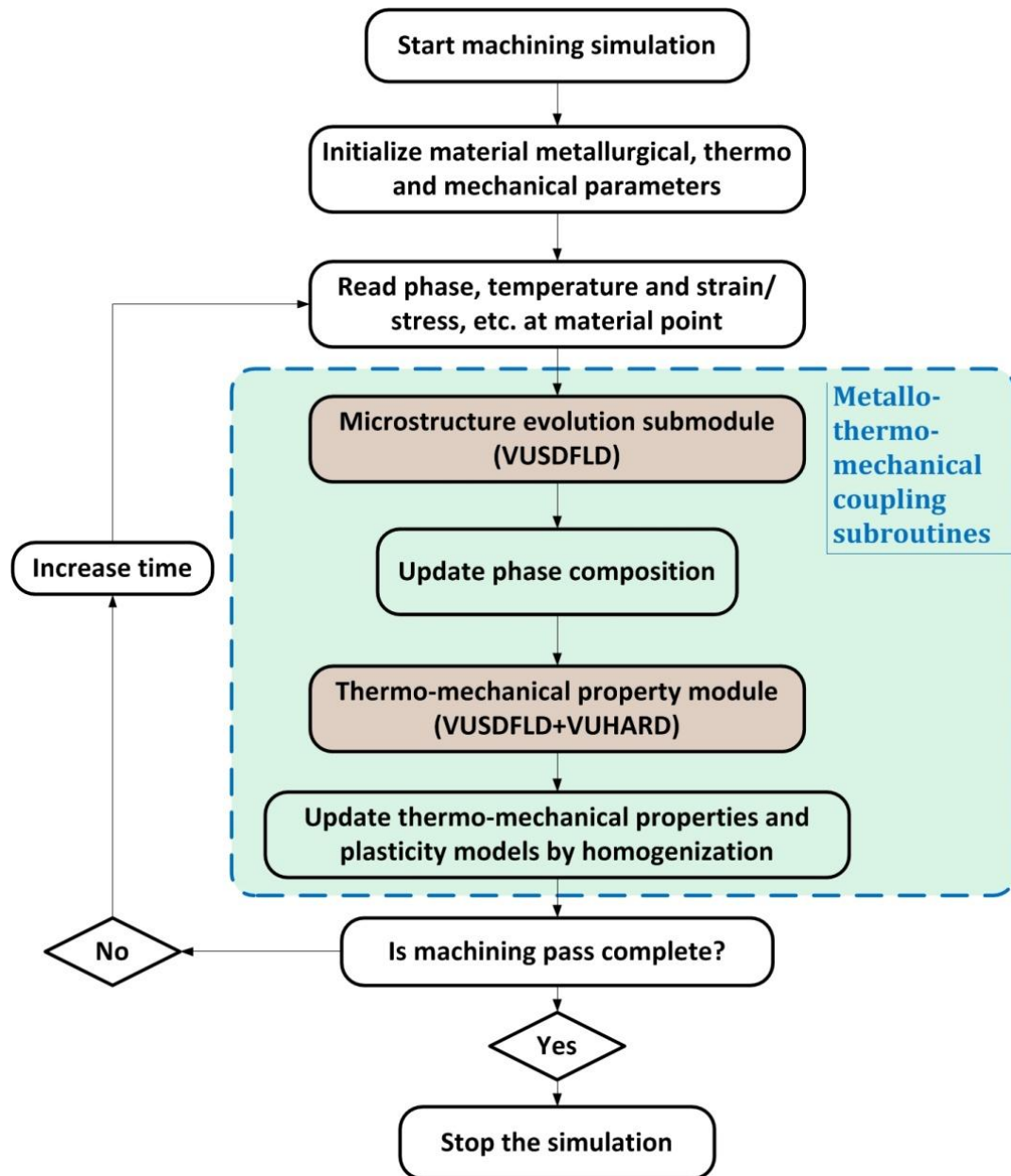


Figure 4.3. Flowchart for implementation of the material model.

4.4.2. Orthogonal Cutting Experiments of 1045 Steel

In order to assess the validity of the coupled metallo-thermo-mechanical analysis solution presented in this study, a set of orthogonal cutting experiments as given in Table 4.4 was simulated for AISI 1045 steel, and the modeling results are compared with the experimental data presented in [156, 176-178]. Orthogonal cutting tests A1-A8 as shown in Table 4.4 were

conducted for AISI 1045 steel by Ivester et al. [156] with varying cutting speeds (V) of 200 and 300 m/min, feeds (f) of 0.15 and 0.3 mm and rake angle (α) tools of 5° and -7° using a general purpose uncoated tungsten carbide / cobalt (WC/Co) insert (grade, Kennametal K68). The AISI 1045 steel workpieces had an equiaxed grain structure of a grain size of 3-8 μm [156]. Prior to machining, the workpiece microstructure was a homogeneously distributed mixture of a pearlite volume fraction of 57% and a ferrite volume fraction of 43%. Orthogonal cutting tests B1-B4 shown in Table 4.4 were conducted by Iqbal et al. [166, 178] for a wide range of cutting speeds from 198 to 879 m/min with a constant feed of 0.1 mm. They used a commercially available uncoated tungsten carbide insert (Sandvik 5015) with a rake angle of 0° . Widths of cut (W) of 1.6 mm and 2.5 mm were applied to tests A1-A8 and B1-B4, respectively, while an edge radius (r_e) of 0.02 mm was used for the sharp cutting edge of the tools for all the tests. All the experiments were conducted without any coolant. The effects of cutting speed, feed and tool rake angle are discussed using tests A1-A8, while significantly higher cutting speeds of 628 m/min and 879 m/min in tests B1-B4 are used to further examine the effect of high cutting speed on phase transform during cutting of AISI 1045 steel.

Table 4.4. Orthogonal cutting conditions for AISI 1045 steel [156, 178].

Test	V (m/min)	f (mm)	α ($^\circ$)	r_e (mm)	W (mm)
A1	200	0.15	5	0.02	1.6
A2	300	0.15	5	0.02	1.6
A3	200	0.15	-7	0.02	1.6
A4	300	0.15	-7	0.02	1.6
A5	200	0.3	5	0.02	1.6
A6	300	0.3	5	0.02	1.6
A7	200	0.3	-7	0.02	1.6
A8	300	0.3	-7	0.02	1.6
B1	198	0.1	0	0.02	2.5
B2	399	0.1	0	0.02	2.5
B3	628	0.1	0	0.02	2.5
B4	879	0.1	0	0.02	2.5

The orthogonal cutting tests investigated in Table 4.4 were all conducted using continuous turning setups [156, 178], and therefore it is essential to model steady-state cutting in this numerical study. The CEL finite element model was used to simulate 2D steady-state orthogonal cutting using the commercial software Abaqus 6.11.1. The metallo-thermo-mechanical coupled material model developed was used for the workpiece material in the 2D FE simulations, while the physical properties of the two carbide tool materials used in the simulations can be found in [156, 176-178].

To define the tool-chip interface behavior, cutting speed-dependent frictional coefficients were used in the simulations for the cutting tests with varying cutting speeds. The applied frictional coefficients were 0.75, 0.73, 0.7, 0.65 and 0.6 for cutting speeds of 200 (as well as 198), 300, 628 and 879 m/min, respectively, which were adopted from the study of frictional behavior in cutting of AISI 1045 steel using uncoated carbide tool at various cutting speeds [178]. A gap conductance of 10^4 W/K·mm² was defined for the heat transfer at the tool-chip interface as in [179]. When the tool face node had no contact with the chip and the workpiece, the gap conductance was set to zero. It was adopted from [180] that 90% of the dissipated energy caused by friction between the chip and the tool face is converted into heat, and the fraction of the heat generation by plastic deformation was set to be 0.9. A mesh-sensitivity analysis was conducted in several trial simulations, and the optimal mesh scheme was found to have about 6000 elements in total with the minimum element size of 3-5 μ m in the workpiece, which considers both computational precision and time. To determine if cutting simulation reaches its steady state, a long enough cutting time, say 0.002 s for a cutting speed of 200 m/min, was used to ensure that the chip morphology, mechanical, thermal and metallurgical fields all remain unchanged as the cutting time further increased. One of the main drawbacks of machining simulation by FEM is the extremely high computational cost of simulations. Using the CEL model, the computational time was reduced to about 4 hours per simulation from more than 20 hours when using a Lagrangian model with ALE in simulating steady-state chip formation for orthogonal cutting conditions given in Table 4.4.

4.5. Simulation Results

Simulation results are presented for chip formation, cutting force, cutting temperature and volume fraction of the phase transformed in the chip produced by orthogonal cutting and compared with the actual experimental data. Figure 4.4 shows the steady-state distributions of temperature, Mises stress and phase composition predicted for orthogonal cutting tests of A7 and A8 conducted at the depth of cut of 0.3 mm with -7° rake angle tools but at different cutting speeds of 200 and 300 m/min. The temperature distribution is shown in the workpiece, chip, and tool while the stress and phase distributions are only shown in the workpiece and chip in Figure 4.4. The simulated steady-state chip morphologies, as can be seen in Figure 4.4, show that a lower cutting speed of 200 m/min produces an average deformed chip thickness (t_c) of 0.71 mm from an uncut chip thickness (t_1) of 0.3 mm and a shear angle (ϕ) of 21° . Increasing the cutting speed to 300 m/min produces a thinner t_c of 0.62 mm and a higher ϕ of 23° . Figure 4.4a and b show the temperature fields predicted by the model and it can be seen that as the material passes the shear plane, the temperature is predicted to be drastically increased from ambient temperature to about 340°C and 380°C for cutting speeds of 200 and 300 m/min, respectively. This is mainly contributed by the heat generation due to the severe shear plastic deformation. As the material deformation continues into the steady-state chip, much higher temperatures are predicted in the secondary shear zone mainly due to the friction between the tool and chip contact interface. The maximum tool-chip interface temperature (T_{int}) is predicted to be 1192°C and 1326°C for cutting speeds of 200 and 300 m/min, respectively. When cutting reaches steady state, very steep temperature gradients are predicted to exist at the tool-chip interface and also in a shallow layer below the machined surface. It can be seen in Figure 4.4c and d that the simulated von Mises stress in the primary shear zone is about 1,280 MPa for both cutting speeds. The predicted phase compositions in the chips are illustrated in Figure 4.4e and f: a layer of material close to the tool-chip interface has transformed from the original mixture of pearlite and ferrite to either pure austenite, or mixture of austenite and ferrite due to the increasing temperature. The thickness of the phase transformed layer was predicted to be 0.14 and 0.16 mm, which accounts for a volume fraction of 19% and 26% of the steady-state chip for cutting speeds of 200 and 300 m/min, respectively. No phase transformation was predicted on the machined subsurface.

Table 4.5 summarizes the details of the model predictions of: maximum tool-chip interface temperature ($T_{int-pred}$), volume fraction of the transformed austenite (f_{gamma}) in the steady-state chip, cutting force (F_{c-pred}) in the tangential direction, thrust cutting force (F_{t-pred}) in the radial direction, average thickness (t_{c-pred}) of the steady-state chip, cutting ratio ($r_{pred} = t_1 / t_{c-pred}$) and shear angle (ϕ_{pred}). Their experimentally-obtained counterparts extracted from [156, 176-178] are also given in Table 4.5 for orthogonal cutting of AISI 1045 steel. All the force data in Table 4.5 is normalized by using the width of cut. The cutting temperature was not measured for tests B1-B4; hence the temperature measurement data was not available for these tests. Note for tests B1-B4 only the average values were reported in literature, and therefore the variance of the experimental data is not discussed for those tests.

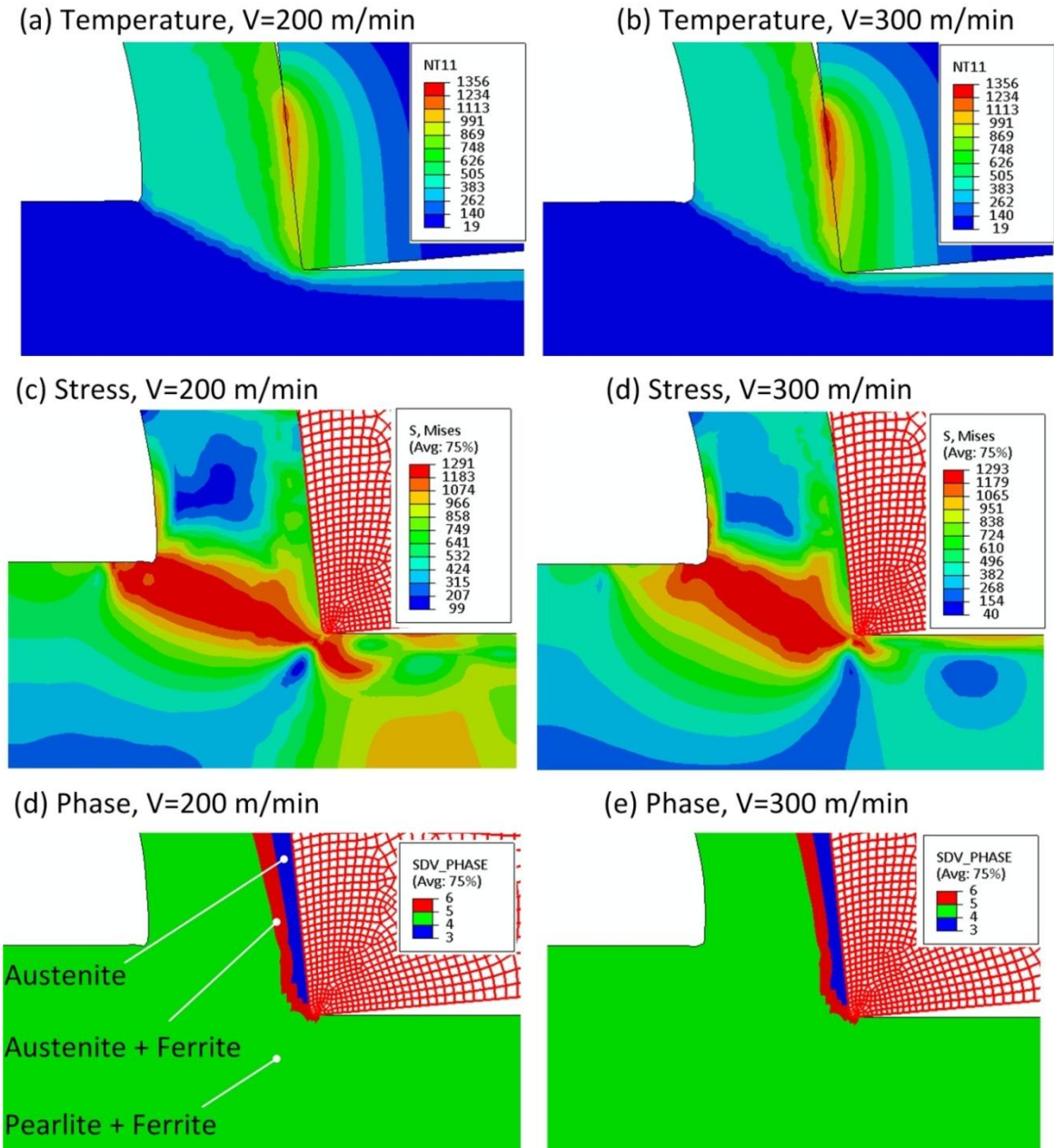


Figure 4.4. Predictions of temperature, Mises stress and phase field for tests A7 and A8.

Table 4.5. Comparison of model predictions with experimental data from [156, 176-178].

<i>Test</i>	F_{c-meas} (N/mm)	F_{t-meas} (N/mm)	$T_{int-meas}$ (°C)	t_{c-meas} (mm)	r_{meas}	φ_{meas} (°)	F_{c-pred} (N/mm)	F_{t-pred} (N/mm)	$T_{int-pred}$ (°C)	f_{gamma} (%)	t_{c-pred} (mm)	r_{pred}	φ_{pred} (°)
A1	354	227	1250	0.42	0.36	20	417	191	1080	24%	0.44	0.34	19
A2	334	183	1300	0.37	0.41	23	361	171	1198	30%	0.38	0.39	22
A3	385	297	1120	0.46	0.33	17	443	257	1109	25%	0.47	0.32	17
A4	374	255	1310	0.43	0.35	18	391	209	1250	35%	0.42	0.36	19
A5	587	298	1220	0.62	0.48	27	659	301	1171	17%	0.59	0.51	28
A6	600	313	1300	0.64	0.47	26	607	278	1281	20%	0.56	0.54	29
A7	725	420	1100	0.75	0.40	21	744	389	1192	19%	0.71	0.42	22
A8	642	375	1305	0.66	0.45	23	633	331	1326	26%	0.62	0.48	24
B1	227	166	-	0.25	0.39	22	235	135	1037	28%	0.29	0.34	20
B2	209	144	-	0.24	0.42	23	219	119	1307	48%	0.27	0.37	21
B3	196	123	-	0.21	0.47	25	205	105	1351	58%	0.26	0.38	22
B4	199	123	-	0.21	0.48	26	209	109	1396	79%	0.24	0.42	24

The steady-state chip morphology varies greatly in cutting tests with different cutting parameters, and the accuracy of the numerical model was first assessed on the deformation field by comparing the average deformed thickness of the steady-state chip predicted by the model with the experimental data as shown in Figure 4.5. The model predicted that a more negative rake angle produces a thicker chip and imposes a larger stain. For instance, the predicted average machined chip thicknesses were 0.59 mm and 0.71 mm for the rake angle of 5° and -7° in tests A5 and A7, respectively, with other machining parameters remaining the same; while the measured average machined chip thicknesses were 0.62 mm and 0.75 mm for tests A5 and A7, respectively. The model also accurately predicted deformed chip thickness for different feeds, i.e., uncut chip thickness in an orthogonal cutting operation. For example, in tests A3 with a feed of 0.15 mm and A7 with a feed of 0.3 mm, the predicted average machined chip thicknesses were 0.47 mm and 0.71 mm, respectively, which are in good agreement with the measured chip thicknesses of 0.46 mm and 0.75 mm, respectively. As for the effect of cutting speed as demonstrated in Figure 4.5b, the model correctly captured a decreasing trend in chip thickness as cutting speed increases, which matched well with the measurement data obtained by Iqbal et al. [178].

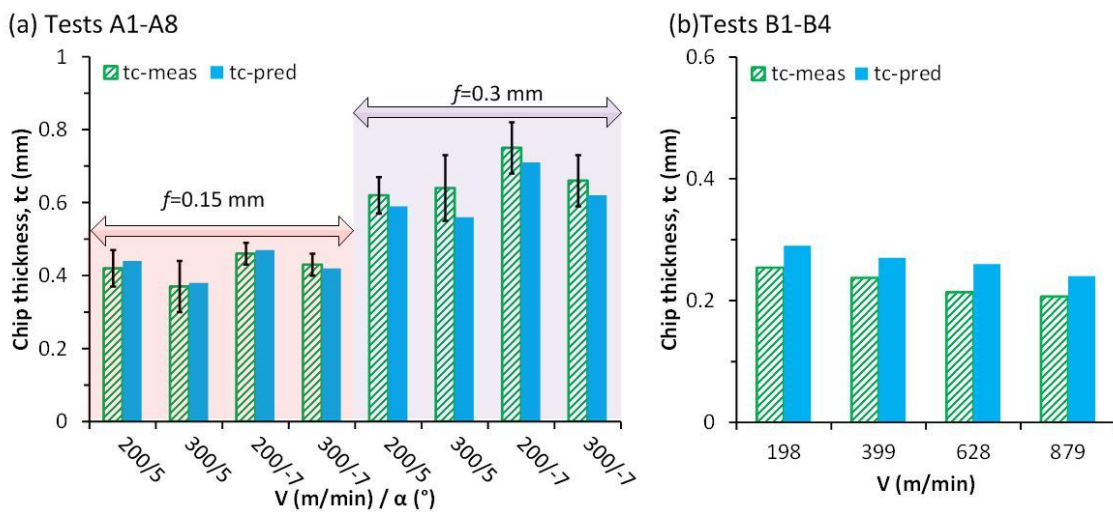


Figure 4.5. Comparison of the deformed chip thickness predicted with the experimental data from [156, 178].

The model performance is demonstrated in Figure 4.6 on the thermal and metallurgical fields. The accuracy of the model predictions on cutting temperature is assessed by a direct comparison of the maximum tool-chip interface temperatures predicted by the model with the experimental data extracted from [156, 176, 177] for orthogonal cutting tests A1-A8 with varying cutting speeds, feeds and tool rake angles. The model predicted an increase in T_{int} of 110-140 °C as the cutting speed increased from 200 m/min to 300 m/min for various combinations of feeds of 0.15 mm and 0.3 mm and tool rake angles of 5° and -7°, which is in a good agreement with the experimentally-determined temperature increase of 50-195 °C. The discrepancy between the model predictions of T_{int} and experimental data is well below 10% (or below 100 °C) for the tests conditions, with a slight larger discrepancy of 14% for test A1.

The volume fraction of the transformed austenite predicted in the steady-state chip is also shown in Figure 4.6 for various cutting parameters. The transformed austenite accounts for volume fractions of 17%-35% of the chips produced by tests A1-A8. Due to a higher cutting temperature at a higher cutting speed, the model predicted a 3-10% increase in f_{γ} as the cutting speed increases from 200 m/min to 300 m/min for various combinations of feeds of 0.15 mm and 0.3 mm and tool rake angles of 5° and -7°. The model predicted a 1-8% increase in f_{γ} when the tool rake angle changes from 5° to -7° while the other cutting parameters remaining the same. A 5-10% decrease is predicted as the feed is increased from 0.15 mm to 0.3 mm, which is mainly caused by the significant increase of the deformed chip thickness at feed increases. As the feed decreases to 0.1 mm and cutting speed increases from 198 m/min to as high as 879 m/min in tests B1-B4, higher volume fractions of 28-79% of the transformed austenite are predicted, which further shows the significant effect of cutting speed and feed on phase transformation in the chip during cutting of AISI 1045 steel.

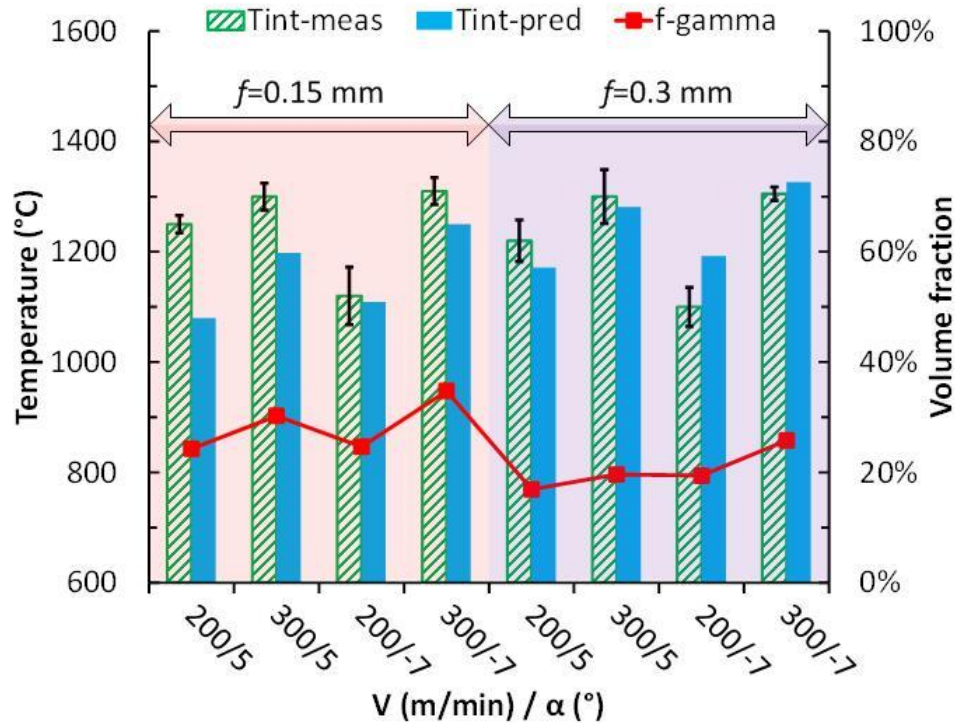


Figure 4.6. Prediction of volume fraction of austenite in the chip and comparison of the predicted T_{int} with experimental data from [156, 176, 177].

The validity of the model is further presented in Figure 4.7 with cutting force predictions in comparison with the measured force data from [156, 178]. It can be seen in Figure 4.7 that the model predicted cutting forces are generally higher than the measured average forces, while the predicted thrust forces are generally lower than the measured values. The discrepancies between the model predictions and the experimental data in F_c are mostly below 8% for the 12 test conditions, while the prediction errors in F_t range mostly from 10% to 19%. The model correctly predicted the effect of cutting speed on force: both F_c and F_t decrease as the cutting speed increases with the other cutting parameters remaining the same. For instance, as the cutting speed increases from 198 m/min to 879 m/min for tests B1-B4, the predicted F_c drops from 235 N/mm to 209 N/mm compared with an experimentally-determined decrease from 227 N/mm to 199 N/mm. The predicted F_t drops from 135 N/mm to 109 N/mm compared with an experimentally-determined decrease from 166 N/mm to 123 N/mm. The model also predicted an increase in both F_c and F_t when using a more negative rake angle from 5° to -7° for tests A1-A8.

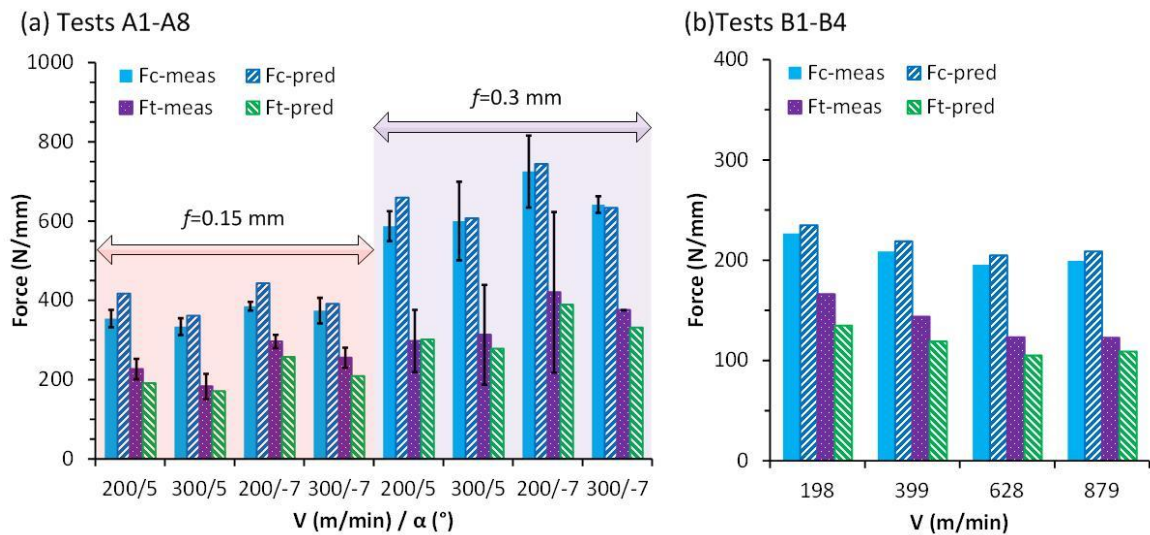


Figure 4.7. Comparison of the predicted cutting force with experimental data from [156, 178].

4.6. Discussions

This analysis is focused on steady-state cutting of AISI 1045 steel and the phase composition of the chips separated from the bulk workpiece. The volume fractions of the transformed austenite predicted in the steady-state chips cannot be directly assessed in this analysis because of a lack of experimental data for phase compositions in the chips. Also, most of the transformed austenite in the chips nearby the tool-chip interface would become martensite due to quenching at a rapid cooling rate, while a part of austenite that does not change into martensite turns into retained austenite. Han et al. [163] conducted orthogonal cutting tests of AISI 1045 steel with no martensite and retained austenite in its initial microstructure at cutting speeds of 100-200 m/min with severely worn carbide tools and measured the volume fractions of retained austenite on the machined surface. Their study showed that retained austenite was found remaining on the machined surface, which was due to a large amount of frictional heat, generated using the severely worn tool. The volume fraction of retained austenite increased from 5% to 15% as the cutting speed increased and the tool wear became more severe. Chou and Evans [36] reported a 22% increase of retained austenite on the machined surface after hard turning of AISI 52100 steel at a cutting speed of 180 m/min. Ramesh et al. [134] reported the volume fraction of retained austenite increased

from 5% to 10% on the machined surface of AISI 52100 steel when the cutting speed increased from 91 m/min to 273 m/min. These experimental studies corroborate the modeling predictions of austenite transformation in this analysis.

Regardless of the experimental evidence of phase transformation during cutting of steels, the metallurgical field has rarely been coupled to the thermo-mechanical analyses of cutting, and the phase change effect upon the material machinability has often been neglected in numerical studies. For an ease of implementation, a unified material model is often tried to cover the workpiece material behaviors both prior to and after phase transformation in cutting. One most notable case of such models was given by Oxley [181], who modeled the strain-hardening flow stress dependent on velocity-modified temperature (T_{mod}) as a function of strain rate and cutting temperature in the range of room temperature to 1000 °C. Oxley's model showed the blue-brittleness effect of steels in cutting experiments, i.e., the flow stress increases with an increase in modified temperature in the range of 520 K to 640 K, which translates to a temperature range of 672 °C to 890 °C and overlaps with the critical temperatures of phase transformation. Lalwani et al. [176] applied an extended Oxley's theory to model the cutting forces and cutting temperatures for orthogonal cutting tests A1-A8 of AISI 1045 steel. Figure 4.8 shows the comparison of the temperature and cutting force predicted in this study with the predicted values by Lalwani et al. [176]. It can be seen in Figure 4.8 that much larger discrepancies from the experimental data are predicted by the extended Oxley's theory in both cutting forces and temperatures for all the cutting conditions. This indicates that compared with the approach using a unified material model not coupled with the metallurgical field, the metallo-thermo-mechanical coupled analysis developed in this study not only has the ability of predicting phase change but also captures the material behaviors more accurately when a phase change occurs in cutting.

The better prediction results using the analysis coupled with the metallurgical field also encourage the development of constitutive models for the basic constituent phases of steel. Constitutive models are available in literature for only a limited number of steels under their certain conditions, which will not work well for other types of steel or the same one but with different microstructures. Ideally, with the development of the constitutive models for different phases, it is possible to simulate cutting of steel using the metallo-thermo-mechanical coupled analysis developed in this study only with the knowledge of its phase compositions.

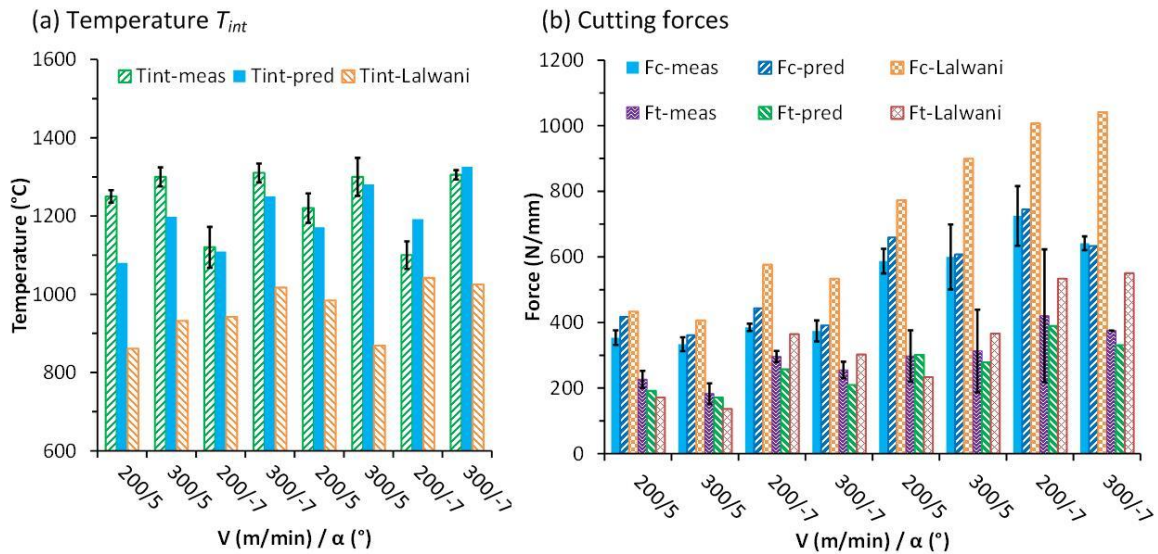


Figure 4.8. Comparison of the predicted temperature and cutting force with the predicted values using an extended Oxley's predictive machining theory from [176].

4.7. Summary

This chapter presented an FE model for orthogonal cutting of AISI 1045 steel based on a true metallo-thermo-mechanical coupled material model. The metallo-thermo-mechanical coupled material model was implemented in ABAQUS, and the CEL model was used to simulate this metallo-thermo-mechanical coupled orthogonal cutting process. The evolution of phase constituents of the workpiece material was modeled using a phase transformation kinetics model, and was solved simultaneously with thermal and mechanical fields in cutting. The thermo-mechanical properties and the rate-independent constitutive models of constituent phases of ferrite-pearlite, austenite and martensite for AISI 1045 steel were used in the coupled analysis. Cutting temperatures, phase compositions, chip morphologies, and cutting forces were all solved simultaneously. The model accurately predicted the chip thickness for different cutting speeds, tool rake angles and feeds compared with the experimental data. The volume fractions of the transformed austenite were predicted in the steady-state chips. The model predicted the tool-chip interface temperature ranging from 1080 °C to 1396 °C for various cutting conditions investigated, and the discrepancy between the model predictions and the experimental data was well below 10%. The model was further validated in cutting force with discrepancies of less than 8% in cutting direction and 10-19% in feed direction.

CHAPTER 5. MULTI-PHYSICS MODELING OF MICROSTRUCTURE ALTERATION IN HARD TURNING

This chapter is to quantitatively disseminate the white layer formation through prediction of the microstructure change using a multi-physics model, which considers both phase transformation and grain refinement. 3D hard turning simulations are undertaken via AdvantEdge FEM software incorporating these two mechanisms as user-defined subroutines to investigate the surface microstructure alteration for AISI 52100 steel.

5.1. Hard Turning Experiments

The workpiece material investigated in this chapter, AISI 52100 steel, is a key alloy in the manufacture of bearings. The nominal chemical composition of AISI 52100 steel is Fe-1.05wt.%C-1.54wt.%Cr as given in [36]. In order to assess the validity of the coupled metal-thermo-mechanical analysis solution, a set of hard turning experiments was simulated for AISI 52100 steel, and the modeling results are compared with the experimental data in literature. Tests A1 and A2, as shown in Table 5.1, were conducted by Ramesh et al. [134] with cutting speeds (V) of 91.4 and 274.3 m/min, a feed (f) of 0.127 mm/rev and depth of cut (doc) of 0.254 mm. Cutting tools used in tests A1 and A2 were low CBN-content inserts (Kennametal KD050 grade, TNG432 geometry) with -5° back rake angle, 0° clearance angle, 0° side cutting angle and 0.8 mm nose radius with no wear. Hard turning tests B1-B5 were conducted by Chou and Evans [36] at various cutting speeds between 45-180 m/min, with a feed of 0.05 mm/rev and depth of cut of 0.2 mm. Cutting tools used in tests B1-B5 were 55° diamond-shaped Al_2O_3 -TiC inserts (Kennametal K090 grade, DNGA432T geometry) with -30° back rake angle, 5° clearance angle and 0.8 mm nose radius with three levels of flank wear land width (VB) of 0.11, 0.21 and 0.3 mm. Prior to hard turning, the AISI 52100 steel workpieces used in all the tests were heat treated under a similar condition: austenitization by heating at 829-843 °C, quenching in oil, and then tempering at 163 °C. The initial microstructure of the workpieces after heat treatment was a

tempered martensitic (*TM*) bulk structure with a hardness of approximately 62 HRC. All the experiments were conducted without any coolant.

Table 5.1. Hard turning conditions.

Test	V (m/min)	f (mm/rev)	d_{oc} (mm)	VB (mm)
A1	91.4	0.127	0.254	0
A2	274.3	0.127	0.254	0
B1	180	0.05	0.2	0.11
B2	180	0.05	0.2	0.21
B3	180	0.05	0.2	0.3
B4	90	0.05	0.2	0.3
B5	45	0.05	0.2	0.3

5.2. Models

5.2.1. Material Properties and Constitutive Models of AISI 52100 Steel

Table 5.2 shows the temperature-dependent physical properties of AISI 52100 steel obtained in [182]. The Johnson-Cook model in [182] defined the constitutive plasticity behavior of AISI 52100 steel of a tempered martensitic bulk structure with a hardness of 62 HRC, and was adopted in this study to model its plasticity prior to any phase change. When the material temperature is raised above its austenitic temperature, the tempered martensite transforms to austenite (γ), and then the austenite converts to un-tempered martensite (M) as the temperature cools down quickly. The constitutive models of austenite and martensite were adopted from the work by Iwamoto et al. [170], who reported constitutive equations for the primary phases of martensite and austenite of the 304 austenitic stainless steels. The constitutive models for austenite and martensite considering strain, strain rate and temperature are given by Eq. 4.7. Table 5.3 shows the constitutive model parameters for all the constituent phases of AISI 52100 steel.

Table 5.2. Physical properties of constituent phases for AISI 52100 steel [182].

Property	Temperature-dependent data
Elastic modulus, E (GPa, $297 < T < 1273$ K)	$E = 247 - 0.146T$
Density, ρ (kg/m ³)	7827
Poisson ratio, ν ($297 < T < 1273$ K)	$\nu = 0.341 - 3.31 \times 10^{-4}T + 3.55 \times 10^{-7}T^2$
Thermal expansion, α ($10^{-6}K^{-1}$, $297 < T < 1077$ K)	$\alpha = 10.2 + 4.79 \times 10^{-3}T$
Thermal conductivity, k (W/m·K)	43
Specific heat, C_p (J/kg·K)	458

Table 5.3. Constitutive model parameters of phases for AISI 52100 steel.

Phase	A_{JC} (MPa)	B_{JC} (MPa)	n_{JC}	C_{JC}	m_{JC}	$\dot{\epsilon}_o$ (1/s)	T_m (K)
<i>TM</i> [182]	2482.4	1498.5	0.19	0.027	0.66	1	1697
Phase	m	$\dot{\epsilon}_o$ (1/s)	C_1	C_2	C_3	C_4	C_5
γ [170]	0.01	5E-4	2084.2	0.31	0.58	1023.9	0.005
<i>M</i> [170]	0.01	5E-4	1180.7	17.8	7.66	1983	0.0059

5.2.2. Phase Transformation Kinetics and Metallo-thermo-mechanical Coupling

To account for the evolution of the phase composition of the workpiece material during hard turning, phase transformation kinetics was solved simultaneously with the energy equation at each time step. The initial workpiece material was defined as a fully tempered martensitic structure. The small amounts of chromium carbide and retained austenite after the heat treatment were considered to be negligible [127, 135]. Tempered martensite can further decompose to ferrite and cementite when heated slowly during a tempering process. However, heating rates are estimated as high as $\sim 10^6$ K/s in a hard turning process, which shall prevent martensite from decomposing within the short period of heating cycle [36, 128]. Instead, diffusionless reverse martensitic transformation may occur if the local workpiece temperature during cutting rises above the austenite-start temperature (A_s), and the initial tempered martensite transforms to austenite. A_s was determined to be 840 °C from a heating Time-Temperature-Transformation (TTT) diagram for AISI 52100 steel [183]. During the heating cycle,

no carbide dissolution needs to be modeled since the initial tempered martensite structure is quite homogeneous with a high carbon concentration [36].

Martensite formation may be better described with the help of cooling TTT diagrams for AISI 52100 steel as shown in Figure 5.1. As the workpiece begins to cool, austenite transforms to martensite if the cooling rate is fast enough or to bainite if the cooling rate is slower. In order to determine if bainite formation will occur, the current cooling time of a material undergoing non-isothermal transformation is compared with the amount of time required to begin bainite formation in an isothermal process. Sheil's Additivity Rule discretizes the process over a number of time steps, allowing for non-isothermal calculations [121]. If the integral in Eq. 4.5 reaches a value of 1 before the temperature drops below the martensite formation temperature (M_s), bainite will begin to form [157]. Under the parameters used in this study, bainite is not formed because the cooling rate is sufficiently fast, thereby avoiding formation of bainite. Once the temperature has dropped below the martensite formation temperature, Eq. 4.6 is used to calculate the volume fraction of martensite in the cooling process [159]. If the cooling rate is sufficiently fast, i.e., no bainite is formed, all austenite that does not change into martensite will be considered as retained austenite. M_s was estimated to be 200 °C in this study, which is an average value in literature [127, 183]. The change of microhardness due to dynamic phase transformation (Δh_{DPT}) can be calculated according to the phase fractions of that element by

$$\Delta h_{DPT} = \sum_{i=1}^v f_i h_i - h_o \quad (5.1)$$

where f_i is the fraction of phase i in the element, h_o is the initial bulk microhardness, h_i is the hardness of phase i , and v represents the number of phases present in the element. In this study, microhardness of 62 HRC (≈ 7.316 GPa), 64 HRC (≈ 7.946 GPa) and 17 HRC (≈ 2.256 GPa) were adopted from [135] for AISI 52100 phases of tempered martensite, untempered martensite and retained austenite, respectively.

The total strain increment for a steel undergoing solid-state phase transformation is updated by summing the individual components of the strain as discussed in Section 4.3. The elastic strain increment $\Delta \varepsilon^E$ is calculated using the isotropic Hook's law with temperature-dependent Young's modulus and Poisson's ratio as given in Table 5.2. The rate-independent constitutive models are used for the plastic strain increment of $\Delta \varepsilon^P$. The thermal strain

increment $\Delta\varepsilon^T$ is computed using the coefficient of thermal expansion. The strain increment due to this volumetric dilatation is given by Eq. 4.10. The percent volume change from austenite to martensite ($\Delta V/V_{V-M}$) was determined to be 1.026% [121]. The formation of martensite induces transformation plasticity, which is also produced when dilatational strains interact with the already-existing stress field [121, 159]. A reduction of 30 MPa in flow stress was used to represent the mechanical effect of transformation plasticity via the formation of martensite.

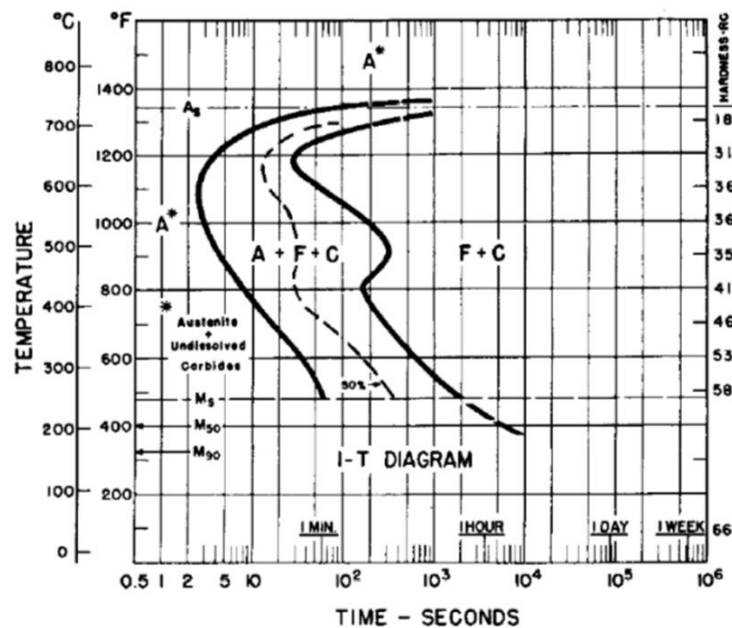


Figure 5.1. Time-Temperature-Transformation cooling diagram for AISI 52100 steel [183].

5.2.3. Grain Refinement and Dislocation Density Evolution

Li et al. [132] investigated hard drilling of bearing steel SUJ2 (with a tempered martensite structure very similar to AISI 52100 steel), and reported that high density of dislocations and refined equiaxed nanocrystalline grain structures were observed in the topmost layers using SEM and TEM. Since the essential characteristics of the deformation field and grain refinement mechanism during cutting were well captured, this dislocation density-based modeling approach developed in Chapter 3 was used in this analysis to model grain refinement due to SPD in hard turning. The material coefficient K in Eq. 3.6 was adopted to be 10 based on an experimental study of dislocation cell structure of the steel workpiece processed by equal

channel angular pressing (ECAP) [105]. The strengthening of material microhardness (Δh_{SPD}) depends on the dislocation density due to SPD, which is given as

$$\Delta h_{SPD} = k_h M_t \alpha_o G b \sqrt{\rho_{tot}} \quad (5.2)$$

where k_h is a constant slope of 0.5 obtained from [184, 185] and α_o is a constant of 0.25 obtained from [105]. The other model parameters as shown in Table 5.4 were determined to reproduce the observed material constitutive behaviors of hardened AISI 52100 steel under various strains, strain rates and temperatures using an approach presented in [105, 186, 187]. In this modeling approach, the numerically calculated cell size d achieved at a large strain is identified as the grain size and can be compared with the experimentally determined grain sizes, using the same assumption applied to steel processed by ECAP in [105].

Table 5.4. Dislocation density-model constants.

α^*	β^*	k_o	n	$\dot{\gamma}_o$	f_o	f_∞	K	M_t	$\tilde{\gamma}'$	G (GPa)	b (mm)	α
0.22	0.08	8.0	50	1E5	0.29	0.16	10	3.06	2.5	80	2.48E-7	0.25

5.2.4. Numerical Solution

3D hard turning was simulated using AdvantEdge FEM, a commercial software specialized for 3D machining simulations, using the user defined subroutines to implement the transformation kinetics grain refinement mechanisms. Figure 5.2 shows the simulation setup of hard turning in AdvantEdge FEM. AdvantEdge FEM uses a fully-automatic adaptive remeshing algorithm of finite element mesh in the workpiece domain to simulate chip formation without using any chip separation criterion [188]. The inserts were modeled using the custom tool editor in AdvantEdge FEM for representing different tool geometries and wear land widths. The thermo-mechanical properties of tool material KD050 was obtained from [127], while the properties of K090 insert were adopted from the default properties of Alumina70-TiC30 tool provided in AdvantEdge FEM software [188]. The applied frictional coefficient at the tool-chip interface was 0.7, which was adopted from a study of frictional behavior in steel cutting [178]. The nose turning configuration as shown in Figure 5.2 (a) in AdvantEdge FEM is suitable for

simulating 3D turning with a large tool nose radius, and hence it was selected for hard turning simulations in this study. Since an option of multiple cuts was not available for the current software version, one cutting pass was simulated in the standard mode with a residual stress analysis option. Constrained by the computation cost, the minimum element size of the workpiece was limited to about 5 μm . When the cutting simulation step is finished, both the chip and tool are removed and the workpiece is allowed to thermo-mechanically relax. Within the relaxation step, the heat is dissipated, the stress fluctuations die out, and then a state of stress in the workpiece is shown. Figure 5.2 (b) shows a steady-state chip formation with a temperature contour in the cutting step, while Figure 5.2 (c) shows the machined surface of a uniform temperature distribution in the relaxation step for simulating residual stresses.

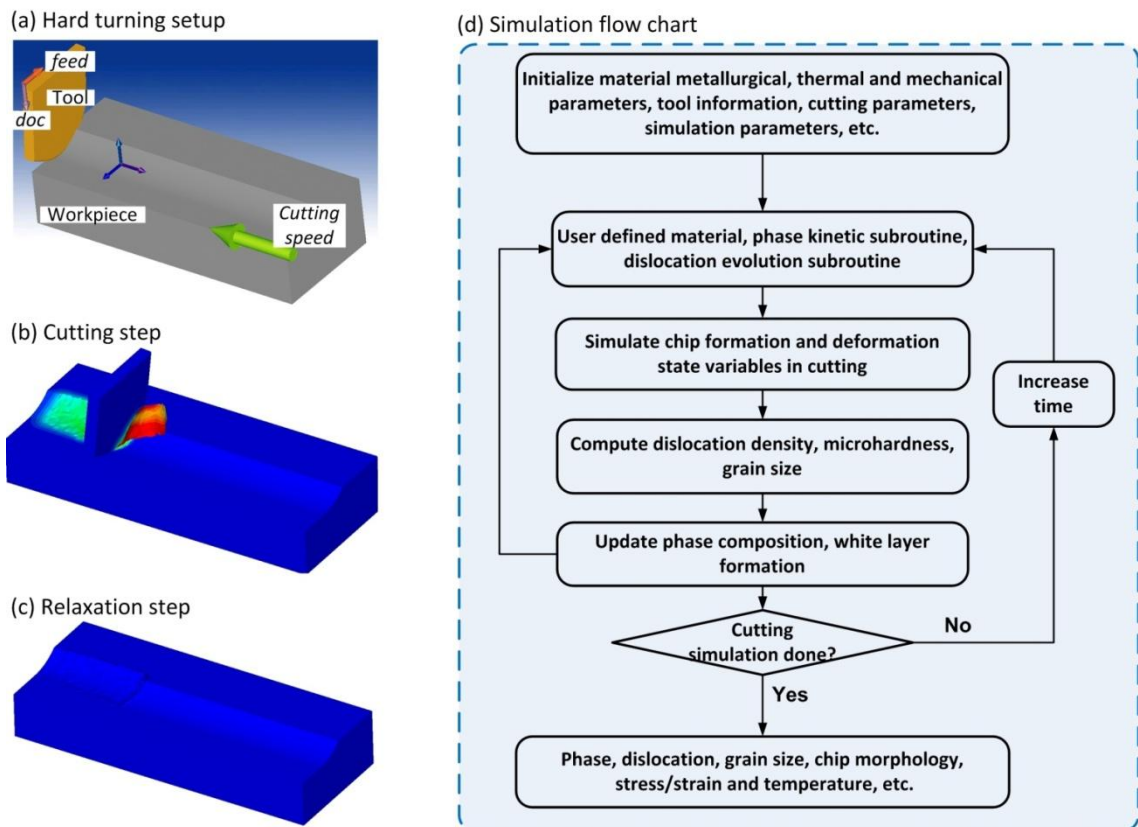


Figure 5.2. Hard turning simulation via AdvantEdge FEM.

A user-defined material model was developed for AISI 52100 steel in FORTRAN as required by AdvantEdge FEM, which consisted of both phase transformation kinetics and dislocation density-based grain refinement subroutines. The computation flowchart as shown in Figure 5.2 (d) illustrates the implementation of the user-defined material model in AdvantEdge FEM. During the simulation, the material subroutines were constantly called at material points within the workpiece domain to update the deformation and user-defined metallurgical fields. The temperature-dependent thermal properties were used to update the cutting temperatures. The constitutive plasticity models were implemented to update the material flow stresses and simulate chip formation using the feedback of the metallurgical field. The evolution of phase constituents was simulated using the kinetics model using the inputs of the thermal and mechanical field variables. The fraction of each phase constituent was used to calculate the phase-dependent volumetric dilatation strain, and to account for the effect of transformation-induced plasticity strain. Using the inputs from the deformation field, the dislocation density-based grain refinement subroutine was used to simulate the evolutions of dislocation density and grain size in the workpiece domain. The microhardness was updated using Eqs. 5.1 and 5.2.

5.3. Results and Discussions

To assess the validity of the material models, hard turning conditions B1-B3 were simulated via AdvantEdge FEM to compare the predicted cutting force with the experimental results presented in [36]. Figure 5.3 compares the predicted tangential cutting force (F_c) in the workpiece rotation direction and the thrust cutting force (F_t) in the radial direction with the experimental data obtained in hard turning tests B1-B3. The force predictions match well with the experimental data for various tool wear amounts with the prediction errors within 17% and 23% for F_c and F_t , respectively. It is evident that the coupled metallo-thermo-mechanical analysis simulations accurately predict the effect of tool wear on the cutting force, particularly the rapid increase of the thrust component with the increase of tool wear.

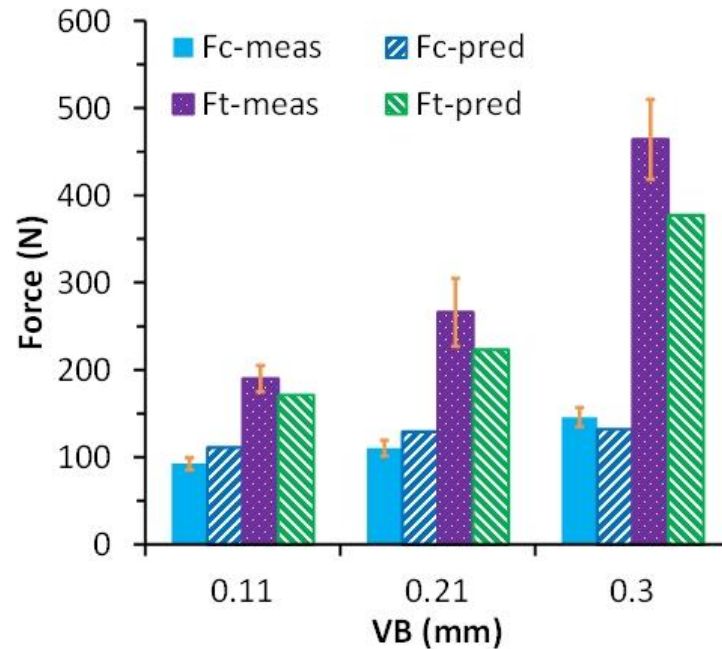


Figure 5.3. Simulation results of cutting force for Tests B1-B3.

The steady-state solution of hard turning is presented in terms of temperature, equivalent plastic strain, phase composition, total dislocation density and grain size in the workpiece and chip for tests A1 and A2 with different cutting speeds, as shown in Figure 5.4. It can be seen in Figure 5.4 (a) that a cutting speed of 91.4 m/min produces an average temperature of about 800 °C in the material near the tool cutting edge, while Figure 5.4 (b) shows the temperature to be around 1000 °C for a higher cutting speed of 274.3 m/min. The predicted phase compositions during steady-state cutting are illustrated in Figure 5.4 (c) and (d) for the two cutting speeds. It can be seen in Figure 5.4 (c) that no phase transformation was predicted on the machined surface, but only a portion of the chip material was austenitized at a cutting speed of 91.4 m/min. In comparison, a major portion of the machined surface and chip were predicted to be austenitized at a higher cutting speed of 274.3 m/min. Also, as the material temperature cooled down below M_s , martensitic transformation occurred with untempered martensite forming on the machined surface as can be seen in Figure 5.4 (d). Although similar levels of plastic strain were induced on the machined surface for tests A1 and A2, a higher cutting speed and hence a higher material temperature for test A2 produced a lower total dislocation density in the chip and machined surface than test A1, as can be seen in

Figure 5.4 (e) and (f). Figure 5.4 (g) and (h) show the predictions of the grain size distributions for the two tests. It can be seen that grain size was greatly reduced to around 100 nm not only in the chip but also near the machined surface for test A1. A larger grain size of about 200 nm was predicted on the machined surface for test A2.

Figure 5.5 shows the experimental results of tests A1 and A2 using an optical microscope and bright-field transmission electron microscopy (TEM) to observe the refined microstructure within the near-surface layers. Although it was not possible to reliably determine the grain size in the TEM images, it is evident that the topmost surface layers produced at the two cutting speeds possess a highly refined microstructure with a grain size of less than 200 nm. For both tests, steep gradients were predicted for grain size changes from a few hundred nanometers to several microns in the near-surface layer, which was also experimentally observed as shown in Figure 5.5 (b) and (d). The model predicted that for a cutting speed of 91.4 m/min in test A1, the microstructure within the near-surface layer of 7.5 micron thickness was mechanically refined to a structure with a grain size less than a micron, which is close to the experimental value of 4~8 μm for the white layer as shown in Figure 5.5 (a). For a cutting speed of 274.3 m/min in test A2, a topmost surface layer of 5 micron thickness was predicted to be mechanically refined to a submicron microstructure, while a deeper surface layer of 10 μm was predicted to be transformed to martensitic phase. The predicted layer thickness of 10 μm for phase transformation matched well with the measured value of 10~15 μm for the white layer formed in test A2 as can be seen in Figure 5.5 (c).

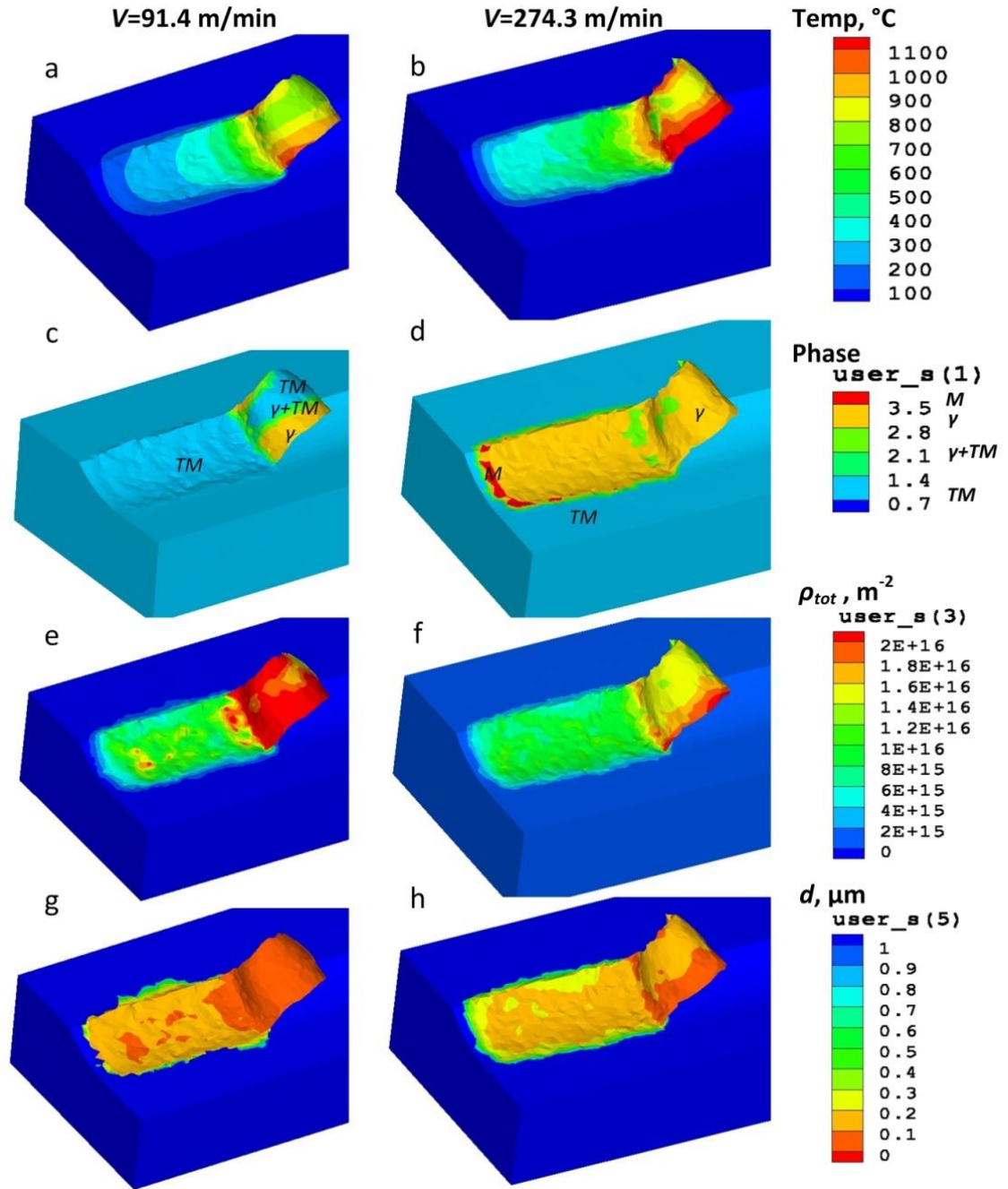


Figure 5.4. Simulation results of surface microstructure for tests A1 and A2.

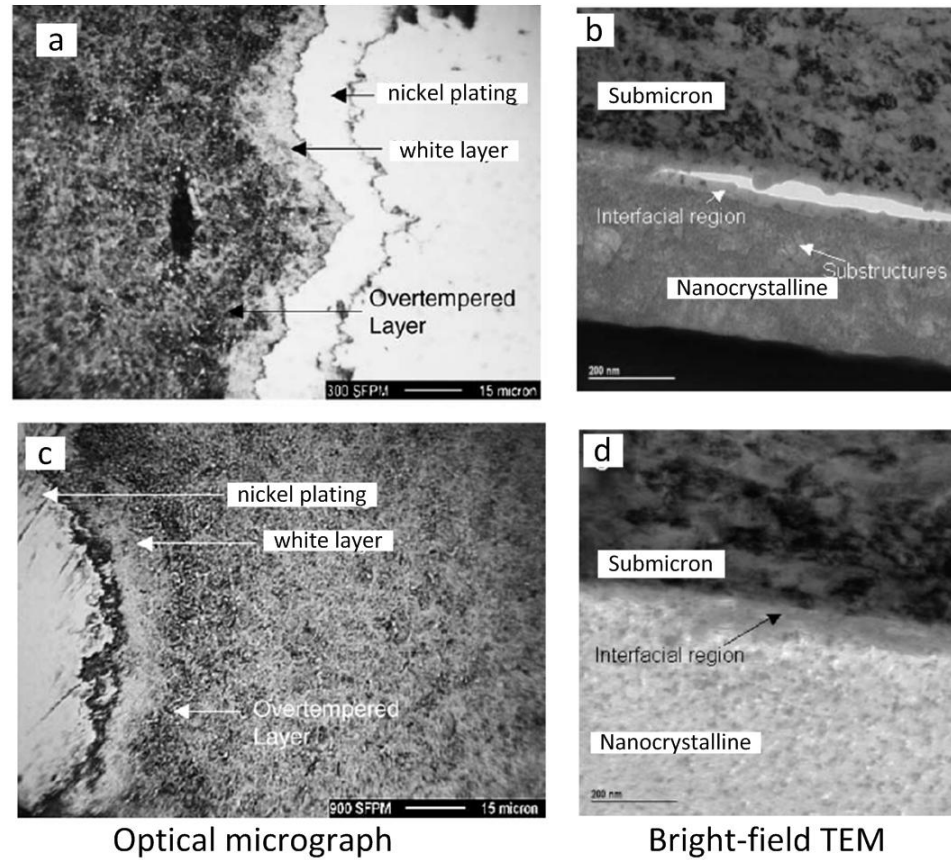


Figure 5.5. Refined surface microstructures (a, b) Test A1, (c, d) Test A2. (Adapted from [134]).

To quantitatively analyze the surface microstructural alteration induced by hard turning, it is necessary to investigate the mechanical property differences between the surface layer and the unaffected bulk material. For microhardness, the multi-physics model proposed in this study considers the surface hardening due to both the thermally driven phase transformation and severe plastic deformation. As a result, the predicted microhardness h is a sum of the initial bulk microhardness h_o , microhardness increase by phase transformation Δh_{DPT} and severe plastic deformation Δh_{SPD} . Multiple nano-indentation tests were performed to determine the microhardness of the surface layer for the samples of tests A1 and A2 by Ramesh et al. [134]. Figure 5.6 shows the surface microhardness distributions predicted for tests 4 and 5 in comparison with the measurement data. An initial microhardness h_o of 7.316 GPa, equivalent to 62 HRC, was assumed for the bulk material in the model. The predicted surface microhardness was obtained by averaging within the selected area of the machined surface as shown in Figure

5.6. For test A1, an increase of surface hardness was attributed to the drastic increase of dislocation density due to SPD, while for test A2, the increase of surface hardness consisted of hardening by phase change and SPD. For test A1, a hardness increase of 0.83 GPa was determined by Eq. 5.2. For test A2, the hardness increase of 1.43 GPa predicted by the model was a sum of strain hardening of 0.8 GPa given by Eq. 5.2 and martensitic phase hardening of 0.63 GPa determined by Eq. 5.1. A good agreement exists between the model predictions and the measurements for both tests A1 and A2.

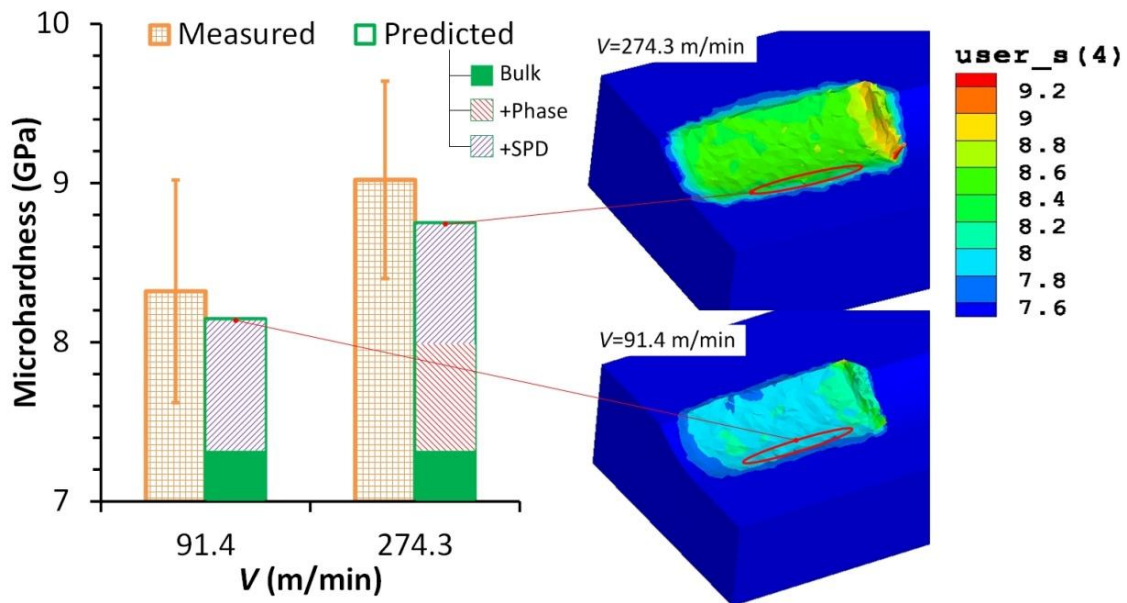


Figure 5.6. Simulation results of surface microhardness for tests A1 and A2.

The residual stress of the machined surface was also investigated using the metal-thermo-mechanical coupling analysis. The X-ray diffraction (XRD) measurement was conducted in detail in [134] to determine the residual stresses. The residual stress volume averaging feature was used in AdvantEdge FEM to predict the residual stress subsurface profile, in which stresses over an area were averaged as a function of depth into the workpiece surface [188]. Figure 5.7 (a) and (b) show the residual stress profiles, which were predicted from the locations circled in Figure 5.6, in the workpiece rotation direction (hoop) and tool feed direction (axial), respectively. Compressive surface residual stresses of about -400 MPa and -200 MPa were predicted for test A1 at a cutting speed of 91.4 m/min in the hoop and axial directions,

respectively, while tensile residual stresses of about 350 MPa and 300 MPa were predicted for test A2 at a cutting speed of 274.3 m/min in the hoop and axial directions, respectively. It can be seen in Figure 5.7 that the simulated residual stresses are similar to the experimental data in terms of the hook-shape profile and magnitude within a 70 μm depth below the surface. The discrepancy of residual stresses between the model prediction and measurement shown in the deeper regions could be caused by the preexisting stresses in the bulk material after the heat treatment. Overall, reasonable predictions of residual stresses were obtained for hard turning at both low and high cutting speeds, which further validated the efficacy of the numerical model.

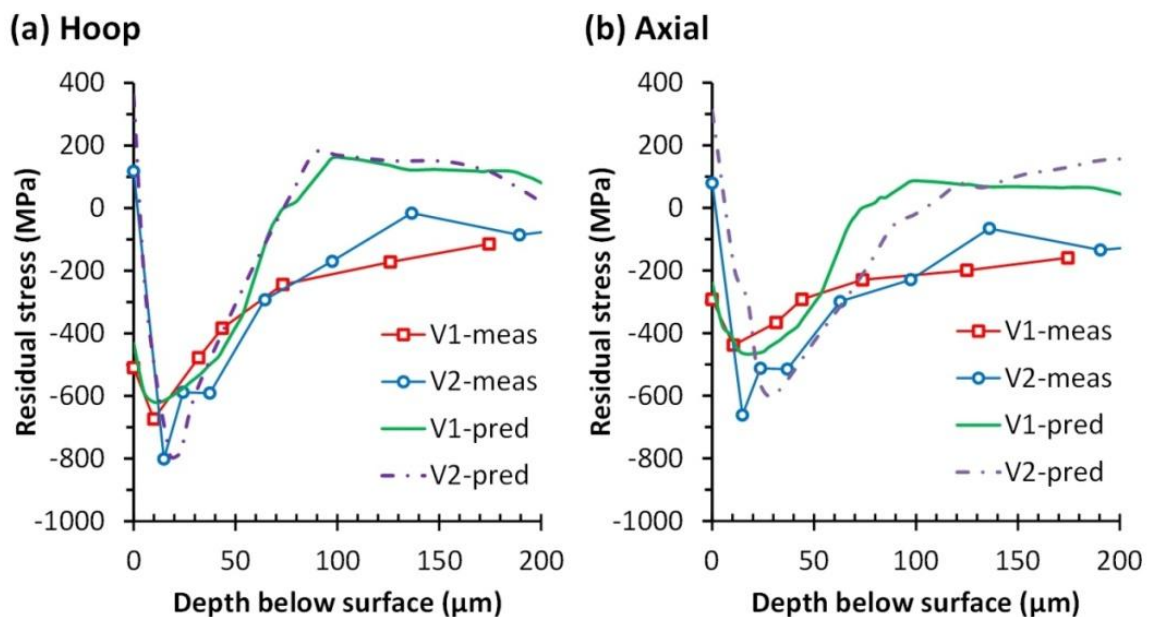


Figure 5.7. Simulation results of subsurface residual stress profile for tests A1 and A2.

The effects of cutting speed and tool condition on the resultant surface microstructure were further evaluated through numerical simulations of tests B1-B5. The white layer formation in tests B1-B3 and tests B4-B5 was simulated to be dominated by phase transformation and grain refinement, respectively. The predictions of white layer thickness are compared with the measured values as shown in Figure 5.8. The model predictions of tests B1-B3 show that the transformed martensitic layer thickness increases from 5 to 15 μm as the tool wear land width

increases from 0.11 to 0.3 mm at a constant cutting speed of 180 m/min, which are in good agreement with the experimentally measured thicknesses of 4.2 to 11.7 μm . For tests B3-B5 with a constant tool wear land width of 0.3 mm, the white layer thickness predicted by either thermally driven phase transformation or SPD increases drastically as the cutting speed increased from 45 to 180 m/min, which also matched well with the experimental data. The effect of cutting speed and tool wear on white layer formation predicted in this study is in line with many experimental studies in literature [39, 189, 190]. A refined layer with the same thickness of 7.5 μm was predicted for both test B4 with a VB of 0.3 mm and test A2 with no tool wear at a similar cutting speed (≈ 90 m/min). Because a greater feed of 0.127 mm/rev was used in test A2 than a feed of 0.05 mm/rev in test B4, a similar SPD effect was predicted to be induced on the surface layer. The effect that a greater feed produces a thicker white layer has also been experimentally demonstrated in other studies [132, 189-191].

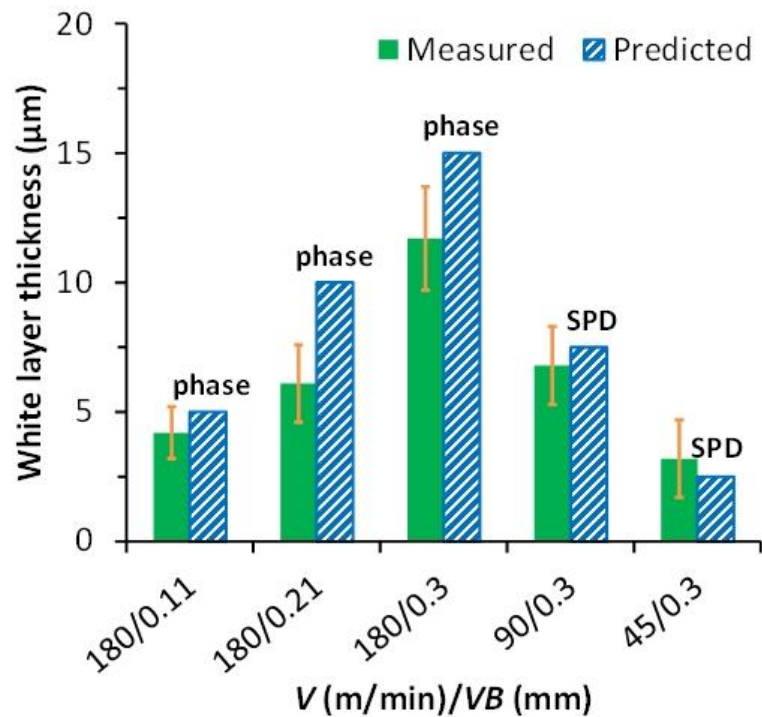


Figure 5.8. Simulation results of martensitic transformation layer thickness for tests B1-B5.

The accuracy of the model prediction was greatly affected by the minimum element size used in AdvantEdge FEM near the machined surface. In this study, an element size of about 5

μm was specified near the surface to achieve the balance of reducing the computation cost and refining the simulation result. A better result could be achieved if a finer mesh with smaller elements was used, however, the computational cost would be drastically increased. Nonetheless, the model predictions prove that the refined microstructure produced at low-to-moderate cutting speeds are mainly caused by severe plastic deformation, whereas white layer formation at high cutting speeds is caused by both thermally driven phase transformation and grain refinement due to SPD.

5.4. Summary

This chapter presented a multi-physics model to investigate the surface microstructure alteration in hard turning of AISI 52100 steel. Both the thermally driven phase transformation and mechanical grain refinement due to severe plastic deformation were considered to model the surface microstructural change using a metallo-thermo-mechanical coupled model. The model considered the critical surface microstructural attributes such as phase composition, grain size, and microhardness, and was implemented for 3D simulations of hard turning via AdvantEdge FEM. Through a quantitative assessment using the experimental data, the 3D simulations proved that the model accurately predicted the formation of white layer due to both thermally driven phase transformation and mechanical grain refinement for different cutting conditions. It was shown that the refined microstructure produced at low-to-moderate cutting speeds were mainly caused by severe plastic deformation, whereas white layer formation at high cutting speeds was caused by both thermally driven phase transformation and grain refinement due to SPD. For the tests studied it was found that at a cutting speed of 91.4 m/min, an increase of surface hardness of 0.83 GPa was predicted to be caused by severe plastic deformation. At a cutting speed of 274.3 m/min, an increase of surface hardness of 1.43 GPa was predicted to be caused by a combination of martensitic transformation and severe plastic deformation. Predicted residual stresses were in a good agreement with the experimental data, which further validated the efficacy of the model. Therefore, the multi-physics model developed in this chapter is shown to be a more comprehensive solution for analyzing the surface microstructure alteration in hard turning.

CHAPTER 6. SURFACE INTEGRITY ANALYSIS OF LASER-ASSISTED MACHINING OF HARDENED STEEL PARTS

In this chapter, one-step LAM process is presented for finish machining the automotive transmission shafts of hardened steels to replace conventional hard turning and grinding operations. The 3D transient thermal model is applied to predict the temperature field in the hollow shaft of varying-thickness undergoing laser-assisted turning. The laser-assist effect on surface quality and subsurface integrity is investigated in terms of surface finish, size control, microhardness, microstructures and residual stresses.

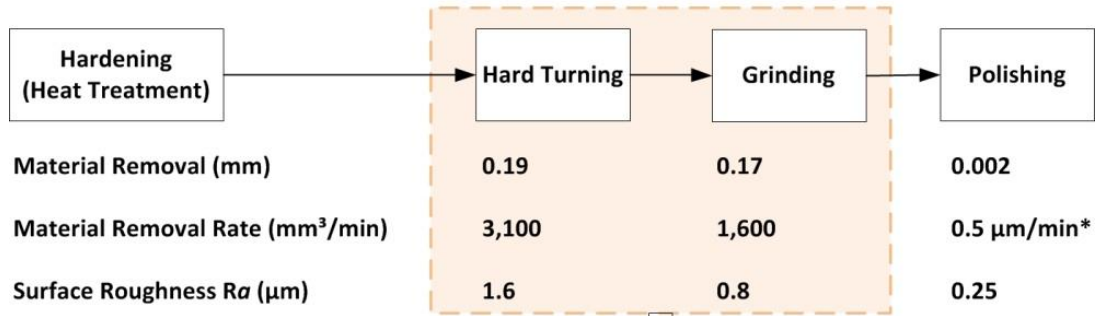
6.1. Problem Statement

Machining of hardened steel components such as gears, bearing rings, crankshafts, camshafts, etc., has traditionally relied on grinding-based technologies [48, 192]. Grinding has been proven to produce good surface quality of these high load bearing steel components. However, its low attendant material removal rate and lack of flexibility in producing complex geometry make the grinding process very expensive and inefficient [48, 49, 192-194]. In order to reduce overall machining costs and to increase the flexibility of production, this study explores the potential of laser-assisted machining as a replacement for the grinding operation. Currently, a three-step process is used to produce an automotive transmission shaft after full heat treatment: hard turning, grinding and polishing.

One-step LAM process needs to be developed to replace the hard turning and grinding operations. It will also allow for a higher material removal rate without compromising the surface integrity. Figure 6.1 shows a schematic comparison between current and proposed processes with the material removal and surface finish after each step. The materials used in this study are automotive transmission shafts of AISI 4130 steel with Rockwell hardness C (HRC) of 50. AISI 4130 is a low alloy steel containing molybdenum and chromium as strengthening agents [195]. The carbon content is nominally 0.30% and the alloy can be hardened by heat

treatment. Machinability is best with the 4130 steel in the normalized and tempered condition. Although the alloy may be machined in the fully heat treated condition, machinability becomes poorer with increasing strength (hardness) of the alloy.

Current Method in Production



Proposed Method

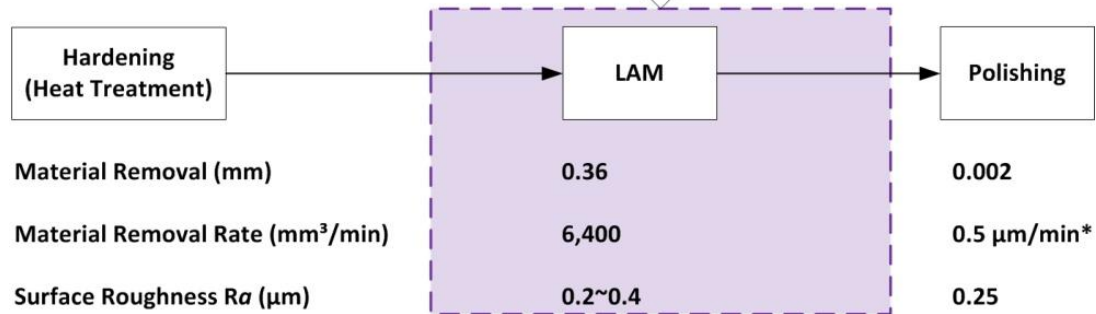


Figure 6.1. Current and proposed methods for machining a transmission shaft. *, material removal rate in radius during polishing.

6.2. Improvement of LAM Thermal Model

6.2.1. Thermal Modeling of Laser-Assisted Face Turning

The heat transfer problem associated with laser-assisted facing with one laser is schematically shown in Figure 6.2, with complex transient boundary conditions and continuous material removal as shown. The Nd:YAG laser attached on the turret travels at the same speed as the cutting tool in the radial direction during the cutting. The cylindrical coordinate system is fixed at the center of the workpiece. The material within the outside circular band (width=1 feed) is removed after one revolution. After each time-step of the simulation, one or two

control volumes in the radial direction, depending on the precision of the simulation, are removed.

The present thermal model is governed by

$$\rho \left(\frac{\partial h}{\partial t} + \omega \frac{\partial h}{\partial \varphi} \right) = \frac{1}{r} \frac{\partial}{\partial r} \left(r k \frac{\partial T}{\partial r} \right) + \frac{1}{r^2} \frac{\partial}{\partial \varphi} \left(k \frac{\partial T}{\partial \varphi} \right) + \frac{\partial}{\partial z} \left(k \frac{\partial T}{\partial z} \right) + S \quad (6.1)$$

where the first term on the left-hand side represents energy storage, and the other comes from circumferential advection due to the rotation of workpiece relative to the coordinate system. The first three terms on the right-hand side represent energy diffusion in the radial, circumferential and axial directions, respectively. The last expression is a source term for internal heat generation, which is zero for opaque materials. The present model uses uniform and relatively finer meshes in the interested zone along radial direction, and treats the laser irradiation and material removal plane physically like the machining process, i.e., moving in the radial direction in the cylindrical coordinate system.

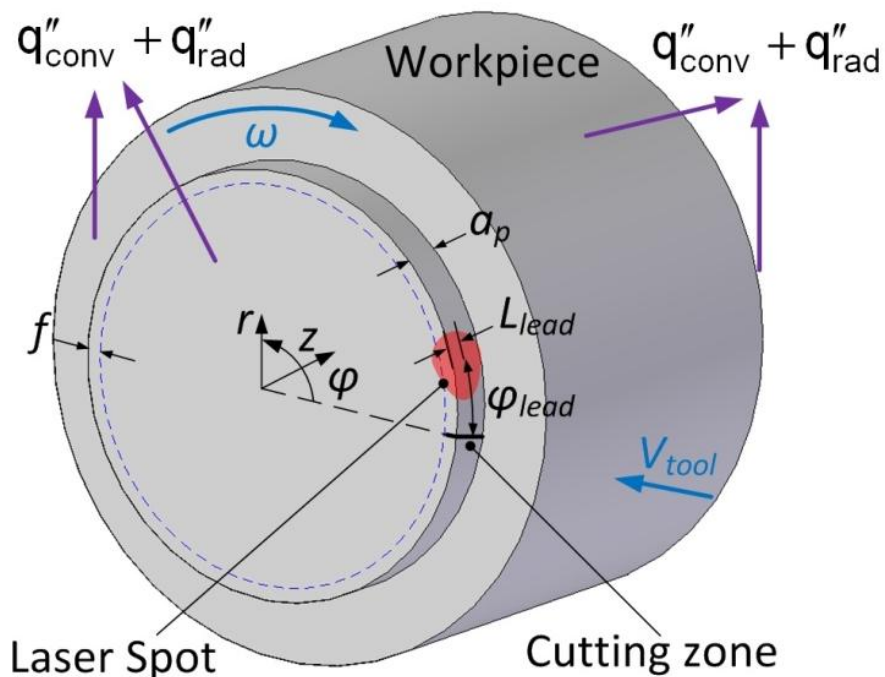


Figure 6.2. Sketch of the laser-assisted facing of a cylindrical workpiece with one laser.

Before the laser heating, the workpiece is under a thermal equilibrium with the surroundings. Within the whole domain, the initial condition of the thermal model is

$$T(\varphi, r, z, t = 0) = T_{\text{inf}}. \quad (6.2)$$

For the surface under the laser irradiation, Eq. 6.3 is used to represent the heat flux into the workpiece through laser irradiation, convection and radiation. The distribution of the laser irradiation on the workpiece, q''_{laser} , is determined by the beam profile. The radiation exchange between the workpiece and the surrounding is determined by using the instant workpiece surface temperature, ambient temperature and the emissivity of the workpiece surface.

$$k \frac{\partial T}{\partial r} \Big|_{\text{chamfer}} = \alpha q''_{\text{laser}}(\varphi, z) - q''_{\text{conv}} - q''_{\text{rad}}. \quad (6.3)$$

For the portion of the workpiece end faces outside the laser irradiation,

$$k \frac{\partial T}{\partial z} \Big|_{z=0, a_p, l_w} = -q''_{\text{conv}} - q''_{\text{rad}} \quad (6.4)$$

where a_p and l_w denote the depth of cut and the workpiece length, respectively. For the circular boundary surface outside the laser irradiation,

$$k \frac{\partial T}{\partial r} \Big|_{r=r_w, r(t)} = -q''_{\text{conv}} - q''_{\text{rad}}. \quad (6.5)$$

Symmetry conditions are assumed at the centerline of the workpiece and result in Eq. 6.6 for numerical implementation, because the rotation of the workpiece enhances the distribution of laser energy in the circumferential direction and results in negligible temperature gradients near the centerline of the workpiece.

$$\frac{\partial T}{\partial r} \Big|_{r=0} = 0. \quad (6.6)$$

Away from the material removal plane, the continuity of temperatures and temperature gradients in the circumferential direction is satisfied by

$$T(r, \varphi, z) = T(r, \varphi + 2\pi, z) \quad (6.7)$$

$$\left. \frac{\partial T}{\partial \phi} \right|_{\phi} = \left. \frac{\partial T}{\partial \phi} \right|_{\phi+2\pi} \quad (6.8)$$

To facilitate the numerical solution of the heat transfer problem in LAM, where material may experience temperatures higher than 1000 °C and the temperature dependence of material thermophysical properties has to be taken into account, Eq. 6.1 is rewritten in the form of Eq. 6.9 following the numerical scheme proposed by Murthy and Mathur [196].

$$\rho \left(\frac{\partial (c_p T)}{\partial t} + \omega \frac{\partial (c_p T)}{\partial \phi} \right) = \frac{1}{r} \frac{\partial}{\partial r} \left(r k \frac{\partial T}{\partial r} \right) + \frac{1}{r^2} \frac{\partial}{\partial \phi} \left(k \frac{\partial T}{\partial \phi} \right) + \frac{\partial}{\partial z} \left(k \frac{\partial T}{\partial z} \right) + S + \rho \frac{\partial}{\partial t} (c_p T^* - h^*) + \rho \omega \frac{\partial}{\partial \phi} (c_p T^* - h^*) \quad (6.9)$$

where T^* and h^* are the values of T and h gained from the previous iteration and used to solve for T in current iteration. When convergence is achieved, T^* and h^* are equal to T and h , respectively, and Eq. 6.9 reverts to Eq. 6.1 since the $c_p T$ terms on both sides cancel each other. All the thermal properties in the center of the control volume (CV) can be directly expressed from the calculated temperature field, while those at the CV faces need to be interpolated. For thermal conductivity k , a harmonic mean interpolation [197] is applied, which keeps the consistency of heat resistance between CVs. For c_p , a pure linear interpolation is applied. In the thermal model, the material removal process is simulated by properly setting the control volumes corresponding to the removed materials inactive, i.e., the thermal conductivity of those inactive control volumes are set to zero [14].

A finite volume thermal model is developed for the laser-assisted face turning process based on the earlier thermal models for the laser-assisted longitudinal turning process developed by the previous students in the Laser-Assisted Materials Processing Lab at Purdue University. Rozzi et al. [9, 12, 198] firstly developed a transient, 3D numerical model of a rotating workpiece undergoing laser heating and material removal. Rozzi's model is restricted to cylindrical workpieces having a uniform machined diameter along the axial direction, because the geometry of the chamfer is fixed in his Eulerian model. Pfefforkorn et al. [41] extended the model to semi-transparent materials by allowing for calculation of the internal radiation inside the workpiece. A significant enhancement in the capabilities of the thermal mode was achieved by Tian and Shin [14] by changing the thermal model from a stationary laser/moving workpiece

of Rozzi's model (Eulerian) to a fixed workpiece/moving laser (Lagrangian) and also by including adaptive geometry change to simulate laser-assisted longitudinal turning of a workpiece with varying depth of cuts. The present model further expands this model to complex profiling by adding facing capabilities to the longitudinal profiling.

The finite volume method is used to discretize the governing equations and the modeled domain is divided into predefined, structured control volumes. The meshing in the radial direction is very fine because of the continuous material removal in this direction; the meshing in the axial direction is fine within the depth of cut; the meshing in the circumferential direction is fine within the laser irradiation and the cutting zone. For example, a cylindrical part can be divided into 60 (circumferential) \times 30 (longitudinal) \times 200 (radial) with a typical control volume size of $0.19 \times 0.075 \times 0.06$ mm. The energy equation is integrated over each control volume with linear profiles expressing the temperatures between grid points. For the advection term, the upwind difference scheme (UDS) [197] is used for interpolating the temperatures at the CV faces according to the flow direction.

The motions of the laser irradiation, the machining chamfer and the material removal plane are treated as the same as those in the physical facing process, i.e., moving in the radial direction towards the center of the workpiece. The laser irradiation and material removal are considered as moving boundary conditions. In order to pass the boundary condition to the internal control volumes, the coefficients associated with the heat transfer in the radial direction and the source terms for the internal CVs at the boundary include all the information, such as laser irradiation, convection over the surface, and conduction heat exchange with the surrounding temperatures. The modeling of the laser beam in the machine chamfer is shown in Figure 6.3. For the boundary control volumes within the laser irradiation, the exposed area, the angle to the laser direction, and the distance to the center of the laser beam are calculated. For Gaussian laser intensity distribution, the laser flux is decided by the distance to the center r , laser radius r_l and laser power P_l . Simpson's rule is used for the numerical integration to calculate the laser flux q_r'' . Figure 6.4 shows a sketch of laser heat absorption by those partially deactivated boundary control volumes in the machine chamfer. According to the chamfer geometry and the meshing condition, there could be only one or multiple control volumes intercepted by the machined edge as shown as in Figure 6.3. The intercepted control volumes are partially deactivated, i.e., the volume remains in the computational domain and the

remaining area in between two neighbors is calculated according to their corresponding geometric portions. The source terms of these control volumes are specified according to their geometry. Figure 6.5 shows the heat transfer at the boundary control volumes.

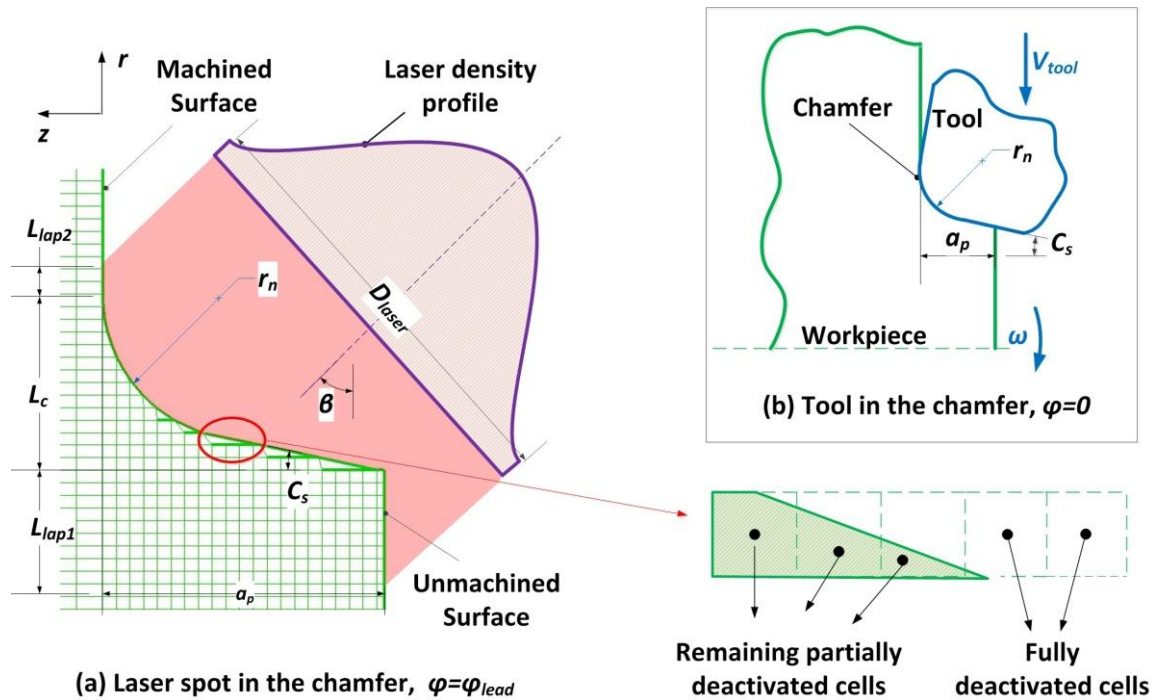


Figure 6.3. Sketch of the laser spot and machine chamfer in laser-assisted face turning.

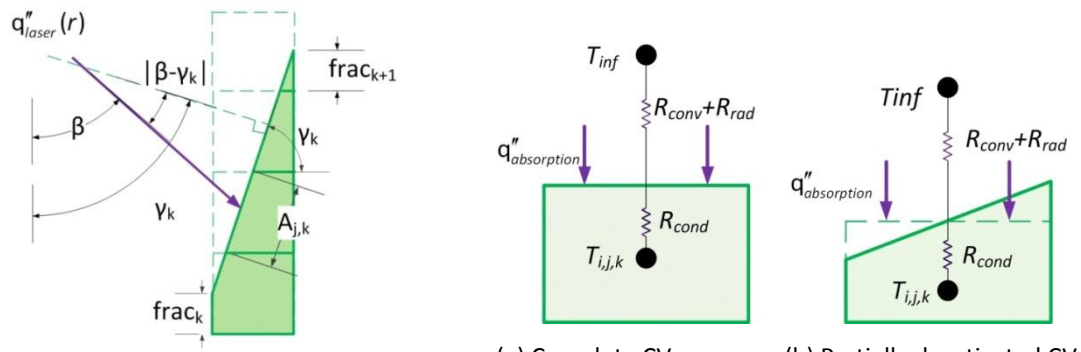


Figure 6.4. Sketch of partial deactivating control volumes and laser absorption at the boundary.

Figure 6.5. Heat transfer at the boundary control volumes.

The discretized equations are formulated in a fully implicit scheme to prevent physically unrealistic oscillations in the converged solution. The Tri-Diagonal Matrix Algorithm (TDMA) solver and the cyclic TDMA solver in the circumferential direction are used to solve the 1-dimensional discrete equation for each line of CVs, which assume the temperatures of the neighbors on sides are temporarily known. Line-by-line TDMA is used for 3D problems: it calls the TDMA for each line and sweeps across lines in all the directions (circumferential, axial and radial) over and over until convergence. Therefore, the resulting algebraic equations are solved iteratively, with one sweep per iteration through the domain in the positive and negative directions of each coordinate. After each iteration, the new temperature field is used to update the temperature dependent variables such as material conductivity and specific heat. Convergence of the solution is checked with a residual less than 10^{-6} , while the unbalanced global energy less than 10^{-6} of the laser power is achieved and the average of specific heat changes less than 10^{-5} between two successive iterations. The program flow and the subroutines of the thermal model are shown in Figure 6.6. The main program defines the material removal at each time step and calculates the laser parameters at various geometric features, such as the boundary control volumes of the laser irradiation, the laser tilted angle to the control volume surface, the distance of the control volume to the center of the laser beam, the exposed area and volume of the control volume. Figure 6.7 shows a preliminary simulation of laser-assisted face turning of a Waspaloy workpiece.

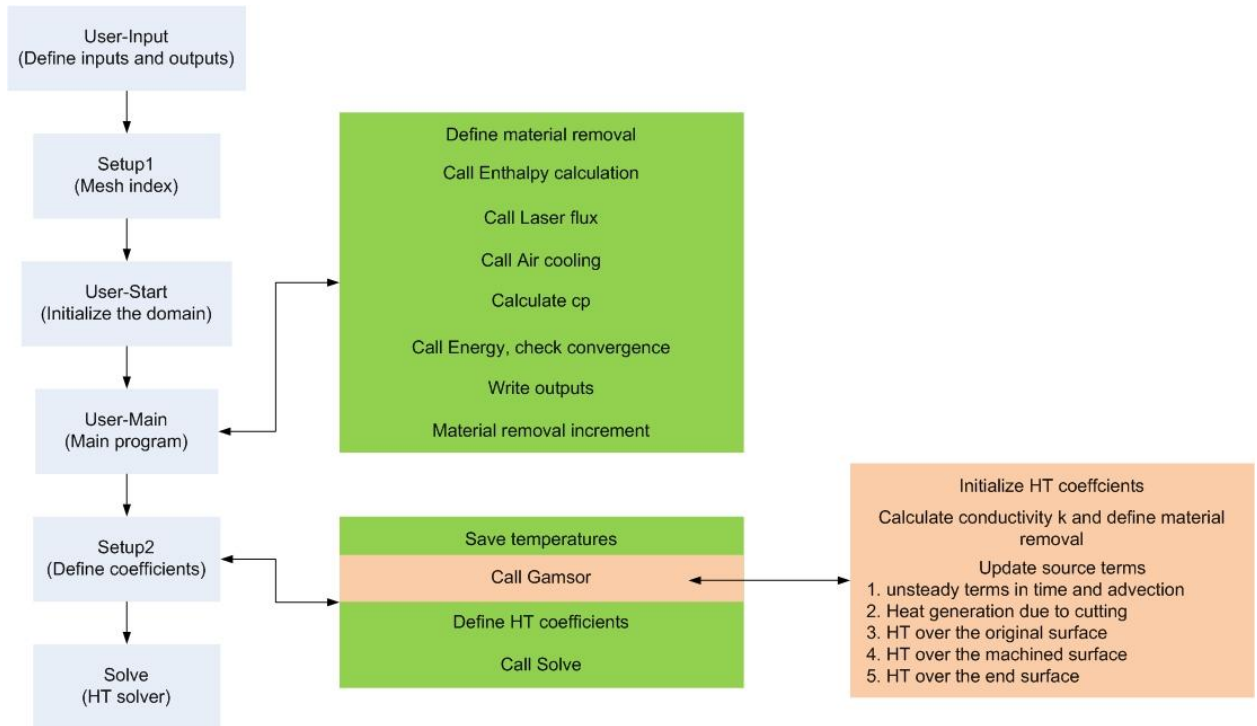


Figure 6.6. Program flow in the LAM thermal model.

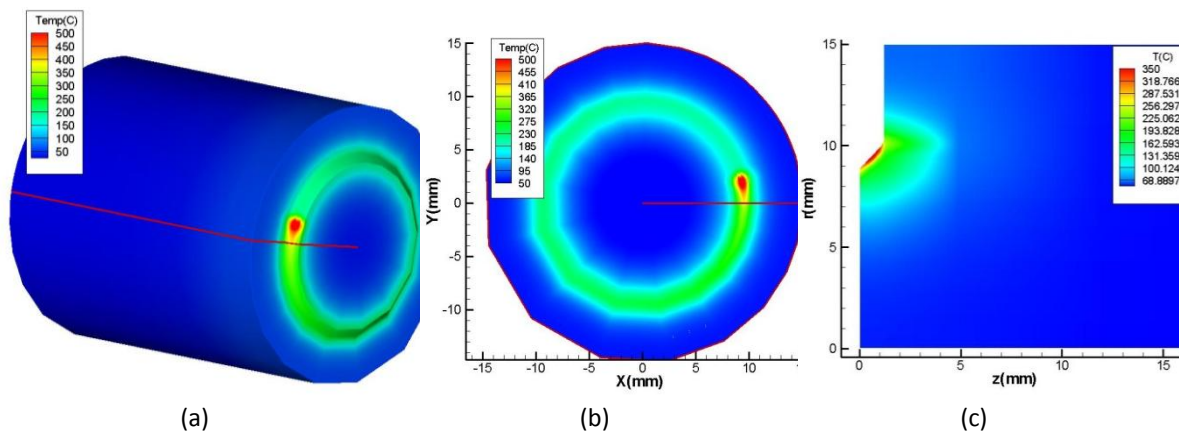


Figure 6.7. Simulation result of laser-assisted face turning. (a) 3D temperature distribution (b) 2D temperature projection onto φ - z plane (c) 2D temperature distribution in r - z plane.

6.2.2. Thermal Modeling of Laser-Assisted Profile Turning

The laser-assisted profile turning process is applied to cylindrical parts with complex geometry features, which require straight longitudinal turning, face turning, taper turning, convex and concave circular arcs, etc. The workpiece has to be properly heated during the different phases of a laser-assisted profile turning operation to achieve a constant T_{mr} and to

ensure a consistent good cutting condition for superior surface finish and long tool life. A representative case is analyzed to demonstrate the application of the methodology, as shown in Figure 6.8 (a). In order to comprehensively study the effects of profile geometry on laser-assist performance, this sample workpiece has concave turning, face turning and straight line turning with zero and 15° slope angles and it is divided by five segments according to the geometric shapes as shown in Figure 6.8 (b). Although contour geometry dealt with in a profile machining process varies greatly from part to part, a continuous profile of complex features usually can be curve-fitted into piecewise parameterized splines, Bezier or NURB (non-uniform rational B-spline) curves. As a matter of fact, the laser-assisted profile turning process essentially consists of two kinds of operations: outside diameter (OD) turning of complex feature with the tool feeding in the longitudinal direction and face turning with the tool moving in the radial direction. Hence, the thermal model of the laser-assisted profiling process basically is a combination of thermal models of both laser-assisted OD turning and face turning.

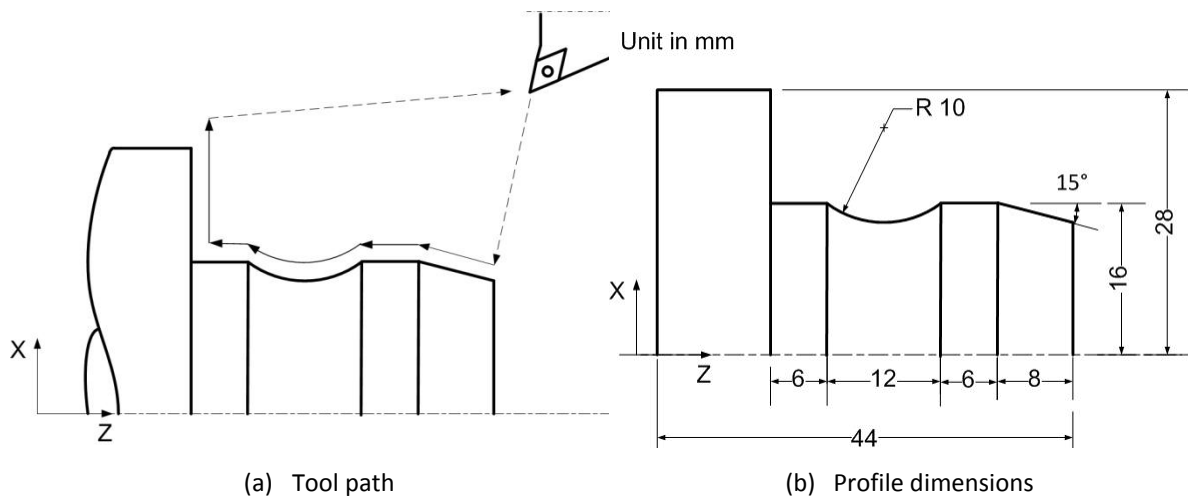


Figure 6.8. A representative case study of laser-assisted profile turning.

During the laser-assisted profile turning process, a single cutting pass is designed and no tool change is required, which removes a small depth of material and keeps the complex geometric features of the part the same (but smaller) as those prior to cutting. One laser is assumed to be in use ahead of the cutting tool, and moves at the same feed rate as the machine tool. The laser beam size is assumed to be constant and the laser lead distance in both circumferential ($^\circ$) and longitudinal directions (mm) are fixed to the tool position. The actual

setup of the lasers during the profiling process needs to be designed for every particular part such that the laser locally heats the workpiece material ahead of the cutting tool without any potential motion conflicts. This usually requires a flexible control of the laser optical path as well as the laser power. For instance, the tool path change from OD turning to facing as shown in Figure 6.8 requires that the laser agilely and automatically change the direction and readjust the focus distance if necessary. For the case study in this report, constant cutting speed, feed rate and depth of cut are applied. The spindle speed varies along with different diameters during different stages and the maximum cutting speed to be applied at a small workpiece diameter will be limited by the spindle. Obviously, the main applications of laser-assisted profile turning are finishing processes; hence its acceptance depends on a high form and size accuracy, high surface finish and good surface integrity of the workpiece. Machining conditions differ from those for conventional laser-assisted turning. The low depth of cut, small feed rate and the large cutting edge radius are typical finishing conditions in hard turning. The machine chamfer is modeled based on the tool geometry and the depth of cut, as can be seen in Figure 6.9.

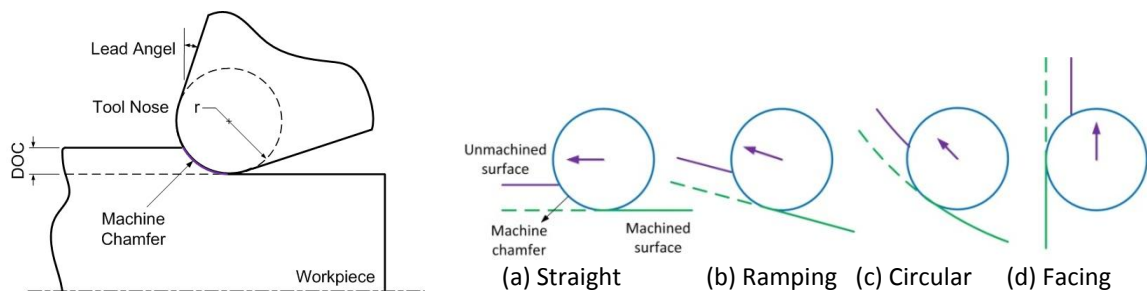


Figure 6.9. The machine chamfer in different stages.

Figure 6.10 (a) shows the structured mesh generated by the thermal model. A finer mesh was generated along the profile of the part. The part geometry prior to cutting is designated by deactivating the control volumes in the empty space by setting the thermal conductivity to zero as shown in Figure 6.10 (b). The 3D finite volume numerical model developed in FORTRAN for laser-assisted face turning has been expanded and integrated with the laser-assisted turning to develop the laser-assisted profile turning model. Similarly, the laser irradiation has been modeled as a moving heat source term as in the actual physical scenario,

which is updated in real time during the simulation. The material removal is modeled by partially deactivating the control volumes along the tool path. The numerical program flow and structure of the subroutines in the thermal model resemble those in the facing model as shown in Figure 6.6. Figure 6.11 and Figure 6.12 show the temperature simulations of a Waspaloy workpiece in OD turning and face turning stages in 2D and 3D views, respectively, which show good continuity of the temperature prediction in turning and the following facing. The model accuracy has yet to be validated by temperature measurement during a laser-assisted profile turning process, which will be conducted after the prelim exam.

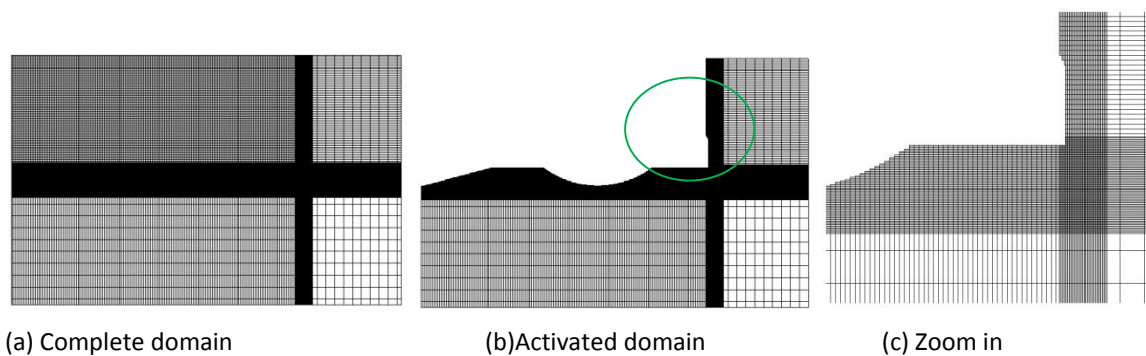


Figure 6.10. Mesh generation in laser-assisted profile turning.

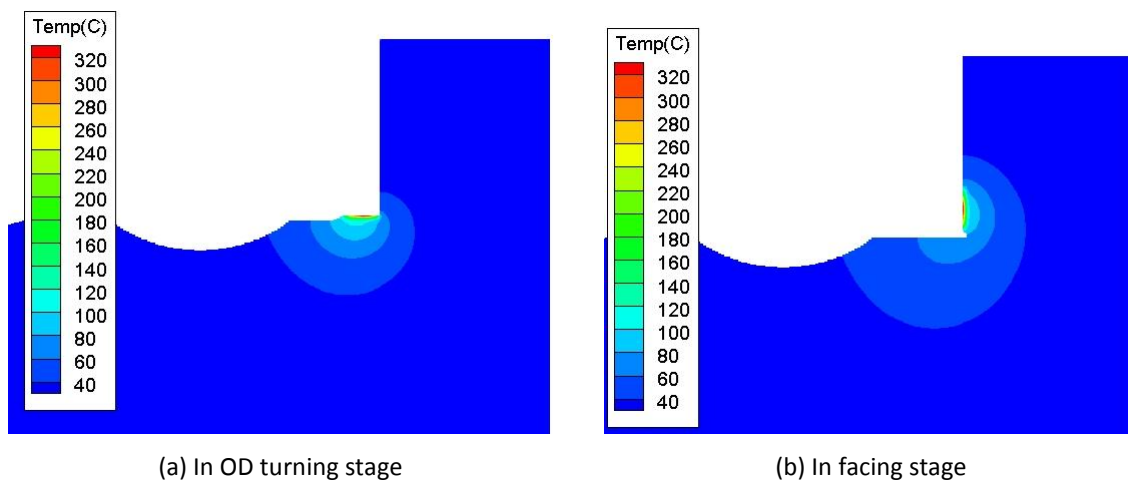
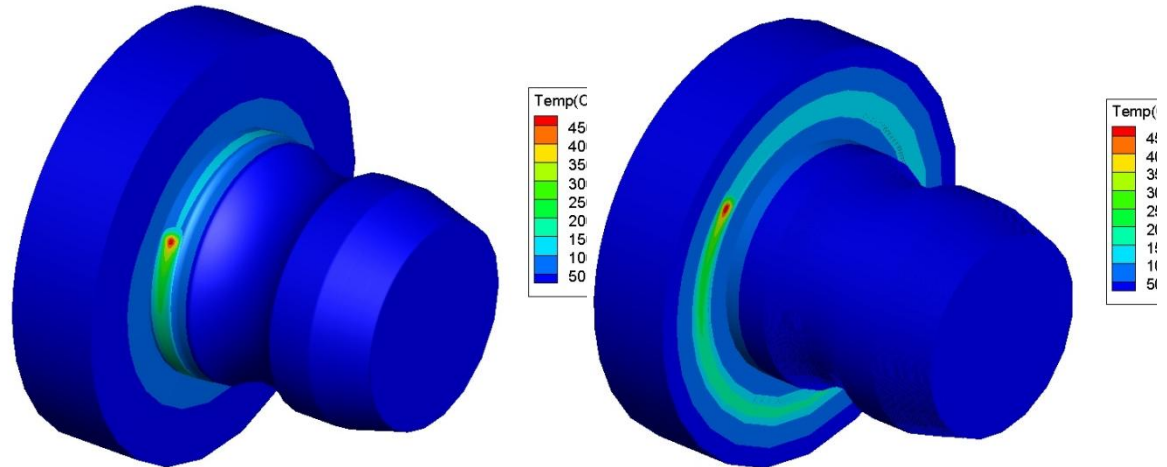


Figure 6.11. 2D temperature simulations at the tool position in laser-assisted profile turning.



(a) In OD turning stage
 (b) In facing stage
 Figure 6.12. 3D temperature simulations in laser-assisted profile turning.

6.3. LAM Process and Modeling

6.3.1. Experimental Setup

Laser-assisted turning experiments were performed on a 20 hp Jones and Lambson CNC lathe. Due to the power limitation, two lasers, a CO₂ and a Nd:YAG laser, have been integrated with the cutting tool and irradiate the workpiece continuously ahead of the tool, which are shown in Figure 6.13. The 1 kW Nd:Yag laser of wavelength of 1.06 μm irradiates the workpiece surface 16° circumferentially ahead of the cutting tool, and its beam is delivered by a fiber optic cable through a lens to a spot size of 3.0 mm. The 1.5 kW CO₂ laser of wavelength of 10.6 μm is positioned 55° ahead of the cutting tool irradiating the workpiece surface to provide requisite preheating. A detailed description of the two-laser LAM experimental setup can be found in the work of Anderson et al. [6]. The PCBN insert (grade BNC 200, made by Sumitomo) used in the OD turning experiments has a tool nose radius of 1.19 mm, side rake angle of -5° and back rake angle of 0°. The workpiece used in the experiments are hollow shafts of heat treated AISI 4130 steel with Rockwell hardness C of 50. Figure 6.14 shows the geometry of a hollow shaft of varying-thickness. It should be noted that the present two-laser LAM setup is not ideal for large parts of hardened steel because of the laser power constraints and the low absorptivity of steel to the long wavelength CO₂ laser. Prior to each LAM test, the workpiece surface was sandblasted and painted with the Cotronics 931 graphite adhesive powder/binder mixture to increase the absorption of the laser energy. In an actual manufacturing practice, however, the

workpiece surface coating can be eliminated with the use of a higher power fiber or Nd:YAG laser at a short wavelength of about 1 μm .

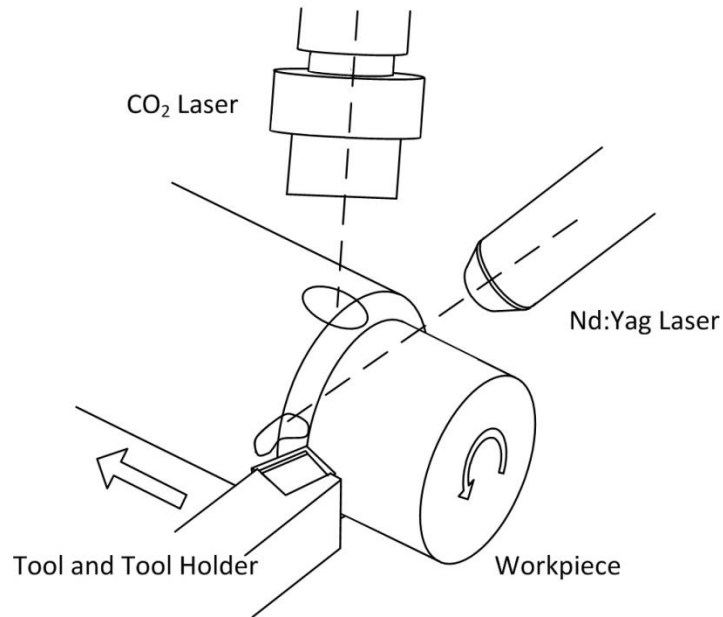


Figure 6.13. LAM experimental setup with both the CO₂ and Nd:YAG laser.

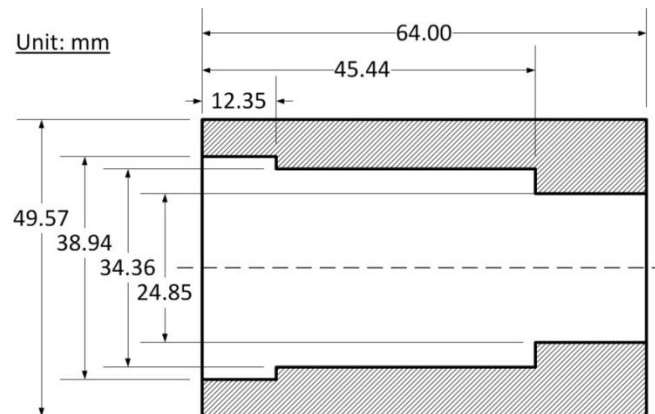


Figure 6.14. Geometry of the hollow shaft of varying-thickness.

The force data was collected using a three component Kistler 9121 dynamometer during LAM. Temperature measurement was performed using a FLIR SC3000 infrared camera with the ThermoCAM2002 software. The tool wear and microstructures were examined with a Zeiss

optical microscope and a JEOL T330 scanning electron microscope. The surface roughness was measured using a Surtronic 3+ surface profilometer. Arithmetic average surface roughness R_a was recorded at 9 locations along the axial and circumferential directions for each part after LAM. Surface hardness and subsurface microhardness were measured using a Mitutoyo ATK-F1000 hardness tester and a Vickers hardness tester respectively. Residual stress measurements were conducted by X-ray diffraction with Siemens diffractometer D500 and data analysis was done using an x-ray line profile fitting program XFIT.

One-step LAM process was developed for finish machining of the automotive transmission shaft of varying-thickness to replace hard turning and grinding operations. Determination of the temperature field in such an irregular-shaped part is necessary because the LAM parameters can be optimized only when the part is heated properly. Figure 6.15 shows the geometric configurations of the CO₂ and the Nd:YAG lasers to the machined chamfer during LAM. To avoid direct heating of the machined surface, the longitudinal laser-tool lead distance is set to 1.2 mm for the CO₂ laser and 0.9 mm for the Nd:YAG laser.

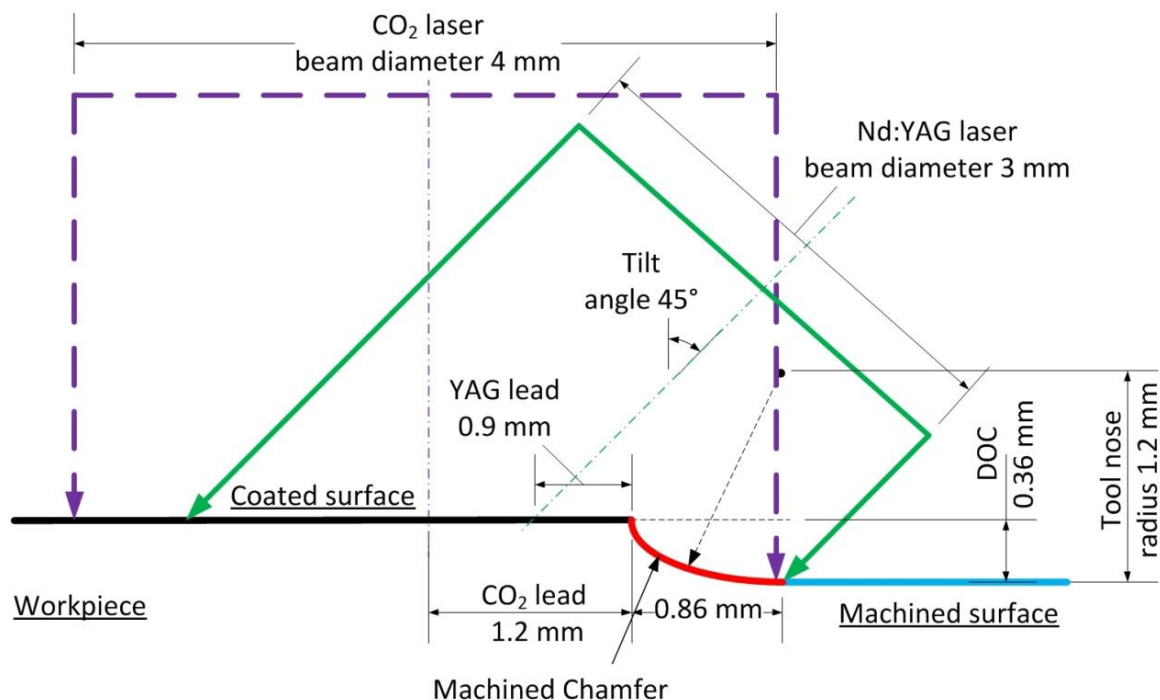


Figure 6.15. Diagram of the CO₂ and Nd:YAG lasers in the machined chamfer.

6.3.2. Temperature Prediction and Measurement

The transient, 3D, finite volume thermal model of a cylindrical workpiece has been expanded to handle the part geometric changes during LAM. The thermal conductivity of the internal vacant area of the shaft was set to zero to deactivate those control volumes. Convection heat transfer was defined on the internal surfaces with a convection coefficient of $19 \text{ W/m}^2\cdot\text{K}$ according to the work by Rozzi et al. [12]. Fine mesh was used within the depth of cut in both the radial and axial directions to model the material removal zone. A typical control volume within the depth of cut area is $80 \mu\text{m}$ in the axial direction and $45 \mu\text{m}$ in the radial direction. The laser heat absorption and conduction heat transfer were defined with great care in the machined chamfer. The developed numerical scheme overcame the convergence problem by partially deactivating multiple control volumes from each column along the machine chamfer and the laser heat flux is defined over every exposed partially-deactivated control volume at the boundary. No material removal was defined in the preheating phase and the machine chamfer gradually enters the workpiece at the beginning of the machining phase. In the new scheme, the temperature at the center of the surface control volume is solved by the three-dimensional heat transfer solver and is used as the surface temperature in the output files.

The accurate absorptivity of the workpiece surface at each particular laser wavelength is important since this parameter has a considerable effect on the workpiece temperature. Since the CO_2 and the Nd:YAG laser irradiate almost entirely on the graphite coated surface of the workpiece as shown in Figure 6.15, the absorptivity at both the wavelengths for the graphite coating must be known. The absorptivity of the graphite coated surface to the CO_2 laser has been measured previously to be 0.80 [6]. Absorptivity tests were conducted on graphite coated AISI 4140 prismatic workpieces to find the absorptivity of the graphite coating to the Nd:YAG laser. By comparing the thermocouple measurements with the thermal model predictions, the absorptivity was inferred. Figure 6.16 shows a comparison between the inferred thermal model predictions at absorptivity of 0.78 and the actual thermocouple measurements from one test. The absorptivity was found to range from 0.75 to 0.80 and the maximum surface temperature within the Nd:YAG laser beam was predicted to range from 400°C to 850°C for the absorptivity tests. The maximum temperature under the Nd:YAG laser beam during a LAM test falls within this range and hence the absorptivity of 0.78 is used for the graphite coated surface in the LAM thermal model.

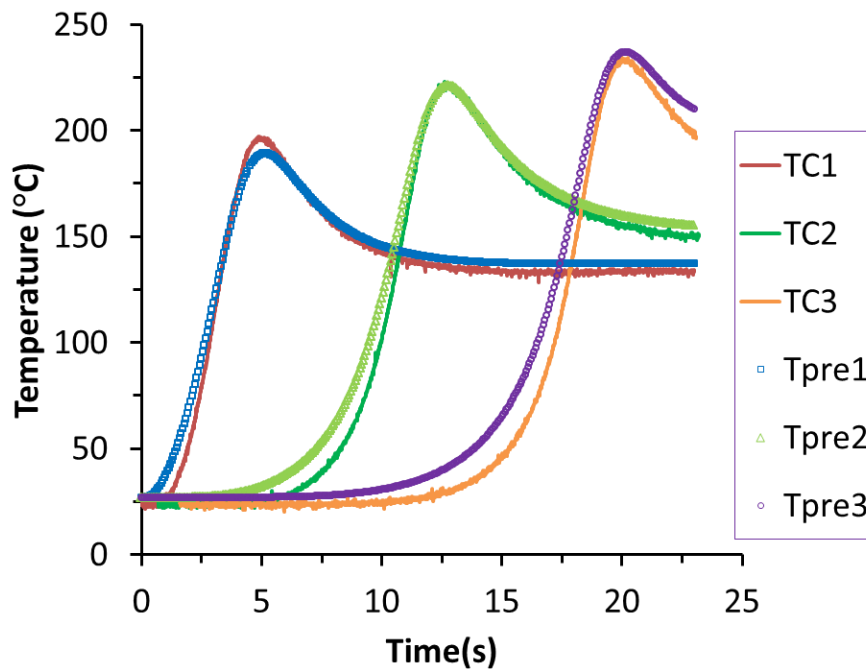


Figure 6.16. Thermal model predictions at absorptivity of 0.78 and thermocouple measurements during an absorptivity test for the graphite coated surface to the Nd:YAG laser.

Following the same procedure as mentioned above, the absorptivity of the machined surface of AISI 4130 steel at the Nd:YAG wavelength was determined. The absorptivity of the non-oxidized surface was 0.43, which matched well with the thermocouple measurements, while the absorptivity of the oxidized surface was about 0.70. In the LAM thermal model, absorptivity of 0.43 was used for the machine chamfer at the Nd:YAG laser wavelength. Absorptivity of 0.10 at the CO₂ laser wavelength was used for the machined chamfer because the absorptivity of low alloy steel to the CO₂ laser varies from 5% to 11% depending on the temperature [199-202]. The density of AISI 4130 at room temperature is 7,833 kg/m³ [195] and is assumed to be constant in the LAM thermal model. In order to apply the temperature dependent properties in the LAM thermal model, thermal conductivity and specific heat are curve fitted as functions of temperature and summarized as follows:

For thermal conductivity k (W/m·K):

$$\text{If } T \leq 1600 \text{ K, } k = 4.15 \times 10^{-8} T^3 - 1.03 \times 10^{-4} T^2 + 6.05 \times 10^{-2} T + 32.3$$

$$\text{If } T > 1600 \text{ K, } k = 35.404.$$

For specific heat C_p (J/kg·K)

$$\text{If } T \leq 950 \text{ K, } C_p = 6.27 \times 10^{-4} T^2 - 0.241T + 489$$

$$\text{If } T > 950 \text{ K, } C_p = 0.08T + 749.$$

Figure 6.17 and Figure 6.18 show the 2D temperature distributions on the longitudinal section and a corresponding 3D temperature distribution predicted by the thermal model, respectively. The following parameters were used in the thermal model: cutting speed of 180 m/min, feed of 0.075 mm/rev, depth of cut of 0.36 mm, CO₂ laser power of 1,100 W, Nd:YAG laser power of 300 W and the preheating time of 3 s. As can be seen in Figure 6.17, the maximum surface temperature is under the CO₂ laser due to the intense laser heating, and the Nd:YAG helps by increasing the temperature in the machine chamfer, while the heat penetration is deepest at the tool cutting position. Figure 6.18 shows both the CO₂ and the Nd:YAG laser spots on the workpiece surface, the tool cutting position (horizontal line) and the varying-thickness feature of the journal.

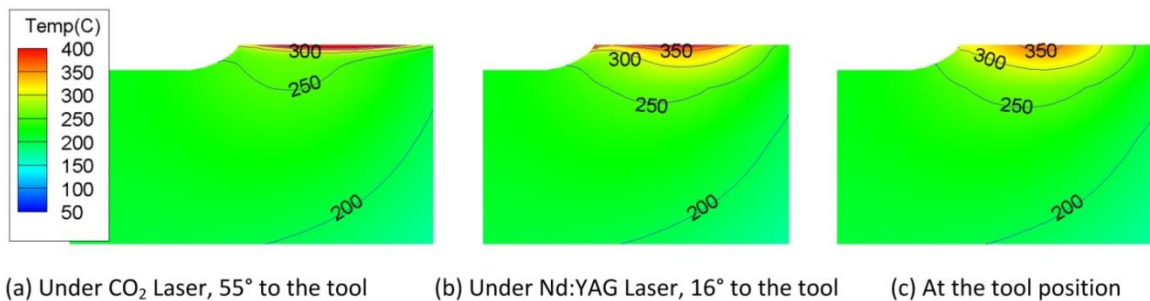


Figure 6.17. 2D temperature distributions in a hollow shaft workpiece undergoing LAM.

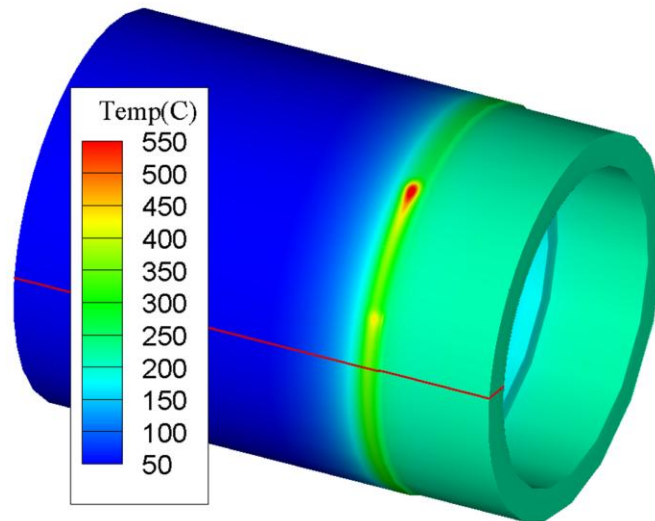


Figure 6.18. 3D temperature distribution in a hollow shaft workpiece undergoing LAM.

To validate the LAM thermal model for the hollow shaft of varying-thickness and to verify the material properties of AISI 4130, a non-contact FLIR SC3000 infrared camera of wavelength ranging from 8 to 9 μm was used to measure the temperature of the graphite coated surface during the LAM tests. The IR camera was set horizontally and 225° downstream from the tool as can be seen in Figure 6.19. The IR camera was set horizontally and 225° downstream from the tool. Emissivity of 0.85 was used for the graphite coated surface in the IR camera. The IR camera tracked the maximum temperature of the center line of the workpiece at 10 frames per second. The following parameters were used during the LAM test: cutting speed of 180 m/min, feed of 0.075 mm/rev, depth of cut of 0.36 mm, CO₂ laser power of 1,060 W and a preheating time of 3 seconds.

A good agreement between the IR temperature measurements and the thermal model predictions is observed in Figure 6.20. During the preheating phase, the workpiece surface temperature at the tool position increased dramatically and became steady during the material removal phase. The varying-thickness of the shaft had a minimal effect on the surface temperature as can be seen in Figure 6.20. High temperature spikes recorded by the IR camera during the LAM process were caused by two factors: the burned graphite powders under the intense laser heating and the hot chips generated during LAM. The IR camera caught these hot

spots, which should not be used for the model validation purpose and were filtered out after the test.

Regression models were developed to determine the average material removal temperature due to laser heating as a function of the machining, laser, and workpiece parameters. The laser power (W, CO₂ laser power P_{CO_2} and YAG laser power P_{YAG}), the cutting speed (V , m/min), and the feed (f , mm/rev) were selected as independent factors for the multivariable regression analysis. A three-level full factorial design was used to generate the simulation runs. The design was then implemented by running the LAM thermal model to obtain the data needed for the regression analysis. Eqs. 6.10 and 6.11 are used for predicting the T_{mr} during LAM process for the CO₂-only and two-laser LAM setups respectively:

$$T_{mr} = 1.8 \frac{P_{CO_2}^{0.85}}{V^{0.47} f^{0.47}} \quad (6.10)$$

$$T_{mr} = 152.7 \frac{P_{YAG}^{0.29}}{V^{0.45} f^{0.47}} \quad (6.11)$$

For the two-laser setup, the CO₂ laser power was fixed at 1,100 W to achieve high T_{mr} .

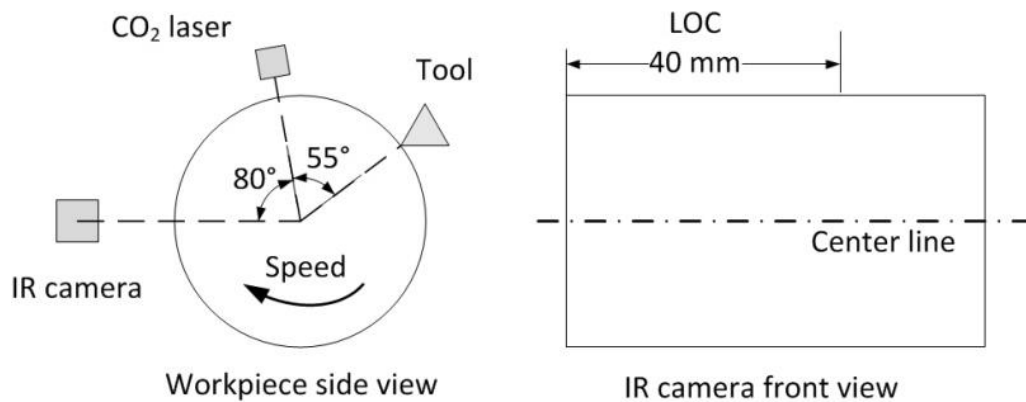


Figure 6.19. Schematic of the IR camera temperature measurement.

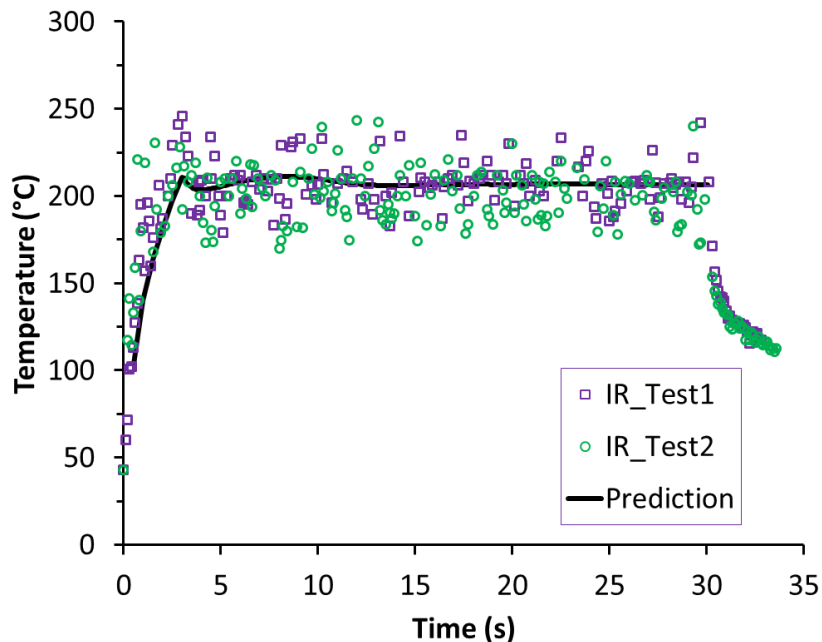


Figure 6.20. Temperature measurements and thermal model predictions in a hollow shaft undergoing LAM.

6.3.3. Microstructural Prediction of the LAM Process

LAM of hardened 4130 steel was simulated using the 3D nose turning option in AdvantEdge FEM. Phase transformation kinetics and grain refinement were modeled in the user defined material subroutines as described in Chapter 5. The thermo-mechanical properties of the PCBN insert and 4130 steel workpiece were obtained from [203] and [204], respectively. The Johnson-Cook model in [205] defined the constitutive plasticity behavior of AISI 4340 steel, and was adopted by adjusting the strain hardening terms in this study to model the plasticity of hardened AISI 4130 steel prior to any phase change. It can be seen in Figure 6.21 that the predicted flow stress at an equivalent strain of 0.008 and elevated temperatures of 4130 steel matches well with experimental data obtained from tensile and compressive tests provided in [206]. The dislocation model parameters of 4130 steel are given in Table 6.1, which were determined to reproduce the observed material constitutive behaviors of hardened AISI 4130 steel under various strains, strain rates and temperatures. A workpiece size of 6(L)x2(H)x4(W) mm in size was used in the simulations with the initial temperature set as the average material removal temperature. An initial microstructure of a tempered martensitic bulk structure with an average grain size of 5 μm was used in the simulations. A minimum element size of 5 μm was

used for meshing the workpiece in AdvantEdge FEM. When the cutting simulation step is finished, both the chip and tool are removed and the workpiece is allowed to thermo-mechanically relax. After the relaxation step, the heat is dissipated, and then a state of the stabilized microstructure in the workpiece is predicted.

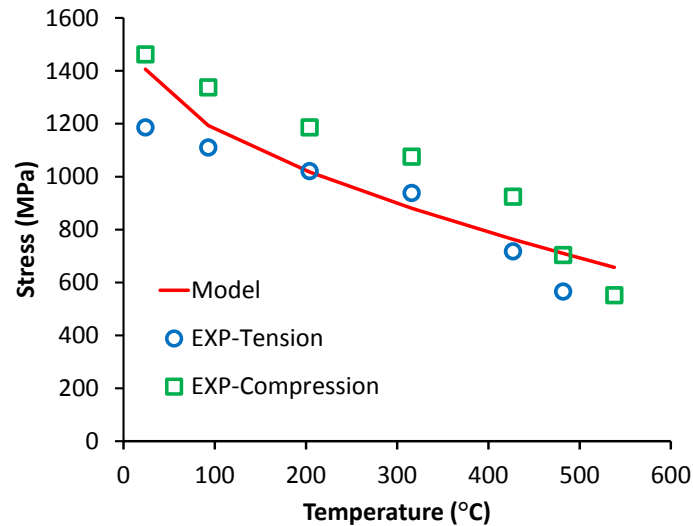


Figure 6.21. Comparison of measured and predicted flow stress at elevated temperatures of 4130 steel.

Table 6.1. Dislocation density-model constants of 4130 steel.

α^*	β^*	k_o	n	$\dot{\gamma}_o$	f_o	f_∞	K	M_t	$\tilde{\gamma}^r$	G (GPa)	b (mm)	α
0.19	0.06	7.8	50	1E5	0.29	0.16	10	3.06	2.5	79	2.48E-7	0.25

The steady-state solution at a cutting speed of 180 m/min and a feed of 0.075 mm/rev are simulated in terms of temperature, phase composition, grain size, etc., for LAM and conventional cutting at T_{mr} of 270 °C and 24 °C, respectively. The simulation results are shown in Figure 6.22. It can be seen in Figure 6.22 (a) and (b) that both LAM and conventional cutting produce very similar temperature profile in the chip and on the machined surface, even though a higher initial temperature of 270 °C was used in the LAM simulation. The highest machined surface temperature was simulated to be around 700 °C, which is less than the phase

transformation temperature, and hence no phase transformation was predicted for either LAM or conventional cutting condition, as can be seen in Figure 6.22 (c) and (d). Figure 6.22 (e) and (f) show the predictions of the grain size distributions for the two tests. It can be seen that grain size was slightly reduced from 5 μm to 1-3 μm near the machined surface for both LAM and conventional cutting conditions. But the grain refinement was predicted to be within a depth of 5 μm .

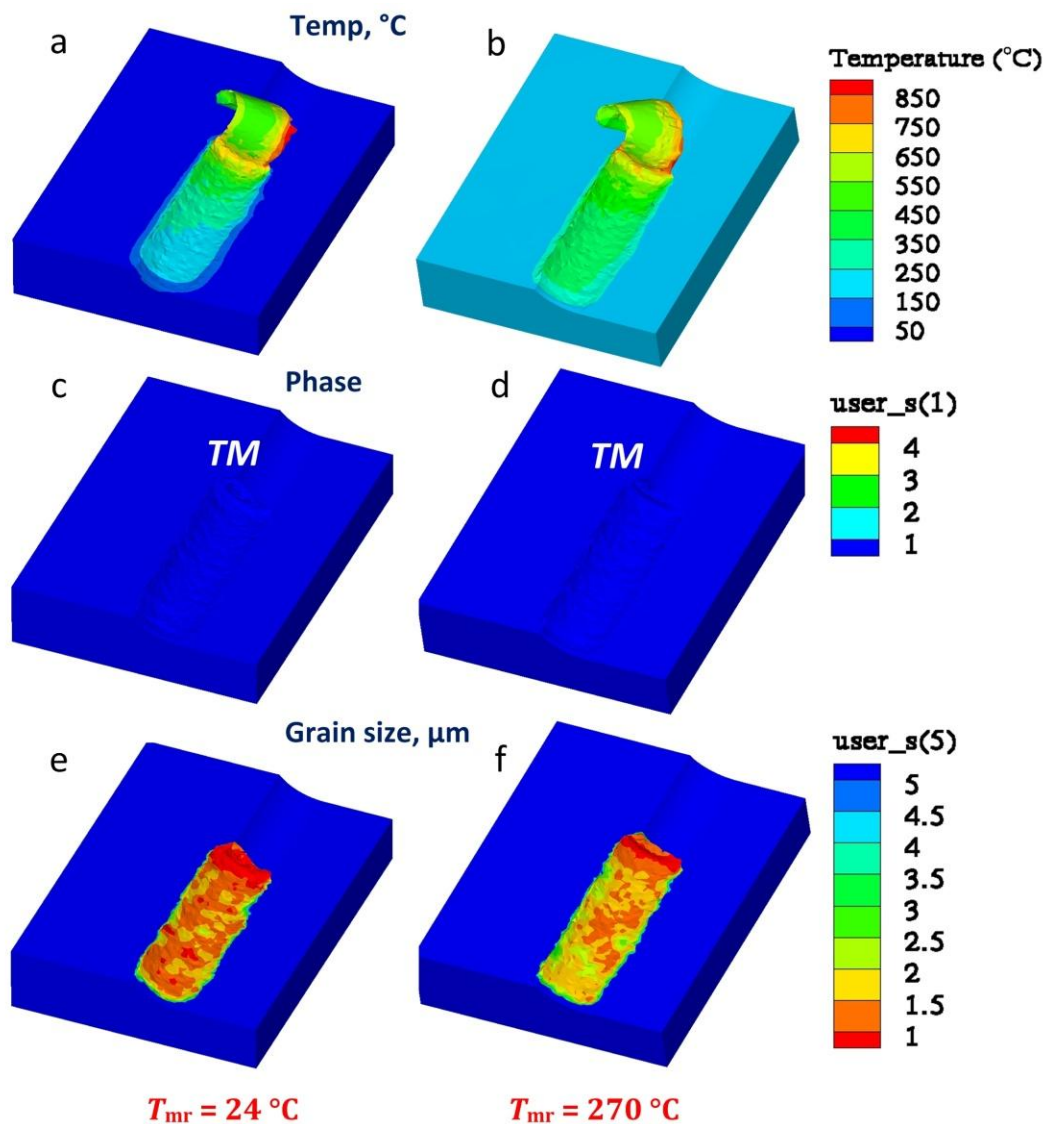


Figure 6.22. Simulation results of workpiece microstructure.

6.4. Surface Integrity Analysis

6.4.1. LAM Experiments

LAM and conventional machining operating conditions of the hardened steel shaft are shown in Table 6.2. The requisite laser power was determined by using Eqs. 6.10 and 6.11. Test conditions 1~6 use the same machining parameters with ascending T_{mr} , which are aimed to determine the optimal T_{mr} . Through the experiments, it is known that T_{mr} should not be increased above 300 °C because the machined surface tends to oxidize in the air after LAM with this high temperature. Different cutting speeds or feed rates are used in test conditions 7~16 to study the effects of cutting speed and feed on the surface integrity produced by LAM.

The temperature effect on the cutting force or the specific cutting energy is significant and consistent for all the conditions. Compared to conventional machining, the specific cutting energy during LAM drops by about 20% as the T_{mr} increases to above 200°C, as shown in Figure 6.23. The cutting speed has little effect on the specific cutting energy while increasing the feed rate results in a higher cutting force but less specific cutting energy.

Table 6.2. LAM experimental conditions.

Condition	V (m/min)	f (mm/rev)	a_p (mm)	t_{pre} (s)	P_{CO2} (W)	P_{YAG} (W)	T_{mr} (°C)
1	180	0.075	0.36	-	-	-	24
2	180	0.075	0.36	3	816	-	160
3	180	0.075	0.36	3	1060	-	200
4	180	0.075	0.36	3	1249	-	230
5	180	0.075	0.36	3	1100	311	270
6	180	0.075	0.36	3	1100	425	300
7	180	0.05	0.36	-	-	-	24
8	180	0.05	0.36	4	666	-	160
9	180	0.05	0.36	4	865	-	200
10	180	0.05	0.36	4	1223	-	270
11	180	0.1	0.36	-	-	-	24
12	180	0.1	0.36	3	1224	-	200
13	180	0.1	0.36	3	1100	467	270
14	150	0.075	0.36	3.5	1100	243	270
15	240	0.075	0.36	2	1100	458	270
16	300	0.075	0.36	2	1100	616	270

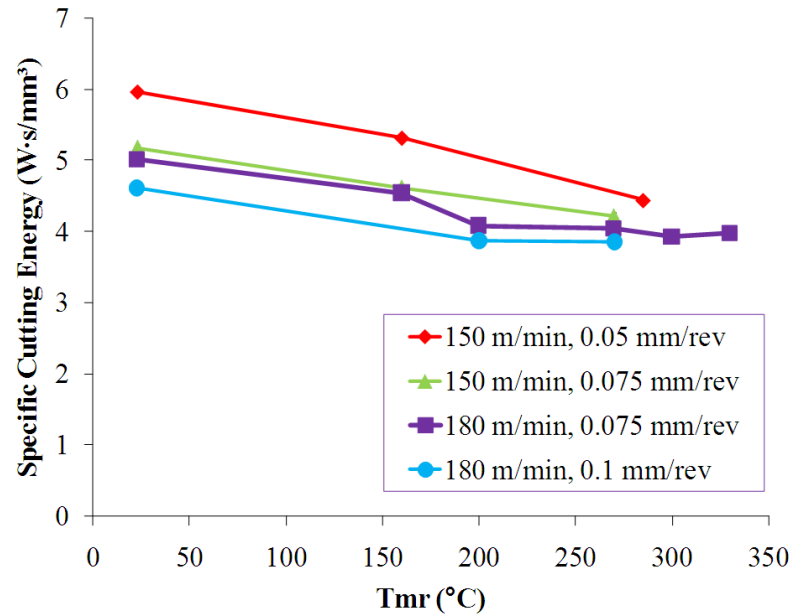


Figure 6.23. Temperature effect on specific cutting energy of hardened 4130 steel.

6.4.2. Surface Finish

Generally, LAM produces a nice surface finish of R_a less than $0.3 \mu\text{m}$ since the feed is less than 0.1 mm/rev , as can be seen in Figure 6.24. Theoretical surface roughness can be determined by the feed and the tool nose radius (r) by $R_a = \frac{f^2}{32r}$. The theoretical R_a is 0.07 , 0.15 and $0.26 \mu\text{m}$ for the feed of 0.05 , 0.075 and 0.1 mm/rev respectively for a tool nose radius of 1.19 mm . The actual average surface roughness R_a generated from conventional machining is about 0.34 , 0.28 and $0.36 \mu\text{m}$ for the feed of 0.05 , 0.075 and 0.1 mm/rev respectively. Because conventional machining already achieves good surface finish at these small feed rates, the effect of increasing T_{mr} is not significant on the surface finish as shown in Figure 6.24.

A smaller feed usually generates a better surface finish. However, at the speed of 150 m/min , a further decrease of the feed to 0.05 mm/rev results in worse surface finish due to plowing. Under this conventional machining condition, the surface roughness varies greatly at different locations of the part indicating that plowing contributes significantly to the surface roughness. Increasing the T_{mr} improves the average surface finish from 0.34 to $0.2 \mu\text{m}$ at the feed of 0.05 mm/rev as shown in Figure 6.24.

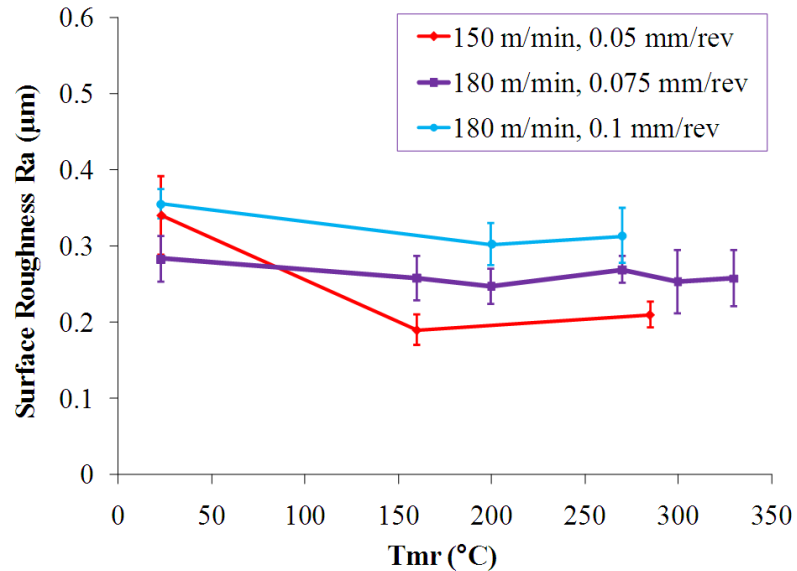


Figure 6.24. Temperature effects on surface finish of hardened 4130 steel.

6.4.3. Precise Size Control

To measure the effect of thermal expansion on size control, the same cutting tool was used throughout the LAM and conventional machining tests. Despite the variations found among the original part diameters, the same radial position was used for all the tests. Thus the actual depth of cut varies for different parts because of the variation of the incoming part size. The diameters of multiple parts produced by LAM and conventional cutting were measured when the parts cooled down. It was found that the actual depth of cut during LAM was 0.035 mm more than that of conventional machining, but the final dimensions or the tolerance of the parts produced by LAM were as consistent as by conventional machining, which is shown in Figure 6.25. Compared to conventional cutting, the slightly larger depth of cut during LAM was mainly caused by two factors: first, more thermal expansion presented in the parts due to the higher temperature gradients during LAM. The thermal expansion during LAM increases the depth of cut by about 0.015 mm, which has been calculated with the temperature profile predicted for the hollow cylindrical part by the thermal model. Secondly, the lower stiffness of the work and tool holding setup used in this study contributes significantly to the dimensional error of the parts produced by conventional cutting. The high radial cutting force during conventional cutting of hardened steel reduces the actual depth of cut from the desired value.

The 20% decrease of the force reduces such a tendency so that the decrease of the depth of cut during LAM becomes less than during conventional cutting, which explains the discrepancy between the measured extra depth of cut and the diameter change due to thermal expansion. Although both the stiffness and thermal expansion are sources to the dimensional error, precise size control is achievable by improving the machine rigidity and finding a suitable LAM depth of cut to minimize the dimensional error. Figure 6.25 shows that LAM produces parts with consistent diameters even with the less machine rigidity of the current system.

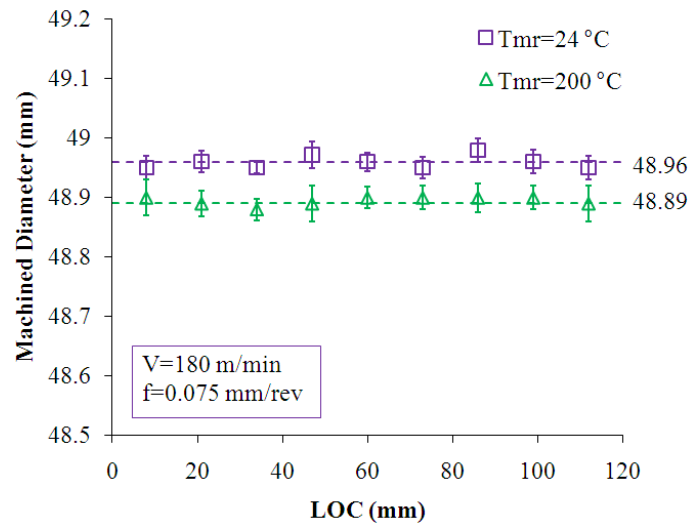


Figure 6.25. Effect of thermal expansion on size control.

6.4.4. Microstructures

All the specimens were prepared by following the standard metallographic preparation techniques, i.e., sectioning with an abrasive cutoff wheel, mounting in Bakelite, grinding and polishing with diamond paste and then chemical etching in a 2% Nital solution. Figure 6.26 shows the subsurface microstructures after LAM and no microstructural change was observed when comparing the machined subsurface after conventional machining with those after LAM. These findings agree well with the microstructures predicted in Section 6.2, i.e., neither phase change nor white layer forms on the machined surface under the LAM condition. This can be explained by the fact that the bulk temperature is increased to around 200-270°C during LAM, which softens the material, reduces the cutting force and heat generation while avoids reaching the critical phase transformation temperature. Also compared with conventional cutting, LAM

alleviates the mechanical deformation effect on grain refinement and reduces the opportunity of forming white layer.

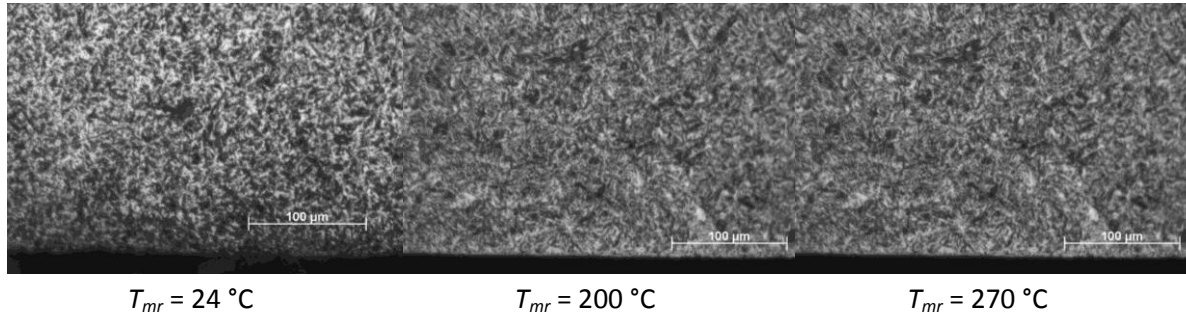


Figure 6.26. Optical microscopy of microstructures of the subsurface after LAM at speed of 180 m/min, feed of 0.075 mm/rev and various T_{mr} , 200X.

6.4.5. Hardness

The surface hardness was measured at 5 different locations for each cylindrical part before and after LAM. The average hardness is 47.5 and 48.0 HRC for the parts as-received and after LAM respectively. Figure 6.27 compares the surface hardness histograms before and after LAM. The hardness of the as-received parts varies between 44 to 50 HRC, and in comparison the hardness after LAM becomes more concentrated and ranges from 47 to 48.5 HRC. The surface hardness measurements indicate that the machined surface produced by LAM was work hardened uniformly due to an increase of dislocations; however the hardening effect due to SPD in LAM is smaller than conventional cutting and does not produce white layer [207].

Before the micro-indentation hardness tests, an abrasive cutoff wheel was used for the initial sectioning of the large workpiece with adequate coolant flow to minimize heat-induced damage. All specimens were mounted in Bakelite, ground and polished with diamond paste. The Vickers hardness tests were carried out on the specimens with the load of 1 kgf. The resultant indentation diagonals were measured by a microscope and were used to calculate the Vickers hardness number (HV). The diagonals of indentations are mostly within a narrow range of 61~62 μm and thus corresponding hardness values are within the range of 482~498 HV. For the hardness between 240 and 1040 HV, Eq. 6.12 was used to convert Vickers hardness number to Rockwell C hardness number:

$$HRC = 119.0 - \sqrt{\frac{2.43 \times 10^6}{HV}}. \quad (6.12)$$

As can be seen from Figure 6.28, the hardness near the machined surface at different T_{mr} is primarily concentrated around 48 HRC and increasing the T_{mr} up to 270 °C does not soften the machined subsurface.

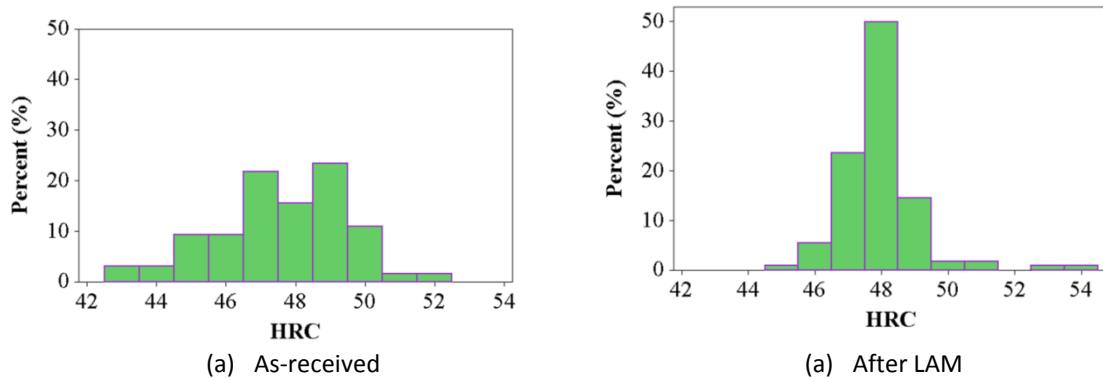


Figure 6.27. Histograms of the hardness of the parts before and after LAM.

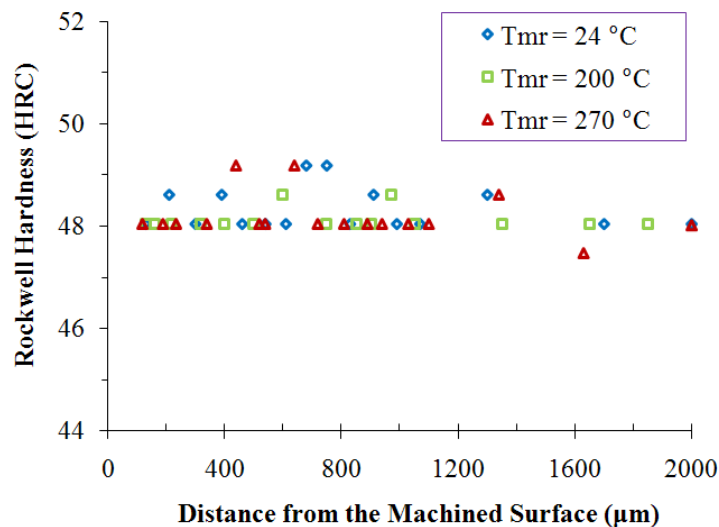


Figure 6.28. Subsurface hardness after LAM at speed of 180 m/min and feed of 0.075 mm/rev.

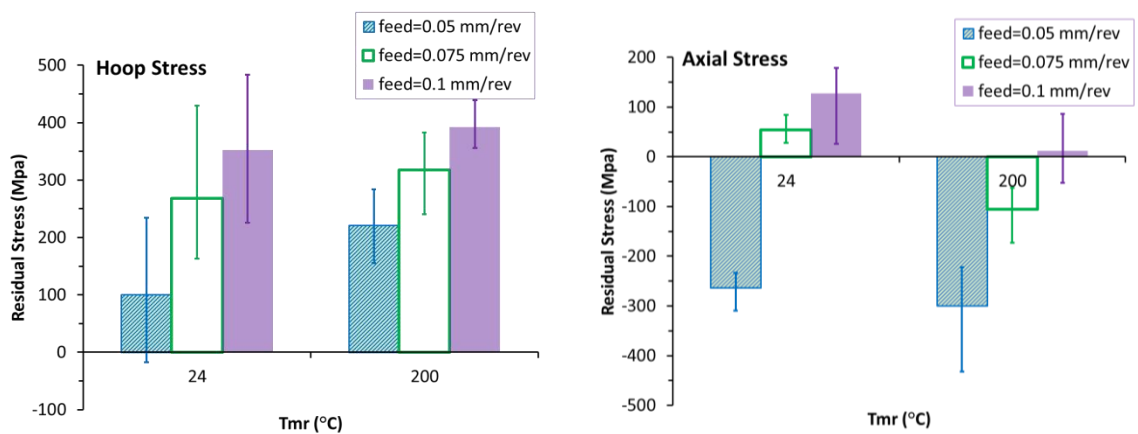
6.4.6. Residual Stress

Residual stress measurements by X-ray diffraction were conducted using the multiple angle $\sin^2\psi$ technique. The x-ray line profile fitting program, XFIT, was used to locate the

diffraction peak of the measurement at each ψ tilt angle. The x-ray parameters for 4340 steel of 50 HRC were used for the 4130 specimens in this study, which are shown in Table 6.3. Multiple surface residual stress measurements were conducted for conditions 1-4, 7-9 and 11-12 using multiple specimens. An electropolishing process was used to remove a layer of material in depth direction for the subsurface measurements for conditions 1, 3, 7 and 9. Figure 6.29 shows the trend of the surface residual stresses at elevated temperatures for both the hoop and axial directions. The residual stress in the hoop direction is tensile and is generally within the range of 200~400 MPa. For the feeds of 0.075 and 0.1 mm/rev, the magnitude of the axial stress is less than that of the hoop stress and ranges from -200 to 200 MPa. For the feed of 0.05 mm/rev, the compressive axial stress has a higher magnitude than that of the hoop stress and ranges from -250 to -300 MPa. As T_{mr} increases from room temperature to 200 °C, the hoop stress also increases by about 50~100 MPa.

Table 6.3. X-ray parameters for 4340 steel [208].

Alloy	Radiation	Lattice plane, (hkl)	Diffraction angle 2θ , (°)	Elastic constants $(E/1 + \nu)$ in (hkl) , (GPa)
4340 (50 HRC)	Cr $K\alpha$	(211)	156.0	168.9 ± 2.8



(a) Hoop

(b) Axial

Figure 6.29. Surface residual stress of LAM of 4130.

LAM produces more compressive residual stress in the axial direction for the feeds of 0.075 and 0.1 mm/rev. Increasing T_{mr} from room temperature to around 200 °C reduces the axial residual stress by about 150 MPa and produces more compressive residual stress. The samples produced by conventional machining display a greater variance in hoop stress than those produced by LAM. Feed has a strong effect on the residual stress. The residual stress becomes more compressive in both the hoop and axial directions as the feed decreases from 0.1 to 0.05 mm/rev. For the feed of 0.05 mm/rev, compressive axial stress, -200~-300 MPa, is evident in both LAM and conventional cutting and its magnitude is higher than that of the hoop stress.

Figure 6.30 shows the subsurface residual stress measurements for the four conditions under conventional machining and LAM. Stresses in both the hoop and axial directions drop sharply within the first 20 μm below the surface. The stress penetration in both directions is around 40~50 μm below the surface. The hoop stress is mainly tensile at the surface, but becomes compressive about 10 μm below the surface with the peak compressive stress in the range from -150 to -300 MPa. The axial stress is less tensile on the surface for the feed of 0.075 mm/rev and even becomes compressive for the feed of 0.05 mm/rev. The peak compressive stress in the axial direction is higher than that in the hoop direction and is about -400 MPa for all the four conditions.

The T_{mr} does not significantly alter the magnitude of the peak compressive stress in both the hoop and axial directions. However, increasing the T_{mr} produces a slightly shallower depth of maximum residual stress for both the hoop and axial directions, where the peak compressive stress produced by LAM is about 5 μm closer to the surface than that produced by conventional cutting. Feed has a strong effect on the hoop stress profile. Larger feed of 0.075 mm/rev generates a deeper stress penetration and a larger peak compressive stress than the smaller feed of 0.05 mm/rev. For the feed of 0.05 mm/rev, the peak compressive stress exists at about 15 μm below the surface for both directions and both temperatures. For the feed of 0.075 mm/rev, the peak compressive stress in the hoop direction is less than that in the axial direction but the overall penetration is greater. The peak compressive stress exists at about 15 μm below the surface in the axial direction but it is about 25~40 μm in the hoop direction.

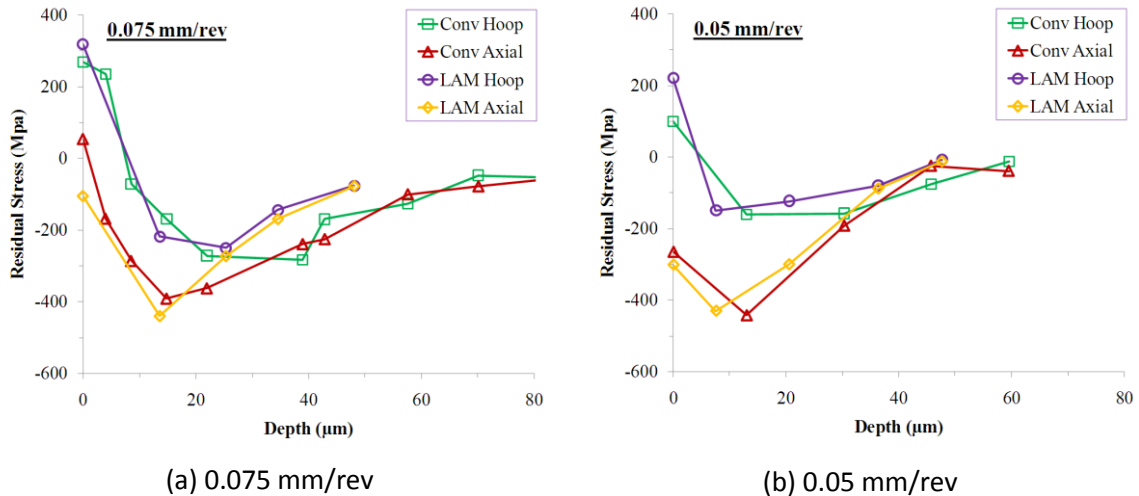


Figure 6.30. Subsurface residual stress of LAM of 4130.

6.4.7. Discussions

The surface integrity of hardened steel transmission shafts produced by LAM has been quantitatively studied in terms of surface roughness, dimensional accuracy, microhardness, microstructures and residual stresses. The results presented in this study are valuable since they show that LAM with at least a four-time faster material removal rate than the two-step hard turning and grinding operations produces a good surface finish of R_a less than $0.3 \mu\text{m}$, a more concentrated surface hardness profile, no softening and no microstructure change in the machined subsurface, less variation in the surface hoop residual stress and more compressive surface axial residual stress. The feasibility of precise size control in LAM of hardened steel components has also been demonstrated, which is usually a great concern for the industrial applications.

The 20% cutting force reduction achieved during LAM reduced the workpiece deflection and also slowed down tool wear progression. Because the tool wear developed at such a low rate during LAM, it was not possible to complete tool wear tests due to the need of a very large number of parts and the associated time and cost. However, the significant tool wear typically encountered in hard turning not only deteriorates the surface finish but also causes the formation of a hardened white layer near the machined surface, which is generally believed to be detrimental to parts performance [49, 193, 194]. Compared to hard turning and grinding, the impact of LAM on the part performance and fatigue life of the hardened steel components is of great interest for the future study. Similar residual stress profiles in depth, but with less

variation, to those produced by conventional cutting prove that laser heating during LAM had no detrimental effects on the workpiece machined subsurface.

6.5. Summary

The results of LAM of AISI 4130 shaft were experimentally analyzed by changing heating and operating conditions, viz., average material removal temperature, cutting speed and feed. The 3D transient thermal model has been expanded to predict the temperature field undergoing laser-assisted profile turning. Compared to various conventional machining conditions, the cutting force or the specific cutting energy during LAM dropped by about 20% as the T_{mr} increased to above 200°C. The hardness of the machined surface after LAM typically ranges from 47 to 48.5 HRC. In comparison, the hardness of the as-received parts spans from 44 to 50 HRC. For both LAM and conventional machining, similar hardness profiles were obtained on the machined subsurface as shown through Vickers micro-indentation hardness testing, which proves that increasing T_{mr} up to 270 °C is not detrimental to the workpiece hardness. The simulation results show that LAM produces neither phase change nor white layer on the machined surface, which has been validated through a microstructural analysis using an optical microscope. During LAM, the actual depth of cut is slightly larger, but the resultant diameters were consistent, indicating that depth of cut can be precisely controlled to achieve the desired dimension. The samples produced by conventional machining display about twice the variance in hoop stress than those produced by LAM. The residual stress becomes more compressive in both the hoop and axial directions as the feed decreases from 0.1 to 0.05 mm/rev. Stresses in both the hoop and axial directions drop sharply within the first 20 μm below the surface. The stress penetration in both directions is around 40~50 μm below the surface. Larger feed of 0.075 mm/rev generates a deeper stress penetration and a larger peak compressive stress than the smaller feed of 0.05 mm/rev in the hoop direction.

CHAPTER 7. CONCLUSIONS AND FUTURE WORK

7.1. Summary

A dislocation density-based numerical framework was developed to simulate grain refinement for metallic materials subject to the machining processes. A coupled Eulerian-Lagrangian finite element model was developed in ABAQUS to simulate steady-state chip formation and grain refinement. Orthogonal cutting tests of Al 6061 T6 and OFHC Cu at cutting speed ranging from 0.01 to 1.25 m/s, rake angle ranging from -20° to 20° , and depth of cut ranging from 0.1 to 0.3 mm were modeled to simulate the cutting temperature, strain, grain size and grain misorientation in the steady state chip and on the machined surface. The predictions of steady-state chip formation, strain and strain rate distributions in the chip all matched well with the actual measurements. The predictions of the average grain size in the chip generally matched well with the measured values obtained in literature for all the tests of Al 6061 T6 and OFHC Cu under varying cutting conditions. It has been shown that the grain size in the machined chips of Al 6061 T6 was refined from an initial grain size of $75\ \mu\text{m}$ to about 160, 100 and 80 nm under varying levels of applied shear strains ranging from 1.8 to 5.2 imposed by tool rake angles ranging from 20° to -20° .

The numerical framework of grain refinement developed in this dissertation has been shown to be a useful tool to design cutting process parameters for optimum refined microstructures. A more negative rake angle tool helps further reduce the grain size in the chip by imposing a larger strain, but the model simulation results show that cutting speed and cutting temperature also strongly affect the final grain structure. Hence, the cutting parameters have to be carefully designed to obtain the optimum microstructure in terms of both grain size and misorientation angle. A small applied strain, high cutting speed and high cutting temperature all contribute to a coarser elongated grain structure during cutting, while a more randomly orientated microstructure should be achieved at a low cutting speed. The simulation results demonstrated that the essential characteristics of the deformation field and grain

refinement mechanism during cutting were well captured by the dislocation density-based material models.

A truly coupled metallo-thermo-mechanical model was proposed to solve for mechanical deformation, thermal history, and microstructural composition in steels cutting. The CEL model was used to simulate orthogonal cutting of AISI 1045 steel under various conditions, with cutting speeds ranging from 198 to 879 m/min, feeds from 0.1 to 0.3 mm, and tool rake angles from -7° to 5° . The evolution of phase constituents of the workpiece material was modeled using a phase transformation kinetics model, and was solved simultaneously with thermal and mechanical fields in cutting. The thermo-mechanical properties and the rate-independent constitutive models of constituent phases of ferrite-pearlite, austenite and martensite for AISI 1045 steel were used in the coupled analysis. A good agreement was achieved in the chip formation, cutting force and cutting temperature between the model predictions and the experimental data. The volume fractions of the transformed austenite were predicted in the steady-state chips. The model predicted the tool-chip interface temperature ranging from 1080 °C to 1396 °C for various cutting conditions investigated, and the discrepancy between the model predictions and the experimental data was well below 10%. The model was further validated in cutting force with discrepancies of less than 8% in cutting direction and 10-19% in feed direction.

The developed metallo-thermo-mechanical coupled analysis was applied to the 3D hard turning process for bearing steels to investigate the surface microstructure alteration, particularly the white layer formation mechanisms. 3D hard turning simulations were undertaken via AdvantEdge FEM software incorporating the material user subroutine for various hard turning conditions, with cutting speeds ranging from 45 to 274.3 m/min, feeds from 0.05 to 0.127 mm, and tool flank wear land width from 0 to 0.3 mm. Both the thermally driven phase transformation and mechanical grain refinement due to SPD were considered to model the surface microstructural change. The model solved for the critical surface microstructural attributes such as phase composition, grain size, and microhardness simultaneously in AdvantEdge FEM. Through a quantitative assessment using the experimental data, the model simulations proved that the white layers formed at low-to-moderate cutting speeds consisted of a refined nanocrystalline microstructure, which was caused by severe plastic deformation but not thermally driven phase transformation. The white layer formation at high cutting speeds

was caused by both thermally driven phase transformation and grain refinement due to SPD. For instance, the simulation results found that at a cutting speed of 274.3 m/min, an increase of surface hardness of 1.43 GPa was caused by a combination of martensitic transformation and severe plastic deformation, whereas at a cutting speed of 91.4 m/min, an increase of surface hardness of 0.83 GPa was predicted to be mainly caused by severe plastic deformation. Subsurface residual stress profiles were also predicted, which agreed well with the experimental data. The multi-physics modeling approach was shown to be a more comprehensive solution for analyzing the surface microstructure alteration in hard turning and thermally enhanced machining processes such as laser-assisted machining.

Microstructure and surface integrity has been further studied both experimentally and numerically for difficult-to-machine materials during laser-assisted machining in both micro and macro scales. For laser-assisted micro-milling, a comprehensive thermal and mechanical analysis was conducted for Ti6Al4V, Inconel 718, and stainless steel AISI 422. The workpiece temperature increase due to the laser heating and temperature variances in the cutting zone were examined by a transient, 3D prismatic thermal model for various LAMM tests in side cutting of bulk and fin workpiece configurations with a 30 W continuous CO₂ laser and 100-300 μm diameter carbide endmills. A novel, arbitrary-Lagrangian–Eulerian based finite element scheme was developed in ABAQUS/Explicit to simulate the continuous chip formation with varying chip thickness in micro-milling. A strain gradient constitutive material model was incorporated to model the size effect in micro-milling. The thermal analysis proved that fin workpiece structure was the optimal design for LAMM within the present system constraints with a temperature variance of 10 to 15 °C in the machined chamfer. The FE simulations predicted uniform specific cutting energy along the cutting depth of 250 μm in LAMM fin side cutting. The steady-state cutting temperature after many micromilling cycles was determined by the heat transfer analysis. An empirical tool wear model was derived for a tungsten carbide tool in fin side cutting based on LAMM bulk side cutting simulations and the model predicted that the tool wear rate dropped from 0.62 to 0.15 μm/min as the workpiece temperature increased from the ambient temperature to about 354 °C in fin side cutting of 422SS. The FE model simulations further showed that built-up edge formation could be eliminated or reduced in LAMM with proper heating of the workpiece material prior to the cutting tool.

One-step laser-assisted machining process was proposed for hardened AISI 4130 steel to replace the hard turning and grinding operations. The surface integrity analysis was experimentally conducted by changing heating and operating conditions, viz., average material removal temperature, cutting speed and feed. The 3D transient thermal model has been expanded to predict the temperature field inside the workpiece of complex geometry undergoing laser-assisted profile turning. Microstructure of 4130 steel workpiece was simulated using the 3D nose turning option in AdvantEdge FEM by considering both phase transformation kinetics and grain refinement due to SPD. With the correct inputs of thermal and optical properties, the infrared camera temperature measurement validated that the thermal model accurately predicted workpiece surface temperatures during LAM. The FE simulation results show that LAM produced neither phase change nor white layer on the machined surface. LAM softened the material and reduced the heat generation by increasing the material bulk temperature to around 200-270°C, which resulted in a surface temperature less than the critical phase transformation temperature. The model prediction showed that grain size was slightly reduced from 5 μm to 1-3 μm near the machined surface for both LAM and conventional cutting conditions and the grain refinement was limited to be within a depth of 5 μm .

The experimental results of LAM of AISI 4130 shaft were presented by changing the average material removal temperature from the room temperature to 300 °C, cutting speed from 150 to 300 m/min and feed from 0.05 to 0.1 mm/rev. Compared to various conventional machining conditions, the specific cutting energy during LAM dropped by about 20% as the T_{mr} increased to above 200°C. The hardness of as-received 4130 steel workpieces varied between 44 to 50 HRC after heat treatment. The machined surface produced by LAM ranged from 47 to 48.5 HRC, which was work hardened uniformly due to an increase of dislocations. The hardening effect due to SPD in LAM was smaller than conventional cutting and did not produce white layer as validated using an optical microscope. Because of thermal expansion, LAM produced a deeper cut; however the resultant diameters after LAM were shown to be very consistent, which indicated that depth of cut can be precisely controlled to achieve the desired dimension. The samples produced by conventional machining displayed about twice the variance in hoop residual stress than those produced by LAM. The residual stress penetration in both directions was around 40~50 μm below the surface of the parts produced by LAM. The

larger feed of 0.075 mm/rev generated a deeper stress penetration and a larger peak compressive stress than the smaller feed of 0.05 mm/rev in the hoop direction.

7.2. Conclusions

In this dissertation, 1) grain refinement due to mechanical deformation in cutting was quantitatively modeled for metallic materials using a dislocation density-based model. This work is the first of its kind in machining and agrees well with experimental measurements. 2) Phase change was truly coupled in the machining models. A metallo-thermo-mechanical coupled numerical framework was developed to solve for the evolution of microstructural phase constituents, grain refinement, cutting temperature, chip morphology, and cutting force simultaneously. This comprehensive machining model has never been successfully done by others before and has been proved as a useful numerical tool in analyzing surface integrity issues, like white layer and subsurface microhardness, which are developed in hard machining and laser-assisted machining. 3) Novel laser-assisted machining and micromachining techniques were exploited to improve machinability and surface integrity for difficult-to-machine materials. Tool performance, surface integrity and microstructure alteration in LAM has been studied by the simultaneous experimental and numerical investigations of the process. In conclusion, LAM showed considerable improvement in the machinability of the difficult-to-machine metal alloys through increased material removal rate, increased tool life, and improved surface finish and surface integrity.

7.3. Future Work

Some ideas for future research on the modeling and experimental sides are summarized as follows:

- The modeling strategy outlined for the dislocation density-based grain refinement simulations can be extended to predict the microstructural evolution in SPD processes, such as surface material enhancement via laser shock peening and surface mechanical attrition treatment. This model would therefore assist in designing the process parameters to achieve the optimal surface microstructure.

- The metallo-thermo-mechanical coupled numerical framework discussed in this dissertation is ideally suited to study surface treatment of large wind turbine gears and bearings for a long lifetime expectancy. As the size of wind turbines increase, the difficulties of producing highly reliable parts are even more challenging to manufacture. The multi-physics model can be further extended to laser hardening and laser cladding of wind turbine gears and bearings to enhance surface properties and improve fatigue life.
- Current manufacturing methods involve the machining process of hardened bearing steels, which often leads to the development of a surface white layer. The white layer formation mechanisms discussed in this dissertation can be applied to milling and drilling of hardened steels to solve for the critical surface microstructural attributes such as phase composition, grain size, and microhardness.
- More experimental analyses are needed for surface integrity and subsurface microstructure of nickel-based high temperature alloys and titanium alloys to demonstrate the benefits of LAMM over conventional micromachining.
- Further experiments are needed to apply laser-assisted profile turning to difficult-to-machine materials including metal alloys, metal matrix composites and ceramics. The thermal model and the metallo-thermo-mechanical coupled model can be applied to help design the LAM experiments to achieve the maximum material removal rate, longest tool life, and best surface integrity.

LIST OF REFERENCES

LIST OF REFERENCES

- [1] Shin, Y. C., "Laser assisted machining: Its potential and future," Proc. 29th International Congress on Applications of Lasers and Electro-Optics, ICALEO 2010, September 26, 2010 - September 30, 2010, Laser Institute of America, pp. 513-522.
- [2] Sun, S., Brandt, M., and Dargusch, M. S., 2010, "Thermally enhanced machining of hard-to-machine materials--A review," *International Journal of Machine Tools and Manufacture*, 50(8), pp. 663-680.
- [3] Ezugwu, E. O., 2005, "Key improvements in the machining of difficult-to-cut aerospace superalloys," *International Journal of Machine Tools and Manufacture*, 45(12-13), pp. 1353-1367.
- [4] Grzesik, W., and Wanat, T., 2005, "Comparative assessment of surface roughness produced by hard machining with mixed ceramic tools including 2D and 3D analysis," *Journal of Materials Processing Technology*, 169(3), pp. 364-371.
- [5] Skvarenina, S., and Shin, Y. C., 2006, "Laser-assisted machining of compacted graphite iron," *International Journal of Machine Tools and Manufacture*, 46(1), pp. 7-17.
- [6] Anderson, M., Patwa, R., and Shin, Y. C., 2006, "Laser-assisted machining of Inconel 718 with an economic analysis," *International Journal of Machine Tools and Manufacture*, 46(14), pp. 1879-1891.
- [7] Dandekar, C. R., Shin, Y. C., and Barnes, J., 2010, "Machinability improvement of titanium alloy (Ti-6Al-4V) via LAM and hybrid machining," *International Journal of Machine Tools and Manufacture*, 50(2), pp. 174-182.
- [8] Ding, H., and Shin, Y. C., 2010, "Laser-assisted machining of hardened steel parts with surface integrity analysis," *International Journal of Machine Tools and Manufacture*, 50(1), pp. 106-114.
- [9] Rozzi, J. C., Pfefferkorn, F. E., Incropera, F. P., and Shin, Y. C., 2000, "Transient, three-dimensional heat transfer model for the laser assisted machining of silicon nitride: I. Comparison of predictions with measured surface temperature histories," *International Journal of Heat and Mass Transfer*, 43(8), pp. 1409-1424.

- [10] Lei, S., Shin, Y. C., and Incropera, F. P., 2000, "Deformation mechanisms and constitutive modeling for silicon nitride undergoing laser-assisted machining," *International Journal of Machine Tools and Manufacture*, 40(15), pp. 2213-2233.
- [11] Lei, S., Shin, Y. C., and Incropera, F. P., 1999, "Experimental investigation of thermo-mechanical characteristics in laser-assisted machining of silicon nitride ceramics," *American Society of Mechanical Engineers, Manufacturing Engineering Division, MED*, 10, pp. 781-788.
- [12] Rozzi, J. C., Incropera, F. P., and Shin, Y. C., 2000, "Transient, three-dimensional heat transfer model for the laser assisted machining of silicon nitride: II. Assessment of parametric effects," *International Journal of Heat and Mass Transfer*, 43(8), pp. 1425-1437.
- [13] Pfefferkorn, F. E., Shin, Y. C., Tian, Y., and Incropera, F. P., 2004, "Laser-assisted machining of magnesia-partially-stabilized zirconia," *Journal of Manufacturing Science and Engineering, Transactions of the ASME*, 126, pp. 42-51.
- [14] Tian, Y., and Shin, Y. C., 2006, "Thermal modeling for laser-assisted machining of silicon nitride ceramics with complex features," *Journal of Manufacturing Science and Engineering, Transactions of the ASME*, 128, pp. 425-434.
- [15] Tian, Y., and Shin, Y. C., 2006, "Laser-assisted machining of damage-free silicon nitride parts with complex geometric features via in-process control of laser power," *Journal of the American Ceramic Society*, 89, pp. 3397-3405.
- [16] Tian, Y., Wu, B., Anderson, M., and Shin, Y. C., 2008, "Laser-assisted milling of silicon nitride ceramics and inconel 718," *Journal of Manufacturing Science and Engineering, Transactions of the ASME*, 130, p. 0310131.
- [17] Tian, Y., Wu, B., and Shin, Y. C., "Laser-assisted milling of silicon nitride ceramics," *Proc. International Conference on Manufacturing Science and Engineering, MSEC 2006, October 8, 2006 - October 11, 2006, American Society of Mechanical Engineers*.
- [18] Dandekar, C. R., and Shin, Y. C., 2010, "Laser-assisted machining of a fiber reinforced metal matrix composite," *Journal of Manufacturing Science and Engineering, Transactions of the ASME*, 132.
- [19] Pfefferkorn, F. E., Lei, S., Jeon, Y., and Haddad, G., 2009, "A metric for defining the energy efficiency of thermally assisted machining," *International Journal of Machine Tools and Manufacture*, 49(5), pp. 357-365.
- [20] Aramcharoen, A., and Mativenga, P. T., 2009, "Size effect and tool geometry in micromilling of tool steel," *Precision Engineering*, 33(4), pp. 402-407.
- [21] Chae, J., Park, S. S., and Freiheit, T., 2006, "Investigation of micro-cutting operations," *International Journal of Machine Tools and Manufacture*, 46(3-4), pp. 313-332.

- [22] Shelton, J. A., and Shin, Y. C., 2010, "Comparative evaluation of laser-assisted micro-milling for AISI 316, AISI 422, Ti-6Al-4V and Inconel 718 in a side-cutting configuration," *Journal of Micromechanics and Microengineering*, 20, p. 075012.
- [23] Shelton, J. A., and Shin, Y. C., 2010, "Experimental evaluation of laser-assisted micromilling in a slotting configuration," *Journal of Manufacturing Science and Engineering, Transactions of the ASME*, 132, p. 0210081.
- [24] Stolyarov, V. V., Zhu, Y. T., Alexandrov, I. V., Lowe, T. C., and Valiev, R. Z., 2003, "Grain refinement and properties of pure Ti processed by warm ECAP and cold rolling," *Materials Science and Engineering A*, 343(1-2), pp. 43-50.
- [25] Ni, H., and Alpas, A. T., 2003, "Sub-micrometer structures generated during dry machining of copper," *Materials Science and Engineering A*, 361(1-2), pp. 338-349.
- [26] Elmadagli, M., and Alpas, A. T., 2003, "Metallographic analysis of the deformation microstructure of copper subjected to orthogonal cutting," *Materials Science and Engineering A*, 355(1-2), pp. 249-259.
- [27] Swaminathan, S., Shankar, M. R., Lee, S., Hwang, J., King, A. H., Kezar, R. F., Rao, B. C., Brown, T. L., Chandrasekar, S., Compton, W. D., and Trumble, K. P., 2005, "Large strain deformation and ultra-fine grained materials by machining," *Materials Science and Engineering A*, 410-411, pp. 358-363.
- [28] Zhang, H., and Alpas, A. T., 2002, "Quantitative evaluation of plastic strain gradients generated during orthogonal cutting of an aluminum alloy," *Materials Science and Engineering A*, 332(1-2), pp. 249-254.
- [29] Shankar, M. R., Rao, B. C., Lee, S., Chandrasekar, S., King, A. H., and Compton, W. D., 2006, "Severe plastic deformation (SPD) of titanium at near-ambient temperature," *Acta Materialia*, 54(14), pp. 3691-3700.
- [30] Shankar, M. R., Verma, R., Rao, B. C., Chandrasekar, S., Compton, W. D., King, A. H., and Trumble, K. P., 2007, "Severe plastic deformation of difficult-to-deform materials at near-ambient temperature," *Proc. Metallurgical and Materials Transactions A: Physical Metallurgy and Materials Science*, Springer Boston, pp. 1899-1905.
- [31] Calistes, R., Swaminathan, S., Murthy, T. G., Huang, C., Saldana, C., Shankar, M. R., and Chandrasekar, S., 2009, "Controlling gradation of surface strains and nanostructuring by large-strain machining," *Scripta Materialia*, 60(1), pp. 17-20.
- [32] Shankar, M. R., Chandrasekar, S., King, A. H., and Compton, W. D., 2005, "Microstructure and stability of nanocrystalline aluminum 6061 created by large strain machining," *Acta Materialia*, 53(18), pp. 4781-4793.
- [33] Shankar, M. R., Rao, B. C., Chandrasekar, S., Dale Compton, W., and King, A. H., 2008, "Thermally stable nanostructured materials from severe plastic deformation of precipitation-treatable Ni-based alloys," *Scripta Materialia*, 58(8), pp. 675-678.

- [34] Shekhar, S., Cai, J., Wang, J., and Shankar, M. R., 2009, "Multimodal ultrafine grain size distributions from severe plastic deformation at high strain rates," *Materials Science and Engineering: A*, 527(1-2), pp. 187-191.
- [35] Swaminathan, S., Brown, T. L., Chandrasekar, S., McNelley, T. R., and Compton, W. D., 2007, "Severe plastic deformation of copper by machining: Microstructure refinement and nanostructure evolution with strain," *Scripta Materialia*, 56(12), pp. 1047-1050.
- [36] Chou, Y. K., and Evans, C. J., 1999, "White layers and thermal modeling of hard turned surfaces," *International Journal of Machine Tools and Manufacture*, 39(12), pp. 1863-1881.
- [37] Jawahir, I. S., Brinksmeier, E., M'Saoubi, R., Aspinwall, D. K., Outeiro, J. C., Meyer, D., Umbrello, D., and Jayal, A. D., 2011, "Surface integrity in material removal processes: Recent advances," *CIRP Annals - Manufacturing Technology*, 60(2), pp. 603-626.
- [38] Umbrello, D., Outeiro, J. C., M'Saoubi, R., Jayal, A. D., and Jawahir, I. S., 2010, "A numerical model incorporating the microstructure alteration for predicting residual stresses in hard machining of AISI 52100 steel," *CIRP Annals - Manufacturing Technology*, 59(1), pp. 113-116.
- [39] Shi, B., and Attia, H., 2010, "Current status and future direction in the numerical modeling and simulation of machining processes: A critical literature review," *Machining Science and Technology*, 14(2), pp. 149-188.
- [40] Rebro, P. A., Pfefferkorn, F. E., Shin, Y. C., and Incropera, F. P., "Comparative assessment of laser-assisted machining for various ceramics," *Proc. NAMRC XXX*, May 21, 2002 - May 24, 2002, Society of Manufacturing Engineers, pp. 1-8.
- [41] Pfefferkorn, F. E., Incropera, F. P., and Shin, Y. C., 2005, "Heat transfer model of semi-transparent ceramics undergoing laser-assisted machining," *International Journal of Heat and Mass Transfer*, 48(10), pp. 1999-2012.
- [42] Gratias, J. F., Fan, L. J., Marot, G., Cohen, P., and Moisan, A., 1993, "Proposition of a method to optimize the machining of XC42 steel with laser assistance," *CIRP Annals - Manufacturing Technology*, 42, pp. 115-118.
- [43] Germain, G., Morel, F., Lebrun, J. L., Morel, A., and Huneau, B., 2006, "Effect of laser assistance machining on residual stress and fatigue strength for a bearing steel (100Cr6) and a titanium alloy (Ti6Al4V)," *Materials Science Forum*, 524-525, pp. 569-574.
- [44] Germain, G., Morel, F., Lebrun, J.-L., and Morel, A., 2007, "Machinability and surface integrity for a bearing steel and a titanium alloy in laser assisted machining (optimisation on LAM on two materials)," *Lasers in Engineering*, 17, pp. 329-344.
- [45] Dumitrescu, P., Koshy, P., Stenekes, J., and Elbestawi, M. A., 2006, "High-power diode laser assisted hard turning of AISI D2 tool steel," *International Journal of Machine Tools and Manufacture*, 46(15), pp. 2009-2016.

- [46] Attia, H., Tavakoli, S., Vargas, R., and Thomson, V., 2010, "Laser-assisted high-speed finish turning of superalloy Inconel 718 under dry conditions," *CIRP Annals - Manufacturing Technology*, 59(1), pp. 83-88.
- [47] Yang, J., Sun, S., Brandt, M., and Yan, W., 2010, "Experimental investigation and 3D finite element prediction of the heat affected zone during laser assisted machining of Ti6Al4V alloy," *Journal of Materials Processing Technology*, 210(15), pp. 2215-2222.
- [48] Liu, C. R., and Mittal, S., 1996, "Single-step superfinish hard machining: Feasibility and feasible cutting conditions," *Robotics and Computer-Integrated Manufacturing*, 12(1), pp. 15-27.
- [49] Rech, J., and Moisan, A., 2003, "Surface integrity in finish hard turning of case-hardened steels," *International Journal of Machine Tools and Manufacture*, 43(5), pp. 543-550.
- [50] Aramcharoen, A., Mativenga, P. T., Yang, S., Cooke, K. E., and Teer, D. G., 2008, "Evaluation and selection of hard coatings for micro milling of hardened tool steel," *International Journal of Machine Tools and Manufacture*, 48(14), pp. 1578-1584.
- [51] Melkote, S., Kumar, M., Hashimoto, F., and Lahoti, G., 2009, "Laser assisted micro-milling of hard-to-machine materials," *CIRP Annals - Manufacturing Technology*, 58, pp. 45-48.
- [52] Jeon, Y., 2008, "Laser-assisted micro end milling," Ph.D., The University of Wisconsin - Madison, Madison, WI.
- [53] Liu, K., and Melkote, S. N., 2007, "Finite element analysis of the influence of tool edge radius on size effect in orthogonal micro-cutting process," *International Journal of Mechanical Sciences*, 49(5), pp. 650-660.
- [54] Lai, X., Li, H., Li, C., Lin, Z., and Ni, J., 2008, "Modelling and analysis of micro scale milling considering size effect, micro cutter edge radius and minimum chip thickness," *International Journal of Machine Tools and Manufacture*, 48(1), pp. 1-14.
- [55] Liu, X., DeVor, R. E., and Kapoor, S. G., 2006, "An analytical model for the prediction of minimum chip thickness in micromachining," *Journal of Manufacturing Science and Engineering, Transactions of the ASME*, 128, pp. 474-481.
- [56] Liu, X., Devor, R. E., and Kapoor, S. G., 2007, "Model-based analysis of the surface generation in microendmilling - Part II: Experimental validation and analysis," *Journal of Manufacturing Science and Engineering, Transactions of the ASME*, 129, pp. 461-469.
- [57] Liu, X., DeVor, R. E., Kapoor, S. G., and Ehmann, K. F., 2004, "The mechanics of machining at the microscale: assessment of the current state of the science," *Transactions of the ASME. Journal of Manufacturing Science and Engineering*, 126, pp. 666-678.
- [58] Simoneau, A., Ng, E., and Elbestawi, M. A., 2006, "Surface defects during microcutting," *International Journal of Machine Tools and Manufacture*, 46(12-13), pp. 1378-1387.

- [59] Lee, K., and Dornfeld, D. A., 2005, "Micro-burr formation and minimization through process control," *Precision Engineering*, 29(2), pp. 246-252.
- [60] Filiz, S., Conley, C. M., Wasserman, M. B., and Ozdoganlar, O. B., 2007, "An experimental investigation of micro-machinability of copper 101 using tungsten carbide micro-endmills," *International Journal of Machine Tools and Manufacture*, 47(7-8), pp. 1088-1100.
- [61] Singh, R., Alberts, M. J., and Melkote, S. N., 2008, "Characterization and prediction of the heat-affected zone in a laser-assisted mechanical micromachining process," *International Journal of Machine Tools and Manufacture*, 48, pp. 994-1004.
- [62] Singh, R., Joseph, V., and Melkote, S., 2010, "A statistical approach to the optimization of a laser-assisted micromachining process," *The International Journal of Advanced Manufacturing Technology*, pp. 1-10.
- [63] Singh, R., and Melkote, S. N., 2007, "Characterization of a hybrid laser-assisted mechanical micromachining (LAMM) process for a difficult-to-machine material," *International Journal of Machine Tools and Manufacture*, 47(7-8), pp. 1139-1150.
- [64] Singh, R., and Melkote, S. N., 2009, "Force modeling in laser-assisted microgrooving including the effect of machine deflection," *Journal of Manufacturing Science and Engineering, Transactions of the ASME*, 131, pp. 0110131-0110139.
- [65] Jeon, Y., and Pfefferkorn, F. E., 2008, "Effect of laser preheating the workpiece on micro end milling of metals," *Journal of Manufacturing Science and Engineering, Transactions of the ASME*, 130, p. 011004.
- [66] Miguélez, M. H., Munoz-Sanchez, A., Cantero, J. L., and Loya, J. A., 2009, "An efficient implementation of boundary conditions in an ALE model for orthogonal cutting," *Journal of Theoretical and Applied Mechanics*, 47(3), pp. 599-616.
- [67] Miguélez, M. H., Zaera, R., Molinari, A., Cheriguene, R., and Rusinek, A., 2009, "Residual stresses in orthogonal cutting of metals: The effect of thermomechanical coupling parameters and of friction," *Journal of Thermal Stresses*, 32, pp. 269-289.
- [68] Nasr, M. N. A., Ng, E. G., and Elbestawi, M. A., 2007, "Modelling the effects of tool-edge radius on residual stresses when orthogonal cutting AISI 316L," *International Journal of Machine Tools and Manufacture*, 47(2), pp. 401-411.
- [69] Nasr, M. N. A., Ng, E. G., and Elbestawi, M. A., 2008, "A modified time-efficient FE approach for predicting machining-induced residual stresses," *Finite Elements in Analysis and Design*, 44(4), pp. 149-161.
- [70] Umbrello, D., and Filice, L., 2009, "Improving surface integrity in orthogonal machining of hardened AISI 52100 steel by modeling white and dark layers formation," *CIRP Annals - Manufacturing Technology*, 58(1), pp. 73-76.

- [71] Lorentzon, J., Järvstråt, N., and Josefson, B. L., 2009, "Modelling chip formation of alloy 718," *Journal of Materials Processing Technology*, 209(10), pp. 4645-4653.
- [72] Calamaz, M., Coupard, D., and Girot, F., 2008, "A new material model for 2D numerical simulation of serrated chip formation when machining titanium alloy Ti-6Al-4V," *International Journal of Machine Tools and Manufacture*, 48(3-4), pp. 275-288.
- [73] Sima, M., and Özel, T., 2010, "Modified material constitutive models for serrated chip formation simulations and experimental validation in machining of titanium alloy Ti-6Al-4V," *International Journal of Machine Tools and Manufacture*, 50(11), pp. 943-960.
- [74] Umbrello, D., 2008, "Finite element simulation of conventional and high speed machining of Ti6Al4V alloy," *Journal of Materials Processing Technology*, 196(1-3), pp. 79-87.
- [75] Rao, B., Dandekar, C. R., and Shin, Y. C., 2011, "An experimental and numerical study on the face milling of Ti-6Al-4V alloy: Tool performance and surface integrity," *Journal of Materials Processing Technology*, 211(2), pp. 294-304.
- [76] Hua, J., and Shivpuri, R., 2005, "A Cobalt Diffusion Based Model for Predicting Crater Wear of Carbide Tools in Machining Titanium Alloys," *Journal of Engineering Materials and Technology*, 127(1), pp. 136-144.
- [77] Lorentzon, J., and Järvstråt, N., 2008, "Modelling tool wear in cemented-carbide machining alloy 718," *International Journal of Machine Tools and Manufacture*, 48(10), pp. 1072-1080.
- [78] Usui, E., Shirakashi, T., and Kitagawa, T., 1984, "Analytical prediction of cutting tool wear," *Wear*, 100, pp. 129-151.
- [79] Chuzhoy, L., DeVor, R. E., Kapoor, S. G., and Bammann, D. J., 2002, "Microstructure-level modeling of ductile iron machining," *Journal of Manufacturing Science and Engineering, Transactions of the ASME*, 124, pp. 162-169.
- [80] Chuzhoy, L., DeVor, R. E., Kapoor, S. G., Beaudoin, A. J., and Bammann, D. J., 2003, "Machining Simulation of ductile iron and its constituents, part 1: estimation of material model parameters and their validation," *Transactions of the ASME. Journal of Manufacturing Science and Engineering*, 125(Copyright 2003, IEE), pp. 181-191.
- [81] Chuzhoy, L., DeVor, R. E., and Kapoor, S. G., 2003, "Machining Simulation of ductile iron and its constituents, part 2: numerical Simulation and experimental validation of Machining," *Transactions of the ASME. Journal of Manufacturing Science and Engineering*, 125, pp. 192-201.
- [82] Park, S., Kapoor, S. G., and DeVor, R. E., 2007, "Microstructure-level model for the prediction of tool failure in coated WC-Co cutting tool materials during intermittent cutting," *Journal of Manufacturing Science and Engineering, Transactions of the ASME*, 129, pp. 893-901.

- [83] Park, S., Kapoor, S. G., and DeVor, R. E., 2006, "Microstructure-level model for the prediction of tool failure in WC-Co cutting tool materials," Transactions of the ASME. Journal of Manufacturing Science and Engineering, 128, pp. 739-748.
- [84] Park, S., Kapoor, S. G., and DeVor, R. E., 2004, "Mechanistic cutting process calibration via microstructure-level finite element simulation model," Transactions of the ASME. Journal of Manufacturing Science and Engineering, 126, pp. 706-709.
- [85] Vogler, M. P., DeVor, R. E., and Kapoor, S. G., 2003, "Microstructure-level force prediction model for micro-milling of multi-phase materials," Journal of Manufacturing Science and Engineering, Transactions of the ASME, 125, pp. 202-209.
- [86] Vogler, M. P., Kapoor, S. G., and DeVor, R. E., 2004, "On the modeling and analysis of machining performance in micro-endmilling, Part II: Cutting force prediction," Transactions of the ASME. Journal of Manufacturing Science and Engineering, 126, pp. 695-705.
- [87] Dikshit, A., Samuel, J., DeVor, R. E., and Kapoor, S. G., 2008, "Microstructure-Level Machining Simulation of Carbon Nanotube Reinforced Polymer Composites---Part I: Model Development and Validation," Journal of Manufacturing Science and Engineering, 130(3), p. 031114.
- [88] Dikshit, A., Samuel, J., DeVor, R. E., and Kapoor, S. G., 2008, "Microstructure-Level Machining Simulation of Carbon Nanotube Reinforced Polymer Composites---Part II: Model Interpretation and Application," Journal of Manufacturing Science and Engineering, 130(3), p. 031115.
- [89] Dhanorker, A., and Özel, T., 2006, "An experimental and modeling study on meso/micro end milling process," Proc. 2006 ASME International Conference on Manufacturing Science and Engineering, MSEC2006 p. 21127.
- [90] Liu, K., and Melkote, S. N., 2006, "Material strengthening mechanisms and their contribution to size effect in micro-cutting," Transactions of the ASME. Journal of Manufacturing Science and Engineering, 128, pp. 730-738.
- [91] Tian, Y., Wu, B., Anderson, M., and Shin, Y. C., 2008, "Laser-assisted milling of silicon nitride ceramics and Inconel 718," Journal of Manufacturing Science and Engineering, Transactions of the ASME, 130, p. 031013.
- [92] Ding, H., Shen, N., and Shin, Y. C., 2011, "Experimental evaluation and modeling analysis of micromilling of hardened H13 tool steels," Transactions of the ASME. Journal of Manufacturing Science and Engineering, 133(4), p. 041007.
- [93] Petryk, H., and Stupkiewicz, S., 2007, "A quantitative model of grain refinement and strain hardening during severe plastic deformation," Materials Science and Engineering A, 444(1-2), pp. 214-219.

- [94] Beygelzimer, Y., 2005, "Grain refinement versus voids accumulation during severe plastic deformations of polycrystals: mathematical simulation," *Mechanics of Materials*, 37(7), pp. 753-767.
- [95] Arsenlis, A., and Parks, D. M., 1999, "Crystallographic aspects of geometrically-necessary and statistically-stored dislocation density," *Acta Materialia*, 47(5), pp. 1597-1611.
- [96] Arsenlis, A., and Parks, D. M., 2002, "Modeling the evolution of crystallographic dislocation density in crystal plasticity," *Journal of the Mechanics and Physics of Solids*, 50(9), pp. 1979-2009.
- [97] Ma, A., and Roters, F., 2004, "A constitutive model for fcc single crystals based on dislocation densities and its application to uniaxial compression of aluminium single crystals," *Acta Materialia*, 52(12), pp. 3603-3612.
- [98] Ma, A., Roters, F., and Raabe, D., 2007, "A dislocation density based constitutive law for BCC materials in crystal plasticity FEM," *Computational Materials Science*, 39(1), pp. 91-95.
- [99] Mohamed, F. A., 2003, "A dislocation model for the minimum grain size obtainable by milling," *Acta Materialia*, 51(14), pp. 4107-4119.
- [100] Starink, M. J., Qiao, X. G., Zhang, J., and Gao, N., 2009, "Predicting grain refinement by cold severe plastic deformation in alloys using volume averaged dislocation generation," *Acta Materialia*, 57(19), pp. 5796-5811.
- [101] Estrin, Y., Tóth, L. S., Molinari, A., and Bréchet, Y., 1998, "A dislocation-based model for all hardening stages in large strain deformation," *Acta Materialia*, 46(15), pp. 5509-5522.
- [102] Tóth, L. S., Molinari, A., and Estrin, Y., 2002, "Strain hardening at large strains as predicted by dislocation based polycrystal plasticity model," *Transactions of the ASME. Journal of Engineering Materials and Technology*, 124, pp. 71-77.
- [103] Baik, S. C., Hellmig, R. J., Estrin, Y., and Kim, H. S., 2003, "Modeling of deformation behavior of copper under equal channel angular pressing," *Zeitschrift fur Metallkunde*, 94, pp. 754-760.
- [104] Baik, S. C., Estrin, Y., Kim, H. S., and Hellmig, R. J., 2003, "Dislocation density-based modeling of deformation behavior of aluminum under equal channel angular pressing," *Materials Science and Engineering: A*, 351(1-2), pp. 86-97.
- [105] Baik, S. C., Estrin, Y., Kim, H. S., Jeong, H.-T., and Hellmig, R. J., 2002, "Calculation of deformation behavior and texture evolution during equal channel angular pressing of IF steel using dislocation based modeling of strain hardening," *Materials Science Forum*, 408-412, pp. 697-702.
- [106] Kim, H. S., and Estrin, Y., 2005, "Microstructural modelling of equal channel angular pressing for producing ultrafine grained materials," *Materials Science and Engineering A*, 410-411, pp. 285-289.

- [107] Lemiale, V., Estrin, Y., Kim, H. S., and O'Donnell, R., 2010, "Grain refinement under high strain rate impact: A numerical approach," *Computational Materials Science*, 48(1), pp. 124-132.
- [108] Hosseini, E., and Kazeminezhad, M., 2009, "A hybrid model on severe plastic deformation of copper," *Computational Materials Science*, 44(4), pp. 1107-1115.
- [109] Hosseini, E., and Kazeminezhad, M., 2011, "Implementation of a constitutive model in finite element method for intense deformation," *Materials & Design*, 32(2), pp. 487-494.
- [110] Zherebtsov, S. V., Dyakonov, G. S., Salem, A. A., Malysheva, S. P., Salishchev, G. A., and Semiatin, S. L., 2011, "Evolution of grain and subgrain structure during cold rolling of commercial-purity titanium," *Materials Science and Engineering: A*, 528(9), pp. 3474-3479.
- [111] Stolyarov, V. V., Zeipper, L., Mingler, B., and Zehetbauer, M., 2008, "Influence of post-deformation on CP-Ti processed by equal channel angular pressing," *Materials Science and Engineering: A*, 476(1-2), pp. 98-105.
- [112] Shin, D. H., Kim, I., Kim, J., Kim, Y. S., and Semiatin, S. L., 2003, "Microstructure development during equal-channel angular pressing of titanium," *Acta Materialia*, 51(4), pp. 983-996.
- [113] Pachla, W., Kulczyk, M., Sus-Ryszkowska, M., Mazur, A., and Kurzydowski, K. J., 2008, "Nanocrystalline titanium produced by hydrostatic extrusion," *Journal of Materials Processing Technology*, 205(1-3), pp. 173-182.
- [114] Wu, S., Fan, K., Jiang, P., and Chen, S., 2010, "Grain refinement of pure Ti during plastic deformation," *Materials Science and Engineering: A*, 527(26), pp. 6917-6921.
- [115] Argon, A. S., and Haasen, P., 1993, "A new mechanism of work hardening in the late stages of large strain plastic flow in F.C.C. and diamond cubic crystals," *Acta Metallurgica et Materialia*, 41(11), pp. 3289-3306.
- [116] Zhu, K. Y., Vassel, A., Brisset, F., Lu, K., and Lu, J., 2004, "Nanostructure formation mechanism of α -titanium using SMAT," *Acta Materialia*, 52(14), pp. 4101-4110.
- [117] Yang, D. K., Cizek, P., Hodgson, P. D., and Wen, C. E., 2010, "Microstructure evolution and nanograin formation during shear localization in cold-rolled titanium," *Acta Materialia*, 58(13), pp. 4536-4548.
- [118] Zhu, Y. T., Huang, J. Y., Gubicza, J., Ungar, T., Wang, Y. M., Ma, E., and Valiev, R. Z., 2003, "Nanostructures in Ti processed by severe plastic deformation," *Journal of Materials Research*, 18, pp. 1908-1917.
- [119] Inoue, T., 2002, "Metallo-thermo-mechanics—Application to quenching," *Handbook of Residual Stress and Deformation of Steel*, G. E. Totten, M. A. H. Howes, and T. Inoue, eds., ASM International, Materials Park, OH, pp. 296-311.

- [120] Denis, S., Archambault, P., Gautier, E., Simon, A., and Beck, G., 2002, "Prediction of residual stress and distortion of ferrous and non-ferrous metals: Current status and future developments," *Journal of Materials Engineering and Performance*, 11(1), pp. 92-102.
- [121] Bailey, N. S., Tan, W., and Shin, Y. C., 2009, "Predictive modeling and experimental results for residual stresses in laser hardening of AISI 4140 steel by a high power diode laser," *Surface and Coatings Technology*, 203, pp. 2003-2012.
- [122] Ashby, M. F., and Easterling, K. E., 1984, "The transformation hardening of steel surfaces by laser beams--I. Hypo-eutectoid steels," *Acta Metallurgica*, 32(11), pp. 1935-1937.
- [123] Skvarenina, S., and Shin, Y. C., 2006, "Predictive modeling and experimental results for laser hardening of AISI 1536 steel with complex geometric features by a high power diode laser," *Surface and Coatings Technology*, 201, pp. 2256-2269.
- [124] Patwa, R., and Shin, Y. C., 2007, "Predictive modeling of laser hardening of AISI5150H steels," *International Journal of Machine Tools and Manufacture*, 47(2), pp. 307-320.
- [125] Mahdi, M., and Zhang, L., 1998, "Applied mechanics in grinding—VI. Residual stresses and surface hardening by coupled thermo-plasticity and phase transformation," *International Journal of Machine Tools and Manufacture*, 38(10-11), pp. 1289-1304.
- [126] Mahdi, M., and Zhang, L., 1999, "Applied mechanics in grinding. Part 7: residual stresses induced by the full coupling of mechanical deformation, thermal deformation and phase transformation," *International Journal of Machine Tools and Manufacture*, 39(8), pp. 1285-1298.
- [127] Ramesh, A., and Melkote, S. N., 2008, "Modeling of white layer formation under thermally dominant conditions in orthogonal machining of hardened AISI 52100 steel," *International Journal of Machine Tools and Manufacture*, 48, pp. 402-414.
- [128] Burns, T. J., Mates, S. P., Rhorer, R. L., Whitenton, E. P., and Basak, D., 2011, "Dynamic properties for modeling and simulation of machining: Effect of pearlite to austenite phase transition on flow stress in AISI 1075 steel," *Machining Science and Technology*, 15, pp. 1-20.
- [129] Burns, T. J., Mates, S. P., Rhorer, R. L., Whitenton, E. P., and Basak, D., "Effect on flow stress of a rapid phase transition in AISI 1045 steel," *Proc. Proceedings of the 2011 ASME International Manufacturing Science and Engineering Conference, MSEC2011-50229*, American Society of Mechanical Engineers.
- [130] Griffiths, B. J., 1987, "Mechanisms of white layer generation with reference to machining and deformation processes," *Journal of Tribology*, 109, pp. 525-530.
- [131] Sauvage, X., Le Breton, J. M., Guillet, A., Meyer, A., and Teillet, J., 2003, "Phase transformations in surface layers of machined steels investigated by X-ray diffraction and Mössbauer spectrometry," *Materials Science and Engineering A*, 362(1-2), pp. 181-186.

- [132] Li, J. G., Umemoto, M., Todaka, Y., and Tsuchiya, K., 2007, "A microstructural investigation of the surface of a drilled hole in carbon steels," *Acta Materialia*, 55, pp. 1397-1406.
- [133] Todaka, Y., Umemoto, M., Li, J., and Tsuchiya, K., 2005, "Nanocrystallization of drill hole surface by high speed drilling," *Journal of Metastable and Nanocrystalline Materials*, 24-25, pp. 601-604.
- [134] Ramesh, A., Melkote, S. N., Allard, L. F., Riester, L., and Watkins, T. R., 2005, "Analysis of white layers formed in hard turning of AISI 52100 steel," *Materials Science and Engineering A*, 390(1-2), pp. 88-97.
- [135] Umbrello, D., Jayal, A. D., Caruso, S., Dillon, O. W., and Jawahir, I. S., 2010, "Modeling of white and dark layer formation in hard machining of AISI 52100 bearing steel," *Machining Science and Technology*, 14, pp. 128-147.
- [136] Shi, J., and Liu, C. R., 2006, "On predicting chip morphology and phase transformation in hard machining," *International Journal of Advanced Manufacturing Technology*, 27, pp. 645-654.
- [137] Umbrello, D., and Jawahir, I. S., 2009, "Numerical modeling of the influence of process parameters and workpiece hardness on white layer formation in AISI 52100 steel," *International Journal of Advanced Manufacturing Technology*, 44, pp. 955-968.
- [138] Caruso, S., Di Renzo, S., Umbrello, D., Jayal, A. D., Dillon, O. W., and Jawahir, I. S., "Finite element modeling of microstructural changes in hard turning," *Proc. 17th CIRP Conference on Modelling of Machining Operations*, May 12, 2011 - May 13, 2011, Trans Tech Publications, pp. 960-968.
- [139] ABAQUS, 2010, *ABAQUS User's Manual*, Version 6.10, Hibbitt, Karlsson & Sorensen, Inc., Pawtucket, RI.
- [140] Joshi, S. S., and Melkote, S. N., 2004, "An explanation for the size-effect in machining using strain gradient plasticity," *Transactions of the ASME. Journal of Manufacturing Science and Engineering*, 126, pp. 679-684.
- [141] Peyre, P., Chaieb, I., and Braham, C., 2007, "FEM calculation of residual stresses induced by laser shock processing in stainless steels," *Model Simul Mater Sci Eng*, 15, pp. 205-221.
- [142] Kobayashi, T., Simons, J. W., Brown, C. S., and Shockey, D. A., 2008, "Plastic flow behavior of Inconel 718 under dynamic shear loads," *International Journal of Impact Engineering*, 35, pp. 389-396.
- [143] CINDAS, 2011, "Thermophysical Properties of Matter Database (TPMD)," CINDAS LLC, West Lafayette, IN.
- [144] Davis, J. W., 1997, "Shear Modulus of Inconel 718," *Iter Material Properties Handbook*, AD02-2112(3), pp. 1-3.

- [145] Fukuhara, M., and Sanpei, A., 1993, "Elastic Moduli and Internal Frictions of Inconel 718 and Ti-6Al-4V as a Function of Temperature," *Journal of Materials Science Letters*, 12, pp. 1122-1124.
- [146] Park, S. S., 2007, "Development of a microstructure-level finite element model for the prediction of tool failure by chipping in tungsten carbide-cobalt systems," Ph.D., University of Illinois at Urbana-Champaign, Urbana, IL.
- [147] Özerdem, B., 2000, "Measurement of convective heat transfer coefficient for a horizontal cylinder rotating in quiescent air," *International Communications in Heat and Mass Transfer*, 27(3), pp. 389-395.
- [148] Ohgo, K., 1978, "The adhesion mechanism of the built-up edge and the layer on the rake face of a cutting tool," *Wear*, 51, pp. 117-126.
- [149] Estrin, Y., and Kim, H. S., 2007, "Modelling microstructure evolution toward ultrafine crystallinity produced by severe plastic deformation," *Journal of Materials Science*, 42, pp. 1512-1516.
- [150] Mohamed, F. A., and Xun, Y., 2003, "Correlations between the minimum grain size produced by milling and material parameters," *Materials Science and Engineering A*, A354, pp. 133-139.
- [151] Ding, H., Shen, N., and Shin, Y. C., 2010, "A numerical approach of predicting grain refinement during multi-pass cold rolling," *Journal of materials processing technology*.
- [152] Fang, N., 2005, "A new quantitative sensitivity analysis of the flow stress of 18 engineering materials in machining," *Transactions of the ASME. Journal of Engineering Materials and Technology*, 127, pp. 192-196.
- [153] Johnson, G. R., and Cook, W. H., 1983, "A constitutive model and data for metals subjected to large strains, high rates and high temperatures," in *Proceedings of the Seventh International Symposium on Ballistics*. The Netherlands: The Hague, pp. 541-547.
- [154] Cai, J., Shekhar, S., Wang, J., and Shankar, M. R., 2009, "Nanotwinned microstructures from low stacking fault energy brass by high-rate severe plastic deformation," *Scripta Materialia*, 60(8), pp. 599-602.
- [155] Pantleon, W., 2005, "On the apparent saturation of the average disorientation angle with plastic deformation," *Scripta Materialia*, 53(6), pp. 757-762.
- [156] Ivester, R. W., Kennedy, M., Davies, M., Stevenson, R., Thiele, J., Furness, R., and Athavale, S., 2000, "Assessment of machining models: progress report," *Machining Science and Technology*, 4(3), pp. 511-538.
- [157] Lakhkar, R. S., Shin, Y. C., and Krane, M. J. M., 2008, "Predictive modeling of multi-track laser hardening of AISI 4140 steel," *Materials Science and Engineering A*, 480, pp. 209-217.

- [158] Lee, C.-H., and Chang, K.-H., 2009, "Finite element simulation of the residual stresses in high strength carbon steel butt weld incorporating solid-state phase transformation," *Computational Materials Science*, 46(4), pp. 1014-1022.
- [159] Lee, C.-H., and Chang, K.-H., 2011, "Prediction of residual stresses in high strength carbon steel pipe weld considering solid-state phase transformation effects," *Computers & Structures*, 89(1-2), pp. 256-265.
- [160] Deng, D., 2009, "FEM prediction of welding residual stress and distortion in carbon steel considering phase transformation effects," *Materials & Design*, 30(2), pp. 359-366.
- [161] Simsir, C., and Gür, C. H., 2008, "3D FEM simulation of steel quenching and investigation of the effect of asymmetric geometry on residual stress distribution," *Journal of Materials Processing Technology*, 207(1-3), pp. 211-221.
- [162] Bailey, N. S., and Shin, Y. C., "Optimization of laser hardening processes for industrial parts with complex geometry via predictive modeling," *Proc. Proceedings of the 2009 ASME International Manufacturing Science and Engineering Conference, MSEC2009, American Society of Mechanical Engineers*, pp. 647-656.
- [163] Han, S., Melkote, S. N., Haluska, M. S., and Watkins, T. R., 2008, "White layer formation due to phase transformation in orthogonal machining of AISI 1045 annealed steel," *Materials Science and Engineering A*, 488, pp. 195-204.
- [164] Lee, S.-J., Pavlina, E. J., and Van Tyne, C. J., 2010, "Kinetics modeling of austenite decomposition for an end-quenched 1045 steel," *Materials Science and Engineering: A*, 527(13-14), pp. 3186-3194.
- [165] Bhadeshia, H. K. D. H., 2002, "Material factors," *Handbook of Residual Stress and Deformation of Steel*, G. E. Totten, M. A. H. Howes, and T. Inoue, eds., ASM International, Materials Park, OH, pp. 3-10.
- [166] Iqbal, S. A., Mativenga, P. T., and Sheikh, M. A., 2007, "Characterization of machining of AISI 1045 steel over a wide range of cutting speeds. Part 2: Evaluation of flow stress models and interface friction distribution schemes," *Proceedings of the Institution of Mechanical Engineers, Part B: Journal of Engineering Manufacture*, 221, pp. 917-926.
- [167] Davis, J. R., 1996, *Cast Irons (ASM Specialty Handbook)*, ASM international, Materials Park, OH.
- [168] Sharma, V. K., Breyer, N. N., Abe, N., and Schwartz, L. H., 1974, "Effects of plastic deformation on the density of a medium carbon martensite," *Scripta Metallurgica*, 8(6), pp. 699-701.
- [169] Jaspers, S. P. F. C., and Dautzenberg, J. H., 2002, "Material behaviour in conditions similar to metal cutting: flow stress in the primary shear zone," *Journal of Materials Processing Technology*, 122(2-3), pp. 322-330.

- [170] Iwamoto, T., Tsuta, T., and Tomita, Y., 1998, "Investigation on deformation mode dependence of strain-induced martensitic transformation in trip steels and modelling of transformation kinetics," *International Journal of Mechanical Sciences*, 40(2-3), pp. 173-182.
- [171] Iwamoto, T., 2004, "Multiscale computational simulation of deformation behavior of TRIP steel with growth of martensitic particles in unit cell by asymptotic homogenization method," *International Journal of Plasticity*, 20(4-5), pp. 841-869.
- [172] Simsir, C., and Gür, C. H., 2008, "A FEM based framework for simulation of thermal treatments: Application to steel quenching," *Computational Materials Science*, 44(2), pp. 588-600.
- [173] Ferro, P., Porzner, H., Tiziani, A., and Bonollo, F., 2006, "The influence of phase transformations on residual stresses induced by the welding process-3D and 2D numerical models," *Modelling and Simulation in Materials Science and Engineering*, 14, pp. 117-136.
- [174] Yaghi, A. H., Hyde, T. H., Becker, A. A., and Sun, W., 2008, "Finite element simulation of welding and residual stresses in a P91 steel pipe incorporating solid-state phase transformation and post-weld heat treatment," *Journal of Strain Analysis for Engineering Design*, 43, pp. 275-293.
- [175] Rammerstorfer, F. G., Fischer, D. F., Mitter, W., Bathe, K. J., and Snyder, M. D., 1981, "On thermo-elastic-plastic analysis of heat-treatment processes including creep and phase changes," *Computers and Structures*, 13, pp. 771-779.
- [176] Lalwani, D. I., Mehta, N. K., and Jain, P. K., 2009, "Extension of Oxley's predictive machining theory for Johnson and Cook flow stress model," *Journal of Materials Processing Technology*, 209(12-13), pp. 5305-5312.
- [177] Karpat, Y., and Özel, T., 2006, "Predictive Analytical and Thermal Modeling of Orthogonal Cutting Process---Part I: Predictions of Tool Forces, Stresses, and Temperature Distributions," *Journal of Manufacturing Science and Engineering, Transactions of the ASME*, 128(2), pp. 435-444.
- [178] Iqbal, S. A., Mativenga, P. T., and Sheikh, M. A., 2007, "Characterization of machining of AISI 1045 steel over a wide range of cutting speeds. Part 1: Investigation of contact phenomena," *Proceedings of the Institution of Mechanical Engineers, Part B: Journal of Engineering Manufacture*, 221, pp. 909-916.
- [179] Ding, H., Shen, N., and Shin, Y. C., 2012, "Thermal and mechanical modeling analysis of laser-assisted micro-milling of difficult-to-machine alloys," *Journal of Materials Processing Technology*, 212(3), pp. 601-613.
- [180] Özel, T., 2006, "The influence of friction models on finite element simulations of machining," *International Journal of Machine Tools and Manufacture*, 46(5), pp. 518-530.

- [181] Oxley, P. L. B., 1989, *The mechanics of machining: an analytical approach to assessing machinability*, Ellis Horwood Ltd., England.
- [182] Zhang, X., Wu, S., Wang, H., and Liu, C. R., 2011, "Predicting the Effects of Cutting Parameters and Tool Geometry on Hard Turning Process Using Finite Element Method," *Journal of Manufacturing Science and Engineering*, 133(4), p. 041010.
- [183] Vander Voort, G. F., 1991, "Atlas of Time-Temperature Diagrams for Irons and Steels," ASM International.
- [184] Li, B. L., Godfrey, A., Meng, Q. C., Liu, Q., and Hansen, N., 2004, "Microstructural evolution of IF-steel during cold rolling," *Acta Materialia*, 52(4), pp. 1069-1081.
- [185] Ding, H., and Shin, Y. C., 2012, "Dislocation density-based modeling of subsurface grain refinement with laser-induced shock compression," *Computational Materials Science*, 53(1), pp. 79-88.
- [186] Ding, H., and Shin, Y. C., "Dislocation density-based grain refinement modeling of orthogonal cutting of commercially pure titanium," *Proc. Proceedings of the 2011 ASME International Manufacturing Science and Engineering Conference, MSEC2011-50220*, American Society of Mechanical Engineers.
- [187] Ding, H., Shen, N., and Shin, Y. C., 2011, "Modeling of grain refinement in aluminum and copper subjected to cutting," *Computational Materials Science*, 50(10), pp. 3016-3025.
- [188] Marusich, T., 2011, *AdvantEdge FEM 5.8 User's Manual*, Third Wave Systems Inc., Minneapolis, MN.
- [189] Chou, Y. K., and Hui, S., 2004, "Tool nose radius effects on finish hard turning," *Journal of Materials Processing Technology*, 148, pp. 259-268.
- [190] Poulachon, G., Albert, A., Schluraff, M., and Jawahir, I. S., 2005, "An experimental investigation of work material microstructure effects on white layer formation in PCBN hard turning," *International Journal of Machine Tools & Manufacture*, 45, pp. 211-218.
- [191] Guo, Y. B., and Sahni, J., 2004, "A comparative study of hard turned and cylindrically ground white layers," *International Journal of Machine Tools and Manufacture*, 44(2-3), pp. 135-145.
- [192] Grzesik, W., Rech, J., and Wanat, T., 2007, "Surface finish on hardened bearing steel parts produced by superhard and abrasive tools," *International Journal of Machine Tools and Manufacture*, 47(2), pp. 255-262.
- [193] XuePing, Z., Liu, C. R., and Zhenqiang, Y., 2007, "Experimental study and evaluation methodology on hard surface integrity," *International Journal of Advanced Manufacturing Technology*, 34, pp. 141-148.

- [194] Jacobson, M., 2002, "Surface integrity of hard-turned M50 steel," Professional Engineering Publishing Ltd., pp. 47-54.
- [195] Zorc, T. B. e. a. E., 1990, "Properties and Selection: Irons, Steels, and High-performance Alloys," Metals Handbook v1, 10th ed., ASM International.
- [196] Murthy, J. Y., and Mathur, S. R., 1998, "A conservative numerical scheme for the energy equation," Transactions of the ASME. Journal of Heat Transfer, 120, pp. 1081-1086.
- [197] Patankar, S. V., 1980, Numerical heat transfer and fluid flow, Hemisphere Pub. Corp. ; McGraw-Hill, Washington; New York.
- [198] Rozzi, J. C., Krane, M. J. M., Incropera, F. P., and Shin, Y. C., "Numerical prediction of three-dimensional unsteady temperatures in a rotating cylindrical workpiece subjected to localized heating by a translating laser source," Proc. Proceedings of the 1995 ASME International Mechanical Engineering Congress and Exposition, November 12, 1995 - November 17, 1995, ASME, pp. 399-411.
- [199] Davis, J. R., 2000, "Alloy Digest," ASM International, Alloy Digest Inc, New Jersey.
- [200] Joeckle, R. C., Schellhorn, M., Stern, G., Sontag, A., and Gautier, B., 1994, "Influence of the wavelength for infrared laser effects on metals and dielectrics," SPIE Laser Applications, 2097, pp. 139-145.
- [201] Stern, G., 1990, "Absorptivity of cw CO₂, CO and YAG-laser beams by different metallic alloys," Proceedings of the 3rd European Conference on Laser Treatment of Materials, Erlangen, Germany, pp. 25-35.
- [202] Pantsar, H., and Kujanp, V., 2004, "Effect of oxide layer growth on diode laser beam transformation hardening of steels, Surface & Coatings Technology," Surface & Coatings Technology, 200, pp. 2627-2633.
- [203] Özel, T., Karpat, Y., and Srivastava, A., 2008, "Hard turning with variable micro-geometry PcbN tools," CIRP Annals - Manufacturing Technology, 57(1), pp. 73-76.
- [204] Lampman, S. R., and Zorc, T. B., 1990, "Properties and Selection: Irons, Steels, and High-performance Alloys," Metals Handbook, ASM International, Materials Park, OH.
- [205] Lee, W.-S., and Yeh, G.-W., 1997, "The plastic deformation behaviour of AISI 4340 alloy steel subjected to high temperature and high strain rate loading conditions," Journal of Materials Processing Technology, 71(2), pp. 224-234.
- [206] Klopp, W. D., 1995, "Aerospace Structural Metals Handbook," Purdue Research Foundation, West Lafayette, Indiana.
- [207] Ding, H., and Shin, Y. C., 2012, "Improvement of machinability of waspaloy via laser-assisted machining," International Journal of Advanced Manufacturing Technology, In Press, DOI: 10.1007/s00170-012-4012-8.

[208] Vander Voort, G. F., 2004, "ASM Handbook: Metallography and Microstructures," ASM International.

VITA

VITA

Hongtao Ding
School of Mechanical Engineering, Purdue University

Hongtao Ding received his BSME (2002, with a minor in Applied Mathematics) from Shanghai Jiao Tong University, China, and MSME (2004) from the University of Michigan at Ann Arbor. His research interests are in experimental analysis and physics-based modeling of manufacturing processes with a focus on a) thermally enhanced machining and micromachining and b) microstructural alteration. He is a recipient of Best Paper Award from ASME/MSEC2011 for his research on grain refinement modeling in titanium cutting, and has received a Lambert Teaching Fellowship from Purdue University.